Investigation of Magnetoelectric Properties in Transition Metal Oxides and Their Applications

Thesis submitted for the degree of

Doctor of Philosophy (Science)

in

Physics (Experimental)

by

Swarnali Hait

Department of Physics
University of Calcutta
2023

Dedicated to Maa, Baba and Dida………

ABSTRACT

Magnetoelectric materials, one kind of multiferroic material, have gained significant interest because of their applications in spintronics, microwave absorption, memory devices, actuators, sensors, etc. However, there are very few multiferroics in nature that exhibit strong enough magnetoelectric coupling at room temperature hindering its applicability in practical purposes. In this thesis, addressing the aforementioned issue, many possible ways such as doping with suitable elements, changing synthesis conditions and morphology, and formation of composites with suitable materials have been investigated in order to improve their applicability in practical uses. Due to the growing interest in using magnetoelectric materials having both electric and magnetic properties along with a coupling existing between the two properties, the application of synthesized magnetoelectric materials as microwave absorbing materials (MAMs) is also reported in the thesis. It is observed that the barium and yttrium co-doping at the bismuth (Bi) site of $BiFeO_3$ (BFO) in the bulk morphology is responsible for a significant improvement in the grain and grain boundary resistances of the materials along with a reduction in conductivity which is a very important aspect for the practical application of the materials. Stronger magnetization having a metamagnetic transition along with higher Neel temperature is also achieved by this doping. However, changing the morphology from bulk to nano further improves the magnetic properties of the materials eliminating the metamagnetic transition. Although no sign of ferroelectric domain switching was observed in the bulk form, the nano-structural form having lower yttrium doping concentrations reports stronger domain switching. Further study of the similar co-doping in the thin film structure also confirms the formation of good quality thin films having stronger piezoelectric response, and stronger magnetic properties than the undoped BFO thin film. Effect of formation of composite with highly resistive garnet, Gadolinium Gallium Garnet ($Gd_3Ga_5O_{12}$, GGG), with another well-known magnetoelectric material with strong magnetoelectric coupling, Gallium Ferrite ($Ga_{2-x}Fe_xO_3$, GFO) is thoroughly investigated at different synthesis conditions. A reduction in leakage by four orders of magnitude along with a lowered conductivity is achieved in (1-x) GFO – x GGG ($0.0 \leq x \leq 0.2$) composites as a result of enhanced grain and grain boundary resistances. Formation of composite with ferromagnetic Yttrium Iron Garnet ($Y_3Fe_5O_{12}$, YIG) enhances the magnetic Curie temperature of GFO beyond room temperature (300 K) along with a significant enhancement in overall magnetization of (1-x) GFO – x YIG ($0.0 \leq x \leq 0.1$) composites. The dielectric properties are greatly improved in both composites while the conductivity is significantly reduced. The large enhancement in the magnetodielectric

properties of both composites indicates stronger coupling between the magnetic and electric properties. The formation of a composite between YIG and a strong room temperature ferroelectric and diamagnetic material, a solid solution of sodium bismuth titanate and strontium titanate ($Sr_{0.5}Na_{0.25}Bi_{0.25}TiO_3$, SNBT50) are observed to induce strong domain switching in the composites along with an increment in electrical breakdown voltage which intensified with increasing concentrations of YIG in the composites. Although no average magnetodielectric factor could be observed in the SNBT50 sample, large values of magnetodielectric factor observed in (1-x) SNBT50 – x YIG ($0.0 \leq x \leq 0.2$) composites implies the implementation of coupling between electric and magnetic properties by the formation of the composites. GFO is observed to have a reflection loss of -67.36 dB for an absorber length of 6.2mm attributed to its high dielectric permittivity, high magnetic permeability, and attenuation constant alongside an optimal impedance matching. Elemental substitution of Bismuth with the optimized concentrations of Barium and Yttrium in Bismuth Ferrite nanoparticles is observed to enhance the reflection loss of Bismuth Ferrite from -38.6 dB to -61.7 dB in an absorber of length 7.5mm attributed to enhanced dielectric permittivity, magnetic permeability, best impedance matching and the best balance observed between $\tan\delta_\varepsilon$ and $\tan\delta_\mu$ based on the match equation, $\tan\delta_\varepsilon = \tan\delta_\mu$. The (1-$x$) SNBT50 – x YIG magnetoelectric composite exhibits a higher microwave absorption compared to its parent sample, SNBT50, due to its improved dielectric constant, magnetic permeability, and impedance matching.

সারাংশ

চুম্বকিয়তড়িৎ পদার্থ, এক প্রকারের মাল্টিফেরোইক পদার্থ, ব্যতিক্রমীভাবে ব্যাপক মনোযোগ অর্জন করেছে স্পিন পরিবহন সংক্রান্ত বৈদ্যুতিন বিদ্যা অথবা স্পিনট্রনিক্স, মাইক্রোতরঙ্গ শোষণ, স্মৃতি ধারণক্ষমতাসম্পন্ন যন্ত্র (memory device), সক্রিয়কারক (actuator), অনুভবক (sensor) ইত্যাদি ক্ষেত্রে তাদের বহুল প্রয়োগের কারণে। তবে প্রকৃতিতে খুব কম সংখ্যক মাল্টিফেরোইক পদার্থ রয়েছে যা ঘরের তাপমাত্রায় যথেষ্ট শক্তিশালী চুম্বকিয়তড়িৎ যুগ্মীকরণ প্রদর্শন করে যা ব্যবহারিক উদ্দেশ্যে এর প্রয়োগযোগ্যতাকে বাধা দেয়। এই প্রবন্ধে, পূর্বোক্ত সমস্যাটির সমাধানার্থে উপযুক্ত উপাদানের দ্বারা প্রতিস্থাপন, সংশ্লেষণের দশার পরিবর্তন, আকৃতিগত পরিবর্তন, এবং উপযুক্ত উপকরণগুলির সাথে যৌগিক গঠনের মতো অনেকগুলি সম্ভাব্য উপায় অনুসন্ধান করা হয়েছে ব্যবহারিক উদ্দেশ্যে এর প্রয়োগযোগ্যতাকে বৃদ্ধি করার জন্য। বৈদ্যুতিক এবং চৌম্বকীয় উভয় বৈশিষ্ট্যযুক্ত চুম্বকিয়তড়িৎ পদার্থের মধ্যে বিদ্যমান অতিরিক্ত চুম্বকিয়তড়িৎ যুগ্মীকরণ এর উপস্থিতির দরুন মাইক্রোতরঙ্গ শোষণকারী উপকরণ হিসাবে এই পদার্থের ব্যবহার যোগ্যতাও এই প্রবন্ধে বিবৃত করা হয়েছে। এটি নিরীক্ষণ করা গেছে যে বাল্ক আকৃতিতে বিসমাথ ফেরাইট ($BiFeO_3$, BFO) এর বিসমাথ (Bi) এর জায়গায় বেরিয়াম (Ba) এবং ইট্রিয়াম (Y) এর দ্বারা ডোপিং করার ফলে গ্রেইন এবং গ্রেইন সীমানার প্রতিরোধ ক্ষমতা উল্লেখযোগ্যভাবে বৃদ্ধিপ্রাপ্ত হয়েছে এবং সামগ্রিক তড়িৎ পরিবাহিতা দারুণভাবে হ্রাসপ্রাপ্ত হয়েছে যেটি ব্যবহারিক প্রয়োগের জন্য খুবই গুরুত্বপূর্ণ দিক। উচ্চ চৌম্বকীয় দশান্তর তাপমাত্রার সাথে একটি মেটাম্যাগনেটিক অবস্থান্তর সহ শক্তিশালী চৌম্বক ক্ষমতাও অর্জন করা হয়েছে এই প্রতিস্থাপনের মাধ্যমে। তবে আকারের পরিবর্তন বাল্ক থেকে ন্যানোমিটার স্কেলে হ্রাস করার মাধ্যমে মেটাম্যাগনেটিক অবস্থান্তর দূর করে পদার্থের চৌম্বকীয় বৈশিষ্ট্যকে আরও উন্নত করা গেছে। যদিও বাল্ক ফর্মে ফেরোবৈদ্যুতিক ডোমেইন পরিবর্তনের কোনও চিহ্ন দেখা যায়নি, ন্যানোকাঠামোতে অপেক্ষাকৃত কম ইট্রিয়াম ডোপিং ঘনত্বের সাথে শক্তিশালী ডোমেইন পরিবর্তন লক্ষিত হয়েছে। ফিল্মের আকৃতিতে অনুরূপ ডোপিং বিসমাথ ফেরাইট এর অধ্যয়ন ভাল মানের পাতলা ফিল্মের গঠন নিশ্চিত করে যাতে অপ্রতিস্থাপিত বিসমাথ ফেরাইট এর পাতলা ফিল্মের তুলনায় শক্তিশালী পাইজোইলেক্ট্রিক প্রতিক্রিয়া এবং শক্তিশালী চৌম্বকীয় বৈশিষ্ট্য নিরীক্ষণ করা গেছে। উচ্চ রোধসম্পন্ন গারনেট, গ্যাডোলিনিয়াম গ্যালিয়াম গারনেট ($Gd_3Ga_5O_{12}$, GGG), শক্তিশালী চুম্বকিয়তড়িৎ যুগ্মীকরণ সহ আরেকটি সুপরিচিত চুম্বকিয়তড়িৎ উপাদান, গ্যালিয়াম ফেরাইট ($Ga_{2-x}Fe_xO_3$,

GFO) এর সাথে যৌগিক গঠনের প্রভাব এর ফলে উৎপন্ন বিভিন্ন অবস্থার পরিবর্তনের পুঙ্খানুপুঙ্খভাবে তদন্ত করা হয়েছে। গ্রেইন এবং গ্রেইন সীমানার রোধ বৃদ্ধির ফলে (1-x) GFO – x GGG ($0.0 \leq x \leq 0.2$) উপাদানগুলিতে বহিঃনির্গত তড়িৎ প্রবাহ প্রায় চতুর্থ মাত্রায় হ্রাসপ্রাপ্ত হয়েছে। অত্যন্ত প্রতিরোধী (~ 10^{12} Ω.cm) গারনেট, ইট্রিয়াম আয়রন গারনেট ($Y_3Fe_5O_{12}$, YIG) এর সাথে GFO এর যৌগিক গঠন GFO এর চৌম্বকীয় কুরি তাপমাত্রা ঘরের তাপমাত্রার (300 K) থেকে বেশি বৃদ্ধি করে এবং (1-x) GFO – x YIG ($0.0 \leq x \leq 0.1$) যৌগিক এর চৌম্বক ক্ষমতা সামগ্রিকভাবে বৃদ্ধি করে। উপরোক্ত উভয় যৌগিক এর অন্তরক বৈশিষ্ট্যগুলি ব্যাপকভাবে উন্নত হয়, এবং তড়িৎ পরিবাহিতা উল্লেখযোগ্যভাবে হ্রাস পায়। উভয় যৌগিক এর চৌম্বকীয় বৈদ্যুতিক বৈশিষ্ট্যের বৃহৎ বর্ধন চৌম্বকীয় এবং বৈদ্যুতিক বৈশিষ্ট্যের মধ্যে শক্তিশালী সংযোগ নির্দেশ করে। YIG এর সাথে একটি শক্তিশালী ফেরোবৈদ্যুতিক এবং ডায়াচৌম্বক উপাদান, সোডিয়াম বিসমাথ টাইটানেট এবং স্ট্রনসিয়াম টাইটানেটের ঘন দ্রবণ ($Sr_{0.5}Na_{0.25}Bi_{0.25}TiO_3$, SNBT50) এর মধ্যে যৌগিক গঠন শক্তিশালী ডোমেইন পরিবর্তন প্ররোচিত করে, যা সর্বাধিক প্রয়োগসাধ্য তড়িৎ-ক্ষেত্রের মতোই যৌগিকগুলিতে YIG-এর ক্রমবর্ধমান ঘনত্বের সাথে ক্রমশ বৃদ্ধিপ্রাপ্ত হয়। যদিও SNBT50 তে কোনো গড় চৌম্বকীয়-পরাবৈদ্যুতিক গুণনীয়ক দেখা যায়নি, তবে যৌগিকগুলিতে চৌম্বকীয়-পরাবৈদ্যুতিক গুণনীয়কের বড় মান পরিলক্ষিত হয়, যা YIG-এর ক্রমবর্ধমান ঘনত্বের সাথে ক্রমশ বৃদ্ধিপ্রাপ্ত হয়। এই পর্যবেক্ষণটি ফেরোবৈদ্যুতিক, SNBT50 এবং ফেরোচৌম্বক, YIG গঠনের মাধ্যমে বৈদ্যুতিক এবং চৌম্বকীয় বৈশিষ্ট্যগুলির মধ্যে সংযোগের বাস্তবায়ন প্রমাণ করে যা YIG-এর ক্রমবর্ধমান ঘনত্বের সাথে তীব্র হয়। 6.2 মিলিমিটার দৈর্ঘ্যের একটি GFO শোষকের প্রতিফলন ক্ষয় –67.36 dB পরিলক্ষিত হয় যা এর উচ্চ অন্তরক ধ্রুবক, উচ্চ চৌম্বক প্রবেশ্যতা এবং উপশম ধ্রুবকের পাশাপাশি একটি সর্বোত্তম প্রতিবন্ধক সাদৃশ্যের জন্য দায়ী। বিসমাথ ফেরাইট ন্যানোকণাগুলিতে বেরিয়াম এবং ইট্রিয়ামের দ্বারা বিসমাথের মৌলিক প্রতিস্থাপনের ফলে একটি 7.5 মিলিমিটার দৈর্ঘ্যের শোষকের প্রতিফলন ক্ষয় –38.6 dB থেকে –61.7 dB পর্যন্ত বৃদ্ধিপ্রাপ্ত করা যায়, যার জন্য বৃদ্ধিপ্রাপ্ত তড়িৎ ভেদ্যতা, চৌম্বক প্রবেশ্যতা এবং $\tan\delta_\varepsilon = \tan\delta_\mu$ সমীকরণের উপর ভিত্তি করে পরিলক্ষিত $\tan\delta_\varepsilon$ এবং $\tan\delta_\mu$ এর মধ্যে সর্বোত্তম ভারসাম্য দায়ী। অপরদিকে, (1-x) SNBT50 – x YIG চুম্বকিয়তড়িৎ যৌগিক তার উন্নত অন্তরক ধ্রুবক, চৌম্বক প্রবেশ্যতা এবং প্রতিবন্ধকতা মিলের কারণে এর মূল নমুনা, SNBT50 এর তুলনায় উচ্চতর মাইক্রোতরঙ্গ শোষণ প্রদর্শন করে।

LIST OF PUBLICATIONS

(Included in Thesis)

1. **Swarnali Hait**, Anupam Gorai, Kalyan Mandal, Origin of different microwave absorption in multiferroic Bismuth and Gallium Ferrite, Mater Lett. 331 (2023).
2. **Swarnali Hait**, Ishita Jana, Kalyan Mandal, Simultaneous improvement of leakage, electric, and magneto-dielectric properties due to the reduction in grain size, J Magn Magn Mater. 565 (2023) 170239.
3. **Swarnali Hait**, Kalyan Mandal, Enhancement of Curie temperature of gallium ferrite beyond room temperature by the formation of $Ga_{0.8}Fe_{1.2}O_3$-$Y_3Fe_5O_{12}$ composite, AIP Adv. 13 (2023).
4. **Swarnali Hait**, Kalyan Mandal, Enhanced ferroelectric, dielectric and magnetodielectric properties of Ba and Y co-doped Bismuth Ferrite nanoparticles, Physica B Condens Matter. 645 (2022).
5. **Swarnali Hait**, Srabantika Ghose, Kalyan Mandal, Effect of Ba and Y co-doping on the structural and magneto-electric properties of $BiFeO_3$ ceramic, J Alloys Compd. 822 (2020) 153614.
6. **Swarnali Hait**, Anupam Gorai, Kalyan Mandal, Barium and Yttrium co-doping in Bismuth Ferrite Nanoparticles to Enhance Microwave Properties (**Accepted at Physica Scripta**)
7. **Swarnali Hait**, Alo Dutta, Anupam Gorai, Kalyan Mandal, Study of ferroelectric, magnetodielectric and microwave properties in 0-3 particulate composite of Barium Sodium Titanate – Strontium Titanate solid solution and Yttrium Iron Garnet (**Submitted**)

(Not Included in Thesis)

1. Anupam Gorai, **Swarnali Hait,** Wolfgang Taute, Michael Höft and Kalyan Mandal, Optimization of Magnetic Coating for Improved Electromagnetic Wave Absorption in Bi-layered Nano-hollow Spheres (**Accepted at IEEE Transactions on Magnetics**)
2. Ishita Jana, **Swarnali Hait**, Kalyan Mandal, Improvement of Leakage, Magnetic and Magnetodielectric Properties in Cobalt doped Gallium Ferrite **(Under Revision)**

ACKNOWLDEGEMENT

It is worth mentioning that my years in S. N. Bose National Centre for Basic Sciences, have transformed me into a new and much better person. This campus provided me with the opportunity to engage in a wide range of pursuits, from academic to cultural to social. I am eternally grateful to S. N. Bose National Centre for Basic Sciences for offering me the freedom to explore myself and delve into the wildest aspirations and for the constraints that helped me to self-discipline and grow into a strong-headed individual.

Next, I would like to convey my profound appreciation to my PhD advisor, Prof. Kalyan Mandal. He provided me with the freedom to perform in-depth and atemporal research, sculpting me into a woman with numerous abilities and aptitudes in the area of experimental physics, who can work independently and collaboratively from anywhere in the globe. His influence motivated me to think intellectually and get an in-depth comprehension of the research I am conducting. I thank him again for encouraging me to independently plan and perform research, and for his insightful talks that helped me improve my conception and enrich my research. At last, I must say after enduring a whole year of the COVID-19 epidemic, it would be impossible to accomplish my thesis without his full support and assistance.

Next, I express my extreme gratitude to two greatest teachers of my life, Dr. Debapriyo Syam and Prof. Swapan Das who motivated me to think creatively and fostered my inquisitive mind. I thank Mrs. Padmaja Rudra, the principal of my high school, who first suggested me to pursue research as career. I thank all the teachers who have influenced me at some point of my life, Prof. Subhrangshu Sekhar Manna, Prof. Priya Mahadevan, Dr. Thirupathaiah Setti, Prof. Punyabrata Pradhan, Prof. Tanusri Saha-Dasgupta, Prof. Amitabha Lahiri, Prof. Samir Kumar Pal, and Dr. Ramkrishna Das from S. N. Bose National Centre for Basic Sciences, Prof. Pradip Mukherjee and Dr. Somnath Bhattacharya from Barasat Government College, Mrs. Kasturi Majumdar and Mrs. Sadhana Chowdhury from my high school, Nabapally Jogendranath Balika Vidyamandir.

Next, I would like to express my immense love and affection to those people who added so much vibrancy to my life, both on and off campus. My friends Anupam Gorai, Surya Narayan Panda, Sudip Majumdar, Atul Rathor, Shantonu Mukherjee, and Shashank Gupta from Integrated PhD group, Dr. Subhamita Sengupta, Dhiraj Tapadar, Dr. Priyanka Saha, Debayan Mondal, Dr. Sucheta Mondal, Dr. Juriti Rajbangshi, Ria Saha, Amrita Mondal, Anish Das, Anusree Sen, Riya Barick, Arundhati Adhikari, Snehamoyee Hazra, Indrani Kar, and Saheli Mukherjee from SNB Dance group, Abhik Ghosh Moulick, Amrita Mondal, Ria Saha, Animesh Hazra, Shivam Mishra, Avik Sasmal, Jayarshi Bhattacharya, Anupam Gorai, Subhajit Singha from SNB Mess Committee 2020-2021 group, Dr. Tuhin Maji, Ram Krishna Patra, Samrat Sen, Subhajit Singha, Sanujakumar Khuntia, Bivas Mallick, Saheli Mukherjee, Ishita Jana, Nishant Garg, Sayan Ghosh, Sudip Chakraborty, Sudip Pramanik, and Sourav Mandal from Photofest 2020, 2022, 2023 groups, Sayan Ghosh, Tanmoy Chakraborty, Krishnendu Sinha, Jayarshi Bhattacharya, Ram Krishna Patra, Shaheerah Shahid, and Sabuj Mandal from Badminton, Table Tennis and Carrom Tournament groups and finally to my childhood chums, Abhishek Das and Arpita Sardar.

I thank my labmates Dr. Dipanjan Maity, Dr. Priyanka Saha, Saheli Samanta, Soham Saha, J Sridhar Mohanty, Sourav Sarkar for their cheerful company, help, and support. Special thanks to my junior Ishita Jana and best friend cum collaborator Anupam Gorai for always being there for me. I thank my seniors Dr. Dipika Mandal, Dr. Subrata Ghosh, Dr. Indranil Chakraborty, Dr. Mahebub Alam, Dr. Souvanik Talukdar, Dr. Deblina Majumdar, Dr. Rupali Rakshit, Dr. Keshab Karmakar, Dr. Debasish Sarkar, Dr. Ashutosh Kumar Singh, Dr. Arka Chaudhuri, Dr. Rajasree Das, and Dr. Srabantika Ghose.

My deepest gratitude to the technical group of our campus, Mr. Debarghya Ghosh, Mr. Sourav Sinha, Mr. Shakti Nath Das, Mr. Amit Kumar Chanda, Mr. Joy Bandopadhyay, and Mrs. Urmi Chakrabarty for bearing with me through those fraught days of extensive revisions.
I thank my seniors Dr. Sumanta Kundu, Dr. Krishnendu Pal, Dr. Sayani Chatterjee, Dr. Biplab Bhattacherjee, Dr. Rakesh Das, Dr. Arghya Das, Dr. Sandip Saha, Dr. Samrat Ghosh, Dr. Subhadip Chakraborti, Dr. Poulami Chakraborty, Dr. Jayita Patwari, Dr. Anita Halder, Dr. Subhasish Chakrabarty for their guidance.

Finally, I express my greatest gratitude to my beloved parents (Mrs. Bina Hait and Mr. Subir Hait), for their unconditional love and sacrifice, never-ending support and inspiration, immense affection and guidance. A lot of love for my late grandmother who always waited for me to come home.

Swarnali Hait

LIST OF ABBREVIATIONS

	A
AFM	Antiferromagnetism, Atomic Force Microscope
ac	Alternating Current
	B
BW	Bandwidth
BFO	Bismuth Ferrite
	C
CFSE	Crystal field splitting energy
CPE	Converse Piezoelectric Effect
	D
DM	Dzyaloshinkii-Moriya
dc	Direct Current
DOS	Density of States
DUT	Device Under Test
	E
EDX	Energy Dispersive X-ray Analysis
EM	Electromagnetic
EMA	EM wave absorbing materials
EMI	EM wave interference
EMF	Electromotive Force
	F
FC	Field Cooled
FM	Ferromagnetism
fM	Ferrimagnetism
FCC	Face Centered Cubic
FEG	Field Electron Gun
FMR	Ferromagnetic Resonance
FESEM	Field Emission Scanning Electron Microscope
FWHM	Full Width at Half Maxima
	G
GB	Grain Boundary

GBLC	Grain Boundary Limited Conduction
GFO	Gallium Ferrite
GGG	Gadolinium Gallium Garnet
	H
HRTEM	High Resolution Transmission Electron Microscope
	M
MUT	Material Under Test
MAM	Microwave Absorption Material
ME	Magnetoelectric
MLCT	Metal-ligand charge transfer
MD	Magneto Dielectric
MFM	Magnetic Force Microscope
MC	Magneto Capacitance
ML	Magneto Loss
MI	Magneto Impedance
MH	Magnetic Hysteresis
	N
NRW	Nicholson-Ross-Weir
NMs	Nanomaterials
NPs	Nano particles
NSs	Nanostructures
	P
PF	Poole-Frenkel
PM	Paramagnetic
PLD	Pulsed Laser Deposition
PFM	Piezoresponse Force Microscope
PPMS	Physical Property Measurement System
	R
RT	Room Temperature
RF	Radio Frequency
RL	Reflection Loss
	S

SNBT50	$Sr_{0.5}Bi_{0.25}Na_{0.25}TiO_3$
SAED	Selected Area Electron Diffraction
SCLC	Space-Charge-Limited Conduction
STO	Strontium Titanate
SqMM	Square Magnetization Model
SMM	Stress Magnetization Model
SWR	Standing Wave Ratio
	T
TE	Transverse Electric
TEM	Transverse Electromagnetic
TM	Transition Metal
	V
VNA	Vector Network Analyser
VSM	Vibrating Sample Magnetometer
VESTA	Visualisation for Electronic Structural Analysis
	X
XRD	X-ray Diffractometer
	Y
YIG	Yttrium Iron Garnet
	Z
ZFC	Zero Field Cooled

LIST OF SYMBOLS

a	Lattice Constant (Å)
A	Area
B	Magnetic Flux Density (T)
c	Lattice Constant, Speed of Light ($3x10^8$ m/s)
C	Capacitance (F)
C_g	Grain Capacitance
C_{gb}	Grain Boundary Capacitance
d	Inter-Planar Spacing
D	Crystallite Size, Grain Size
	Electric Displacement (μC/cm^2)
e	Electronic Charge (1.602×10^{-19} C)
E	Electric Field (kV/cm)
E_a	Activation Energy (eV)
f	Frequency (Hz)
f_C	Cut-Off Frequency (Hz)
F	Landau's Free Energy
F_0	Ground State Free Energy
G	Conductance
H	Magnetic Field
H_C	Coercivity
H_p	Critical Magnetic Field
I	Electric Current (A)
J	Electric Current Density (A/cm^2)
k_B	Boltzmann Constant (1.3806488×10^{-23} J/K)
k	Wave Number
k_C	Cut-Off Wave Number (Hz)
K	Magnetic Anisotropy, Dielectric Constant
L	Inductance
M	Magnetization (emu/g)
M_S	Saturation Magnetization
M_R	Remnant Magnetization

N	Number of Loops in Pickup Coils
P	Electric Polarization ($\mu C/cm^2$)
P_S	Saturation Polarization
P_r	Remnant Polarization
Q	Charge
r	Distance Vector
R	Resistance (Ω)
R_g	Grain Resistance
R_{gb}	Grain Boundary Resistance
s	Temperature Dependent Parameter of Conduction
S	Spin Operator
S_{ij}	S Parameters
t	Time
T	Temperature (K)
T_C	Curie Temperature
T_N	Neel Temperature
V	Volume, Electric Voltage (V)
Z	Complex Impedance
Z'	Real Part of Complex Impedance
Z''	Imaginary Part of Complex Impedance
Z_i	Input Impedance
Zo	Output Impedance
α	Attenuation Constant
β	Phase Constant
η	Intrinsic Impedance of Conducting Medium
η_0	Intrinsic Impedance of Free Space ($\sim 377\ \Omega$).
γ	Gyromagnetic Ratio Magnetoelectric Coupling Coefficient
δ	Nano particles
ε	Complex Electric Permittivity
ε_0	Free Space Permittivity (8.854×10^{-12} F/m)
ε_r	Relative Complex Permittivity
ε'_∞	Permittivity at Infinitely High Frequency

ε'	Real Part of Complex Electric Permittivity
ε''	Imaginary Part of Complex Electric Permittivity
$tan\delta_{\varepsilon}$	Electric Loss Tangent
$tan\delta_{\mu}$	Magnetic Loss Tangent
θ	Phase, Angle
λ	Wave Length
μ	Complex Magnetic Permeability, Effective Mass
μ_0	Free Space Permeability ($4\pi \times 10^{-7}$ H/m)
μ_r	Relative Complex Permeability
μ'	Real Part of Complex Magnetic Permeability
μ''	Imaginary Part of Complex Magnetic Permeability
ω	Angular Frequency, Octahedral Tilt
χ	Susceptibility
φ	Radio Frequency
τ	Relaxation Time Constant (s)
σ	Conductivity, Saturation Magnetostriction
σ_{ac}	AC Conductivity
σ_{ac}	DC Conductivity
ρ	Resistivity, Free Charge Density
Γ	Reflection Coefficient
T	Transmission Coefficient
Φ	Magnetic Flux

CONTENTS

LIST OF FIGURES

CHAPTER 1

INTRODUCTION

This chapter introduces the multiferroic phenomena, its historical background, and the origin of multiferroic properties in materials. Besides this, this chapter discusses several multiferroic materials existing in nature, their applications in practice, different properties and characteristics that are investigated to understand the existence of multiferroic properties observed in a material. Finally, this chapter introduces to the motive of this thesis and its organization along with a brief overview of the works discussed in following chapters.

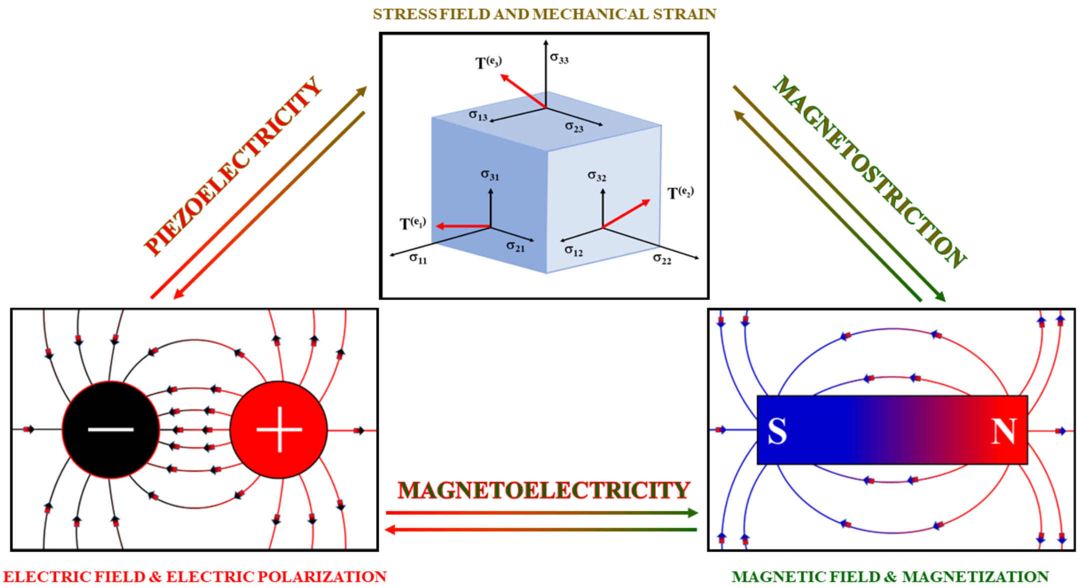

1.1 PREAMBLE

The term "multiferroic" was first used in 1993 by Hans Schmid to describe the ferroic materials as Aizu had categorized them[1,2]. In this phase, two or more than two of the primary ferroic orders (ferroelasticity, ferroelectricity, ferromagnetism, and ferrotoroidicity) are displayed by the materials as illustrated in Figure 1.1. Today, however, this term is used more broadly to describe a class of magnetoelectric materials that has been the subject of extensive research. It now applies to substances with coexisting anti- and ferri- orders (Figure 1.2). Materials that can have their magnetic properties changed by electric fields and their electric polarisation altered by magnetic fields are referred to as magnetoelectric materials[3,4]. Even though the term "coupling" was first used to refer to the linear coupling between an electric field and magnetic properties or a magnetic field and electric properties, it is now used to refer to any kind of connection between an electric charge dipole and magnetic spins[5–9].

1.2 HISTORICAL BACKGROUND

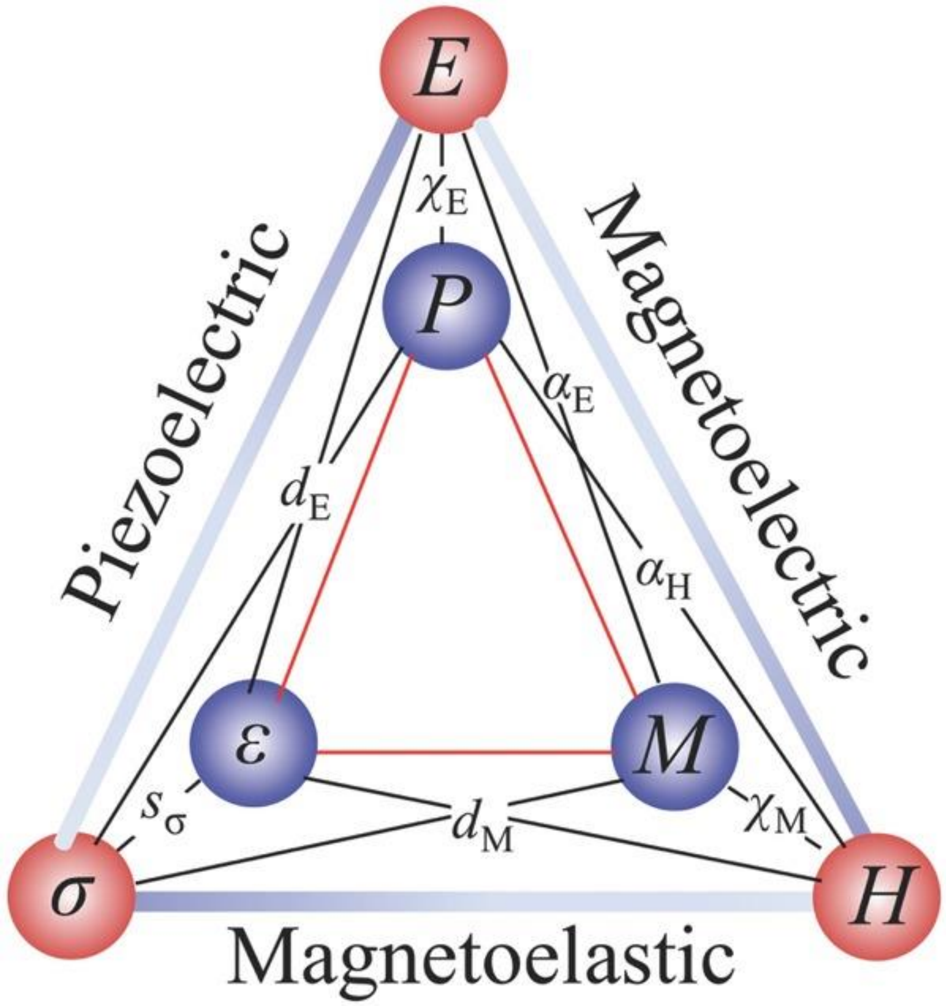

Figure 1.1. Coupling electric-elastic-magnetic properties in multiferroic heterostructures, showing order parameters (blue) and conjugate fi elds (red). Other symbols represent response functions (coupling coefficients). Modified from a similar diagram on electric elastic-thermal properties[8]

Scientists and engineers have been fascinated by the interaction between electricity and magnetism since Hans Christian Oersted unintentionally found that the deflection of a magnetic compass needle is caused by the switching on or off of the current in a nearby battery. Although André Marie Ampère and Michael Faraday made substantial contributions to the formulation of the classical theory of electromagnetism in the subsequent 40 years, James Maxwell's unified theory of electromagnetism represented the major advancement in the 1860s. Since then, efforts have already been made to find a strong coupling between magnetic and electric properties in order to create low-power, voltage-controlled magnetic devices. Despite the fact that theoretical issues were the primary focus of research during these years, the experimental approach to studying these materials was still novel. In the 1950s, Smolenskii and Ioffe used magnetic ions to establish long-range magnetic spin order while maintaining ferroelectricity in ferroelectric perovskite[10]. This research resulted in the successful fabrication of a magnetoelectric material, $Pb(Fe_{0.5}Nb_{0.5})O_3$, where magnetic Fe ions were doped at the site of Niobium in ferroelectric $PbNbO_3$. The same research led to the synthesis of a polycrystalline solid solution of $(1\text{-}x)Pb(Fe_{0.66}W_{0.33})O_3$ - $xPb(Mg_{0.5}W_{0.5})O_3$. The hexagonal manganites

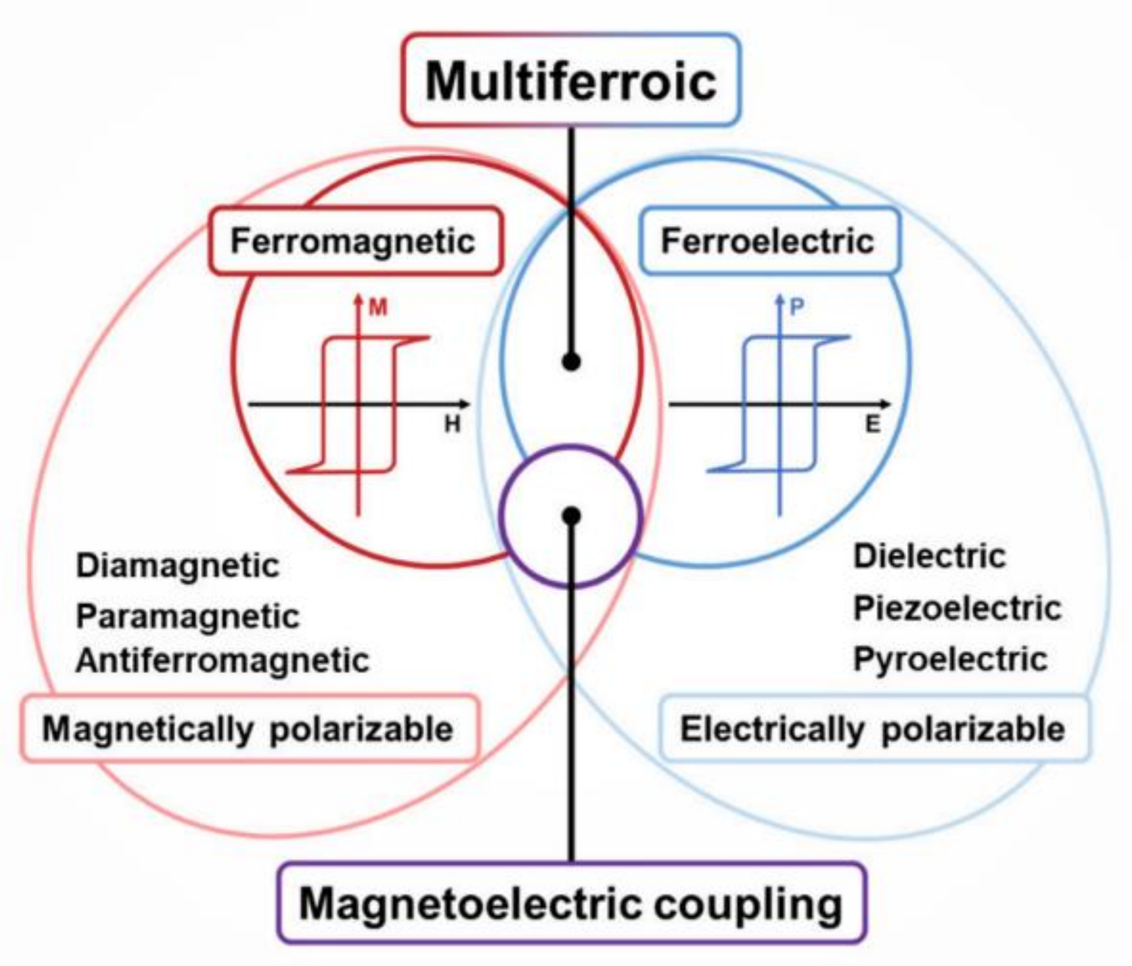

Figure 1.2. Venn diagram defining magnetoelectric multiferroics[9]

($RMnO_3$) and $BiFeO_3$, the most thoroughly researched multiferroics that continue to pique the interest of scientists, were discovered simultaneously. In 1966, Asher and colleagues discovered a massive linear magnetoelectric effect in $Ni_3B_7O_{13}I$. This effect permits the hysteretic transition between multiple states when an electric or magnetic field is applied. Around 1970, Aizu created a comprehensive taxonomy of ferroics, which contributed to the current understanding of (multi-)ferroics, as Hans Schmid coined the term[1,2,11].

During this time, around 50 multiferroic systems were discovered, but none of them had properties that could be used in technological applications[12]. Since then, research on multiferroics had become extremely slow, with only two significant papers published up until the 1990s. In one article, the scientists described how the presence of a spin spiral can result in spontaneous electric polarisation by breaking the spatial inversion symmetry, and in another, they provided a phenomenological model to explain the phenomenon. In 1993, Hans Schmid's Magnetoelectric Phenomena in Crystals (MEIPIC-2) conference reignited the interest of scientists in magnetoelectric materials. The focus of the conference was on theoretical aspects and phenomena associated with the magnetoelectric effect, as well as potential experimental methods for visualizing and validating the interactions between multiferroic domains.

The concept of incorporating magnetic ions into ferroelectric perovskites was first proposed by Ioffe and Smolenskii. In 2000, Spaldin (then Hill) revisited the idea and elaborated on the contradictory nature of the coexistence of magnetic and ferroelectric properties as a potential explanation for the paucity of multiferroic materials[13,14]. In support of the possibility that magnetic and ferroelectric orders could coexist in a material, new aspects of the synthesis of multiferroic materials with stronger coupling have been discovered, advancing research even two decades after their discovery.

1.3 ORIGIN OF MULTIFERROIC PROPERTY

For the design of new multiferroic materials, it is essential to comprehend the coexistence of ferroelectric and magnetic orders as well as their potential interactions. In the section that follows, different multiferroic characteristics is covered in depth, along with several examples. A magnetoelectric material must concurrently exhibit ferromagnetism and ferroelectricity in order to meet the definition. Its structural, physical, and electrical properties are therefore limited to those factors that give rise to these characteristics in a material. Below is a discussion of the limiting elements or properties that lead to ferromagnetism and ferroelectricity.

Symmetry: Ferroelectricity and electric polarisation in a material are fundamentally dependent on the absence of centrosymmetry. The material's electric polarisation is the result of a structural distortion that distorts the unit cell in a manner that eliminates inversion symmetry. In 31 point groups, both spontaneous polarisation (P) and spontaneous magnetization (M) are permitted. 13 point groups among them, permit spontaneous polarisation and magnetization simultaneously, these are 1, 2, 2′, m, m′, 3, 3m′, 4, 4m′m′, m′m2′, m′m′2′, 6, and 6m′m′[15].

Electrical and Magnetic Properties: In order for the applied electric field to result in electrical polarisation as opposed to the flow of charge carriers or current, the polarising material must be an insulator. As a result of the large density of states at the Fermi level, which also results in metallicity, ferromagnetism, on the other hand, does not require any insulating feature and is typically metallic in nature[16]. However, since most antiferromagnets or ferrimagnets are insulators, expanding the search to ferrimagnetic or antiferromagnetic materials makes it conceivable to obtain ferroelectric insulators with magnetic ordering.

Chemistry d^0-ness: It has been noted that the B-site of ABO_3-type perovskite materials contains d^0 electrons in the majority of insulators that exhibit ferroelectricity. On the other hand, if the *d*-shell is devoid of electrons, there will be no magnetic order. The biggest barrier to obtaining single-phase multiferroic materials is this contradiction. The tendency of the B ion to cause structural distortion by moving away from the oxygen octahedron's centre decreases when the *d* shell of the ion fills up.

Structural Distortion: At lower temperatures, ferroelectric materials must undergo a phase transition into a non-centrosymmetric phase. This phase shift is caused by the movement of the smaller B ion away from the centre of the oxygen octahedron in ferroelectric perovskite materials. However, the potential to experience Jahn-Teller distortion is significantly more pronounced and can act as the primary driving force behind structural distortion for perovskites with non-zero *d*-shells. For instance, the Ti^{3+} ions in Yttrium Titanate ($YTiO_3$) have a d^1 configuration, while those in Lanthanum Manganite ($LaMnO_3$) have a d^4 configuration. Both materials have a *d*-type Jahn-Teller distortion, but neither in ferroelectric. $YTiO_3$ is a strongly correlated ferromagnetic Mott-Hubbard insulator, whereas $LaMnO_3$ is an insulator and exhibits an antiferromagnetic character[17].

On the basis of these requirements, possible methods for implementing ferroelectricity and ferromagnetism in a material have been classified. According to Khomskii's theory, this origin

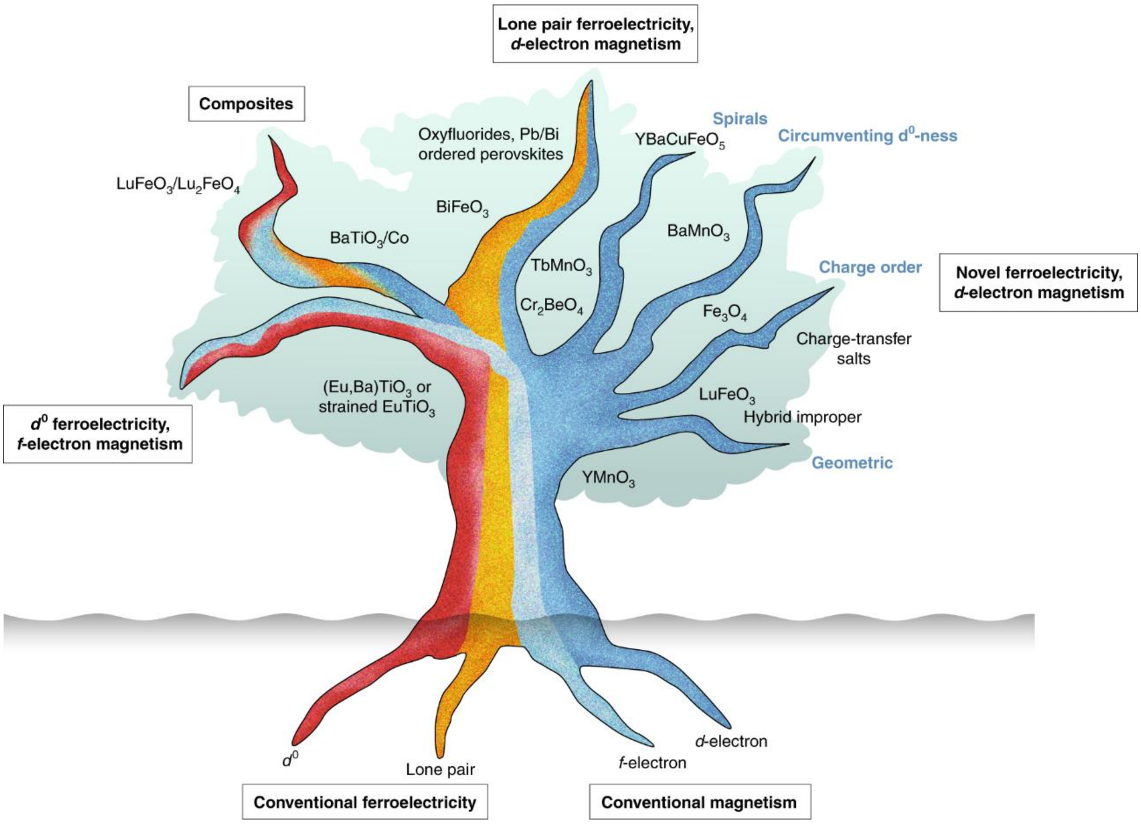

Figure 1.3. Multiferroicity, arising from the combined interplay of magnetic and ferroelectric mechanisms, can result from several different sources. Here, we outline different combinations of these 'root' mechanisms and how they are responsible for different types of multiferroic materials. This visualization shows the combinations of magnetic and ferroelectric mechanisms that occur in existing multiferroics, and also suggests less-explored options that may prove fruitful in the future[14].

gives rise to two distinct types of multiferroic materials. These are multiferroics of types I and II, which are discussed in greater detail in the following section.

1.3.1 TYPE-I MULTIFERROIC

The ferroelectricity in these kinds of materials lacks any magnetic component, resulting in an extremely weak coupling between the two.

***d^0 ferroelectricity and f-electron magnetism**:* Since it has already been demonstrated that d^0-ness is necessary for ferroelectricity but, paradoxically, eliminates the magnetic ordering from the material, it is possible to create magnetic ordering in a d^0 ferroelectric material via *f*-electron magnetism[13]. For example, in Eu-substituted $BaTiO_3$[18], the ferroelectric polarisation arises from d^0-ness of Ti^{4+} ion ([Ar] $3d^2$ $4s^2$) and magnetism part comes from *f*-electrons of Eu^{2+} ions after substitution of Ba^{2+} ([Xe] $6s^2$) ions with Eu^{2+} ions ([Xe] $4f^7$ $6s^2$)[19,20].

***Lone pair ferroelectricity and d-electron magnetism**:* In this instance, the substance is a single-phase material made up of two cations, one of which is responsible for ferroelectricity and the other for ferromagnetism. In this situation, the "lone pair" at the cation is stereochemically active and produces the structural distortion that results in the ferroelectricity that is observed. For instance, the strong antiferromagnetism in $BiFeO_3$ comes from the Fe electrons, and the significant polarization in that material is caused by the stereochemical activity of the Bi^{3+} $6s^2$ lone pair of electrons. $BiXO_3$ (X are transition metal ions) structures have been created and researched as a result of these characteristics[21]. $BiCoO_3$ is found to be polar at high Neel temperatures, T_N = 470 K, although flipping the polarisation has not yet been successful due to the large *c/a* ratio of the tetragonal structure. Due to the lone pair at the Pb ions, $PbXO_3$-type materials also belong to this group[22].

Novel ferroelectricity and d-electron magnetism branch*:* The ferroelectric properties of these materials are the result of an unconventional method of breaking the inversion symmetry, which generates ferroelectricity. These materials' magnetism is generated by conventional *d*-electrons. For instance,

Circumventing the d^0-ness requirement for ferroelectricity: Even though the cation's *d* orbital is only partially filled with electrons in this instance, the cation nevertheless manages to alter the structure and cause ferroelectricity via the second-order Jahn-Teller effect. Examples include ferroelectricity brought on by strain, as in the perovskite $SrMnO_3$[23], and ferroelectricity brought on by negative chemical pressure, as in the case of $BaMnO_3$[24,25]. Due to the highly unstable nature of the high-symmetry paraelectric phase, even minor structural perturbations become significant in these situations and can cause the material to become ferroelectric.

Charge Order: This type of ferroelectricity has been observed in organic charge transfer salts, where the formation of charge ordering is responsible for the emergence of ferroelectricity[26,27]. The tiny band gap, high conductivity, and poor ferroelectric hysteresis of these materials continue to present obstacles.

Geometrically driven multiferroics: In such situations, the geometric position of the small A-site cation becomes crucial. $BaNiF_4$ is an example of a small A-site cation that permits rotation of the surrounding polyhedral [28], which is either polar on its own or is associated with a secondary polar distortion as in $YMnO_3$[29–31]. In these materials, the coupling between polarisation and magnetization is extremely strong since the rotation of such polyhedra also causes magnetism.

1.3.2 TYPE-II MULTIFERROICS

The ferroelectricity in this particular form of multiferroic material is typically induced by magnetic ordering. Spontaneous polarisation is caused when a non-centrosymmetric magnetic ordering, such as spin spirals, disrupts the lattice's inversion symmetry. As a result, there is a strong link between magnetic and ferroelectric properties. These are also referred to as multiferroics driven by magnetism. At very low temperatures, this type of multiferroic is present in $TbMnO_3$ and $TbMn_2O_5$[32,33]. For $TbMnO_3$, at extremely low temperatures (T = 28 K), the magnetic structure only changes to the point where the electric polarisation is visible. When a particular magnetic field is applied, the polarisation of this material is observed to

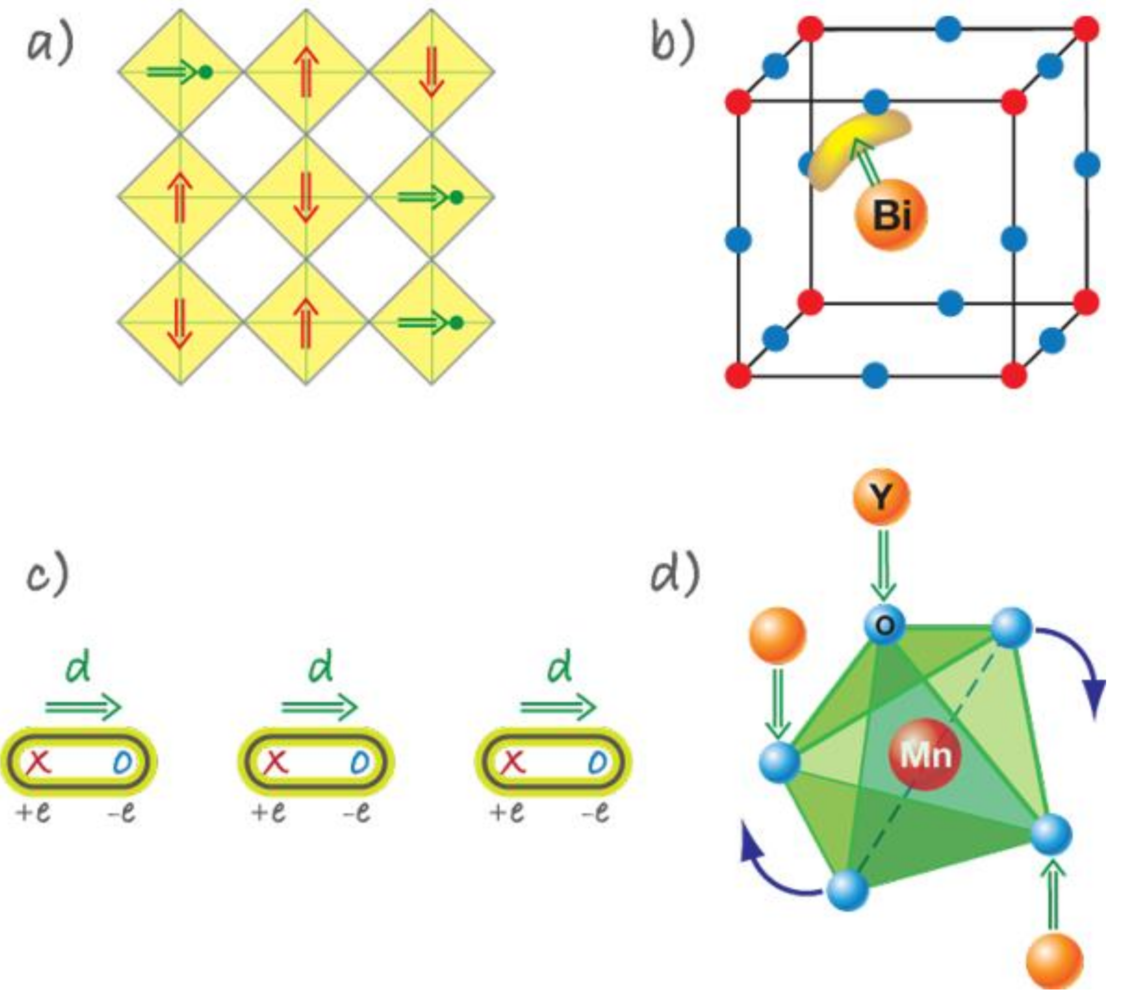

Figure 1.4. Different microscopic mechanisms observed in type-I multiferroics. (a) In "mixed" perovskites containing ferroelectrically active d^0 ions (green circles) and magnetic d^n ions (red), d^0 ion shifts from the centers (green arrows) of O_6 octahedra (yellow plaquettes) coexist with polarization (red arrows). (b) In materials like $BiFeO_3$ and $PbVO_3$, the ordering of lone pairs (yellow "lobes") of Bi^{3+} and Pb^{2+} ions (orange), contributes to the polarization (green arrow). (c) In charge-ordered systems, ferroelectricity results from the coexistence of inequivalent sites with different charges and inequivalent (long and short) bonds. (d) The "geometric" mechanism of generation of polarization in $YMnO_3$ describes the tilting of a rigid MnO_5 block with a magnetic Mn remaining at the center [31]. As a result of the tilting, the Y-O bonds form dipoles (green arrows), and there are two "down" dipoles for every "up" dipole, resulting in a ferroelectric system (and multiferroic when Mn spins order at lower temperatures).

rotate by 90 degrees. However, in $TbMn_2O_5$, the effect of the magnetic field on polarization is so powerful that it causes a comparable oscillation in polarization when the magnetic field alternates between -1.5 T and +1.5 T.

Based on the multiferroic behaviour mechanism, the Type-II multiferroics can be further split into two groups. which are,

Spiral Magnetic Structure: As seen in $TbMnO_3$, $Ni_3V_2O_6$, and other materials, the ferroelectricity in this instance appears as a result of a magnetic spiral. The following equation can be used to phenomenologically express the polarisation, P[34–36]:

$$P \sim r_{ij} \times \left[S_i \times S_j\right] \sim [Q \times e] \tag{1.1}$$

Where, r_{ij} is the distance vector between the two spins S_i and S_j, Q is the wave vector describing the spiral structure, and e is the spin rotation axis given by $\left[S_i \times S_j\right]$.

Collinear Magnetic Structure: In such instances, ferroelectricity manifests in a collinear magnetic structure in which all magnetic spins are aligned in one direction. Since the magnetic coupling varies with atomic position, the polarization of this material appears to be the result

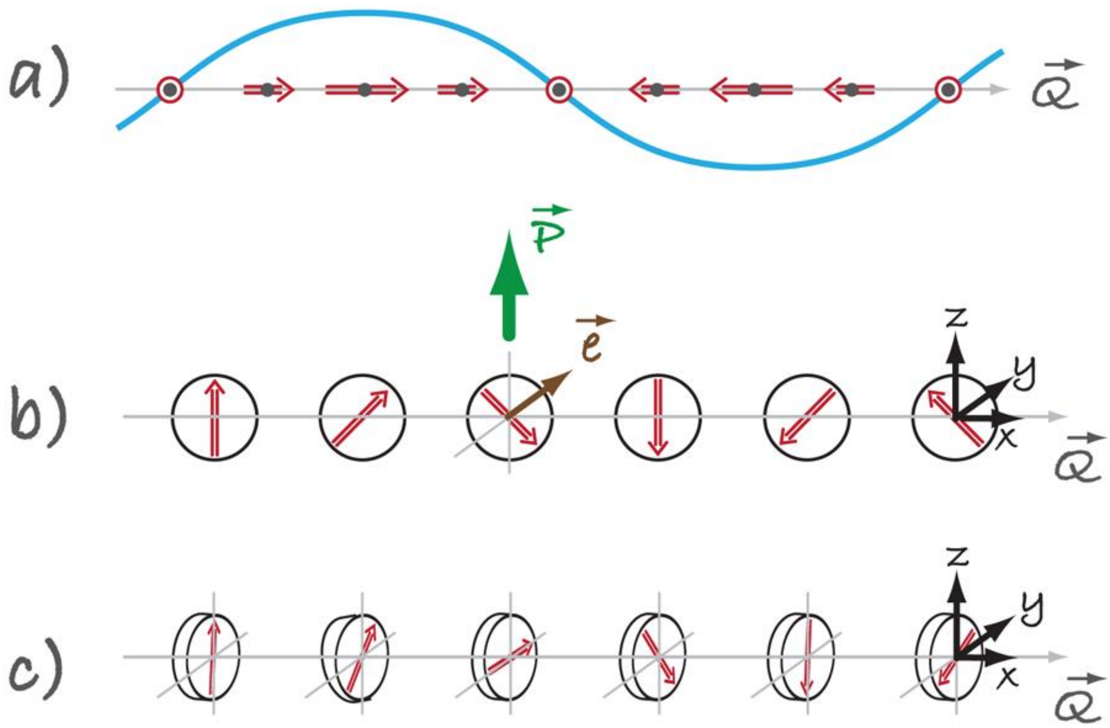

Figure 1.5. Different types of relevant spin structures for type-II multiferroics. (a) Sinusoidal spin density wave, wherein the spins point in a single direction but vary in magnitude. This structure is centro-symmetric and is not ferroelectric as a result. (b) The cycloidal spiral with wave vector $\boldsymbol{Q} = \boldsymbol{Q_x}$ rotates in the (x, z) plane. In this instance, there is nonzero polarization, $\boldsymbol{P_z} \neq \boldsymbol{0}$. (c) The spins of a so-called "proper screw" rotate in a plane that is perpendicular to Q. Here, the inversion symmetry is broken, but this typically does not result in polarization, although it is possible in some instances.

of exchange striction. For example, Ca_3CoMnO_6 [37] consists of both Co^{2+} and Mn^{4+} ions alternatively situated along one dimension and contributing different magnetic moments. However, as the magnetic spins here change depending on the position of Co and Mn ion, the exchange striction occurs and the difference between ferro (↑↑) and antiferro (↑↓) bonds leads to a non-centrosymmetric structure and ferroelectricity.

1.4 STRUCTURES OF MATERIALS

1.4.1 SINGLE PEROVSKITE MATERIALS

The general chemical formula for single perovskite multiferroic oxides is ABX_3. Here, A and B are two distinct cations, with A being bigger than B, while X is an anion that binds to both. For a perfect cubic structure, the B cation is 6-fold coordinated, surrounded by an octahedral of anions, while the A cation is 12-fold coordinated. Single-phase multiferroics may be subdivided based on their chemical formula or the origin of their ferroic properties. It has recently been of interest to study the magnetoelectric coupling between two types of dipoles in single-phase thin film multiferroic systems like perovskite-type $BiFeO_3$ or $BiMnO_3$, the boracite family, $BaMF_4$ families where M is the divalent transition metal, and hexagonal $RMnO_3$ where R is rare earth metals [31,38–40]. These materials exhibit two phase transitions: one from paraelectric to ferroelectric, and another from ferri/ferro/antiferromagnetic to paramagnetic. Magnetoelectric effect is seen by a family-specific mechanism in single phase materials. Charge ordering in doped perovskites [41], magnetoelastic lattice modulations in $TbMnO_3$, and the stereochemical activity of Bi lone pairs in $BiFeO_3$ are just a few examples. The magnetoelectric (ME) effect in single-phase magnetoelectric (ME) materials is quite weak. The downside of these materials is that they degrade in cyclic circumstances and can only be employed at extremely low temperatures and with costly materials and production techniques. This is due to the presence of two order factors, polarization and magnetization, in single-phase materials. Minor ME exchange occurs between the two subsystems because one of the order parameters is often big and the other is small. Some single-phase perovskite structures with strong magnetoelectric coupling are discussed below.

1.4.1.1 BISMUTH FERRITE ($BiFeO_3$ or BFO)

Crystal Structure: $BiFeO_3$ or BFO has a distorted rhombohedral perovskite crystal structure belonging to the *R*3*c* space group[42]. In this representation, shown in Fig. 1.6, the lattice cell parameters are given by, $a_{rhombohedral} = 3.96\,\text{Å}$ and $\alpha = 89.3° - 89.4°$ [43]. This rhombohedral structure are also defined in terms of the hexagonal unit cell as $[001]_{hexagonal} \| [111]_{pseudocubic}$[44]. In the hexagonal representation, the lattice parameters are found to be,

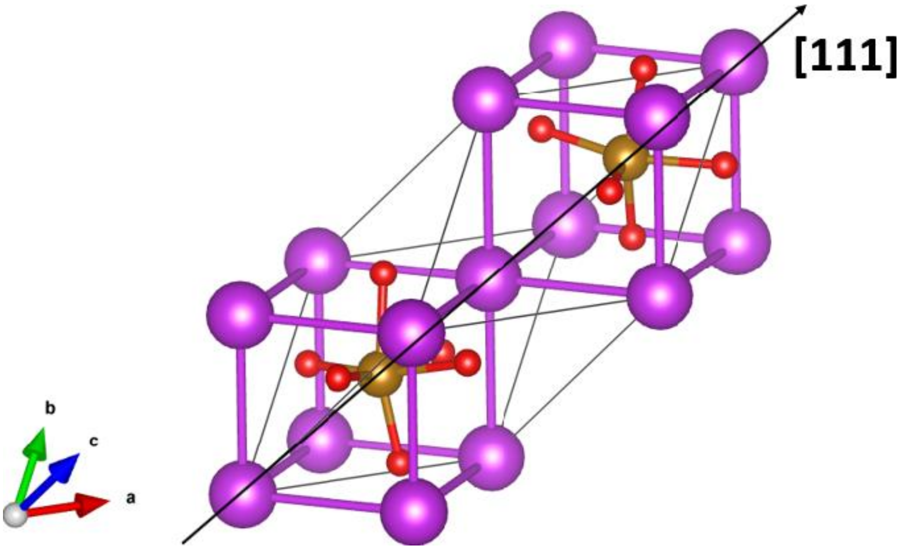

Figure 1.6. The rhombohedral structure of Bismuth Ferrite, $BiFeO_3$. The ferroelectric polarization is located along the [111] direction of pseudocubic representation

$a_{hexagonal} = 5.58$ Å, $c_{hexagonal} = 13.89$Å [45]. In a true cubic structure, the oxygen octahedral rotation angle should be zero, whereas in BFO the oxygen octahedral rotation angle around the $[111]_{pseudocubic}$ axis ranges between 11° and 14° [1,42,43]. This alteration in BFO's rotation angle tilts the oxygen octahedra and modifies the angle of the Fe-O-Fe bond [43,46]. The Fe-O-Fe bond angle is crucial because it controls the magnetic exchange and overlap of Fe and O orbitals in BFO. It also influences the conductivity and magnetic ordering temperature [47].

Magnetic Properties**:** Both short-range and long-range magnetic orderings exist concurrently in BFO. However, BFO's short-range magnetic ordering is G-type antiferromagnetic [48]. Each Fe^{3+} spin is surrounded by six antiparallel spins of its closest neighbours, as shown in Fig. 1.7. Due to magnetoelectric interaction, the spins are not entirely antiparallel; they form an angle to produce a weak canting moment [47]. In the case of long-range antiferromagnetic

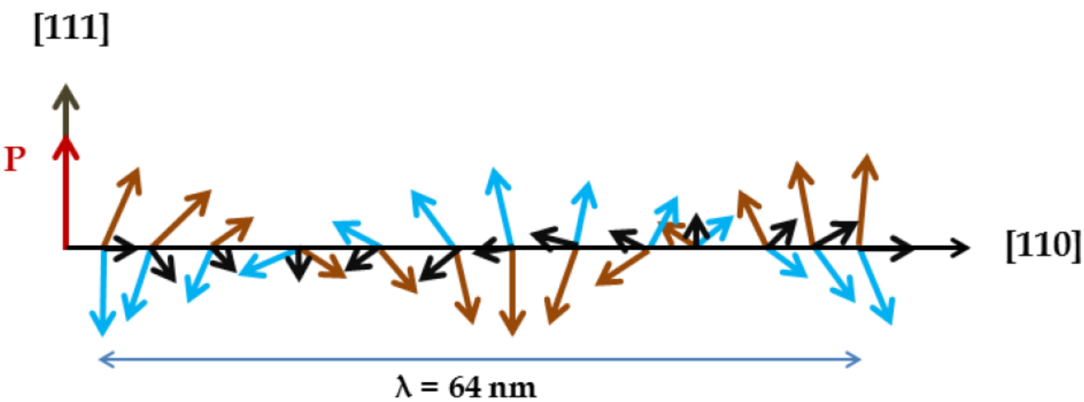

Figure 1.7. Fe^{3+} spins create an incommensurate cycloid spin structure with a length period of 62-64 nm along [110] direction.

ordering, however, the spin structure is not uniform consisting of an incommensurate cycloid spin structure with a fixed length period of 62 to 64 nm along the [110] direction [49], first suggested by Sosnowska in 1982 [48]. In 2000 and 2003, Zalesskii and his colleagues claimed that the cycloid spin structure is deformed at low temperatures owing to spin reorientation [50,51]. However, they were unaware of the phase transition temperature. The spin reorientation transition temperatures discovered separately by several research groups are 140 K and 200 K [52,53]. At 140 K, magnon anomalies are seen, while phonon-magnon coupling occurs at 200 K [54]. The replacement of Fe ions by Nb, Sc, Mn, Zr, Ti, and Co ions improves magnetism as well [55–59]. Changes in the Fe–O–Fe bond angle and the Fe valance state owing to charge compensation enhance the spin in this instance.

Ferroelectric Properties: Magnetoelectric material BFO has a high ferroelectric polarization with critical temperature (T_C = 1103 K) [60]. For ferroelectric polarization, ferroelectric (FE) perovskite typically comprises transition metal (TM) ions with an empty *d*-orbital. In the case of BFO, however, substantial ferroelectric polarization results from the arrangement of the $6s^2$ lone pairs situated in Bi^{3+} ions, identical to the d^0 configuration. These $6s^2$ lone pair electrons violate the local inversion symmetry to generate the coordinate bond along [111] direction (Fig. 1.8). The FE polarization in bulk BFO is oriented along the $[001]_{hexagonal}/[111]_{pseudocubic}$ direction. The group of Ramesh revealed that a high-quality BFO thin film exhibits residual polarization as high as, $P_r \sim 55\ \mu C/cm^2$ in the [001] direction [60]. According to studies [61,62], poor FE polarization in BFO is mostly caused by a high defect density and non-stoichiometry.

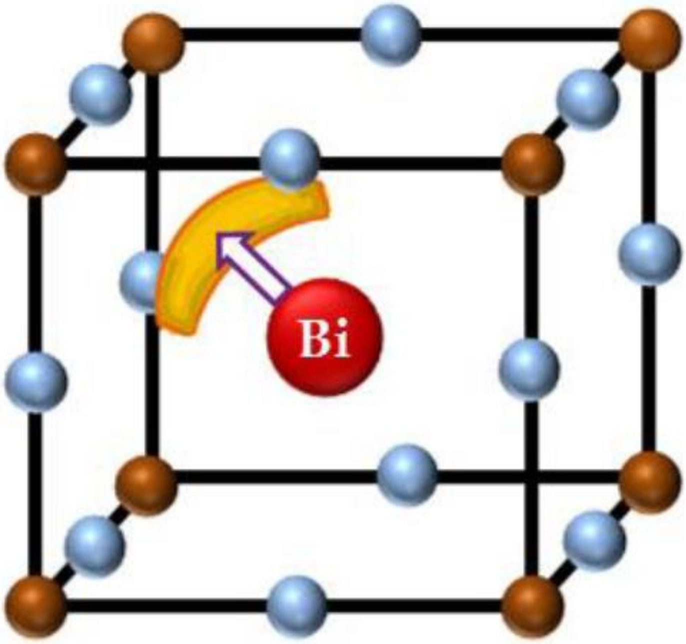

Figure 1.8. The 6 s^2 lone pair in Bi^{3+} ion violate the local inversion symmetry generating a coordinate bond along [111] direction.

1.4.1.2 GALLIUM FERRITE ($Ga_{2-x}Fe_xO_3$)

Crystal Structure: Recent neutron [63,64] and X-ray diffraction [65–67] studies on both powder and single crystals across a broad temperature range (4-700 K) have verified the first structural study that the structure of $Ga_{2-x}Fe_xO_3$ is orthorhombic with $Pc2_1n$ symmetry[68–70]. The room temperature lattice parameters are $a = 8.75$ Å, $b = 9.39$ Å, $c = 5.08$ Å[64,66,71,72], and the orthorhombic unit cell consists of eight formula units. There are two types of Ga and Fe ions, namely Ga1, Ga2, Fe1, and Fe2 ions and six types of inequivalent O ions (O1, O2, O3, O4, O5, and O6) in the unit cell shown in Fig. 1.9. Oxygen coordinates octahedrally with the Ga2, Fe1, and Fe2 ions, but only tetrahedrally with the Ga1 ion[73].

Magnetic Properties: The magnetic transition temperature of gallium ferrite ($Ga_{2-x}Fe_xO_3$ or GFO) is near to room temperature, making it both a room temperature (RT) piezoelectric and a ferrimagnet. As previously discussed, the unit cell of GFO contains 4 types of Ga and Fe ions, namely Ga1, Ga2, Fe1, and Fe2, where Fe1 and Fe2 are antiferromagnetically coupled [66,74]. However, due to similar ionic size of Ga and Fe ions, there is a significant site-disorder. As a result, experimentally, Ga and Fe sites are only partially occupied by the corresponding ions. The observed ferrimagnetism in GFO is also thought to be due to this disorder at the cation sites. To control the transition temperature to values above RT, researchers have found that adjusting the Ga: Fe ratio in the single-phase region ($0.7 \leq x \leq 1.4$ for $Ga_{2-x}Fe_xO_3$) is crucial [73]. Increasing total iron concentrations compared to Ga is observed to linearly increase the Curie temperature (T_C). So, compositionally controlled GFO is an interesting RT magnetoelectric material with a large magnetoelectric coupling in stoichiometric GFO ($\alpha_{bc} \approx 1 \times 10^{-11}\ S.m^{-1}$ at 77 K [71]) shown by Rado [69], especially when combined with its strong piezoelectric response [73].

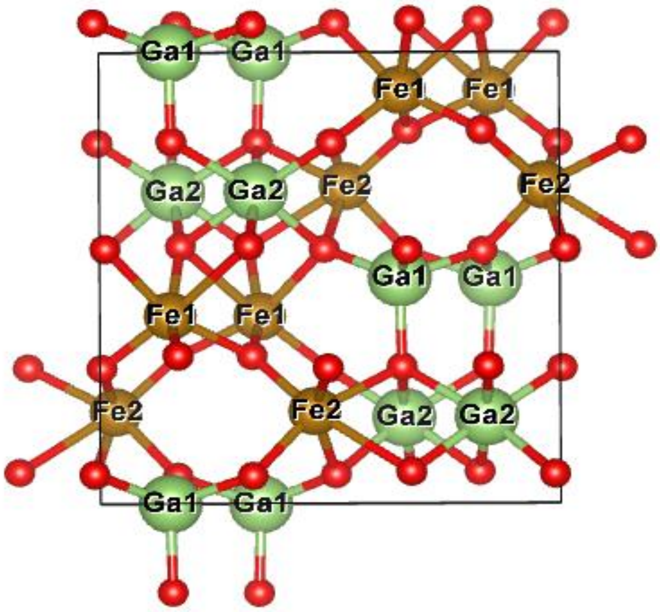

Figure 1.9. Orthorhombic unit cell of Gallium Ferrite having Ga1, Ga2, Fe1, Fe2 and 6 types of inequivalent oxygen ions (red ones) namely O1, O2, O3, O4, O5, and O6.

Piezoelectric Properties: Although not much is known about the structural distortion in GFO, its high piezoelectric coefficient—nearly twice as that of a quartz[73]—is assumed to be mainly due to the asymmetric Ga1-O tetrahedron.

1.4.2 DOUBLE PEROVSKITE MATERIALS ($A_2BB'O_6$)

The double perovskite families of multiferroic materials with the formula, $A_2BB'O_6$, are being investigated in recent years with the purpose of finding new kinds of multiferroic materials suitable for practical applications. In general, ABO_3 is the chemical formula for single-phase multiferroic perovskite oxides. In double perovskites however, the transition metal ions here form a 6-coordinated octahedral, whereas the A cation has 12-coordination. There are two distinct cations, B and B', producing two different types of BO_6 and $B'O_6$ octahedra. As a result, the spatial distribution of B and B' cations determines several crucial features in this type of materials. As can be seen in Fig. 1.10, complex double perovskites may take on three distinct structures depending on the orientation of B and B' which are layered, columnar, and rocksalt. However, the majority of synthetic double perovskites have rocksalt-like structure of B and B' cations. In a small fraction of double perovskite multiferroics [75], B and B' cations are ordered in layers. The layered form is preferred mainly when the B and B' cations have differing numbers of valence electrons and is more stable than rocksalt ordering in the case when the BO_6 and $B'O_6$ octahedra have different geometry, such that the BO_6 is Jahn-Teller deformed while $B'O_6$ is not. There are very few double perovskite materials that have been studied, these are Bi_2FeCrO_6, Bi_2NiMnO_6, La_2CuIrO_6, Ca_2CoWO_6, La_2CuMnO_6, Sr_2CoTeO_6, Y_2NiMnO_6, Ca_2CoTeO_6, Tb_2NiMnO_6, Sr_2CoWO_6, Bi_2CoMnO_6, and La_2NiMnO_6 [76–80]. In certain multiferroic double perovskites, ferroelectricity and ferromagnetism arise from distinct sites. Among them, ferroelectric polarization is generated by exotic magnetic ordering in certain double perovskite multiferroics, such as ↑↑↓↓ spin structure induced type-II multiferroics. Super-exchange interaction between B^{2+} and B'^{4+} ions cause ferromagnetism in this form of multiferroic [81–83]. The magnetocapacitance and magnetoresistance effect [84] demonstrates the link between electronic, magnetic, and dielectric characteristics in single-phase La_2NiMnO_6

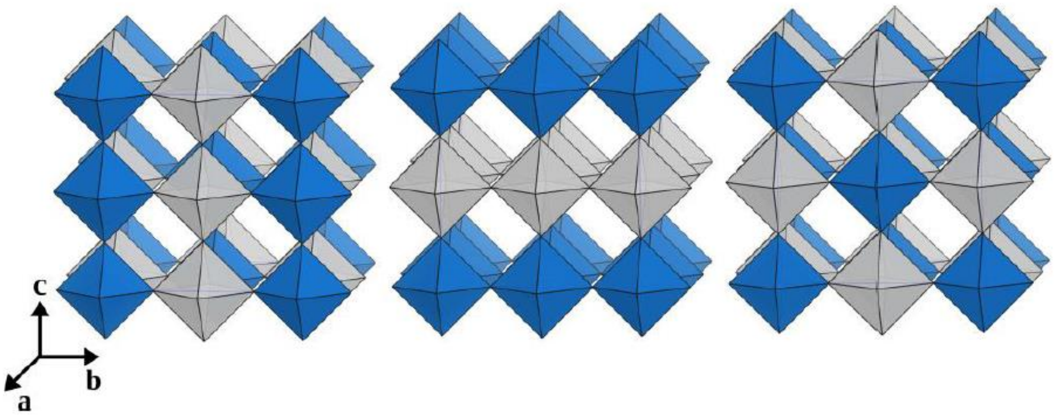

Figure 1.10. Complex double perovskites take on three distinct structures depending on the orientation of B and B' which are layered, columnar, and rocksalt (from left to right)

(LCMO). In LCMO, the magnetic field is observed to have a dramatic effect on the dielectric and resistive characteristics at temperatures about 280 K indicating high coupling. Curie's temperature is close to the RT (around 280 K). Similar to LCMO, the magnetic and electric transition temperatures of other multiferroic double perovskites are rather high. The bilayer thin film $Bi_2FeCrO_6/Nd_{0.1}Bi_{0.9}FeO_3$ has a transition temperature of around 440 K [85]. The Bi_2FeCrO_6 thin film produced on $LaAlO_3$ substrate also exhibits a ferromagnetic transition temperature of 600–800 kelvins and a ferroelectric transition temperature of 900 kelvins. The double perovskite materials are therefore very promising for use in devices because of their high ferroelectric and ferromagnetic transition temperatures and required further study.

1.4.3 MAGNETOELECTRIC COMPOSITES

One very effective strategy for creating new kinds of magnetoelectric materials with strong magnetoelectric coefficient is via the use of composites. In composites, a non-magnetic ferroelectric (FE) material and a non-ferroelectric ferromagnetic (FM) material are mixed to make multiferroic composites. The piezoelectricity of ferroelectric materials causes structural or mechanical strain in response to an applied electric field. Because of the magnetostriction feature of the magnetic material of the composite, this strain alters the magnetic properties. Therefore, the magnetoelectric (ME) effect is denoted as the result of the piezoelectric effect from the ferroelectric phase and the magnetostriction from the magnetic phase in following way.

$$ME = \frac{Magnetic}{Mechanical} \times \frac{Mechanical}{Electric} \tag{1.2}$$

The two phases can be arranged in a number of different geometries, illustrated in Fig. 1.11, including (1) 0-3 particulate composite, where particles (0) of one phase are embedded in a matrix (3) of another phase, (2) 2-2 bi-layer composite, where one phase's layer is deposited on top of another phase's layer, and (3) 1-3 composite, where one phase's nanotube pillar is embedded in another phase's matrix. The best results, however, are shown in the 0-3 particle composite phase, whereas 2-2 is constrained by the clamping effect between layers, and 1-3 is constrained by the high conductivity brought on by the connected magnetic phase.

Recently, atomic-scale observations of multiferroic superlattices have shown the layer-by-layer growth of ferroelectric and anti-ferromagnetic $LuFeO_3$ with ferromagnetic but non-polar $LuFe_2O_4$. Vertically aligned nanocomposites (VAN) are especially fascinating to study because of the enhanced coupling that occurs from the higher interfacial contact between the

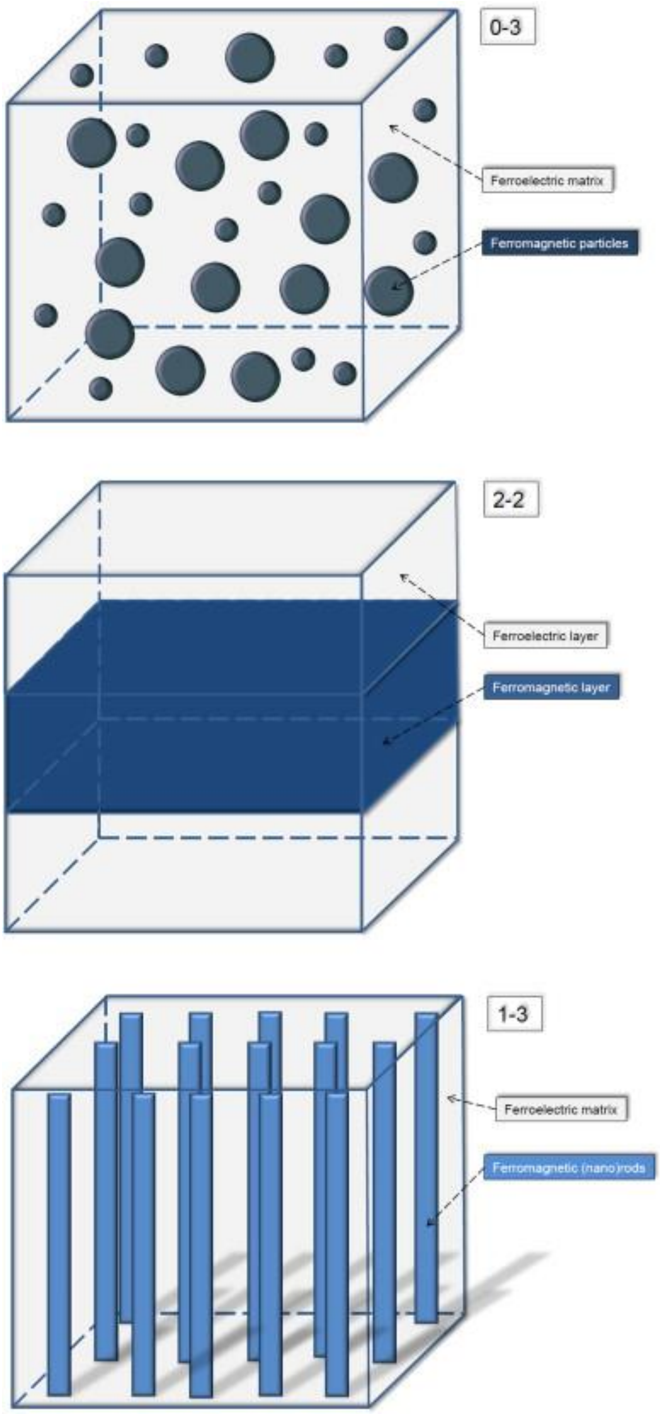

Figure 1.11. The two phases in a multiferroic composite can be arranged in a number of different geometries including (1) 0-3 particulate composite, where particles (0) of one phase are embedded in a matrix (3) of another phase, (2) 2-2 bi-layer composite, where one phase's layer is deposited on top of another phase's layer, and (3) 1-3 composite, where one phase's nanotube pillar is embedded in another phase's matrix.

two components. This suggests a considerable potential in the study of multiferroic materials, given the rich chemistry of composites. $BaTiO_3$ - $CoFe_2O_4$ was successfully synthesized at the Philips Laboratory in 1972, after Suchtelen's first proposal of two-phase composite type materials [86]. For the composite material's preparation, they used the unidirectional solidification technique and the quinary Fe-Co-Ti-Ba-O system. Compared to the single-phase multiferroic material, the resulting composite material displayed dramatically enhanced magnetoelectric coupling property. After 20 years, a simple, low-cost method of producing a composite material was developed [87,88]. Although traditional sintering was used to make particulate composite ceramics like PZT and $BaTiO_3$ in the early 1990s, their ME coupling coefficient was relatively small [87–89]. The issue was resolved by strict regulation of the synthesis process [90]. Previous research by Ryu et al. [90–92] has looked into the sintered behaviour and ME characteristics of a specific PZT and Ni-based ferrite composite. Many additional composites with a high ME coefficient were subsequently discovered [91]. Recently, researchers have been concentrating on multiferroic nano-composites thin film, in which a variety of techniques, including Pulsed Laser Deposition and Polymer-Assisted [93–97], are employed to deposit FE (such as $BaTiO_3$, $BiFeO_3$, PZT) and

FM (such as $CoFe_2O_4$, $NiFe_2O_4$) oxides such that the ME effect is improved by the nano-structured thin film's increased lattice strain or interlayer contact. However, a mechanical barrier develops between the film and the base affecting the ME coupling interaction in the nano-structured two-phase thin films [96,98,99].

1.5 DIFFERENT MORPHOLOGIES

The structure, size, and form of materials are intimately tied to their functioning. Quantum effects are related with the occurrence of strange events in this environment. Due to the predominance of anisotropy in magnetism when one or more dimensions are decreased [100–103], the magnetic characteristics become particularly sensitive to the morphology. The appearance of a material's exposed surface and interface plays a crucial influence in determining its qualities. This specific component has remarkable magnetic characteristics at smaller scales. The exposed surface exhibits decreased metal coordination, resulting in the formation of a few voids. This decreases the electrons' ability to jump from site to site, hence enhancing their Coulomb interactions. This also increases the propensity for the production of surface magnetism, owing mostly to the existence of uncompensated spins resulting from quantum confinements [103–105]. In recent years, the combination of theoretical and experimental methodologies has enabled the creation of functional materials in which morphological modulation is regarded as a crucial tool for controlling multiple degrees of freedom involved in various physical and chemical processes. Various applications, including as catalysis, gas sensing, energy conversion and storage, and magnetoresistance, are dependent on the atomic surface organization [106–109]. The magnetic properties are also impacted by the sample's chemical composition, shape, and size, as well as the core and surface local characteristics. The presence of superparamagnetism, gigantic magnetic resistance, and enhanced multiferroic characteristics [110–114] is also reliant on interactions with the surrounding environment.

1.5.1 BULK

Bulk materials consist of particles with diameters greater than 100 nm, observable with the naked eye or a basic microscope. Low surface-to-volume ratio of materials in this morphology improves performance in applications such as catalysis, solar veils, and gas sensors. Due to the low concentration of atoms and molecules on the surface, their characteristics are determined more importantly by surface forces than bulk forces. Bulk metal has normal scattering characteristics. In the electronic band structure of bulk semiconductors, there may not be any restricted energy states. Adsorption and absorption of molecules (in gaseous or liquid phases) in bulk morphologies is sluggish and weak. Examples of materials in bulk form include sand, cement, alumina, ore, salts, etc.

1.5.2 NANOSTRUCTURE

Nanomaterials (NMs) are chemical compounds or materials with dimensions between 1 and 100 nm in at least one dimension, therefore invisible with a basic microscope or with the naked eye. The observation of these type of materials requires advanced microscopic methods. Large surface-to-volume ratios of nano-structural materials improve performance in applications such as catalysis, solar veils, and gas sensors. Nanoparticles have a very high aspect ratio, and hence a greater surface area making them highly effective in adhesion with the matrix or surface and enhancement of mechanical performance of the parent material. Surfaces having a high concentration of atoms or molecules have distinctive characteristics where surface forces are quite significant. Metal nanoparticles have unique scattering characteristics. Nanoparticles of semiconductors may show constrained energy states within the electronic band structure. Their unique chemical and physical features vary with their size and form. The characteristics of NM may be "tuned" by modifying the particle size (e.g., changing the fluorescence color so a particle can be identified). The rate of adsorption and absorption of molecules (in gaseous or liquid phases) is quite high. Examples include nanosilica, nanotitania, nanoalumina, etc.

Compared to their counterparts at the microscale, nanoscale materials offer a range of enhanced features. This is due to the following factors: (i) having more surface atoms than inner atoms, (ii) having more free energy surface available (as a result of the increased surface area and surface atoms, the surface energy associated with the particles increases), (iii) increasing a substance's surface area enhances the rate of a chemical reaction, in general, (iv) low wavelength and high frequency and energy, (v) the blue shift of atoms for optical absorption spectra, (vi) super paramagnetism occurs when the nanoparticle is smaller than the magnetic domain in a material [115–117]. There are several types of nanomaterials, they are[118],

- Type one, 0D: All three dimensions of 0-dimensional NMs are inside the nanoscale range. Examples include arrays of heterogeneous nanoparticles, arrays of uniform nanoparticles (quantum dots), hollow spheres, and nanolenses.
- Type two, 1D: One-dimensional nanomaterials have one dimension within the nanoscale range. Nanotubes, nanowires, nanorods, nanobelts, nanoribbons and nanographene platelets are examples of 1D nanostructures.

- Type three, 2D: Two-dimensional nanomaterials have two dimensions at the nanoscale level. Thin films, nanoprisms, nanoplates, nanosheets, nanowalls, and nanodisks are examples of such nanostructures.
- Type four, 3D: Multiple 0D, 1D, or 2D materials are arranged to produce the 3D structure. Nanoballs (dendritic structures), nanocoils, nanocones, nanopillers, nanoflowers, graphite, and multi-nanolayers are examples of nanostructures.

Type three - 2D Thin Film: Thin films vary significantly from bulk ceramics in their morphology (physical structure) from the micrometer level (i.e., microstructure) to the nanoscale level (i.e., nanostructure). Many vapor-deposited films have columnar morphologies as a result of the low processing temperatures and the variations in nucleation and growth. Consequently, despite the fact that the top surface of certain films may have a ceramic-like microstructure in two dimensions, they may only be one grain thick. In addition, as explained below, the "grain boundaries" may have a different character than the "bulk" of the film due to differences in local density and stoichiometry, and may range from crystalline grain boundaries to density fluctuations, commonly known as voids, surrounding 1–10 nm-sized amorphous clusters or crystallites. Due to their very high surface-to-volume ratios, nanoscale crystallites often exhibit properties distinct from their counterparts in bulk. Therefore, it is essential to take into account the elements that impact the formation of film morphology in ceramic systems at all length scales.

The 2D thin film structure is crucial for the practical uses of magnetoelectric materials. Nano-structured thin films provide for more degrees of freedom and enhance lattice strain or interlayer contact, hence boosting the magnetoelectric (ME) effect. Between the thin layer and the substrate, a mechanical limitation also develops. This mechanical limitation and the nanostructured two-phase thin films have a tremendous effect on the ME coupling interaction [119–121]. However, the controlled production of materials as thin films (the deposition process) is a critical step in several applications. A common example is the home mirror, which normally has a reflecting surface formed by a thin metal coating on the back of a sheet of glass. In the past, silvering was routinely employed to manufacture mirrors, but nowadays the metal layer is produced using methods such as sputtering. During the 20th century, advances in thin film deposition techniques enabled numerous technological advances in fields such as magnetic recording media, electronic semiconductor devices, integrated passive devices, LEDs, optical coatings (such as antireflective coatings), hard coatings on cutting tools, and energy generation (such as thin-film solar cells) and storage (thin-film batteries). Through thin-film drug delivery, it is also used to medicines. A collection of thin films is known as a multilayer.

1.6 APPLICATIONS

1.6.1 Data Storage: The need for data storage and access that does not generate a great deal of data traffic or consume a great deal of energy has increased dramatically as a result of the current rapid growth of data each year. Due to their low energy consumption, multiferroic materials now have a wide range of potential applications in memory and data storage technology. To begin with, the memories where we can read, write, and modify the stored memories are called Random-Access Memory, or RAM. As a result, in order to create a RAM, it is crucial to be able to (a) read or retrieve data, (b) keep or store data, and (c) write data. Based on their operating principles, RAMs can be classified into various categories according to their power usage, logic density, speed, etc. These are the fundamental variables that must be investigated and improved in order to increase speed or storage capacity. Static RAM, or SRAM, is the most popular type of RAM utilized in computers' cache memory in high-speed CPUs like Intel 486 and Pentium. These are constructed using flip-flops and store the bits as voltages, requiring 6 transistors per cell. Because of this, this RAM has a very low logic density

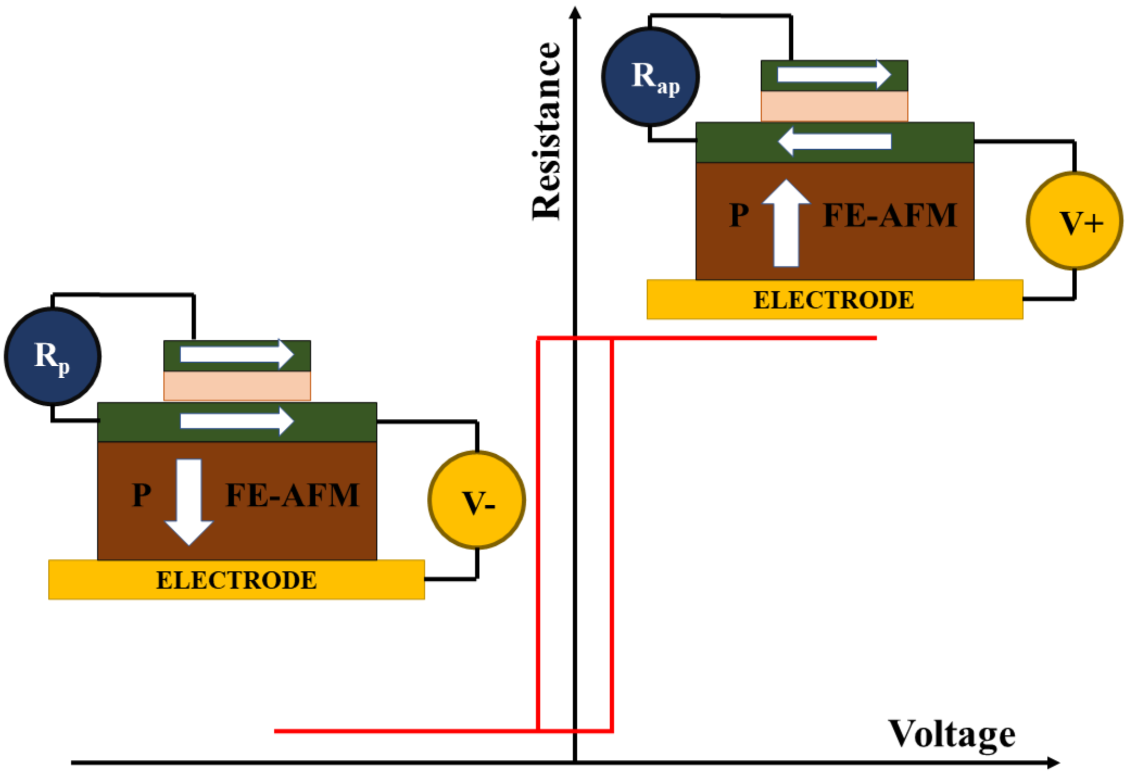

Figure 1.12. MERAMs that make use of exchange-bias coupling between a ferroelectric and antiferromagnetic multiferroic (FE-AFM, brown layer) and a thin ferromagnetic electrode (green layer). A tunnelling barrier layer provides the two resistive states (R_p and R_{ap}) between the two ferromagnetic layers at the top.

yet a very high speed. Dynamic Random-Access Memory, or DRAM, is the name of the RAM that is currently utilized in smartphones and computers. In DRAM, the 1 and 0 bits are represented by distinct capacitors that are in the process of charging or discharging, respectively. Its logic density is higher since just one transistor and one capacitor are used per bit. But because even nonconducting transistors leak a tiny amount of charge, capacitors continue to discharge and are unable to store any information. Despite being slower than SRAM, it is frequently employed in current computers due to its inexpensive cost and straightforward design. For its non-volatility, unlike DRAM, ferroelectric RAM, or FERAM, uses a ferroelectric layer rather than a dielectric layer. The two bits of 1 and 0 are represented by the two ferroelectric polarisation states. When a magnetic field is applied, the various resistance states correspond to 1 and 0 bits in magneto-resistive RAM, or MRAM, which can be used to read or recover data. Information is stored or retained through magnetic anisotropy. However, the stored information can be changed from 1 to 0 or vice versa using a magnetic field. Hard Drives, which use magnetic memory to store gigabytes or terabytes of data, are an example. The magnetic materials are tailored using polyethylene terephthalate (PET) for magnetic tapes and alumina discs for drives (γ-Fe_2O_3 previously, currently Cobalt-based alloy). A flux is created when these discs are passed through an electromagnet, and this flux causes an electromagnetic flux (EMF) voltage to be induced. The signal is transformed into information by this EMF voltage. A magnetoelectric material is an exchange linked with another ferromagnetic material in magnetoelectric RAM, also known as MERAM[122]. While the ferromagnetic layer is utilized to store data similarly to MRAM, the ME layer functions as a drive[123,124]. An electric field is applied to the magnetoelectric layer in place of a magnetic field, changing or writing the ferromagnetic material's magnetic state as a result of ME coupling (Figure 1.12). And, unlike DRAM, the magnetic junction tunnel (MT) acts like a capacitor to store information. This RAM uses a lot less energy than other RAMs.

1.6.2 Microwave Absorption: Its potential for successful application as a microwave absorber has been increased by the presence of both electric and magnetic characteristics. Crystal engineering has the ability to overcome the constraints of reducing the electromagnetic energy absorption of BFO by enhancing the magnetic loss or achieving a better balance between the dielectric loss and the magnetic loss. Examples include the capacity of Nd-doped BFO to generate ordered domains with modified electromagnetic and energy absorption properties[125]. The phase boundary can be adjusted with a Ca doping BFO to increase the microwave absorption bandwidth[126].

1.6.3 Actuators and Sensors: The coexistence of strain and ferroelectricity in the same materials enables these materials to be used as actuators ad sensors.

1.6.4 Optoelectronic Devices: The utilization of multiferroic materials in optical and electrical device manufacturing is widespread[127–132]. The adequate band gaps and conductivities of these materials enhance their photo-ferroelectric properties. $BiFeO_3$ is used to create antennas for terahertz spectroscopy that can detect terahertz frequency due to its ability to emit electromagnetic waves in the terahertz frequency range.

1.7 MAGNETOELECTRIC PROPERTIES

1.7.1 MAGNETOELECTRIC COUPLING

The magnetoelectric effect defines the coupling of electric and magnetic fields in matter, i.e., the generation of polarization (P) by a magnetic field (H) or the induction of magnetization (M) by an electric field (E)[3]. In 1888, Rontgen noticed that a moving dielectric body placed in an electric field becomes magnetized. Later, he noticed the opposite effect: a moving dielectric generating polarisation in a magnetic field. But neither is an inherent property of the substance. Curie suggested the possibility of an intrinsic magnetoelectric effect in some crystals in 1894 when considering crystal symmetry. This type of effect is known as a "magnetoelectric effect" according to Debye. The magnetoelectric coupling coefficient was 4.13 $ps.m^{-1}$ when the magnetoelectric phenomenon was first successfully observed in Cr_2O_3. More than 100 different compounds have been found or created so far that shows the magnetoelectric effect.

Using Landau's theory[133] for free energy, we can write the free energy as,

$$F(E,H) = F_0 - P_i^s E_i - M_i^s H_i - \frac{1}{2}\varepsilon_0 \varepsilon_{ij} E_i E_j - \frac{1}{2}\mu_0 \mu_{ij} H_i H_j - \alpha_{ij} E_i H_j - \frac{1}{2}\beta_{ijk} E_i H_j H_k - \frac{1}{2}\gamma_{ijk} H_i E_j E_k - \cdots \tag{1.3}$$

Where, F_0 is the ground state free energy, subscripts (i, j, k) refer to the three components of a variable in spatial coordinates, E_i and H_i the components of the electric field E and magnetic field H, respectively, P_i^s and M_i^s are the components of spontaneous polarization P^s and magnetization M^s, ε_0 and μ_0 are the dielectric and magnetic susceptibilities of vacuum, ε_{ij} and μ_{ij} are the second-order tensors of dielectric and magnetic susceptibilities, β_{ijk} and γ_{ijk} are the third-order tensor coefficients and, most importantly, α_{ij} is the components of tensor α which is designated as the linear magnetoelectric effect and corresponds to the induction of polarization by a magnetic field or a magnetization by an electric field. The rest of the terms in the preceding equations correspond to the high-order magnetoelectric effects parameterized by α and β tensors. Then the polarization is,

$$P_i(E,H) = -\frac{\partial F}{\partial E_i} = P_i^s + \varepsilon_0\varepsilon_{ij}E_j + \alpha_{ij}H_j + \frac{1}{2}\beta_{ijk}H_jH_k + \gamma_{ijk}H_iE_j + \cdots, \quad (1.4)$$

And the magnetization is,

$$M_i(E,H) = -\frac{\partial F}{\partial H_i} = M_i^s + \mu_0\mu_{ij}H_j + \alpha_{ij}E_j + \beta_{ijk}H_jE_i + \frac{1}{2}\gamma_{ijk}E_jE_k + \cdots, \quad (1.5)$$

The α_{ij} in above equations is known as the Magnetoelectric coupling coefficient.

1.7.2 DIELECTRIC PROPERTIES

To design high-frequency circuits, a thorough understanding of the electrical properties of materials, specifically the dielectric constant and loss tangent under operating conditions, is required. In general, materials can be categorized as conductors, semiconductors, or insulators based on their conductivity, and as dielectric, paraelectric, or ferroelectric based on their polarizability[134]. Typically, ferrites belong to the semiconductor and dielectric ranges. The measurement of complex dielectric properties of materials at radio frequency (RF) and microwave frequency is particularly important in the research fields of material science, communication, microwave circuit design, and biology[135]. Moreover, measurements in *ac* frequency provide insight into the microscopic nature of the ionic conducting process, whereas the technically more difficult *dc* measurements provide less information regarding the entire dynamic behaviour of the sample. Consequently, *ac* techniques are used to measure material properties including bulk conductivity, surface, grain boundary effect, ionic transport, and double layer formation at the electrode/sample interface, etc.[136]. Dielectric properties pertaining to polarization behaviour, conduction, and relaxation mechanisms of a material vary with both external and internal parameters such as frequency, temperature, and pressure, as well as sample orientation, composition, and molecular structure. In the section that follows, therefore, important topics pertaining to the dielectric properties of a material are discussed.

1.7.2.1 IMPEDANCE SPECTROSCOPY

It is common knowledge that impedance spectroscopy is a potent method for investigating the dielectric properties of materials, such as conductivity (σ), dielectric constant (ε), transport phenomena, interfacial capacitance, mobility of charges and their equilibrium concentration, etc. When an *ac* signal with electric field strength significantly less than breakdown voltage is applied to a system, the impedance of the system follows Ohm's law, as the ratio of voltage (V) to current (I) in the time domain,

$$V(t) = V_0 \exp(j\omega t) \tag{1.6}$$

$$I(t) = I_0 \exp(j\omega t - \theta) \tag{1.7}$$

$$Z(\omega) = |Z|cos\theta - j|Z|sin\theta = Z' - jZ'' = \frac{1}{j\omega C} \tag{1.8}$$

Here, Z' and Z'' are the real and imaginary components of the complex impedance (Z), ω ($= 2\pi f$) or the angular frequency of the signal and C is the complex capacitance of the dielectric sample. As the relative dielectric constant or, permittivity (ε) of the material is related to the capacitance in a way, $\varepsilon = C/C_0$, from the impedance it can be calculated using the following formula,

$$\varepsilon = \frac{1}{j\omega C_0 Z} = \varepsilon' - j\varepsilon'' \tag{1.9}$$

Where, capacitance of free space, $C_0 = \frac{\varepsilon_0 A}{d}$, ε_0, A, and d are free space permittivity (8.854×10^{-12} F/m), area of the active region, and thickness of the sample respectively. Expanding Eq. (1.9), the real and imaginary parts of dielectric constant in terms of impedance can be given by,

$$\varepsilon' = \frac{Z''}{\omega C_0 (Z'^2 + Z''^2)} \tag{1.10}$$

$$\varepsilon'' = \frac{Z'}{\omega C_0 (Z'^2 + Z''^2)} \tag{1.11}$$

Moreover, real part of conductivity can be found using the formula $\sigma = \omega\varepsilon_0\varepsilon''$. Permittivity values reveal how an external field interacts with the electric dipole moments of a sample. The ε' represents the amount of dipole or charge alignment (both induced and permanent) due to polarization and ε'' measures the energy required to align the dipoles or move the ions. Loss tangent ($tan\delta_\varepsilon = \frac{\varepsilon''}{\varepsilon'}$) is expressed as measure of energy loss from the material due to an external electric field. Generally, with rising temperatures, ε increases in dielectric material with an increase in participating dipoles or ions. Frequency dependence of ε' according to ideal Debye's dispersion equation is,

$$\varepsilon' = \varepsilon'_\infty + \frac{(\varepsilon'_0 - \varepsilon'_\infty)}{1 + (\omega\tau)^2} \tag{1.12}$$

$$\varepsilon'' = \frac{(\varepsilon'_0 - \varepsilon'_\infty)\omega\tau}{1 + (\omega\tau)^2} \tag{1.13}$$

Where, ε'_{∞} and ε'_0 are the permittivity values at high and at low frequency respectively and τ is relaxation time constant. With increasing frequency ε' falls due to the lagging of dipoles behind the field whereas ε'' exhibits a maximum at $\omega = {}^{1}/_{\tau}$, where the oscillating charges are coupled with the oscillating field and absorbs maximum electrical energy. Numerous materials exhibit a non-Debye dielectric behaviour that is characterized by a broader asymmetric loss peak where multiple ions are responsible for dielectric dispersion[137]. The non-Debye behaviour of a material could be described by the Cole-Cole, Davidson-Cole, and empirical expression proposed by Havriliak-Negami[138]. Electric modulus (M), which is defined as the inverse of relative permittivity, is used to analyse dielectric behaviour at relatively higher temperatures, where ε typically becomes extremely high due to electrode polarization and carrier transport.

1.7.2.2 POLARIZATION

The cations in ferrites are surrounded by densely packed oxygen anions and can be considered isolated. Consequently, the electrons or holes associated with a particular ion will remain localized, leading to the formation of a potential well. The transition to a neighbouring lattice site for a trapped carrier charge at a lattice site in such a deep well may be triggered by thermal activation or at a higher frequency. This trapped charge, known as a small polaron, is the result of a defect in the crystal lattice and, when an electric field is applied, causes polarization[139]. The placement of cations in A or B sites of ferrites greatly affects the migration of charge carriers as well as the dielectric properties' defining characteristics. In addition, the interaction of electron hopping between cations results in the formation of dipole pairs in ferrites, which contribute to dipolar polarization[135]:

$$T^{2+} + Fe^{3+} \leftrightarrow T^{3+} + Fe^{2+} + E_a \tag{1.14}$$

Where E_a is the activation energy, required for transfer of electron from T^{2+} to Fe^{3+} and vice versa. This polarization originates from a number of sources:

Electronic Polarization: In the presence of an external field, the electron cloud moves relative to the nucleus. The required time for this type is the shortest (~ 10^{-15} s), and as a result, its negligible contribution is amplified at optical frequencies. Electronic polarisation rules at frequencies higher than 10^{12} Hz.

Atomic Polarization: Atomic polarization occurs when positive and negative ions adjacent to one another "stretch" in response to an applied electric field. In addition to being a rapid process with a response time of 10^{-13} s and rules at frequencies between 10^{9} Hz and 10^{12} Hz, this type of polarization is effective at THz and microwave frequencies. In addition to dielectric relaxation, resonance-type dielectric response occurs in the dielectric system at high frequency. Inertial effects in charge movement or anomalous dispersion are also considered[140].

Dipolar Polarization: Dipolar or orientation polarization refers to the alignment of dipoles through orientation in an electric field. Typically, orientation polarization requires 10^{-9} s and dominates between 10^3 Hz - 10^9 Hz[141].

Space Charge Polarization: Space charge accumulation at the structural interfaces of an inhomogeneous dielectric material causes interfacial polarization. The trapped charge carriers are involved in this process, and as the temperature rises, this type of polarization increases as thermal agitation activates more carriers. At room temperature, its operating frequency range is less than 10^7 Hz and falls between the microwave and radio-wave frequency ranges.

As frequency increases, slower mechanisms are eliminated, leaving only faster mechanisms to contribute to values. In Figure 1.13, a schematic dielectric constant, ε, versus frequency curve illustrating various types of polarization is depicted. This dielectric relaxation can be characterized by the Maxwell-Wagner grain-grain boundary model for ferrites and represented by the Cole-Cole plot.

1.7.2.3 MAXWELL-WAGNER MODEL AND COLE-COLE PLOT

Koops[142] proposed a theory in which conducting grains and grain boundary layers of ferrite material can be understood as an inhomogeneous polycrystalline dielectric structure introduced by Maxwell and Wagner. Charge carriers migrate easily from the grain and accumulate (space charge) at the grain's resistive boundaries when an external electric field is applied. At low frequencies, this process can produce a large polarization and a high ε′. The presence of charge movement inertia would result in a relaxation of dipoles with respect to the polarizing field, resulting in a finite phase difference with the field. After a sufficiently high characteristic cut-off frequency, the phase lag in the carriers becomes pronounced, causing ε′ to decrease. At these frequencies, conductive grains become more active and electron hopping occurs, increasing the material's conductivity.

The Cole-Cole plot is essentially a simple real part of impedance (Z′) versus imaginary part of impedance (Z″) plot that can represent the Maxwell-Wagner two-layer model and the electrical processes occurring within the system as well as the relaxation mechanism. A Debye type material exhibits a perfect semi-circular plot at a specific temperature, whereas a non-Debye type material exhibits a distorted semi-circle and an electrode-sample interface exhibits an inclined line plot.

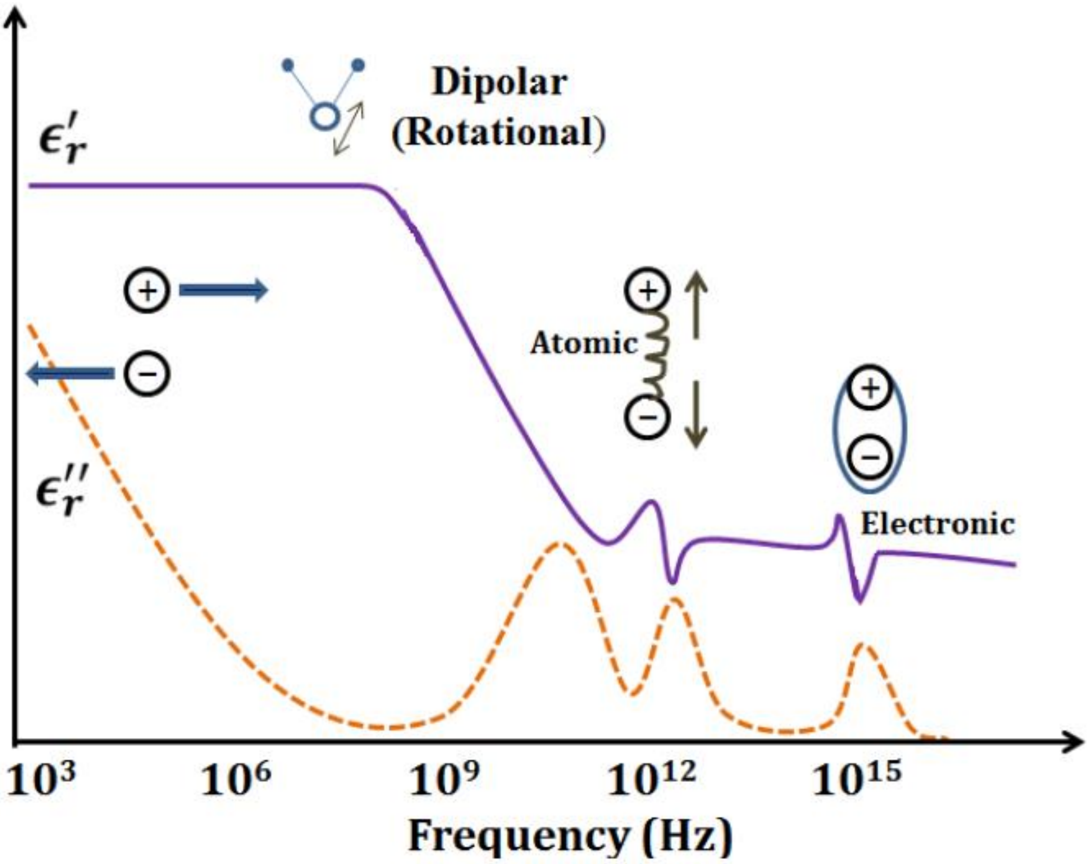

Figure 1.13. Dielectric response with varying frequency

Figure 1.14 illustrates the equivalent circuit of a grain and grain boundary model of a material, using which the resistive and capacitive components of complex impedance (Z) of the material can be analysed. The grain and grain boundaries with resistances, R_g and R_{gb} and capacitances, C_g and C_{gb} are depicted in the equivalent circuit, respectively. The resistance and capacitance components are connected in parallel to each other, whereas the grain and grain boundaries are connected in series with each other.

Therefore, the equivalent impedance is given by,

$$Z = Z_g + Z_{gb} \tag{1.15}$$

Here, $Z_g$is the complex impedance of the grain and $Z_{gb}$is the complex impedance of the grain boundary.

Therefore,

$$\frac{1}{Z_g} = \frac{1}{R_g} + j\omega C_g \tag{1.16}$$

$$Z_g = \frac{R_g}{1+j\omega C_g R_g} \tag{1.17}$$

And,

$$\frac{1}{Z_{gb}} = \frac{1}{R_{gb}} + j\omega C_{gb} \tag{1.18}$$

$$Z_{gb} = \frac{R_{gb}}{1+j\omega C_{gb} R_{gb}} \tag{1.19}$$

Substituting these expressions in Eq. 1.15, we get,

$$Z = Z_g + Z_{gb} = \frac{R_g}{1+j\omega C_g R_g} + \frac{R_{gb}}{1+j\omega C_{gb} R_{gb}} \tag{1.20}$$

$$Z' - jZ'' = \frac{R_g(1-j\omega C_g R_g)}{1+\omega^2 C_g^2 R_g^2} + \frac{R_{gb}(1-j\omega C_{gb} R_{gb})}{1+\omega^2 C_{gb}^2 R_{gb}^2} \tag{1.21}$$

$$Z' - jZ'' = \left[\frac{R_g}{1+\omega^2 C_g^2 R_g^2} + \frac{R_{gb}}{1+\omega^2 C_{gb}^2 R_{gb}^2}\right] - j\omega\left[\frac{C_g R_g^2}{1+\omega^2 C_g^2 R_g^2} + \frac{C_{gb} R_{gb}^2}{1+\omega^2 C_{gb}^2 R_{gb}^2}\right] \tag{1.22}$$

Equating the real and imaginary parts from both sides of the above equation,

$$Z' = \left[\frac{R_g}{1+\omega^2 C_g^2 R_g^2} + \frac{R_{gb}}{1+\omega^2 C_{gb}^2 R_{gb}^2}\right] \tag{1.23}$$

$$Z'' = \left[\frac{\omega C_g R_g^2}{1+\omega^2 C_g^2 R_g^2} + \frac{\omega C_{gb} R_{gb}^2}{1+\omega^2 C_{gb}^2 R_{gb}^2}\right] \tag{1.24}$$

1.7.2.4 CONDUCTION

As the frequency of the applied field increases in dielectric ferrites, the conductive grains become more active by encouraging the hopping of electrons and holes between Fe^{2+} and T^{3+} ions and vice versa, thereby accelerating the hopping rate. Consequently, a gradual increase in conductivity can be observed with an accompanying decrease in polarization as the frequency of the applied field increases. Jonscher's power law provides a straightforward expression for the frequency dependence of conductivity[143,144],

$$\sigma_{ac}(\omega, T) = \sigma_{dc}(\omega, T) + A\omega^S(T) \tag{1.25}$$

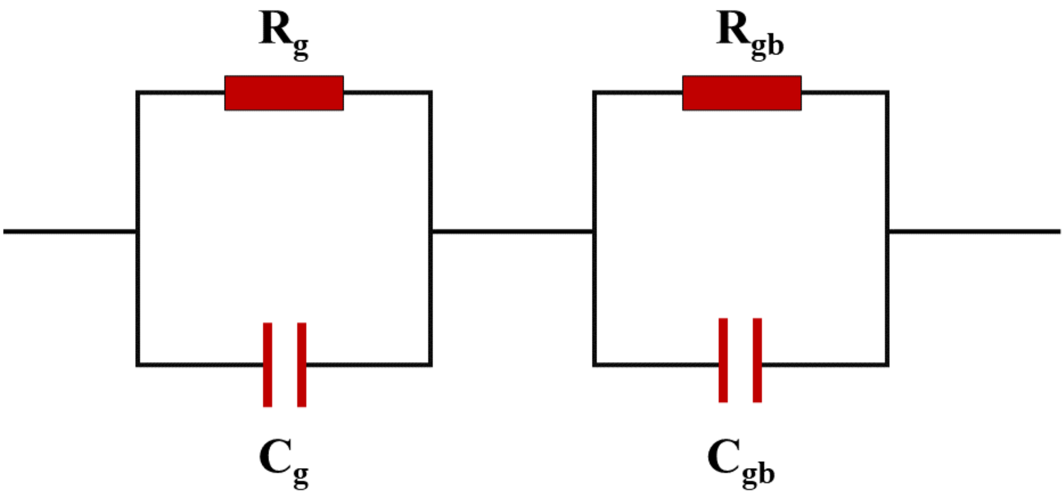

Figure 1.14. Equivalent circuit of grain and grain boundary resistances and capacitances in a material

Here, σ_{dc} is the *dc* conductivity of the material, A is material dependent constant and s is the temperature dependent parameter, varies within $0 < s < 1$ depending on the mechanism of conduction. Despite the fact that grain boundaries are resistive and may impede ionic transport, the presence of a high defect density in the interfacial region contributes to the high conduction path. Thermal excitation facilitates charge hopping by increasing the mobility and concentration of charge carriers. Activation energy (taking it also as thermally activated) for dc conduction (E_{dc}) is found by fitting Arrhenius equation of conductivity to ln (σ_{ac}) vs. $1/k_B T$ plot at low frequency.

1.7.3 MICROWAVE PROPERTIES

With the widespread evolution of technology, including wireless information transfer, global navigation, and radar (radio detection and ranging) communication, the demand for ferrites for high-frequency applications is expanding rapidly[145–147]. A recent survey reveals that approximately 23 percent of engineering research focuses on ferrites, which, as an effect on application, increases production while decreasing the price of microwave devices[148]. Ferrites are iron-based ferrimagnetic oxides that combine the characteristics of a magnetic material and an electrical insulator[149]. In contrast to highly conductive metals, they permit electromagnetic (EM) waves to penetrate the material and, due to their high resistivity, reduce eddy current loss, thereby expanding the range of applications for high-frequency devices. In non-reciprocal devices such as circulators, fast sensors ferrite characteristics including high anisotropy, low FMR (ferromagnetic resonance) bandwidth, and low loss are required[149–151]. In contrast, for microwave absorbers, lossy material with broad resonance bandwidth and a proper matching of relative permittivity ($\varepsilon = \varepsilon' - j\varepsilon''$) and permeability ($\mu = \mu' - j\mu''$) is essential.

Electromagnetic Interference (EMI) has emerged as a significant problem in recent years as a result of the increased use of high-frequency devices[140]. Interference of electromagnetic waves from multiple sources causes misinterpretation of carried information, noise, and consequently a slowing of electronic devices. In addition, this undesirable wave pollution is detrimental to the environment and human health. Therefore, Electromagnetic absorbers (EMA) are crucial for suppressing and shielding unwanted electromagnetic waves[152,153]. As frequency-selective band pass filters, EMA materials can be used in the form of films in circuit components. In addition, since the 19th century, the military has made extensive use of EMA materials in 'stealth technology' to make aircrafts and ships invisible to radar[154,155]. Despite ferrite's predominance in high-frequency devices, their heaviness is their primary drawback; for practical applications, thin, light, and inexpensive microwave absorbers are anticipated to be most effective[145,152,156]. Ferrite-based EMA materials prevent the reflection of EM waves and convert the majority of their energy into heat. In relation to this dissipation of heat and rise in temperature of the material, ferrites with their lower thermal coefficient and stability can perform adequately up to 200 °C due to their thermal resistance. Typically, ferrite fillers are dispersed and precisely shaped within a suitable polymer matrix for research and application purposes. Over time, numerous methods for measuring permeability and permittivity have been developed. These techniques include free-space methods, open-ended coaxial probe techniques, cavity resonators, full-body resonance techniques, and transmission-line techniques[157]. Each technique has its own scope of applicability and inherent limitations. For instance, cavity-based techniques are precise, but not broadband[157]. Transmission line techniques are the simplest and most accurate techniques for measuring the characteristic properties of materials. Transmission line technique and electromagnetic wave theory in relation to microwave absorption are described in detail in the following sections.

1.7.3.1 RELATED ELECTROMAGNETIC THEORY

Electric and magnetic phenomena and electromagnetic wave propagation at the macroscopic level are described by Maxwell's equations, published in 1873, laid the groundwork for the practical applications of guided waves and transmission lines. Following are the Maxwell's equations for a material:

$$\vec{\nabla}.\vec{D} = \rho \tag{1.26}$$

$$\vec{\nabla}.\vec{B} = 0 \tag{1.27}$$

$$\vec{\nabla} \times \vec{E} = -\frac{\partial \vec{B}}{\partial t} \tag{1.28}$$

$$\overrightarrow{\nabla \times} \vec{H} = \vec{J} + \frac{\partial \vec{D}}{\partial t} \tag{1.29}$$

Here, $\vec{D} = \varepsilon_0 \vec{E} + \vec{P} = \varepsilon \vec{E}$, is electric displacement, $\vec{B} = \mu_0(\vec{H} + \vec{M})$, magnetic flux density, ρ, free charge density and $\vec{J} = \sigma \vec{E}$, current density in the material. Orientation of the $\vec{E}$, $\vec{H}$, and $\vec{k} = k\hat{n}$ vectors for a general plane wave is schematically represented in Figure 1.15. $\vec{H}$ can be written in terms of $\vec{E}$ as,

$$\vec{H} = -\frac{1}{j\omega\mu_0} \vec{\nabla} \times (\vec{E}_0 e^{-j\vec{k}.\vec{r}}) \tag{1.30}$$

$$= \frac{1}{\omega\mu_0}\vec{\mathrm{k}} \times \vec{E}_0 e^{-j\vec{k}.\vec{r}} \tag{1.31}$$

$$= \sqrt{\frac{\varepsilon_0}{\mu_0}}(\hat{n} \times \vec{E}) \tag{1.32}$$

Considering wave equation, $\vec{E} = E_0 \cos{(\omega t + \varphi)}\hat{x}$, Maxwell's equations are in phasor form,

$$\vec{\nabla}.\vec{D} = \rho \tag{1.33}$$

$$\vec{\nabla}.\vec{B} = 0 \tag{1.34}$$

$$\overrightarrow{\nabla \times} \vec{E} = -j\omega\vec{B} \tag{1.35}$$

$$\overrightarrow{\nabla \times} \vec{H} = \vec{J} + j\omega\vec{D} \tag{1.36}$$

Propagation of *ac* EM wave suggests permittivity of a material to be complex. In that case, Eq. 1.36 takes the form below and dielectric loss tangent is defined as follows,

$$\vec{\nabla} \times \vec{H} = j\omega(\varepsilon' - j\varepsilon'')\vec{E} + \sigma\vec{E} \tag{1.37}$$

$$tan\delta_\varepsilon = \frac{(\sigma + \omega\varepsilon'')}{\varepsilon'} \tag{1.38}$$

Solving for $\vec{E}$ or $\vec{H}$ from 1.35 and 1.36 gives Helmholtz wave equations:

$$\vec{\nabla} \times \vec{\nabla} \times \vec{E} = -j\omega\mu\vec{\nabla} \times \vec{H} = \omega^2\mu\varepsilon\vec{E}$$

$$\nabla^2\vec{E} + \omega^2\mu\varepsilon\vec{E} = 0 \tag{1.39}$$

A constant $k = \omega\sqrt{\mu\varepsilon}$ is defined as the propagation constant (also known as the phase constant, or wave number) of the medium. The resulting wave equation for $\vec{E}$ for plane waves in a general lossy (with finite conductivity σ) medium is:

$$\nabla^2\vec{E} + \omega^2\mu\varepsilon(1 - j\frac{\sigma}{\omega\varepsilon})\vec{E} = 0 \tag{1.40}$$

Then a complex propagation constant for the medium is defined as,

$$\gamma = \alpha + j\beta = j\omega\sqrt{\mu\varepsilon}\sqrt{1 - j\frac{\sigma}{\omega\varepsilon}} \tag{1.41}$$

where α is the attenuation constant and β is the phase constant.

The expression of complex propagation constant, (γ), consists of real part, (a) α, known as attenuation constant and imaginary part, (b) β, known as phase constant.

From Figure 1.15 and considering modified Helmholtz equation, relation between magnetic and electric field transforms to,

$$\vec{H} = \frac{\gamma}{j\omega\mu}\vec{E} \tag{1.42}$$

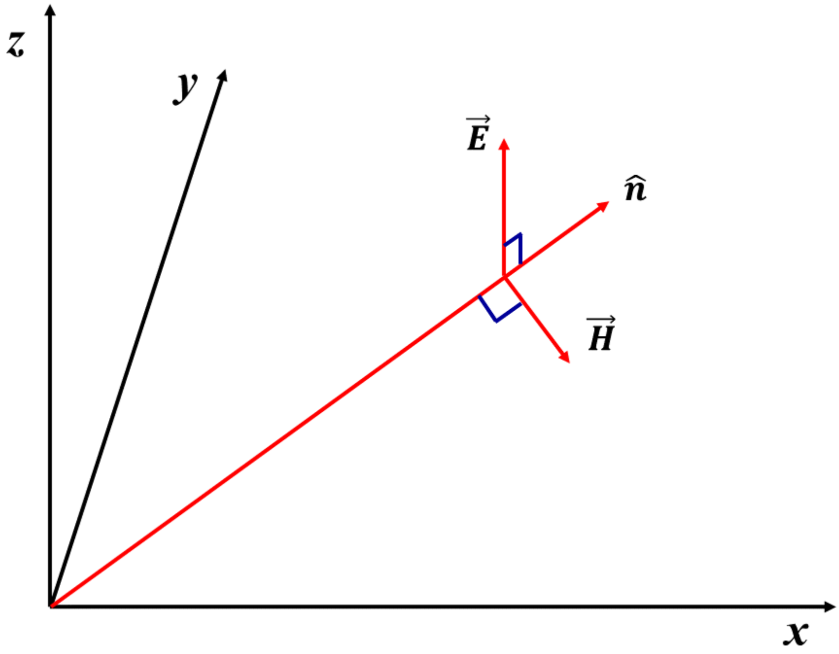

Figure 1.15. Orientation of the $\vec{E}, \vec{H}, \vec{k} = k\hat{n}$ vectors for a general plane wave

Here, $\eta = \frac{j\omega\mu}{\gamma}$ is the intrinsic impedance of the conducting medium. For highly conducting media like metal (high σ), EM wave does not penetrate into material as the skin-depth, $\delta = {}^{1}/_{\alpha} = \sqrt{{}^{2}/_{\omega\mu\sigma}}$ becomes much lower. The average power (P_l) dissipated in the volume V of a lossy medium due to conductivity, dielectric, and magnetic losses is,

$$P_l = \frac{\sigma}{2}\int E^2 dv + \frac{\omega}{2}\int (\varepsilon'' E^2 + \mu'' H^2) dv \tag{1.43}$$

However, magnetic hysteresis and domain wall resonance become less significant at low fields and high frequencies ($f > 100$ MHz for ferrites), whereas characteristic FMR and eddy current loss become more prominent in the gigahertz region[158,159].

When an electromagnetic wave propagating in the z-direction strikes a media interface, some of it reflects and some of it passes through the material. Considering normal incidence (as shown in Figure 1.16), the expressions for incident waves (E_i, H_i), reflected (E_r, H_r) and transmitted (E_t, H_t) will be,

(at $z < 0$)

$$\vec{E}_i = \hat{x}E_0 e^{-jk_0 z} \tag{1.44}$$

$$\vec{H}_i = \hat{y}\frac{1}{\eta_0}E_0 e^{-jk_0 z} \tag{1.45}$$

$$\vec{E}_r = \hat{x}\Gamma E_0 e^{jk_0 z} \tag{1.46}$$

$$\vec{H}_i = -\hat{y}\frac{\Gamma}{\eta_0}E_0 e^{jk_0 z} \tag{1.47}$$

(at $z > 0$)

$$\vec{E}_t = \hat{x}TE_0 e^{-\gamma z} \tag{1.48}$$

$$\vec{H}_t = \hat{y}\frac{T}{\eta}E_0 e^{-\gamma z} \tag{1.49}$$

Here, Γ is the reflection coefficient, T, the transmission coefficient and η_0, intrinsic impedance of free space (~ 377 Ω). Since the tangential field components must be continuous at $z = 0$, applying boundary conditions, obtained equations are,

$$1 + \Gamma = T \tag{1.50}$$

$$1 - \frac{\Gamma}{\eta_0} = \frac{T}{\eta} \tag{1.51}$$

Solving the equations, Γ and T can be expressed as,

$$\Gamma = \frac{\eta - \eta_0}{\eta + \eta_0} \tag{1.52}$$

$$T = \frac{2\eta}{\eta + \eta_0} = 1 + \Gamma \tag{1.53}$$

Reflection loss (RL) related to reflected power of EM wave from a material is defined from Γ value as, RL (in dB) = $-20\log|\Gamma|$. In this thesis, the sign for RL is taken negative (−) as per convention.

When an EM wave is contained within a waveguide, optical fibre, or resonator, different transverse modes are associated with it based on the transmission line boundary conditions. The next section will continue the discussion.

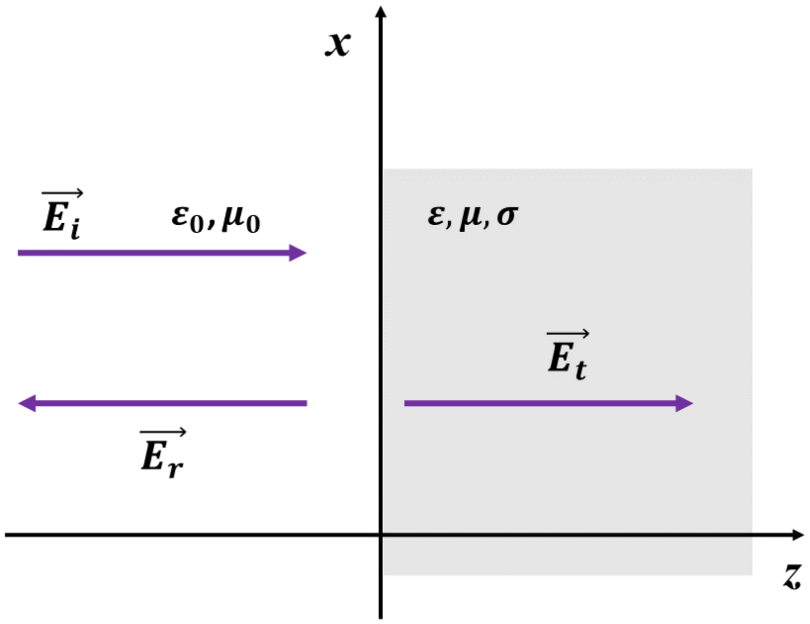

Figure 1.16. Plane wave reflection from an arbitrary medium: normal incidence

1.7.3.2 TRANSMISSION LINE ANALOGY

Transmission lines typically comprise multiple conducting lines. The circuit elements associated with such conductors are series resistance (R) for their length, series inductance (L) from conductors, shunt capacitance (C) from parallelly placed conductors, and an additional shunt conductance (G) from added load[160]. Thus, a transmission line is a distributed parameter network in which the magnitude and phase of voltages and currents can vary significantly along its length. These transmission lines are small, inexpensive, and can be easily integrated with active circuit devices; therefore, they are of great importance in the analysis of microwave circuits and devices[161]. Multiple conductor transmission lines can only support transverse electromagnetic (TEM) waves, as longitudinal field components are absent. On the other hand, waveguides with a single conductor support transverse electric (TE) and/or transverse magnetic (TM) waves, which are characterized by the presence of longitudinal magnetic or electric field components, respectively. From Maxwell equations, fields with their transverse components are[162],

$$\vec{E}(x,y,z) = [\overrightarrow{E_0}(x,y) + \hat{z}E_z(x,y)]e^{-j\beta z} \tag{1.54}$$

$$\vec{H}(x,y,z) = [\overrightarrow{H_0}(x,y) + \hat{z}H_z(x,y)]e^{-j\beta z} \tag{1.55}$$

And,

$$H_x = \frac{j}{k_c^2}\left(\omega\varepsilon\frac{\partial E_z}{\partial y} - \beta\frac{\partial H_z}{\partial x}\right) \tag{1.56}$$

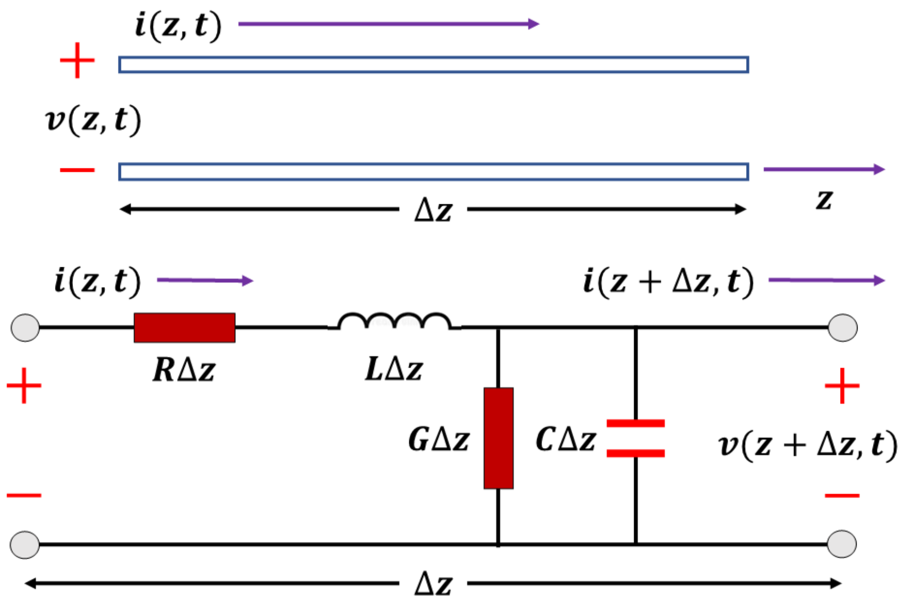

Figure 1.17. Equivalent circuit for an incremental length of transmission line

$$H_y = -\frac{j}{k_c^2}\left(\omega\varepsilon\frac{\partial E_z}{\partial x} + \beta\frac{\partial H_z}{\partial y}\right) \tag{1.57}$$

$$E_x = -\frac{j}{k_c^2}\left(\beta\frac{\partial E_z}{\partial x} + \omega\mu\frac{\partial H_z}{\partial y}\right) \tag{1.58}$$

$$E_y = \frac{j}{k_c^2}\left(-\beta\frac{\partial E_z}{\partial y} + \omega\mu\frac{\partial H_z}{\partial x}\right) \tag{1.59}$$

where $k_c = \sqrt{k^2 - \beta^2}$, is cut-off wave number. Solution for TE mode characterized by $E_z = 0$ and $H_z \neq 0$, from $H_z(x, y, z) = h_z(x, y)e^{-j\beta z}$ and reduced Helmholtz wave equation,

$$\left(\frac{\partial^2}{\partial x^2} + \frac{\partial^2}{\partial y^2} + \frac{\partial^2}{\partial z^2}\right) h_z = 0 \tag{1.60}$$

For rectangular waveguide with breadth 'a' and width 'b', general solution of 1.60 gives,

$$h_z(x, y) = X(x)Y(y)$$

$$h_z(x, y) = (A\, cosk_x x + B\, sink_x x)(C\, cosk_y y + B\, sink_y y) \tag{1.61}$$

Considering the following boundary conditions on the electric field components tangential to the waveguide walls,

$$e_x(x, y) = 0\ at\ y = 0, b$$

$$e_y(x, y) = 0\ at\ x = 0, a$$

The final solution for H_z is,

$$H_z(x, y, z) = A_{mn} cos\frac{m\pi x}{a} cos\frac{n\pi y}{b} e^{-j\beta z} \tag{1.62}$$

Where, the propagation constant for TE_{mn} mode is $\beta = \sqrt{k^2 - \pi^2\left[\left(\frac{m}{a}\right)^2 + \left(\frac{n}{b}\right)^2\right]}$. The associated cut-off frequency is given by $f_{c_{mn}} = \frac{1}{2\pi\sqrt{\mu\varepsilon}}\pi^2\left[\left(\frac{m}{a}\right)^2 + \left(\frac{n}{b}\right)^2\right]$. The dominant mode is the mode with the lowest cut-off frequency, which is TE_{10} mode in this case. At a given operating frequency f only those modes having $f > f_c$ will propagate, modes with $f < f_c$ will lead to an imaginary β (or real α), that means all field components will decay exponentially from the source of excitation. Such modes are referred to as evanescent modes, which can lead to overmodulation; as a result, signal noise can be generated.

Transverse electromagnetic (TEM) waves are characterized by $E_z = H_z = 0$. Here, from Equations 1.56-1.59, both k and β equals to $\omega\sqrt{\mu\varepsilon}$. The cut-off wave number, $k_c = \sqrt{k^2 - \beta^2}$, is thus zero for TEM waves. When a gradient of a scalar potential, $\varphi(x, y)$ arises between two conductors in a waveguide, TEM mode can propagate. Solving Laplace's equation between the two conductors,

$$\nabla_t^2 h(x, y) = 0 \tag{1.63}$$

$$\vec{E}(x, y) = \overrightarrow{\nabla_t}\varphi(x, y) \tag{1.64}$$

With an understanding of wave mode propagation in transmission lines, the voltage (v) and current (i) definitions of a two-wire line are derived through circuit analysis. Figure 1.17 depicts the schematic representation of a transmission line and its components.

From the circuit diagram, Kirchhoff's voltage and current laws can be applied to give,

$$v(z,t) - R\Delta z i(z,t) - L\Delta z \frac{\partial i(z,t)}{\partial t} - v(z+\Delta z,t) = 0 \tag{1.65}$$

$$i(z,t) - G\Delta z v(z+\Delta z,t) - C\Delta z \frac{\partial v(z+\Delta z,t)}{\partial t} - i(z+\Delta z,t) = 0 \tag{1.66}$$

For the steady-state condition, the above equations can be simplified into their phasor forms,

$$\frac{dV(z)}{dz} + (R + j\omega L)I(z) = 0 \tag{1.67}$$

$$\frac{dI(z)}{dz} + (G + j\omega C)V(z) = 0 \tag{1.68}$$

Comparing these with wave equations for $V(z)$ and $I(z)$, with propagation constant, $\gamma = \sqrt{(R + j\omega L)(G + j\omega C)}$,

$$V(z) = V_0^+(e^{-\gamma z} + \Gamma e^{\gamma z}) \tag{1.69}$$

$$I(z) = \frac{V_0^+}{Z_0}(e^{-\gamma z} - \Gamma e^{\gamma z}) \tag{1.70}$$

where the $e^{-\gamma z}$ term represents wave propagation in the $+z$ direction, and the $e^{\gamma z}$ term, wave propagation in the $-z$ direction. Characteristic impedance (Z_0) of the circuit is defined as,

$$Z_0 = \frac{V_0^+}{I_0^+} = \sqrt{\frac{R+j\omega L}{G+j\omega C}} \tag{1.71}$$

For a coaxial line with inner diameter (a) and outer diameter (b), geometry dependent characteristic impedance is related to intrinsic or wave impedance in the way,

$$Z_0 = \frac{E_\rho \ln\left(\frac{b}{a}\right)}{2\pi H_\varphi} = \sqrt{\frac{\mu}{\varepsilon}} \frac{\ln\left(\frac{b}{a}\right)}{2\pi} = \eta \frac{\ln\left(\frac{b}{a}\right)}{2\pi} \tag{1.72}$$

When transmission line is terminated in an arbitrary load impedance Z_L, at load point, $Z_L = \frac{V}{I} = \frac{V_0^+ + V_0^-}{V_0^+ - V_0^-} Z_0$. Therefore, solving for V_0^- gives,

$$\frac{V_0^-}{V_0^+} = \frac{Z_L - Z_0}{Z_L + Z_0} = \Gamma \tag{1.73}$$

At a distance $z = -l$ from the load, the input impedance (Z_{in}) seen looking toward the load is (from equations 1.69, 1.70, and 1.73),

$$Z_{in} = \frac{V(-l)}{I(-l)} = Z_0 \frac{Z_L + Z_0 \tanh \gamma L}{Z_0 + Z_L \tanh \gamma L} \tag{1.74}$$

As a special case of this transmission line impedance equation, a line is terminated in a short circuit, i.e., Z_L = 0, input impedance takes the form,

$$Z_{in} = Z_0 \tanh \gamma L \tag{1.75}$$

1.7.3.3 ATTENUATION CONSTANT

The γ can be expressed using the well-known formula[160]:

$$\gamma = j\omega\sqrt{\mu\varepsilon} \tag{1.76}$$

Where, μ is the complex permeability and ε is the complex permittivity.

$$\mu = \mu_0(\mu' - i\mu'') \tag{1.77}$$

$$\varepsilon = \varepsilon_0(\varepsilon' - i\varepsilon'') \tag{1.78}$$

Where, ε', ε'' are the real and imaginary parts of complex permittivity, μ', μ'' are the real and imaginary parts of the complex permeability, ε_0 and μ_0 are the free space permittivity and permeability respectively.

Putting these expressions of μ and ε in γ,

$$\gamma = j\omega\sqrt{\mu_0\varepsilon_0}[(\mu' - i\mu'')(\varepsilon' - i\varepsilon'')]^{1/2}$$

$$\gamma = j\omega\sqrt{\mu_0\varepsilon_0}[(\mu'\varepsilon' - \mu''\varepsilon'') - i(\mu'\varepsilon'' + \mu''\varepsilon')]^{1/2}$$

$$\gamma^2 = -\omega^2\mu_0\varepsilon_0[(\mu'\varepsilon' - \mu''\varepsilon'') - i(\mu'\varepsilon'' + \mu''\varepsilon')] \tag{1.79}$$

Replacing, $c^2 = \frac{1}{\sqrt{\mu_0\varepsilon_0}}$ in Eq. 1.79:

$$\gamma^2 = \frac{\omega^2}{c^2}[(\mu''\varepsilon'' - \mu'\varepsilon') + i(\mu'\varepsilon'' + \mu''\varepsilon')] \tag{1.80}$$

Replacing, $\gamma = \alpha + j\beta$ in Eq. 1.80:

$$\alpha^2 - \beta^2 + 2j\alpha\beta = \frac{\omega^2}{c^2}[(\mu''\varepsilon'' - \mu'\varepsilon') + i(\mu'\varepsilon'' + \mu''\varepsilon')] \tag{1.81}$$

Equating, real and imaginary parts from both sides of Eq. 1.81:

$$\alpha^2 - \beta^2 = \frac{\omega^2}{c^2}(\mu''\varepsilon'' - \mu'\varepsilon') \tag{1.82}$$

$$2\alpha\beta = \frac{\omega^2}{c^2}(\mu'\varepsilon'' + \mu''\varepsilon')$$

Or,

$$\beta = \frac{\omega^2}{2\alpha c^2}(\mu'\varepsilon'' + \mu''\varepsilon') \tag{1.83}$$

Replacing the expression of β in Eq. 1.82,

$$\alpha^2 - \frac{\omega^4}{4\alpha^2c^4}(\mu'\varepsilon'' + \mu''\varepsilon')^2 = \frac{\omega^2}{c^2}(\mu''\varepsilon'' - \mu'\varepsilon')$$

$$\alpha^4 - \frac{\omega^4}{4c^4}(\mu'\varepsilon'' + \mu''\varepsilon')^2 = \frac{\omega^2}{c^2}\alpha^2(\mu''\varepsilon'' - \mu'\varepsilon')$$

$$\alpha^4 - \frac{\omega^2}{c^2}\alpha^2(\mu''\varepsilon'' - \mu'\varepsilon') = \frac{\omega^4}{4c^4}(\mu'\varepsilon'' + \mu''\varepsilon')^2$$

$$\alpha^4 - 2.\alpha^2.\frac{\omega^2}{2c^2}(\mu''\varepsilon'' - \mu'\varepsilon') = \frac{\omega^4}{4c^4}(\mu'\varepsilon'' + \mu''\varepsilon')^2$$

$$\alpha^4 - 2.\alpha^2.\frac{\omega^2}{2c^2}(\mu''\varepsilon'' - \mu'\varepsilon') + \frac{\omega^4}{4c^4}(\mu''\varepsilon'' - \mu'\varepsilon')^2$$

$$= \frac{\omega^4}{4c^4}(\mu'\varepsilon'' + \mu''\varepsilon')^2 + \frac{\omega^4}{4c^4}(\mu''\varepsilon'' - \mu'\varepsilon')^2$$

$$[\alpha^2 - \frac{\omega^2}{2c^2}(\mu''\varepsilon'' - \mu'\varepsilon')]^2 = \frac{\omega^4}{4c^4}[(\mu'\varepsilon'' + \mu''\varepsilon')^2 + (\mu''\varepsilon'' - \mu'\varepsilon')^2]$$

$$\alpha^2 - \frac{\omega^2}{2c^2}(\mu''\varepsilon'' - \mu'\varepsilon') = \frac{\omega^2}{2c^2}[(\mu'\varepsilon'' + \mu''\varepsilon')^2 + (\mu''\varepsilon'' - \mu'\varepsilon')^2]^{1/2}$$

$$\alpha^2 = \frac{\omega^2}{2c^2}(\mu''\varepsilon'' - \mu'\varepsilon') + \frac{\omega^2}{2c^2}[(\mu'\varepsilon'' + \mu''\varepsilon')^2 + (\mu''\varepsilon'' - \mu'\varepsilon')^2]^{1/2}$$

$$\alpha = \frac{\omega}{\sqrt{2}c}\sqrt{(\mu''\varepsilon'' - \mu'\varepsilon') + \sqrt{(\mu'\varepsilon'' + \mu''\varepsilon')^2 + (\mu''\varepsilon'' - \mu'\varepsilon')^2}} \tag{1.84}$$

Replacing, $\omega = 2\pi f$

$$\alpha = \frac{\sqrt{2}\pi f}{c}\sqrt{(\mu''\varepsilon'' - \mu'\varepsilon') + \sqrt{(\mu'\varepsilon'' + \mu''\varepsilon')^2 + (\mu''\varepsilon'' - \mu'\varepsilon')^2}} \tag{1.85}$$

1.7.3.4 EXPRESSION OF MAGNETIC TANGENT LOSS

The permeability μ, of a material, is defined as,

$$\vec{B} = \mu\vec{H} \tag{1.86}$$

where $\vec{B}$ is the flux density (T), $\vec{H}$ is the magnetic field intensity (A/m), and μ_0 is the permeability of free space (4π x 10^{-7} H/m).

In an analogous way to the electric losses, the losses that occur due to a time-varying magnetic field can be described by a complex relative permeability

$$\mu = \mu' - i\mu'' \tag{1.87}$$

where $\mu'$is the permeability and μ'' describes all the magnetic losses. An analogous magnetic loss tangent, $tan\delta_\mu$ can also be defined,

$$\tan\delta_\mu = \frac{\mu''}{\mu'} \tag{1.88}$$

On the other hand, the power P, absorbed per unit volume (W/m^3) of the sample at a given instant in time can be given by[163],

$$P = 2\pi f\mu_0\mu''\left|\vec{H}\right|^2 = 2\pi f\mu_0\mu'\tan\delta_\mu\left|\vec{H}\right|^2 \tag{1.89}$$

It can be seen that the power absorbed varies linearly with frequency, permeability, and the loss tangent and with the square of the magnetic field.

The energy dissipation (W) due to eddy current varies for different sample shapes but in all cases, it increases with the square of the frequency (f), magnetic field ($\vec{B}$) and sample dimension (d) and increases linearly with conductivity (σ)[163–165].

Thus,

$$W \propto \sigma f^2 \left|\vec{B}\right|^2 d^2 = k\sigma f^2 \left|\vec{B}\right|^2 d^2 \tag{1.90}$$

Where, k = proportionality constant.

If the total magnetic loss is only due to Eddy current loss, then,

$$\text{Total loss } (P) \sim k\sigma f^2 \vec{B}^2 d^2 \tag{1.91}$$

Substituting the expression of total loss from Eq. (1.89) in Eq. (1.91), we obtain,

$$2\pi f \mu_0 \mu' \tan\delta_\mu \left|\vec{H}\right|^2 \sim k\sigma f^2 \left|\vec{B}\right|^2 d^2$$

$$2\pi f \mu_0 \mu' \tan\delta_\mu \left|\vec{H}\right|^2 \sim k\sigma f^2 {\mu_0}^2 {\mu'}^2 \left|\vec{H}\right|^2 d^2$$

$$\tan\delta_\mu \sim \frac{k}{2\pi} \sigma f \mu_0 \mu' d^2$$

$$\frac{\mu''}{\mu'} \sim \left(\frac{k}{2\pi}\right) \mu_0 \mu' (d^2\sigma) f \tag{1.92}$$

The formula derived above is the approximate expression of magnetic tangent loss when the loss generates only due to eddy current.

1.7.3.5 SCATTERING PARAMETERS

Interconnecting EM field theory and circuit analysis, microwave network analysis is a more practical and straightforward procedure. Due to the difficulty in measuring voltage or current at microwave frequencies, a terminal pair must be clearly defined. Typically, impedance, admittance, and scattering matrices from circuit theory serve as these terminal or port quantities. This type of representation results in the development of equivalent circuits of arbitrary networks, which will be of great assistance in the design of passive components such as couplers and filters. The impedance, admittance, and scattering parameters in matrix form for a network with multiple ports are as follows:

$$[V] = [Z][I]$$

$$[I] = [Y][V]$$

$$[V^-] = [S][V^+]$$

At high RF and microwave frequencies, it is difficult to measure Y or Z parameters directly for transmission lines due to the lack of equipment to measure port current and voltage directly

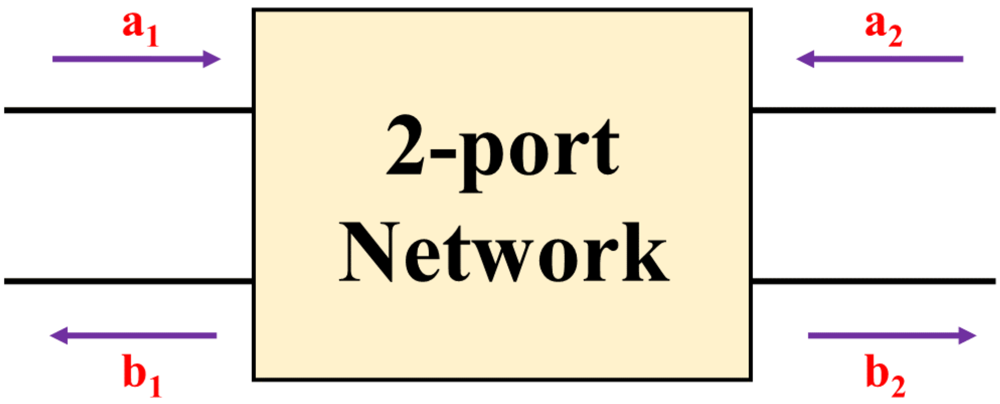

Figure 1.18. Schematic representation of a 2-port network

and the difficulty of obtaining perfect opens/shorts. The scattering matrix provides direct measurements for incident, reflected, and transmitted waves under these conditions. A particular component of the scattering matrix can be identified as,

$$S_{ij} = \frac{V_i^-}{V_j^+}\Big|_{V_k^+=0,\ \ k\neq j} \tag{1.93}$$

In words, Eq. 1.93 says that Sij is the ratio of the reflected or transmitted wave amplitude V_i^- coming out of port i while the incident wave at port *j* is voltage V_j^+. The four S-parameters for a two-port device are S_{11}, S_{21}, S_{12}, and S_{22}. Figure 1.18 depicts a schematic representation of a 2-port network's S-parameters. Here, S_{11} and S_{22} represent the forward and reverse reflection coefficients, while S_{21} and S_{12} represent the forward and reverse gains.

The expression for 2-port S-parameters is shown below,

$$\begin{bmatrix} b_1 \\ b_2 \end{bmatrix} = \begin{bmatrix} S_{11} & S_{12} \\ S_{21} & S_{22} \end{bmatrix} \begin{bmatrix} a_1 \\ a_2 \end{bmatrix} \tag{1.94}$$

1.7.3.6 NICHOLSON-ROSS-WEIR ALGORITHM

In cases where a material under test (MUT) is contained within a wave guide or coaxial cable, Figure 1.19 depicts the reflection and transmission of incident waves. Placing a sample in a section of waveguide or coaxial line and measuring the two-port complex scattering parameters with a vector network analyser (VNA) are required for Transmission/Reflection line measurements. Using various algorithms, the conversion of S-parameters to complex permittivity and permeability is computed by solving equations. Nicholson-Ross-Weir (NRW) is the most common method for measuring the values of ferrite and other magnetic materials[166]. and values are typically determined by solving a transcendental equation

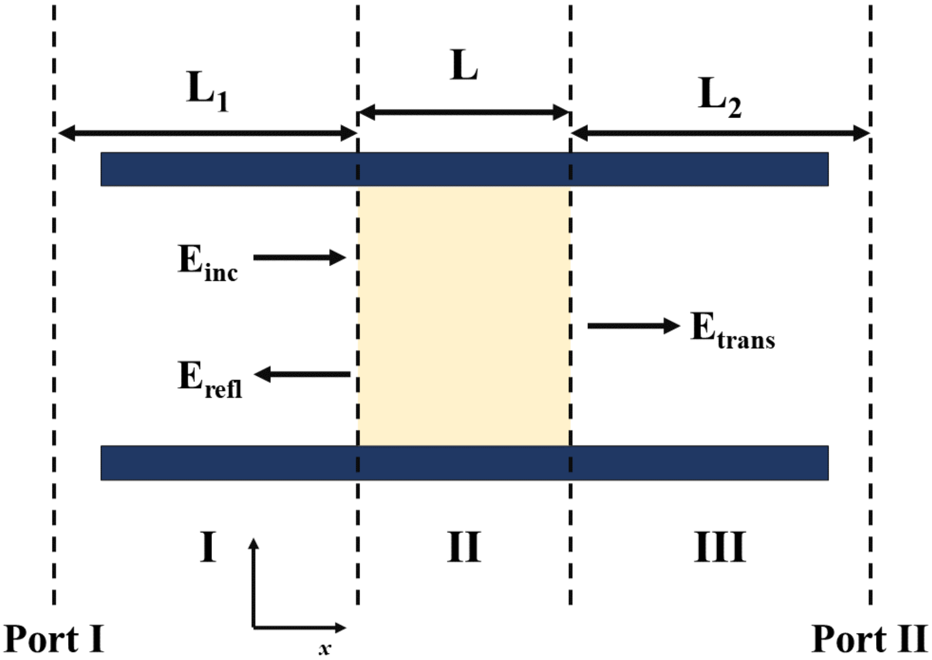

Figure 1.19. Electromagnetic waves transmitting and reflecting from a sample in a transmission line

involving the sample length, sample position, and reflection coefficient. The detailed steps of the NRW method are outlined below.

The first step will be to obtain relations of μ and ε values with Γ. Some parameter expressions such as γ, k_c, η are recalled, $\gamma^2 = k_c^2 - k^2$, $k_c = {}^{2\pi}/_{\lambda_c}$ (λ_c = cut-off wavelength), $k = \omega\sqrt{\varepsilon\mu}$ and $\eta = {}^{j\omega\mu}/_{\gamma}$. Reflection co-efficient Γ is written as,

$$\Gamma = \frac{\eta-\eta_0}{\eta+\eta_0} = \frac{\frac{\gamma_0}{\gamma}\mu-1}{\frac{\gamma_0}{\gamma}\mu+1} \tag{1.95}$$

Where, γ_0 is the complex propagation constant in the air. Solving for μ,

$$\mu = \left(\frac{1+\Gamma}{1-\Gamma}\right)\frac{\gamma}{\gamma_0}$$

$$\frac{\gamma}{\gamma_0} = \frac{\sqrt{\frac{\omega^2\varepsilon\mu}{c^2}-\left(\frac{2\pi}{\lambda_c}\right)^2}}{j\sqrt{\left(\frac{\omega}{c}\right)^2-\left(\frac{2\pi}{\lambda_c}\right)^2}} = \frac{\gamma}{j2\pi\sqrt{\frac{1}{\lambda_0^2}-\frac{1}{\lambda_c^2}}} \tag{1.96}$$

Defining $\frac{1}{\Lambda} = \frac{\gamma}{j2\pi}$ and from 1.95 and 1.96,

$$\mu = \left(\frac{1+\Gamma}{1-\Gamma}\right)\frac{1}{\Lambda\sqrt{\frac{1}{\lambda_0^2}-\frac{1}{\lambda_c^2}}} \tag{1.97}$$

From, $\gamma^2 = (2\pi)^2\left[\frac{1}{\lambda_0^2} - \frac{\mu\varepsilon}{\lambda_c^2}\right]$, solving for ε gives,

$$\varepsilon = \frac{\lambda_0^2\left[\frac{1}{\lambda_c^2}-\left(\frac{\gamma}{2\pi}\right)^2\right]}{\mu} = \frac{\lambda_0^2}{\mu}\left[\frac{1}{\lambda_c^2}+\frac{1}{\Lambda^2}\right] \tag{1.98}$$

The next step aims at clarifying the relationship between Γ, γ and the scattering matrix, which carries the information of the incident, reflected and transmitted waves as shown in Figure 1.20. Assuming normal incidence in an isotropic material ($S_{12} = S_{21}$), the sum of reflected fields at the interface with the sample (Γin) is given by,

$$\Gamma_{in} = \Gamma_{12} + T_{12}\Gamma_{in}T_{21}e^{-2\gamma L} + T_{12}\Gamma_{21}\Gamma_{23}^{2}T_{21}e^{-4\gamma L} + \cdots$$

$$\Gamma_{in} = \Gamma_{12} + \frac{T_{12}T_{21}\Gamma_{23}e^{-2\gamma L}}{1-\Gamma_{21}\Gamma_{23}e^{-2\gamma L}} \qquad (1.99)$$

Here Γ_{ij} and T_{ij} are the reflection coefficient and transmission coefficient of the wave respectively that propagates from material 'i' to material 'j'. At the traditional setup, material 1 and material 3 are air. Based on 1.93 and 1.94, we can conclude that,

$$\Gamma_{12} = -\Gamma_{21} = -\Gamma_{23} \qquad (1.100)$$

Further, applying the boundary condition of continuality for tangential component of electric fields across the interface,

$$T_{12} = 1 + \Gamma_{21} \qquad (1.101)$$

Defining $z = e^{-\gamma L}$ and $\Gamma = \Gamma_{12}$, we obtain from 1.99,

$$\frac{\sum E_{reflected}}{E_{incident}} = S_{11} = \frac{\Gamma(1-z^2)}{1-\Gamma^2 z^2} \qquad (1.102)$$

In a similar manner, the transmission co-efficient results in,

$$\frac{\sum E_{transmitted}}{E_{incident}} = \frac{T_{32}T_{21}e^{-\gamma L}}{1-\Gamma_{21}\Gamma_{23}e^{-2\gamma L}} = \frac{(1-\Gamma^2)z}{1-\Gamma^2 z^2} = S_{21} \qquad (1.103)$$

To obtain expression of Γ and z in terms of S_{11} and S_{21},

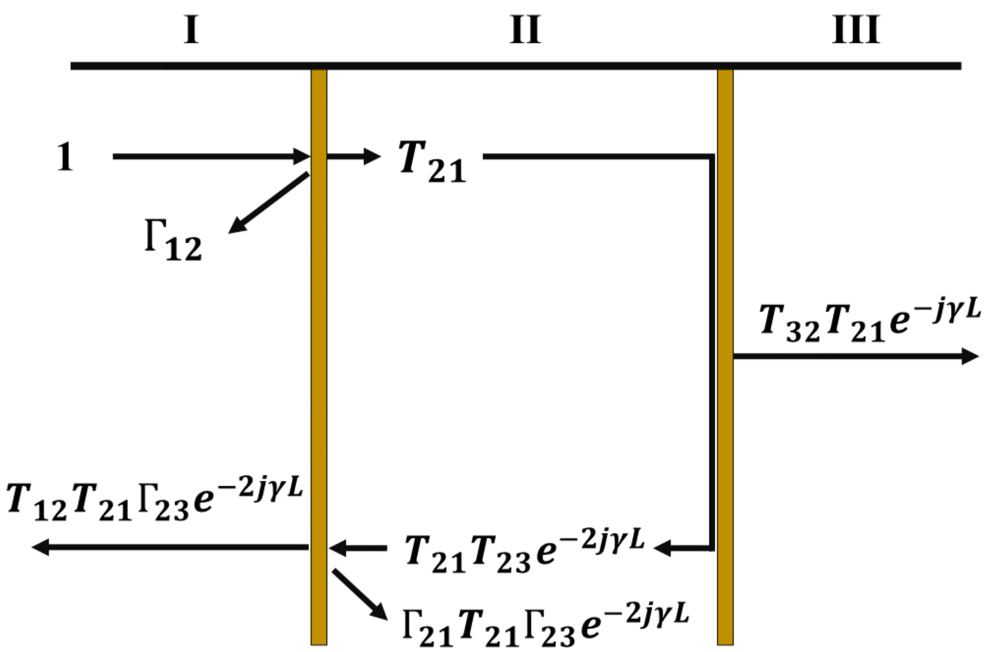

Figure 1.20. Multiple reflection at three materials interfaces

$$K = \frac{S_{11} - S_{21} + 1}{2S_{11}}$$

$$\Gamma^2 - 2\Gamma K + 1 = 0$$

$$\Gamma = K \pm \sqrt{K^2 - 1} \quad (1.104)$$

The quadratic equation of Γ has two solutions. To determine the correct solution for a passive medium, the physical restriction $\Gamma < 1$ is used. From 1.101, 1.102, and 1.104,

$$Z = \frac{S_{11}+S_{21}-\Gamma}{1-(S_{21}+S_{11})\Gamma} = e^{-\gamma L} \quad (1.105)$$

1.8 MOTIVE OF THE THESIS

There are a very few materials in nature that exhibit two or more ferroic orders in the same phase at room temperature. Having a good coupling is essentially impossible due to the complexity of the coupling mechanism. Many materials have good coupling; however, this typically occurs at very low temperatures, making commercial use impractical. Therefore, a material having strong magnetoelectric coupling at room temperature is still not achieved and need further research.

Bismuth Ferrite (BFO) belongs to the category of "lone pair" ferroelectricity and *d*-electron magnetism. With an antiferromagnetic Neel temperature of 643 K and a ferroelectric Curie temperature of 1103 K, it is an antiferromagnetic, ferroelectric multiferroic. Weak ferromagnetism in $BiFeO_3$ is generated by spin canting in the antiferromagnetic sublattices. However, the cycloidal spin structure of period 62 nm eliminates the macroscopic magnetization. To reduce this spiral structure and improve the magnetoelectric characteristics of $BiFeO_3$, it has been seen to be very successful to dope with promising elements at the Bi-site or Fe-site. For instance, Ba-doped single-phase BFO ceramics have been found to have enhanced magnetic properties. The production of secondary phase and leakage current, on the other hand, is reduced by doping the Bi-site with Yttrium (Y). We have studied the effect of Barium and Yttrium co-doping on structural, electric, magnetic and magnetodielectric properties of Bismuth Ferrite with a changing morphology from bulk, nanoparticle, to thin film. Magnetoelectric (ME) gallium ferrite ($Ga_{2-x}Fe_xO_3$ or GFO) is another fascinating magnetoelectric material with stronger magnetoelectric (ME) coupling than Bismuth Ferrite. It is low temperature ferrimagnet and an RT piezoelectric with a large ME coupling (10^{-11} s/m at 4.2 K). GFO is stable throughout a broad composition range ($0.8 \leq x \leq 1.3$) and the ferri (fM) to paramagnetic (PM) transition temperature (T_C) is a function of composition and tuneable beyond room temperature (300 K). However, high leakage and a low magnetic transition temperature prevent this material from being used in practical applications. On the other hand, Bismuth Sodium Titanate–Strontium Titanate ($Sr_{0.5}Bi_{0.25}Na_{0.25}TiO_3$, SNBT50) solid solution is a strong ferroelectric and diamagnetic at room temperature with high dielectric constant. Our objective is to create composites of GFO and SNBT50 with Gadolinium Gallium Garnet (GGG) and Yttrium Iron Garnet (YIG), materials chosen for their high density and resistivity. Formation of GFO-GGG composites is observed to reduce the leakage current of the material by five orders of magnitude, whereas GFO-YIG composites increased the magnetic Curie temperature of GFO beyond room temperature. The SNBT50-YIG composite exhibits magnetic properties in addition to vastly improved ferroelectric and magnetodielectric properties. Multiferroic ferrites with magnetoelectric (ME) coupling and magnetic and electric properties, such as BFO, are advantageous for shielding microwave-frequency electromagnetic radiation. In contrast to Bismuth Ferrite, which has been the subject of numerous experiments aimed at enhancing its microwave capabilities, Gallium Ferrite, another promising magnetoelectric material, has not been subjected to such treatment. As a result, the microwave absorption properties of gallium ferrite are investigated in depth, revealing notably high microwave absorption. The microwave properties of Barium- and Yttrium-doped Bismuth ferrite are also studied in depth, revealing an increase in absorption along with a broadening of the material's bandwidth. Due to the high likelihood of employing YIG in the high-frequency range, the microwave properties of SNBT50-YIG are also investigated for their potential use as microwave absorption materials (MAMs).

In conclusion, extensive research has focused on the synthesis of single-phase and composite magnetoelectric materials with varying morphology and synthesis conditions for cutting-edge technological applications. Additionally, the applicability of the synthesized materials as microwave absorbers has also been investigated in depth.

1.9 THESIS ORGANIZATION

The entire thesis has been separated into six chapters. The following is a brief summary of each chapter.

Chapter 1: The first chapter provides an overview of multiferroic properties, their origin, and various multiferroic materials. Different methods and characteristic of multiferroic materials are discussed in detail. Also included are the motivation for the thesis and an outline of the completed work.

Chapter 2: The second chapter focuses on synthesis procedures, characterization techniques, and measurements.

Chapter 3: The third chapter describes the effect of co-doping of barium and yttrium at the bismuth site of bismuth ferrite. Electric and magnetic properties are investigated and reported. A nanostructured form of the same composition that exhibits excellent ferroelectric, magnetic, and magnetodielectric properties is developed.

Chapter 4: The fourth chapter describes all the composite systems investigated in this thesis to improve magnetoelectric properties. The composite formation of Gallium Ferrite with Gadolinium Gallium garnet and Yttrium Iron Garnet is studied, revealing promising enhancements in electric, magnetic, and magnetodielectric properties. This chapter also examines the composite of Sodium Bismuth Titanate–Strontium Titanate solid solution and Yttrium Iron Garnet.

Chapter 5: The fifth chapter discusses the use of gallium ferrite as a microwave absorption material. The enhancement of Bismuth Ferrite's bandwidth, microwave absorption, and impedance matching as a result of co-doping with Barium and Yttrium is also investigated. The microwave properties of Sodium Bismuth Titanate–Strontium Titanate solid solution and Yttrium Iron Garnet composite is also discussed in detail.

Chapter 6: The sixth chapter draws conclusions and discusses the scope of future work.

REFERENCES

[1] H. Schmid, Multi-ferroic magnetoelectrics, Ferroelectrics. 162 (1994) 317–338. https://doi.org/10.1080/00150199408245120.

[2] K.A. Hay, J.B. Torranc E, I.F. Silvera, J.H. M Thornley, M. Tinkham, A. Abragam, M.H. L Pryce, P. Roy Soc, A.A. Misetich, T. Buch, J. Chem Phys, R.E. Watson, J.B. Torrance, I.S. Jacobs, S. Roberts, P.E. Lawrence, R. Silberglitt, P. Rev, K. Aizu, ~M. Tinkham, Springer-Verlag, 1963.

[3] W. Eerenstein, N.D. Mathur, J.F. Scott, Multiferroic and magnetoelectric materials, Nature. 442 (2006) 759–765. https://doi.org/10.1038/nature05023.

[4] J.-H. Cho, W. Jo, A Brief Review on Magnetoelectric Multiferroic Oxides, (n.d.). https://doi.org/10.4313/JKEM.2021.34.3.149.

[5] P. Barone, S. Picozzi, Mechanisms and origin of multiferroicity, C R Phys. 16 (2015) 143–152. https://doi.org/10.1016/j.crhy.2015.01.009.

[6] J. Ma, J. Hu, Z. Li, C.W. Nan, Recent progress in multiferroic magnetoelectric composites: From bulk to thin films, Advanced Materials. 23 (2011) 1062–1087. https://doi.org/10.1002/adma.201003636.

[7] Y. Tokura, S. Seki, Multiferroics with spiral spin orders, Advanced Materials. 22 (2010) 1554–1565. https://doi.org/10.1002/adma.200901961.

[8] J.M. Hu, L.Q. Chen, C.W. Nan, Multiferroic Heterostructures Integrating Ferroelectric and Magnetic Materials, Advanced Materials. 28 (2016) 15–39. https://doi.org/10.1002/adma.201502824.

[9] R. Thomas, J.F. Scott, D.N. Bose, R.S. Katiyar, Multiferroic thin-film integration onto semiconductor devices, Journal of Physics Condensed Matter. 22 (2010). https://doi.org/10.1088/0953-8984/22/42/423201.

[10] G.A. Smolenskii, I.E. Chupis, Ferroelectromagnets, 1982. http://iopscience.iop.org/0038-5670/25/7/R02.

[11] K. Aizu, Possible Species of “Ferroelastic” Crystals and of Simultaneously Ferroelectric and Ferroelastic Crystals, J Physical Soc Japan. 27 (1969) 387–396. https://doi.org/10.1143/JPSJ.27.387.

[12] R.E. Newnham, J.J. Kramer, W.A. Schulze, L.E. Cross, Magnetoferroelectricity in Cr2BeO4, J Appl Phys. 49 (1978) 6088–6091. https://doi.org/10.1063/1.324527.

[13] N.A. Hill, Why are there so few magnetic ferroelectrics?, Journal of Physical Chemistry B. 104 (2000) 6694–6709. https://doi.org/10.1021/jp000114x.

[14] N.A. Spaldin, R. Ramesh, Advances in magnetoelectric multiferroics, Nat Mater. 18 (2019) 203–212. https://doi.org/10.1038/s41563-018-0275-2.

[15] S. Ivanov, Multiferroic complex metal oxides: Main features of preparation, structure, and properties, in: Science and Technology of Atomic, Molecular, Condensed Matter and Biological Systems, Elsevier B.V., 2012: pp. 163–238. https://doi.org/10.1016/B978-0-44-453681-5.00007-8.

[16] H. Lee, Density of States, Fermi Energy, and Energy Bands 11.1 Current and Energy Transport, 2017.

[17] T. Mizokawa, D.I. Khomskii, G.A. Sawatzky, Interplay between orbital ordering and lattice distortions in LaMnO, n.d.

[18] K.Z. Rushchanskii, S. Kamba, V. Goian, P. Vaněk, M. Savinov, J. Prokleška, D. Nuzhnyy, K. Knžek, F. Laufek, S. Eckel, S.K. Lamoreaux, A.O. Sushkov, M. Ležaić, N.A. Spaldin, A multiferroic material to search for the permanent electric dipole moment of the electron, Nat Mater. 9 (2010) 649–654. https://doi.org/10.1038/nmat2799.

[19] E. Bousquet, N.A. Spaldin, P. Ghosez, Strain-induced ferroelectricity in simple rocksalt binary oxides, Phys Rev Lett. 104 (2010). https://doi.org/10.1103/PhysRevLett.104.037601.

[20] J.H. Lee, L. Fang, E. Vlahos, X. Ke, Y.W. Jung, L.F. Kourkoutis, J.-W. Kim, P.J. Ryan, T. Heeg, M. Roeckerath, V. Goian, M. Bernhagen, R. Uecker, P.C. Hammel, K.M. Rabe, S. Kamba, J. Schubert, J.W. Freeland, D.A. Muller, C.J. Fennie, P. Schiffer, V. Gopalan, E. Johnston-Halperin, D.G. Schlom, A strong ferroelectric ferromagnet created by means of spin–lattice coupling, Nature. 476 (2011) 114–114. https://doi.org/10.1038/nature10219.

[21] A.A. Belik, Polar and nonpolar phases of BiMO 3: A review, J Solid State Chem. 195 (2012) 32–40. https://doi.org/10.1016/j.jssc.2012.01.025.

[22] J.B. Goodenough, J. Zhou, Varied roles of Pb in transition-metal PbMO3 perovskites (M = Ti, V, Cr, Mn, Fe, Ni, Ru), Sci Technol Adv Mater. 16 (2015). https://doi.org/10.1088/1468-6996/16/3/036003.

[23] J.H. Lee, K.M. Rabe, Epitaxial-strain-induced multiferroicity in SrMnO3 from first principles, Phys Rev Lett. 104 (2010). https://doi.org/10.1103/PhysRevLett.104.207204.

[24] H. Sakai, J. Fujioka, T. Fukuda, D. Okuyama, D. Hashizume, F. Kagawa, H. Nakao, Y. Murakami, T. Arima, A.Q.R. Baron, Y. Taguchi, Y. Tokura, Displacement-type ferroelectricity with off-center magnetic ions in perovskite Sr1-xBaxMnO3, Phys Rev Lett. 107 (2011). https://doi.org/10.1103/PhysRevLett.107.137601.

[25] J.M. Rondinelli, A.S. Eidelson, N.A. Spaldin, Non- d0 Mn-driven ferroelectricity in antiferromagnetic BaMnO3, Phys Rev B Condens Matter Mater Phys. 79 (2009). https://doi.org/10.1103/PhysRevB.79.205119.

[26] S. Ren, M. Wuttig, Organic exciton multiferroics, Advanced Materials. 24 (2012) 724–727. https://doi.org/10.1002/adma.201104250.

[27] A. Stroppa, P. Barone, P. Jain, J.M. Perez-Mato, S. Picozzi, Hybrid improper ferroelectricity in a multiferroic and magnetoelectric metal-organic framework, Advanced Materials. 25 (2013) 2284–2290. https://doi.org/10.1002/adma.201204738.

[28] S. Zhou, J. Wang, X. Chang, S. Wang, B. Qian, Z. Han, Q. Xu, J. Du, P. Wang, S. Dong, Magnetoelectricity coupled exchange bias in BaMnF4, Sci Rep. 5 (2015). https://doi.org/10.1038/srep18392.

[29] C.J. Fennie, K.M. Rabe, Ferroelectric transition in YMnO3 from first principles, Phys Rev B Condens Matter Mater Phys. 72 (2005). https://doi.org/10.1103/PhysRevB.72.100103.

[30] Y.S. Oh, X. Luo, F.T. Huang, Y. Wang, S.W. Cheong, Experimental demonstration of hybrid improper ferroelectricity and the presence of abundant charged walls in (Ca,Sr)3Ti2O7 crystals, Nat Mater. 14 (2015) 407–413. https://doi.org/10.1038/nmat4168.

[31] B.B. Van Aken, T.T.M. Palstra, A. Filippetti, N.A. Spaldin, The origin of ferroelectricity in magnetoelectric YMnO3, Nat Mater. 3 (2004) 164–170. https://doi.org/10.1038/nmat1080.

[32] N. Hur, S. Park, P.A. Sharma, J.S. Ahn, S. Guha, S.-W. Cheong, Electric polarization reversal and memory in a multiferroic material induced by magnetic fields, Nature. 429 (2004) 392–395. https://doi.org/10.1038/nature02572.

[33] T. Kimura, T. Goto, H. Shintani, K. Ishizaka, T. Arima, Y. Tokura, Magnetic control of ferroelectric polarization, 2003. www.nature.com/nature.

[34] M. Mostovoy, Ferroelectricity in spiral magnets, Phys Rev Lett. 96 (2006). https://doi.org/10.1103/PhysRevLett.96.067601.

[35] H. Katsura, N. Nagaosa, A. V. Balatsky, Spin current and magnetoelectric effect in noncollinear magnets, Phys Rev Lett. 95 (2005). https://doi.org/10.1103/PhysRevLett.95.057205.

[36] T.H. Arima, Ferroelectricity induced by proper-screw type magnetic order, J Physical Soc Japan. 76 (2007). https://doi.org/10.1143/JPSJ.76.073702.

[37] Y.J. Choi, H.T. Yi, S. Lee, Q. Huang, V. Kiryukhin, S.W. Cheong, Ferroelectricity in an ising chain magnet, Phys Rev Lett. 100 (2008). https://doi.org/10.1103/PhysRevLett.100.047601.

[38] T. Kimura, T. Goto, H. Shintani, K. Ishizaka, T. Arima, Y. Tokura, Magnetic control of ferroelectric polarization, 2003. www.nature.com/nature.

[39] T. Lottermoser, T. Lonkai, U. Amann, D. Hohlwein, J. Ihringer, M. Fiebig, Magnetic phase control by an electric field, Nature. 430 (2004) 541–544. https://doi.org/10.1038/nature02728.

[40] M. Fiebig, Th. Lottermoser, D. Fröhlich, A. V Goltsev, R. V Pisarev, Observation of coupled magnetic and electric domains, Nature. 419 (2002) 818–820. https://doi.org/10.1038/nature01077.

[41] S. Priya, R. Islam, S. Dong, D. Viehland, Recent advancements in magnetoelectric particulate and laminate composites, J Electroceram. 19 (2007) 149–166. https://doi.org/10.1007/s10832-007-9042-5.

[42] J.M. Moreau, C. Michel, R. Gerson, W.J. James, FERROELECTRIC BiFeO3 X-RAY AND NEUTRON DIFFRACTION STUDY, Pergamon Press, 1971.

[43] B.F. Kubel, H. Schmid, Nonstoichiometry and Crystal Structures of Barium-Bismuth Oxides, 1985.

[44] A.M. Glazer, The classification of tilted octahedra in perovskites, Acta Crystallographica Section B. 28 (1972) 3384–3392. https://doi.org/10.1107/S0567740872007976.

[45] J.D. Bucci, B.K. Robertson, W.J. James, The precision determination of the lattice parameters and the coefficients of thermal expansion of BiFeO 3, J Appl Crystallogr. 5 (1972) 187–191. https://doi.org/10.1107/S0021889872009173.

[46] A. Palewicz, T. Szumiata, R. Przeniosło, I. Sosnowska, I. Margiolaki, Search for new modulations in the BiFeO3 structure: SR diffraction and Mössbauer studies, Solid State Commun. 140 (2006) 359–363. https://doi.org/10.1016/j.ssc.2006.08.046.

[47] G. Catalan, J.F. Scott, Physics and applications of bismuth ferrite, Advanced Materials. 21 (2009) 2463–2485. https://doi.org/10.1002/adma.200802849.

[48] A.K. Zvezdin, A.P. Pyatakov -, I. Sosnowskat, T. Peterlin-Neumaier, E. Steichele, Spiral magnetic ordering in bismuth ferrite, 1982.

[49] D. Lebeugle, D. Colson, A. Forget, M. Viret, Very large spontaneous electric polarization in BiFeO3 single crystals at room temperature and its evolution under cycling fields, Appl Phys Lett. 91 (2007) 022907. https://doi.org/10.1063/1.2753390.

[50] A. V Zalesski Oe, A.K. Zvezdin, A.A. Frolov, A.A. Bush, Translated from Pis'ma v Zhurnal Éksperimental'no oe i, 2000.

[51] 1.1630133, (n.d.).

[52] M. Cazayous, Y. Gallais, A. Sacuto, R. De Sousa, D. Lebeugle, D. Colson, Possible observation of cycloidal electromagnons in BiFeO3, Phys Rev Lett. 101 (2008). https://doi.org/10.1103/PhysRevLett.101.037601.

[53] M.K. Singh, W. Prellier, M.P. Singh, R.S. Katiyar, J.F. Scott, Spin-glass transition in single-crystal BiFe O3, Phys Rev B Condens Matter Mater Phys. 77 (2008). https://doi.org/10.1103/PhysRevB.77.144403.

[54] J.F. Scott, M.K. Singh, R.S. Katiyar, Critical phenomena at the 140 and 200 K magnetic phase transitions in BiFeO3, Journal of Physics Condensed Matter. 20 (2008). https://doi.org/10.1088/0953-8984/20/32/322203.

[55] J. Wei, R. Haumont, R. Jarrier, P. Berhtet, B. Dkhil, Nonmagnetic Fe-site doping of BiFeO3 multiferroic ceramics, Appl Phys Lett. 96 (2010) 102509. https://doi.org/10.1063/1.3327885.

[56] Y. Wang, Q. Jiang, H. He, C.-W. Nan, Multiferroic BiFeO3 thin films prepared via a simple sol-gel method, Appl Phys Lett. 88 (2006) 142503. https://doi.org/10.1063/1.2191947.

[57] Z.L. Hou, H.F. Zhou, J. Yuan, Y.Q. Kang, H.J. Yang, H.B. Jin, M.S. Cao, Enhanced ferromagnetism and microwave dielectric properties of Bi 0.95Y0.05FeO3 nanocrystals, Chinese Physics Letters. 28 (2011). https://doi.org/10.1088/0256-307X/28/3/037702.

[58] S.R. Shannigrahi, A. Huang, N. Chandrasekhar, D. Tripathy, A.O. Adeyeye, Sc modified multiferroic BiFeO3 thin films prepared through a sol-gel process, Appl Phys Lett. 90 (2007) 022901. https://doi.org/10.1063/1.2430652.

[59] M. Kumar, K.L. Yadav, Rapid liquid phase sintered Mn doped BiFeO3 ceramics with enhanced polarization and weak magnetization, Appl Phys Lett. 91 (2007) 242901. https://doi.org/10.1063/1.2816118.

[60] J. Wang, J.B. Neaton, † H Zheng, † V Nagarajan, S.B. Ogale, B. Liu, D. Viehland, V. Vaithyanathan, D.G. Schlom, U. V Waghmare, N.A. Spaldin, K.M. Rabe, M. Wuttig, R. Ramesh, Epitaxial BiFeO 3 Multiferroic Thin Film Heterostructures, n.d. https://www.science.org.

[61] X. Qi, J. Dho, R. Tomov, M.G. Blamire, J.L. MacManus-Driscoll, Greatly reduced leakage current and conduction mechanism in aliovalent-ion-doped BiFeO3, Appl Phys Lett. 86 (2005) 062903. https://doi.org/10.1063/1.1862336.

[62] S.K. Singh, C. V Tomy, T. Era, M. Itoh, H. Ishiwara, Improved multiferroic properties in Sm-doped BiFeO3 thin films deposited using chemical solution deposition method, J Appl Phys. 111 (2012) 102801. https://doi.org/10.1063/1.4714650.

[63] T. Arima, D. Higashiyama, Y. Kaneko, J.P. He, T. Goto, S. Miyasaka, T. Kimura, K. Oikawa, T. Kamiyama, R. Kumai, Y. Tokura, Structural and magnetoelectric properties of Ga2-xFe xO3 single crystals grown by a floating-zone method, Phys Rev B Condens Matter Mater Phys. 70 (2004). https://doi.org/10.1103/PhysRevB.70.064426.

[64] M.B. Mohamed, A. Senyshyn, H. Ehrenberg, H. Fuess, Structural, magnetic, dielectric properties of multiferroic GaFeO3 prepared by solid state reaction and sol-gel methods, J Alloys Compd. 492 (2010). https://doi.org/10.1016/j.jallcom.2009.11.099.

[65] E.A. Wood, The unit cell and space group of gallium iron oxide, a piezoelectric ferromagnetic crystal, Acta Crystallogr. 13 (1960) 682. https://doi.org/10.1107/S0365110X6000162X.

[66] S.C. Abrahams, J.M. Reddy, J.L. Bernstein, Crystal Structure of Piezoelectric Ferromagnetic Gallium Iron Oxide, J Chem Phys. 42 (2004) 3957–3968. https://doi.org/10.1063/1.1695868.

[67] S. Mukherjee, A. Garg, R. Gupta, Probing magnetoelastic coupling and structural changes in magnetoelectric gallium ferrite, Journal of Physics Condensed Matter. 23 (2011). https://doi.org/10.1088/0953-8984/23/44/445403.

[68] J.P. Remeika, GaFeO3: A Ferromagnetic-Piezoelectric Compound, J Appl Phys. (1960). https://doi.org/10.1063/1.1984690.

[69] G.T. Rado, Observation and Possible Mechanisms of Magnetoelectric Effects in a Ferromagnet, Phys Rev Lett. 13 (1964) 335–337. https://doi.org/10.1103/PhysRevLett.13.335.

[70] R.B. Frankel, N.A. Blum, S. Foner, A.J. Freeman, M. Schieber, Ferrimagnetic Structure of Magnetoelectric ${\mathrm{Ga}}_{2\ensuremath{-}x}{\mathrm{Fe}}_{x}{\mathrm{O}}_{3}$, Phys Rev Lett. 15 (1965) 958–960. https://doi.org/10.1103/PhysRevLett.15.958.

[71] T. Arima, D. Higashiyama, Y. Kaneko, J.P. He, T. Goto, S. Miyasaka, T. Kimura, K. Oikawa, T. Kamiyama, R. Kumai, Y. Tokura, Structural and magnetoelectric properties of Ga2-xFe xO3 single crystals grown by a floating-zone method, Phys Rev B Condens Matter Mater Phys. 70 (2004). https://doi.org/10.1103/PhysRevB.70.064426.

[72] S. Mukherjee, A. Garg, R. Gupta, Spin glass-like phase below ∼210 K in magnetoelectric gallium ferrite, Appl Phys Lett. 100 (2012). https://doi.org/10.1063/1.3693400.

[73] S. Mukherjee, V. Ranjan, R. Gupta, A. Garg, Compositional dependence of structural parameters, polyhedral distortion and magnetic properties of gallium ferrite, Solid State Commun. 152 (2012) 1181–1185. https://doi.org/10.1016/j.ssc.2012.03.010.

[74] E.A. Wood, The unit cell and space group of gallium iron oxide, a piezoelectric ferromagnetic crystal, Acta Crystallogr. 13 (1960) 682. https://doi.org/10.1107/S0365110X6000162X.

[75] M.T. Anderson, K.B. Greenwood, G.A. Taylor, K.R. Poeppelmeiert, B-CATION ARRANGEMENTS IN DOUBLE PEROVSKITES, 1993.

[76] G. Blasse, M.G.J. Van Leur, LUMINESCENCE AND ENERGY TRANSFER IN THE COLUMBITE STRUCTURE, 1985.

[77] H.S. Nair, D. Swain, H. N., S. Adiga, C. Narayana, S. Elzabeth, Griffiths phase-like behavior and spin-phonon coupling in double perovskite Tb2NiMnO6, J Appl Phys. 110 (2011) 123919. https://doi.org/10.1063/1.3671674.

[78] A.P. Ayala, I. Guedes, E.N. Silva, M.S. Augsburger, M. del C. Viola, J.C. Pedregosa, Raman investigation of A2CoBO6 (A=Sr and Ca, B=Te and W) double perovskites, J Appl Phys. 101 (2007) 123511. https://doi.org/10.1063/1.2745088.

[79] J. Su, Z.Z. Yang, X.M. Lu, J.T. Zhang, L. Gu, C.J. Lu, Q.C. Li, J.M. Liu, J.S. Zhu, Magnetism-Driven Ferroelectricity in Double Perovskite Y2NiMnO6, ACS Appl Mater Interfaces. 7 (2015) 13260–13265. https://doi.org/10.1021/acsami.5b00911.

[80] H. Jian Zhao, X. Ming Chen, First-principles study on the differences of possible ferroelectric behavior and magnetic exchange interaction between Bi2NiMnO 6 and La2NiMnO6, AIP Adv. 2 (2012). https://doi.org/10.1063/1.4768268.

[81] N.S. Rogado, J. Li, A.W. Sleight, M.A. Subramanian, Magnetocapacitance and magnetoresistance near room temperature in a ferromagnetic semiconductor: La2NiMnO6, Advanced Materials. 17 (2005) 2225–2227. https://doi.org/10.1002/adma.200500737.

[82] I. Dass, J.Q. Yan, B. Goodenough, Oxygen stoichiometry, ferromagnetism, and transport properties of La2-xNiMnO6+δ, Phys Rev B Condens Matter Mater Phys. 68 (2003). https://doi.org/10.1103/PhysRevB.68.064415.

[83] J.B. Goodenovgh, Theory of the Role of Covalence in the Perovskite-Type Manganites g,a, M(II) jMnOsf, n.d.

[84] S. Zhao, L. Shi, S. Zhou, J. Zhao, H. Yang, Y. Guo, Size-dependent magnetic properties and Raman spectra of La2NiMnO6 nanoparticles, J Appl Phys. 106 (2009) 123901. https://doi.org/10.1063/1.3269707.

[85] S. Kamba, D. Nuzhnyy, R. Nechache, K. Závěta, D. Nižňanský, E. Šantavá, C. Harnagea, A. Pignolet, Infrared and magnetic characterization of multiferroic Bi2 FeCr O6 thin films over a broad temperature range, Phys Rev B Condens Matter Mater Phys. 77 (2008). https://doi.org/10.1103/PhysRevB.77.104111.

[86] J. Van Den Boomgaard, A.M.J.G. Van Run, J. Van Suchtelen, Magnetoelectricity in piezoelectric-magnetostrictive composites, Ferroelectrics. 10 (1976) 295–298. https://doi.org/10.1080/00150197608241997.

[87] S. Lopatin, I. Lopatina, I. Lisnevskaya, Magnetoelectric PZT/ferrite composite material, Ferroelectrics. 162 (1994) 63–68. https://doi.org/10.1080/00150199408245091.

[88] M.I. Bichurin, I.A. Kornev, V.M. Petrov, I. V Lisnevskaya, Investigation of magnetoelectric interaction in composite, Ferroelectrics. 204 (1997) 289–297. https://doi.org/10.1080/00150199708222209.

[89] T.G. Lupejko, I. V Lisnevskaya, M.D. Chkheidze, B.I. Zvyagintsev, Layered magnetoelectric composites based on nickel ferrite and lead zirconate-titanate materials, Neorganicheskie Materialy. 31 (1995) 1245–1248. http://inis.iaea.org/search/search.aspx?orig_q=RN:27043814.

[90] J. Ryu, A.V. Carazo, K. Uchino, H.-E. Kim, Magnetoelectric Properties in Piezoelectric and Magnetostrictive Laminate Composites, 2001.

[91] J. Ryu, A. Carazo, K. Uchino, H. Kim, Piezoelectric and Magnetoelectric Properties of Lead Zirconate Titanate/Ni-Ferrite Particulate Composites, Kluwer Academic Publishers, 2001.

[92] J. Ryu, S. Priya, K. Uchino, & H.-E. Kim, Magnetoelectric Effect in Composites of Magnetostrictive and Piezoelectric Materials, Kluwer Academic Publishers, 2002.

[93] N. Dix, V. Skumryev, V. Laukhin, L. Fàbrega, F. Sánchez, J. Fontcuberta, Sputtering growth and characterization of CoFe2O4-BaTiO3 nanostructures, Mater Sci Eng B Solid State Mater Adv Technol. 144 (2007) 127–131. https://doi.org/10.1016/j.mseb.2007.07.050.

[94] H. Zheng, J. Wang, S.E. Lofland, Z. Ma, L. Mohaddes-Ardabili, T. Zhao, L. Salamanca-Riba, S.R. Shinde, S.B. Ogale, F. Bai, D. Viehland, Y. Jia, D.G. Schlom, M. Wuttig, A. Roytburd, R. Ramesh, Bose National Centre for Basic Sciences on, 2004. www.sciencemag.org.

[95] H. Luo, H. Yang, S.A. Baily, O. Ugurlu, M. Jain, M.E. Hawley, T.M. McCleskey, A.K. Burrell, E. Bauer, L. Civale, T.G. Holesinger, Q. Jia, Self-assembled epitaxial nanocomposite BaTiO3-NiFe 2O4 films prepared by polymer-assisted deposition, J Am Chem Soc. 129 (2007) 14132–14133. https://doi.org/10.1021/ja075764u.

[96] X.M. Liu, S.Y. Fu, C.J. Huang, Synthesis and magnetic characterization of novel CoFe2O 4-BiFeO3 nanocomposites, Mater Sci Eng B Solid State Mater Adv Technol. 121 (2005) 255–260. https://doi.org/10.1016/j.mseb.2005.04.009.

[97] F. Yang, M.H. Tang, Z. Ye, Y.C. Zhou, X.J. Zheng, J.X. Tang, J.J. Zhang, J. He, Eight logic states of tunneling magnetoelectroresistance in multiferroic tunnel junctions, J Appl Phys. 102 (2007) 044504. https://doi.org/10.1063/1.2768075.

[98] D.H. Kim, T.C. Kim, S.H. Lee, S.H. Han, K.S. Han, C.A. Ross, Self-assembled growth of Sr(Ti,Fe)O3-CoFe2O4 magnetic nanocomposite thin films, J Appl Phys. 121 (2017). https://doi.org/10.1063/1.4982162.

[99] G. V. Duong, R.S. Turtelli, R. Groessinger, Magnetoelectric properties of CoFe2O4-BaTiO3 core-shell structure composite studied by a magnetic pulse method, J Magn Magn Mater. 322 (2010) 1581–1584. https://doi.org/10.1016/j.jmmm.2009.09.022.

[100] D. Lisjak, A. Mertelj, Anisotropic magnetic nanoparticles: A review of their properties, syntheses and potential applications, Prog Mater Sci. 95 (2018) 286–328. https://doi.org/10.1016/j.pmatsci.2018.03.003.

[101] D.L. Leslie-Pelecky, R.D. Rieke, Magnetic Properties of Nanostructured Materials, 1996. https://pubs.acs.org/sharingguidelines.

[102] Y.P. Feng, L. Shen, M. Yang, A. Wang, M. Zeng, Q. Wu, S. Chintalapati, C.R. Chang, Prospects of spintronics based on 2D materials, Wiley Interdiscip Rev Comput Mol Sci. 7 (2017). https://doi.org/10.1002/wcms.1313.

[103] R. Singh, Unexpected magnetism in nanomaterials, J Magn Magn Mater. 346 (2013) 58–73. https://doi.org/10.1016/j.jmmm.2013.07.005.

[104] Q.A. Pankhurst ’, R.J. Pollard, Origin of the Spin-Canting Anomaly in Small Ferrimagnetic Particles, 1991.

[105] M. Springborg, M. Zhou, M. Molayem, B. Kirtman, Surfaces, Shapes, and Bulk Properties of Crystals, Journal of Physical Chemistry C. 122 (2018) 11926–11932. https://doi.org/10.1021/acs.jpcc.8b03041.

[106] A. Seyed-Razavi, I.K. Snook, A.S. Barnard, Origin of nanomorphology: Does a complete theory of nanoparticle evolution exist?, J Mater Chem. 20 (2010) 416–421. https://doi.org/10.1039/b915383g.

[107] Y. Xia, X. Xia, H.C. Peng, Shape-Controlled Synthesis of Colloidal Metal Nanocrystals: Thermodynamic versus Kinetic Products, J Am Chem Soc. 137 (2015) 7947–7966. https://doi.org/10.1021/jacs.5b04641.

[108] S.J.L. Billinge, I. Levin, The Problem with Determining Atomic Structure at the Nanoscale, n.d. https://www.science.org.

[109] G.D. Barmparis, Z. Lodziana, N. Lopez, I.N. Remediakis, Nanoparticle shapes by using Wulff constructions and first-principles calculations, Beilstein Journal of Nanotechnology. 6 (2015) 361–368. https://doi.org/10.3762/bjnano.6.35.

[110] H. Wu, L. Li, L.Z. Liang, S. Liang, Y.Y. Zhu, X.H. Zhu, Recent progress on the structural characterizations of domain structures in ferroic and multiferroic perovskite oxides: A review, J Eur Ceram Soc. 35 (2015) 411–441. https://doi.org/10.1016/j.jeurceramsoc.2014.09.037.

[111] B. Issa, I.M. Obaidat, B.A. Albiss, Y. Haik, Magnetic nanoparticles: Surface effects and properties related to biomedicine applications, Int J Mol Sci. 14 (2013) 21266–21305. https://doi.org/10.3390/ijms141121266.

[112] M. Mikhaylova, D.K. Kim, N.P. Bobrysheva, M. Osmolowsky, V. Semenov, T. Tsakalakos, M. Muhammed, Superparamagnetism of Magnetite Nanoparticles: Dependence on Surface Modification, Langmuir. 20 (2004) 2472–2477. https://doi.org/10.1021/la035648e.

[113] D.-X. Chen, A. Sanchez, E. Taboada, A. Roig, N. Sun, H.-C. Gu, Size determination of superparamagnetic nanoparticles from magnetization curve, J Appl Phys. 105 (2009) 083924. https://doi.org/10.1063/1.3117512.

[114] N.H. Hong, J. Sakai, N. Poirot, V. Brizé, Room-temperature ferromagnetism observed in undoped semiconducting and insulating oxide thin films, Phys Rev B Condens Matter Mater Phys. 73 (2006). https://doi.org/10.1103/PhysRevB.73.132404.

[115] T.A. Saleh, Chapter 1 - Overview of surface and interface science, in: T.A. Saleh (Ed.), Interface Science and Technology, Elsevier, 2022: pp. 1–38. https://doi.org/https://doi.org/10.1016/B978-0-12-849876-7.00001-4.

[116] E. Roduner, R.S. of C. (Great Britain), Nanoscopic Materials: Size-dependent Phenomena, RSC Pub., 2006. https://books.google.co.in/books?id=LFkryuW-doMC.

[117] B.D. Cullity, Introduction to Magnetic Materials, Addison-Wesley Publishing Company, 1972. https://books.google.co.in/books?id=CkNBAQAAIAAJ.

[118] N. Baig, I. Kammakakam, W. Falath, I. Kammakakam, Nanomaterials: A review of synthesis methods, properties, recent progress, and challenges, Mater Adv. 2 (2021) 1821–1871. https://doi.org/10.1039/d0ma00807a.

[119] G. V. Duong, R.S. Turtelli, R. Groessinger, Magnetoelectric properties of CoFe2O4-BaTiO3 core-shell structure composite studied by a magnetic pulse method, J Magn Magn Mater. 322 (2010) 1581–1584. https://doi.org/10.1016/j.jmmm.2009.09.022.

[120] D.H. Kim, N.M. Aimon, X.Y. Sun, L. Kornblum, Fred.J. Walker, Charles.H. Ahn, C.A. Ross, Integration of Self-Assembled Epitaxial BiFeO 3 -CoFe 2 O 4 Multiferroic Nanocomposites on Silicon Substrates , Adv Funct Mater. 24 (2014) 5889–5896. https://doi.org/10.1002/adfm.201401458.

[121] D.H. Kim, T.C. Kim, S.H. Lee, S.H. Han, K.S. Han, C.A. Ross, Self-assembled growth of Sr(Ti,Fe)O3-CoFe2O4 magnetic nanocomposite thin films, J Appl Phys. 121 (2017). https://doi.org/10.1063/1.4982162.

[122] M. Bibes, A. Barthélémy, Multiferroics: Towards a magnetoelectric memory, Nat Mater. 7 (2008) 425–426. https://doi.org/10.1038/nmat2189.

[123] F. Yang, M.H. Tang, Z. Ye, Y.C. Zhou, X.J. Zheng, J.X. Tang, J.J. Zhang, J. He, Eight logic states of tunneling magnetoelectroresistance in multiferroic tunnel junctions, J Appl Phys. 102 (2007) 044504. https://doi.org/10.1063/1.2768075.

[124] M. Gajek, M. Bibes, S. Fusil, K. Bouzehouane, J. Fontcuberta, A. Barthélémy, A. Fert, Tunnel junctions with multiferroic barriers, Nat Mater. 6 (2007) 296–302. https://doi.org/10.1038/nmat1860.

[125] Y. Li, W.Q. Cao, J. Yuan, D.W. Wang, M.S. Cao, Nd doping of bismuth ferrite to tune electromagnetic properties and increase microwave absorption by magnetic-dielectric synergy, J Mater Chem C Mater. 3 (2015) 9276–9282. https://doi.org/10.1039/c5tc01684c.

[126] Z.J. Li, Z.L. Hou, W.L. Song, X. Da Liu, W.Q. Cao, X.H. Shao, M.S. Cao, Unusual continuous dual absorption peaks in Ca-doped BiFeO3 nanostructures for broadened microwave absorption, Nanoscale. 8 (2016) 10415–10424. https://doi.org/10.1039/c6nr00223d.

[127] A.M. Kloxin, A.M. Kasko, C.N. Salinas, K.S. Anseth, Photodegradable hydrogels for dynamic tuning of physical and chemical properties, Science (1979). 324 (2009) 59–63. https://doi.org/10.1126/science.1169494.

[128] S.R. Basu, L.W. Martin, Y.H. Chu, M. Gajek, R. Ramesh, R.C. Rai, X. Xu, J.L. Musfeldt, Photoconductivity in BiFeO3 thin films, Appl Phys Lett. 92 (2008). https://doi.org/10.1063/1.2887908.

[129] S.J. Clark, J. Robertson, Band gap and Schottky barrier heights of multiferroic BiFeO3, Appl Phys Lett. 90 (2007) 132903. https://doi.org/10.1063/1.2716868.

[130] S.R. Basu, L.W. Martin, Y.H. Chu, M. Gajek, R. Ramesh, R.C. Rai, X. Xu, J.L. Musfeldt, Photoconductivity in BiFeO3 thin films, Appl Phys Lett. 92 (2008) 091905. https://doi.org/10.1063/1.2887908.

[131] Vladimir M Fridkin, B N Popov, Anomalous photovoltaic effect in ferroelectrics, Soviet Physics Uspekhi. 21 (1978) 981. https://doi.org/10.1070/PU1978v021n12ABEH005722.

[132] T. Choi, S. Lee, Y.J. Choi, V. Kiryukhin, S.-W. Cheong, Switchable Ferroelectric Diode and Photovoltaic Effect in BiFeO3, Science (1979). 324 (2009) 63–66. https://doi.org/10.1126/science.1168636.

[133] M. Fiebig, Revival of the magnetoelectric effect, J Phys D Appl Phys. 38 (2005) R123. https://doi.org/10.1088/0022-3727/38/8/R01.

[134] R. Dorey, Chapter 4 - Microstructure–property relationships: How the microstructure of the film affects its properties, in: R. Dorey (Ed.), Ceramic Thick Films for MEMS and Microdevices, William Andrew Publishing, Oxford, 2012: pp. 85–112. https://doi.org/https://doi.org/10.1016/B978-1-4377-7817-5.00004-3.

[135] G. Datt, A.C. Abhyankar, Dopant driven tunability of dielectric relaxation in MxCo(1-x)Fe2O4 (M: Zn2+, Mn2+, Ni2+) nano-ferrites, J Appl Phys. 122 (2017) 034102. https://doi.org/10.1063/1.4990275.

[136] C. v Ramana, Y.D. Kolekar, K. Kamala Bharathi, B. Sinha, K. Ghosh, Correlation between structural, magnetic, and dielectric properties of manganese substituted cobalt ferrite, J Appl Phys. 114 (2013) 183907. https://doi.org/10.1063/1.4827416.

[137] Andrew K Jonscher, Dielectric relaxation in solids, J Phys D Appl Phys. 32 (1999) R57. https://doi.org/10.1088/0022-3727/32/14/201.

[138] A.K. Jonscher, R. Holloway, Physics To cite this article: Andrew K Jonscher, 1999.

[139] K. Vasundhara, S.N. Achary, S.K. Deshpande, P.D. Babu, S.S. Meena, A.K. Tyagi, Size dependent magnetic and dielectric properties of nano CoFe2O4 prepared by a salt assisted gel-combustion method, J Appl Phys. 113 (2013) 194101. https://doi.org/10.1063/1.4804946.

[140] R. Tang, C. Jiang, W. Qian, J. Jian, X. Zhang, H. Wang, H. Yang, Dielectric relaxation, resonance and scaling behaviors in Sr3Co2Fe24O41 hexaferrite, Sci Rep. 5 (2015). https://doi.org/10.1038/srep13645.

[141] S.K. Pradhan, B.K. Roul, Electrical behavior of high resistivity Ce-doped BiFeO 3 multiferroic, Physica B Condens Matter. 407 (2012) 2527–2532. https://doi.org/10.1016/j.physb.2012.03.061.

[142] C.G. Koops, On the Dispersion of Resistivity and Dielectric Constant of Some Semiconductors at Audiofrequencies, Physical Review. 83 (1951) 121–124. https://doi.org/10.1103/PhysRev.83.121.

[143] N Ponpandian, P Balaya, A Narayanasamy, Electrical conductivity and dielectric behaviour of nanocrystalline NiFe2O4 spinel, Journal of Physics: Condensed Matter. 14 (2002) 3221. https://doi.org/10.1088/0953-8984/14/12/311.

[144] A.K. Jonscher, The 'universal' dielectric response, Nature. 267 (1977) 673–679. https://doi.org/10.1038/267673a0.

[145] J. Liu, R. Che, H. Chen, F. Zhang, F. Xia, Q. Wu, M. Wang, Microwave absorption enhancement of multifunctional composite microspheres with spinel Fe 3O 4 cores and anatase TiO 2 shells, Small. 8 (2012) 1214–1221. https://doi.org/10.1002/smll.201102245.

[146] Y. Yin, X. Liu, X. Wei, R. Yu, J. Shui, Porous CNTs/Co Composite Derived from Zeolitic Imidazolate Framework: A Lightweight, Ultrathin, and Highly Efficient Electromagnetic Wave Absorber, ACS Appl Mater Interfaces. 8 (2016) 34686–34698. https://doi.org/10.1021/acsami.6b12178.

[147] C.-Y. Wen, H.-Y. Xie, Z.-L. Zhang, L.-L. Wu, J. Hu, M. Tang, M. Wu, D.-W. Pang, Fluorescent/magnetic micro/nano-spheres based on quantum dots and/or magnetic nanoparticles: preparation, properties, and their applications in cancer studies, Nanoscale. 8 (2016) 12406–12429. https://doi.org/10.1039/C5NR08534A.

[148] V. Shukla, Review of electromagnetic interference shielding materials fabricated by iron ingredients, Nanoscale Adv. 1 (2019) 1640–1671. https://doi.org/10.1039/c9na00108e.

[149] R. Valenzuela, Novel Applications of Ferrites, Physics Research International. 2012 (2012) 591839. https://doi.org/10.1155/2012/591839.

[150] M. Green, X. Chen, Recent progress of nanomaterials for microwave absorption, Journal of Materiomics. 5 (2019) 503–541. https://doi.org/10.1016/j.jmat.2019.07.003.

[151] M. Pardavi-Horvath, M. Pardavi-Horvath, Microwave applications of soft ferrites, 2000. http://www.rec-usa.com/rmhor.htm.

[152] F. Wang, J. Liu, J. Kong, Z. Zhang, X. Wang, M. Itoh, K.I. MacHida, Template free synthesis and electromagnetic wave absorption properties of monodispersed hollow magnetite nano-spheres, J Mater Chem. 21 (2011) 4314–4320. https://doi.org/10.1039/c0jm02894k.

[153] R. Panigrahi, S.K. Srivastava, Trapping of microwave radiation in hollow polypyrrole microsphere through enhanced internal reflection: A novel approach, Sci Rep. 5 (2015). https://doi.org/10.1038/srep07638.

[154] X. Bai, Y. Zhai, Y. Zhang, Green approach to prepare graphene-based composites with high microwave absorption capacity, Journal of Physical Chemistry C. 115 (2011) 11673–11677. https://doi.org/10.1021/jp202475m.

[155] X.G. Liu, D.Y. Geng, H. Meng, P.J. Shang, Z.D. Zhang, Microwave-absorption properties of ZnO-coated iron nanocapsules, Appl Phys Lett. 92 (2008) 173117. https://doi.org/10.1063/1.2919098.

[156] T. Tian, X. Shi, L. Cheng, Y. Luo, Z. Dong, H. Gong, L. Xu, Z. Zhong, R. Peng, Z. Liu, Graphene-based nanocomposite as an effective, multifunctional, and recyclable antibacterial agent, ACS Appl Mater Interfaces. 6 (2014) 8542–8548. https://doi.org/10.1021/am5022914.

[157] J. Baker-Jarvis, M. Janezic, J.G. Jr, R. Geyer, Transmission/Reflection and Short-Circuit Line Methods for Measuring Permittivity and Permeability, (1992).

[158] D. Zhang, T. Liu, J. Cheng, J. Chai, X. Yang, H. Wang, G. Zheng, M. Cao, Light-weight and low-cost electromagnetic wave absorbers with high performances based on biomass-derived reduced graphene oxides, Nanotechnology. 30 (2019). https://doi.org/10.1088/1361-6528/ab35fa.

[159] J.Z. He, X.X. Wang, Y.L. Zhang, M.S. Cao, Small magnetic nanoparticles decorating reduced graphene oxides to tune the electromagnetic attenuation capacity, J Mater Chem C Mater. 4 (2016) 7130–7140. https://doi.org/10.1039/c6tc02020h.

[160] Pozar_Microwave Engineering(2012), (n.d.).

[161] R.E. Collin, A C LA SSlC REISSUE Foundations for Microwave Engineering SECOND EDITION, n.d.

[162] D.J. Griffiths, Introduction to Electrodynamics, 4th ed., Cambridge University Press, Cambridge, 2017. https://doi.org/DOI: 10.1017/9781108333511.

[163] H. Mamiya, B. Jeyadevan, Design Criteria of Thermal Seeds for Magnetic Fluid Hyperthermia - From Magnetic Physics Point of View, in: Nanomaterials for Magnetic and Optical Hyperthermia Applications, Elsevier, 2018: pp. 13–39. https://doi.org/10.1016/B978-0-12-813928-8.00001-6.

[164] J. Barranger, N A S A T E C H N I C A L N O T E w-HYSTERESIS A N D A TRANSFORMER A N APPLICATION EDDY-CURRENT LOSSES OF LAMINATION VIEWED AS OF THE POYNTING THEOREM, n.d.

[165] S. Dobák, C. Beatrice, V. Tsakaloudi, F. Fiorillo, magnetochemistry Magnetic Losses in Soft Ferrites, (2022). https://doi.org/10.3390/magnetochemistry.

[166] A.N. Vicente, G.M.I. Dip, C. Junqueira, The step by step development of NRW method, in: SBMO/IEEE MTT-S International Microwave and Optoelectronics Conference Proceedings, 2011: pp. 738–742. https://doi.org/10.1109/IMOC.2011.6169318.

CHAPTER 2

EXPERIMENTAL DETAILS

2.1 PREAMBLE

Various techniques for producing nanoparticles and composites, as well as a number of techniques for analysing the properties of the produced materials, have been discussed in depth in this chapter.

The Rietveld Refinement Analysis and Field Emission Scanning Electron Microscopy (FESEM) and Energy Dispersive X-Ray Analysis (EDAX) using FEG source 200V-30kV, Transmission Electron Microscopy (TEM), High Resolution Transmission Electron Microscopy (HRTEM), Selected Area Diffractometer, and X-Ray Diffraction Method (XRD) are used to conduct the structural and morphological investigations (AFM). The ferroelectric polarisation hysteresis loop tracer (TREK Model 609B) and piezoelectric field microscope from Radiant Technologies Incorporated have been used to study the ferroelectric characteristics (PFM). Vibrating Sample Magnetometer (VSM) with Lakeshore VSM, Physical Property Measurement System (PPMS) with Quantum Design, DYNACOOL, and Magnetic Field Microscopy have all been used to study the magnetic characteristics (MFM). LCR metres are used to measure the dielectric characteristics (ZM2376). Electromagnets are used to measure the magnetodielectric characteristics.

2.2 SYNTHESIS TECHNIQUES

2.2.1 SOL-GEL SYNTHESIS METHOD

Utilizing precursors in liquid-based chemical reactions under controlled experimental conditions. There is no universal guideline for wet chemical synthesis because each synthesis process is unique. At lower temperatures, it can produce significantly smaller grains and particles, and it can form the desired phase more quickly than the conventional solid-state method. The desired material is synthesized from the bottom up. This research involved the wet chemical synthesis of gallium ferrite composites on a basis of double-distilled water.

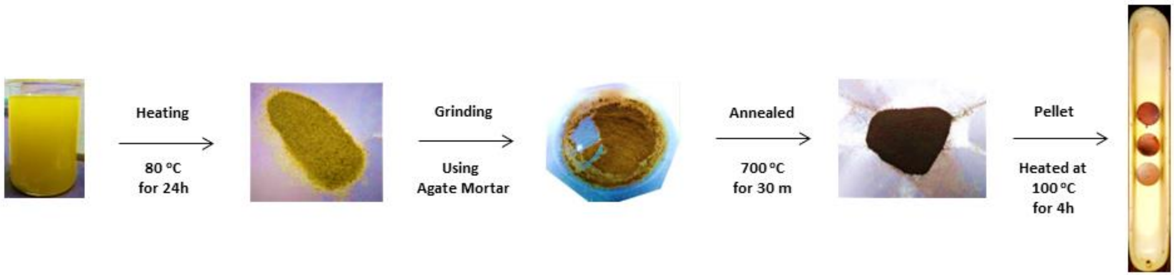

Figure 2.1 Preparation of Bismuth Ferrite nanoparticles using tartaric acid assisted sol-gel method

Figure 2.1 depicts the sol-gel method of barium and yttrium co-doped bismuth ferrite using tartaric acid as a chelating agent and the nitrate salts in nitric acid mixed with double-distilled water.

2.2.2 SOLID STATE REACTION METHOD

The standard solid state reaction approach for the production of multiferroics involves calcining the mixture at a very high temperature to allow cations to diffuse between one another in order to mix the proper metallic oxides and carbonates over hours. The extremely sluggish chemical reaction is carried out by ion diffusions in solid states using this technique. The reaction in this approach begins when the chemicals come into touch with one another, making an equivalent distribution of the components and adequate mixing crucial in this synthesis method. Short diffusion paths cause the reactions to begin quickly at first, but as they progress, they gradually slow down. This approach may experience irregular particle shape and size, loss of stoichiometry, creation of undesired phases, etc. as a result of the mixture's inhomogeneity. In this thesis, the traditional solid state reaction technique is used to synthesise Sodium Bismuth Titanate-Strontium Titanate Solid Solution and Yttrium Iron Garnet Composites.

2.2.3 PULSED LASER DEPOSITION

Pulsed Laser Deposition (PLD) is a well-known method for synthesizing high-quality thin film samples with the required patterns for particular applications[1,2]. Concentrating a powerful laser beam in a vacuum chamber in order to deposit a thin film on a target material. As a plasma plume, the substance is vaporized and deposited on a substrate. In the presence of a background gas or a very high vacuum, this procedure is carried out.

The detail mechanism of a PLD is very complex and divided into four stages:

Plasma generation and laser ablation of the target material:

A laser beam strikes the surface of the bulk material and penetrates it to the penetration depth in this instance. A strong electric field generated by the laser beam is enough to remove an electron from the bulk material of the volume-penetrating material. This procedure occurs in a very brief period of time (ps). These electrons oscillate within the permeable volume and collide with the atoms of the bulk material. During collision, electrons transfer energy to the

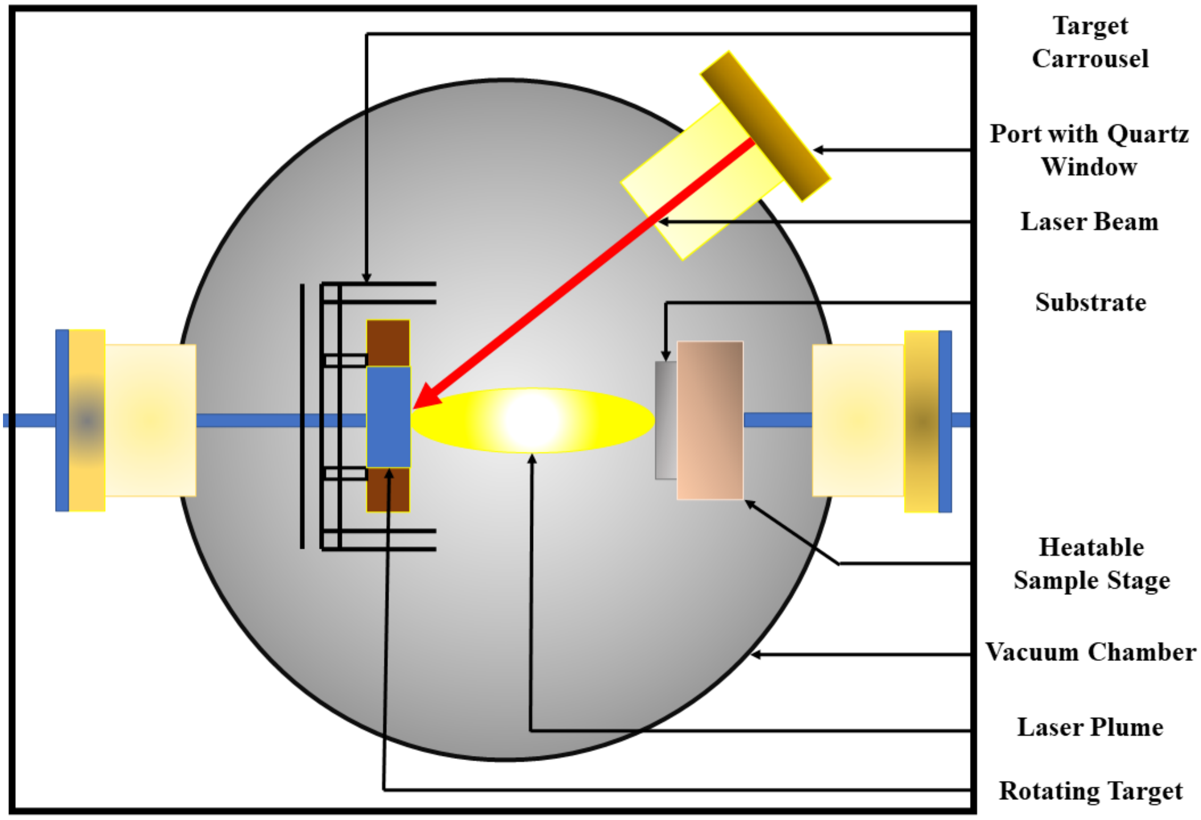

Figure 2.2 Schematic diagram of PLD set up.

surface lattice of the target material. This energy heated the substance's surface, causing it to evaporate.

Dynamic of the plasma:

The vaporized plasma plume is directed towards the substrate in a direction parallel to the normal vector of the target surface due to columbic repulsion. The distribution of the plasma plume depends on the chamber's background pressure and is characterized by a $cos^n(x)$ law with a Gaussian-like curve shape.

Depositing the ablation material onto the substrate :

Typically, the third stage determines the film's quality. In this instance, plasma plumes of high energy bombard the surface of the substrate, causing atoms to sputter from the surface. The collision region formed by atoms and plasma particles sputtered from the target material functions as a particle condensation. When the condensation rate is high, thermal energy is quickly attained and the surface film grows at a constant rate.

Film nucleation and growth on the surface of the substrate :

The nucleation and growth kinetics of the film depends on several parameters such as, *Laser parameter*: Film quality, stoichiometry, and deposition flux are influenced by laser intensity (Joule/cm^2), laser energy, and ionization degree of the ablated material.

Surface temperature: The nucleation density is significantly affected by the surface temperature. Generally, the nucleation density decreases as the temperature rises.

Substrate surface: The nucleation and growth of the film are also affected by the substrate's surface roughness and the target material's and substrate's mismatched lattices.

Background pressure: The ambient pressure is essential for the stoichiometric transfer from target to substrate. At low oxygen background pressure, for instance, non-stoichiometric film will grow, affecting nucleation density and film quality. The schematic diagram of a PLD setup is depicted in Figure 2.2. Bismuth Ferrite thin films reported in this thesis are deposited on $SrTiO_3$ (111) substrates using the PLD technique.

2.3 MEASUREMENT TECHNIQUES

2.3.1 STRUCTURE AND MORPHOLOGY

2.3.1.1 X-RAY DIFFRACTION (XRD)

When a monochromatic X-Ray is incident upon a material it scatters from the atoms situated in the material [Figure 2.2] due to the comparable wavelength of X-Rays with the atomic size[3]. These scattered waves produce constructive and destructive interferences when it satisfies the Bragg's law,

$$2d_{hkl} sin\theta = n\lambda \quad (2.1)$$

Where d_{hkl} is the spacing between two planes, θ is the incident angle of X-Rays, n is any integer number, and λ is the wavelength of the X-Rays. The Bragg’s law is portrayed in Figure 2.3.

X-Ray powder diffraction (XRD) is a useful analytical technique which is widely used for phase identification of crystalline materials. It can provide with following information about a material under investigation,

1. Phase composition,
2. Crystallite size,
3. Quantitative phase analysis,
4. Unit cell lattice parameters,

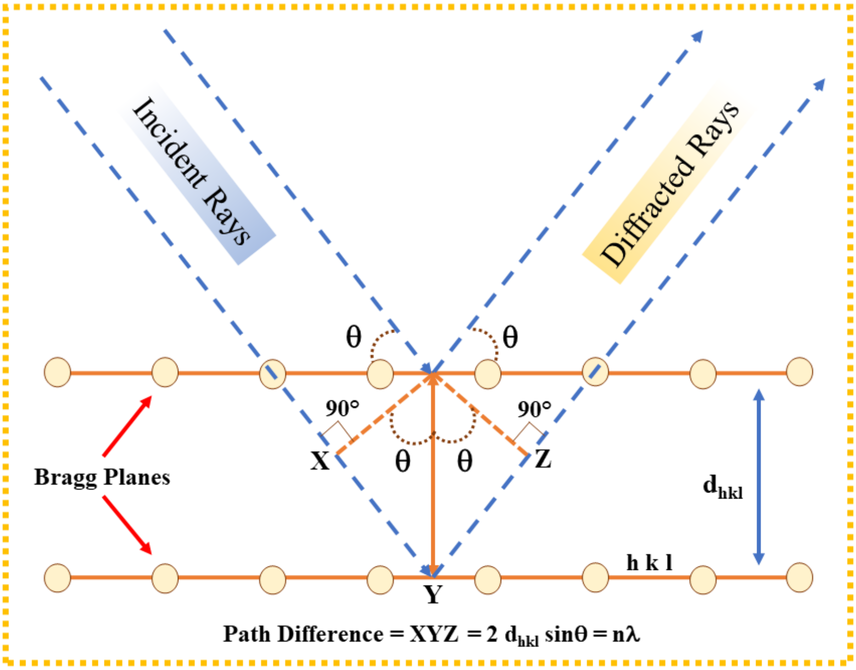

Figure 2.3 Schematic diagram of diffraction of X-rays by a crystal

5. Micro-strain, etc.

On the other hand, keeping the incident angle of source X - Ray at a very low angle ($\omega < 5°$) such that the ray is entirely focused on the material situated at the top-most surface of a sample, is able to the determine the phase of the material. This technique is widely used to provide following information about thin films and known as Grazing Index XRD (GIXRD), Orientation of thin film with respect to the substrate,

1. Lattice mismatch between the thin film and the substrate,
2. Epitaxy or texture,
3. Macro and micro strains,

The phase and structure of the all samples reported in this thesis are investigated by X-ray diffraction (XRD) recorded at room temperature with Panalytical X'Pert Pro diffractometer using the Cu K_α line ($\lambda = 1.54$ Å) at the scanning rate of 0.6° per minute and Rigaku SmartLab automated multipurpose X-ray Diffractometer.

2.3.1.2 RIETVELD REFINEMENT

Rietveld refinement is a fitting technique first described by Hugo Rietveld, used to characterise the crystalline materials[4,5]. In this method, X-Ray powder diffraction data or neutron diffraction data are fitted using non-linear least square method in order to achieve

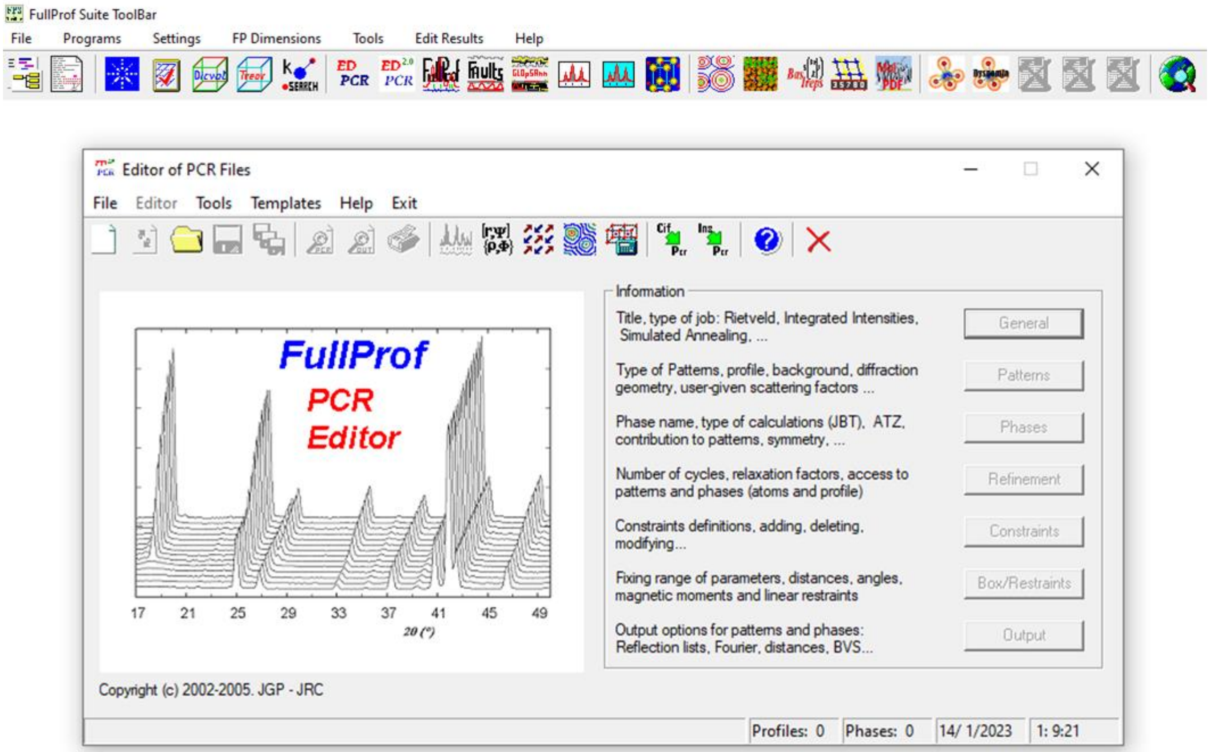

Figure 2.4 FullProf Suite software for performing Rietveld refinement analysis

crystalline information such as lattice parameters, peak shifts, positions of atoms in the unit cell, occupancy of atoms etc. Defined by Rietveld, a function M, defined below, is minimized to achieve best fitting of profiles.

$$M = \sum_i W_i \left\{ y_i^{obs} - \frac{1}{c} y_i^{calc} \right\}^2 \tag{2.2}$$

Where Wi is the statistical weight and c is an overall scaling factor such that $y^{calc} = cy^{obs}$. And the background is calculated using Chebyshev polynomial. In this thesis, FullProf Suite (Figure 2.4) and MAUD software are used to perform Rietveld refinement of the measured XRD data.

2.3.1.3 RAMAN SPECTROSCOPY

Raman spectroscopy is non-destructive chemical analysis technique where scattered light is used to measure the vibrational energy modes of a sample[6]. Raman spectroscopy probes the chemical structure of a material and provides information about,

1. Chemical structure and identity,
2. Phase and polymorphism,
3. Intrinsic stress or strain,
4. Contamination and impurity,

A Raman spectrum can be like a "Fingerprint" for a particular molecule or material, a unique identity of a material.

Raman analysis using a microscopic laser spot and high magnification sample visualisation are both made possible by a Raman microscope, which joins a Raman spectrometer to a conventional optical microscope [Figure 2.5]. When a molecule scatters light, the photon's fluctuating electromagnetic field polarises the cloud of molecular electrons, elevating the molecule to a higher energy state. This unstable and high-energy state, also known as the virtual state, is transient. It quickly emits the energy that the photon imparted to it as a result.

After a molecule interacts with a photon, its energy typically remains constant, and the light that is released has the same wavelength as the wave that was first incident[7,8]. This is the main process and is referred to as Rayleigh Scattering. It is known as Raman Scattering when, in incredibly rare instances (1 in 10 million photons), light is released that is of a

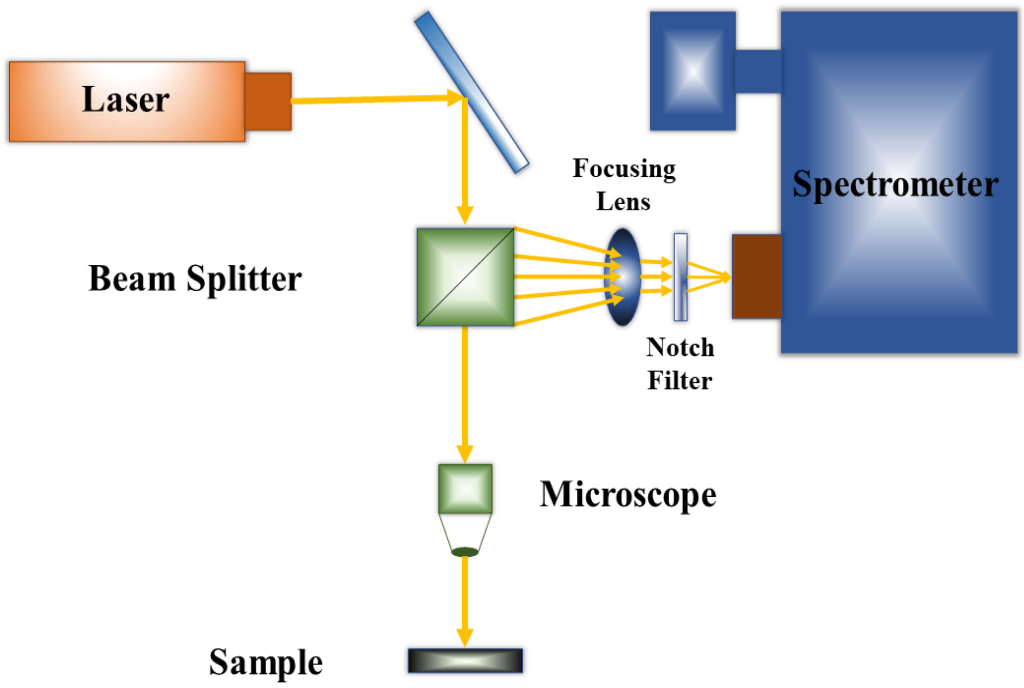

Figure 2.5 Schematic of Raman spectroscopic system

different wavelength from that which was incident. The phenomenon known as Stokes Raman Scattering occurs when a molecule absorbs energy to excite it to a higher vibrational state while emitting less energy. However, if the molecule loses energy lowering to lower vibrational level, then the emitted wavelength will have higher energy and lower wavelength than the incident wave, known as Anti-Stokes Raman Scattering.

In this thesis, Micro-Raman Spectrometer from LabRam HR Evolution; HORIBA France SAS is used for all the studies.

2.3.1.4 FIELD EMISSION SCANNING ELECTRON MICROSCOPE (FESEM)

The Field Emission Scanning Electron Microscope (FESEM) is a microscope that uses a focussed electron beam to take topographical pictures of things[9,10].

In FESEM, a strong electrical field gradient is utilised to focus and accelerate an electron beam. Secondary electrons are released from the target area on the item as the beam bombards it. The surface structure of the item is associated with the secondary electron emission angle and velocity. The secondary electrons that are released are detected, and the data is then further processed to provide a digital image.

An FESEM mainly consists of parts discussed below [Figure 2.6],

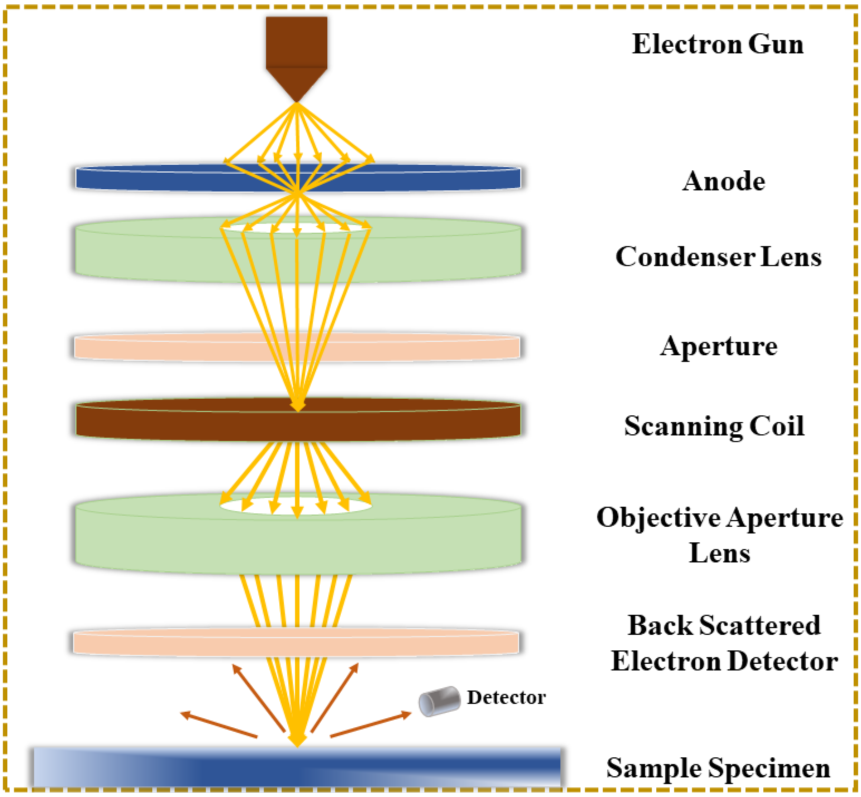

Figure 2.6 Schematic diagram of Field Electron Scanning Electron Microscope

Electron Gun: In a standard electron microscopes electrons are mainly generated by heating a tungsten filament by means of a current to a temperature of about 2800 °C. In a field emission (FE) scanning electron microscope no heating is involved for the emission of electrons beam. Instead, an extremely thin and sharp tungsten needle (tip diameter 10^{-7} –10^{-8} m) functioning as a cathode, is placed in front of a primary anode to generate a voltage in the order of magnitude of 0.5 to 30 kV. The electron beam produced by the FE source being 1000 times smaller than standard microscope, the image quality is remarkedly better.

Condenser lens: The main function of the condenser lenses is to modify the beam diameter. Low current produces small diameter but lacks in good signal to noise ratio or resolution whereas high current reverses the situation.

Scan coils: The scan coils guide the deflection of the electron beam towards the object according to a zig-zag pattern. The scan movement and velocity determine the clarity and the refreshing rate of the image on the screen.

The objective lens: The objective lens focusses the electron beam on the object. For an object placed close to the objective lens, it needs to apply larger force to deflect the electron beam. However, short working distance produces best resolution due to smallest beam diameter.

Detector: The secondary electrons emitted after the primary probe bombards the object possess different velocity depending on the levels and angle of the surface of the object from where it is emitted. The scintillators illuminate as the emitted secondary electrons hits it. The illumination and the location of the illumination varies depending on the properties of the secondary electrons. The signal is amplified and transduced to a video signal to get the digital image.

When electron beam falls on the material, electrons ejected from the atoms including the surface. At this point, an electron from higher energy shells fills the electron vacancy and emits X-Ray, which is characteristic X-Ray and holds information about the elements in the material. This process is called Energy dispersive analysis of X-Ray or EDAX. EDAX is used to understand the chemical elements present on the sample surface.

2.3.1.5 TRANSMISSION ELECTRON MICROSCOPE (TEM)

A very thin material is passed through by a high energy electron beam in a transmission electron microscope (TEM) to create a image[11,12]. Then, properties like particle size,

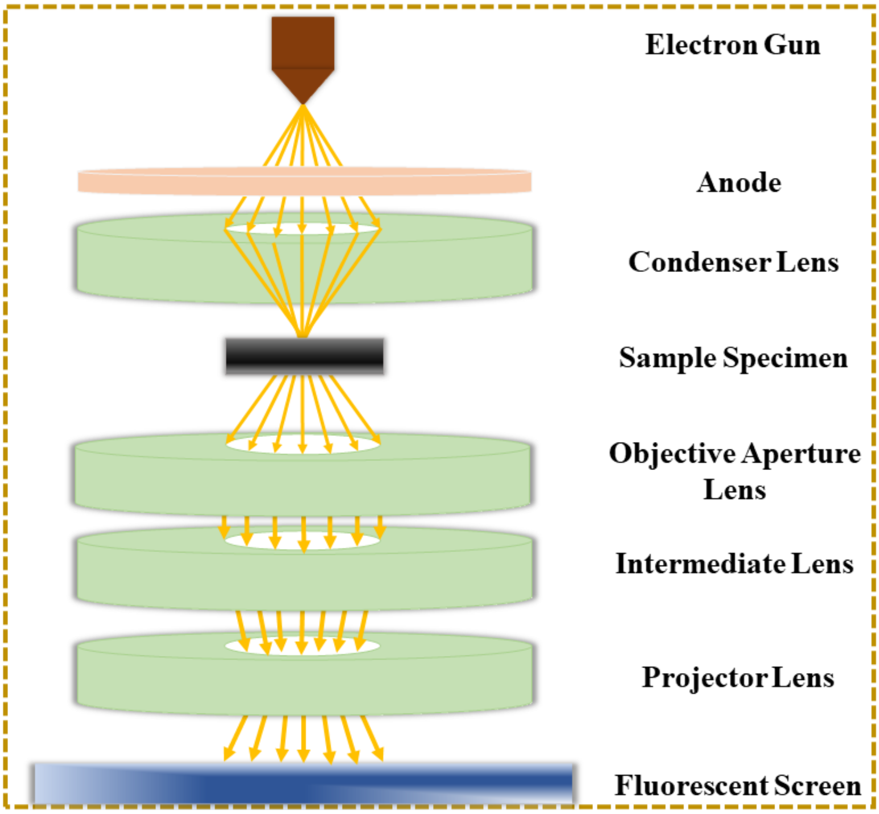

Figure 2.7 Schematic diagram of transmission electron microscope system

crystal structure, and chemical analysis are seen using the interactions between the electrons and the atoms. When an electron beam contacts a specimen, transmission and scattering are the two main types of interactions that take place.

Imaging: To get image, the electron beam emitting from the electron gun is passed through the condenser lens which focuses the beam into small, thin, coherent beam, as shown in Figure 2.7. Then the beam falls on the specimen where parts of it transmits through the sample. The transmitted beam is passed through Objective aperture lens in order to enhance the contrast by blocking out high angle diffracted electrons. The beam is then passed through intermediate lens and projector lens to enlarge it. As the image strikes the fluorescent screen, user is able to see the image. The darker areas of the image represent those areas of the sample through which fewer electrons are able to pass through.

2.3.1.6 ATOMIC FORCE MICROSCOPY (AFM)

Atomic force microscopy (AFM) is used to capture very high-resolution (in the order of Å) images of sample surface at nanometre range[13,14]. In this method, a mechanical probe is used to get the morphology of the sample surface. The probe is chosen such that the end is

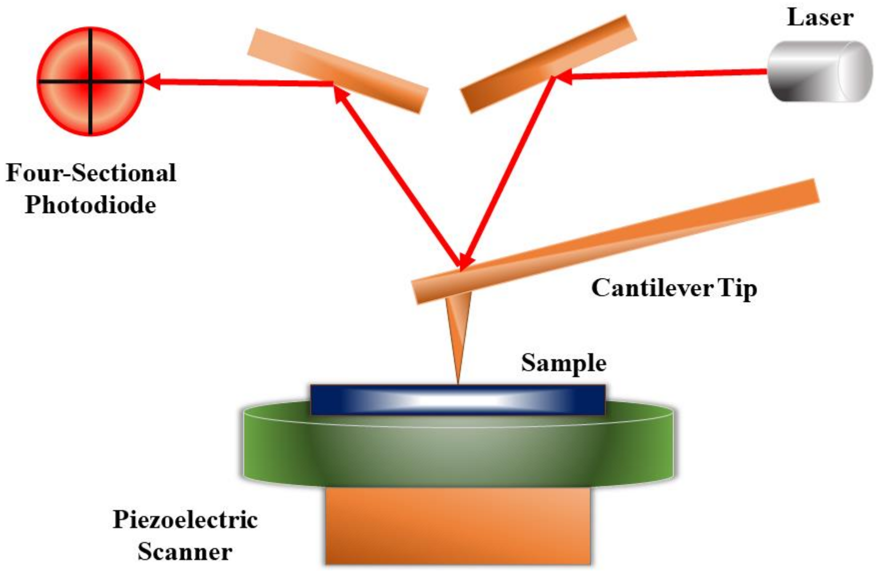

Figure 2.8 Schematic diagram of an Atomic Force Microscope system

very thin and sharp with a tip radium in 5 – 20 nm range. The cantilever probe mainly works in two basic ways, contact mode and non-contact mode. In contact mode, the probe is connected to the sample surface and it interacts to the sample following Van der Waal's force. The non-contact mode, a piezoelectric crystal driven by an applied electric field of frequency in the range between 10 kHz to 1 MHz. This crystal mechanically oscillates the cantilever probe near tis resonance frequency close to the sample surface. The oscillation frequency varies based on the probe's contact with the sample surface. As seen in Figure 2.9, the movement of the cantilever is monitored using a laser light. The laser light incident on the cantilever moves depending on the movement of the cantilever. This is detected using photodetector to map the movement of the cantilever and determine the surface image.

2.3.2 ELECTRICAL PROPERTIES MEASUREMENT TECHNIQUES

2.3.2.1 DIELECTRIC MEASUREMENT

An Impedance analyser or an LCR meter (Inductance (L), Capacitance (C), and Resistance (R)) is very widely used equipment needed to measure the capacitance, inductance and resistance of a sample. In this method, the inductance and capacitance of the material is not measured directly, instead the impedance is measured and converted into corresponding inductance and capacitance values. LCR meter is used measure impedance parameters at wide range of frequencies along with the equivalent series resistance, capacitance etc. and the Q factor of inductive sample.

The dielectric constant (ε) of a sample is calculated assuming a parallel plate capacitor setup, using the formula,

$$\varepsilon = \frac{Cd}{A\varepsilon_0} \tag{2.3}$$

Where C is the capacitance of the sample in Farad (F), d is the thickness of the sample in meter (m), A is the area of the electrode in square meter (m^2), ε_0 is the free space permittivity (8.854×10^{-12} F/m), and ε is the dielectric constant or relative permittivity of the sample.

As shown in Figure 2.9, the sample or the device under test (DUT) is subjected to an *ac* voltage using the function generator. The analyser then measures the voltage across the DUT and the current through the DUT. The impedance is measured from the ratio of the measured voltage and current. The phase angle of voltage and current is calculated from the equivalent inductance or capacitance and the resistance of the sample.

2.3.2.2 FERROELECTRIC HYSTERESIS LOOP TRACER

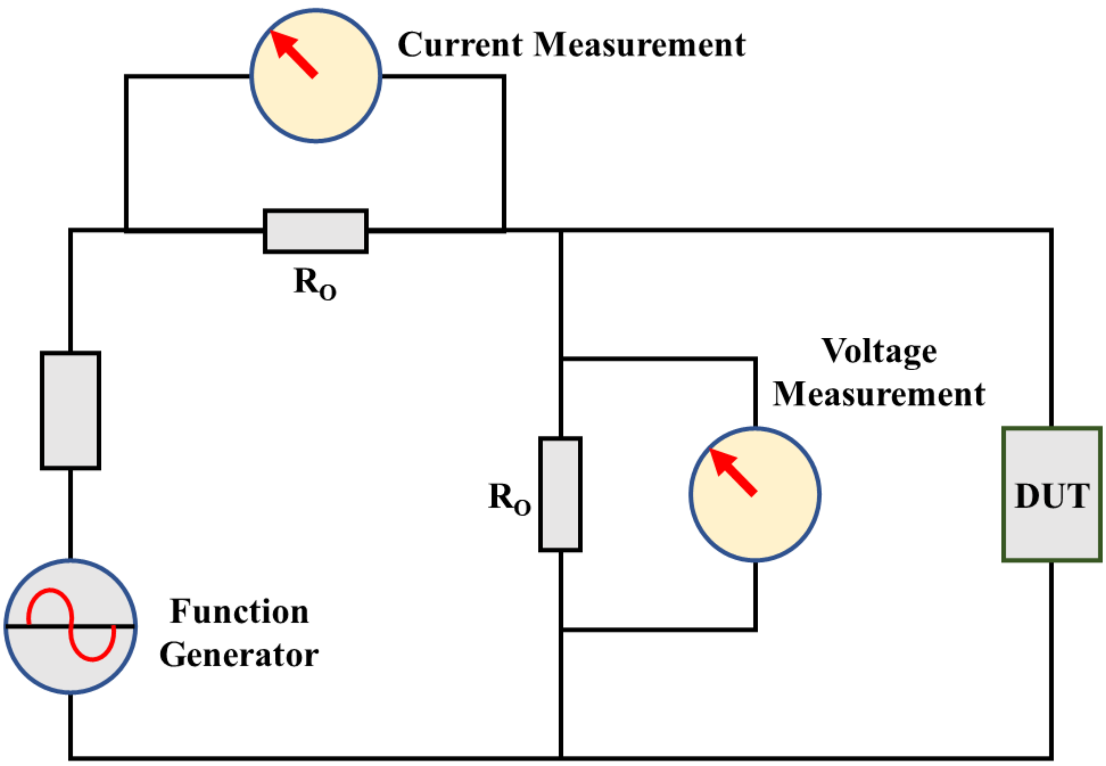

Figure 2.9 Schematic diagram of an LCR meter used to measure dielectric properties

The Polarization (P) vs. Electric Field (E) hysteresis loop is measured based on Sawyer-Tower circuit as shown in Figure 2.10[15]. In this method, a voltage is applied across the sample with capacitance, and the voltage is measured across a reference capacitor. If the capacitance across the reference is much larger than that of the sample, then the voltage drop across the sample is very small such that the input and output voltage is similar. The electric field is calculated using this input voltage according to the following formula,

$$E = \frac{V_{in}}{t} \tag{2.4}$$

Where, E is the electric field, t is the sample thickness and V_{in} is the input voltage generated from the function generator.

To construct the ferroelectric P-E hysteresis loop, the voltage across the reference capacitor is measured (V_{out}) and polarization is measured using following formula,

$$Q = \frac{V_{out}}{C_{ref}} \tag{2.5}$$

$$P = \frac{Q}{A} \tag{2.6}$$

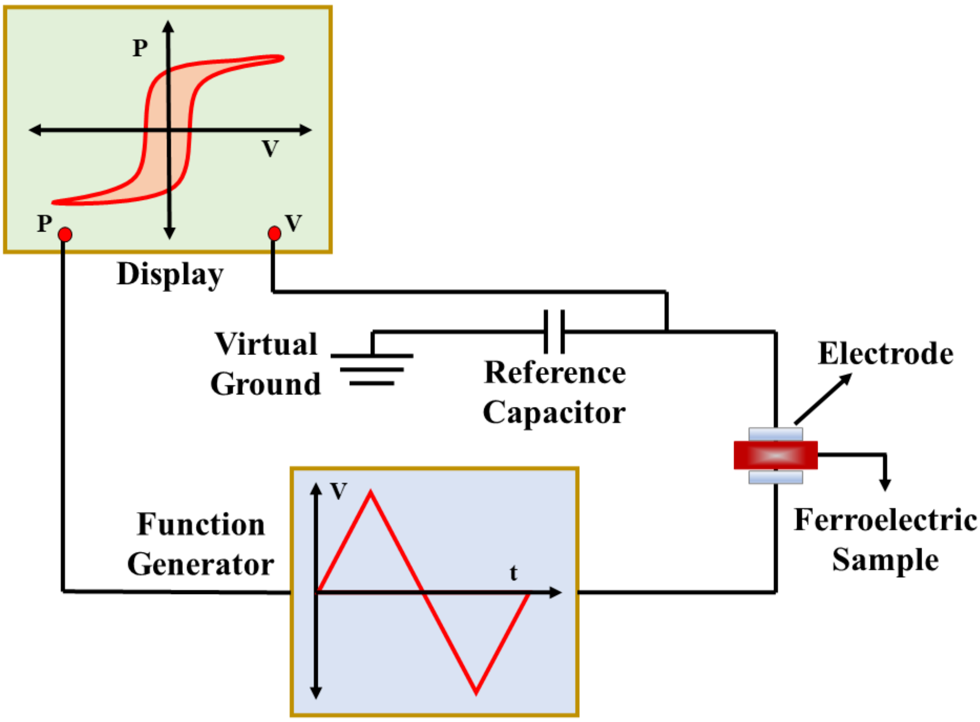

Figure 2.10 Schematic diagram of a Ferroelectric Measurement System

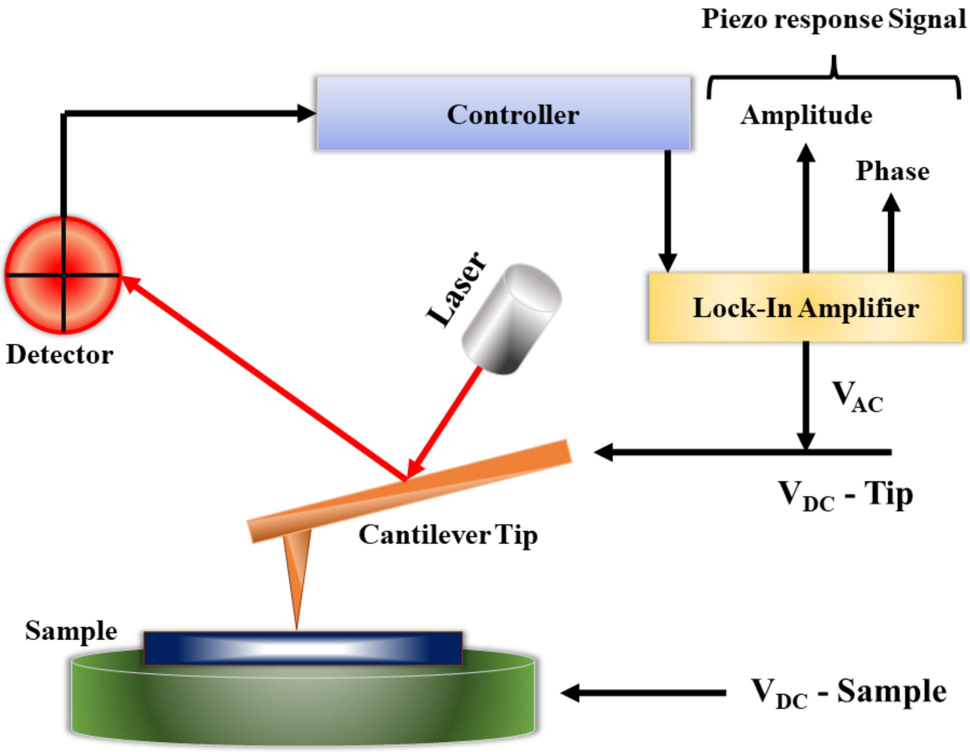

Figure 2.11 Schematic diagram of a piezo response force microscope

Where, Q is the charge, A is the area of the electrode, and P is the electric polarization.

For an ideal resistor, the current and the voltage are in same phase, which gives a circular PE loop. On the other hand, the P-E loop of a capacitor is a straight line as the current and voltage are in out-of-phase condition.

2.3.2.3 PIEZORESPONSE FORCE MICROSCOPY (PFM)

Piezoresponse force microscope (PFM) is used to understand the topography and piezoelectric/ferroelectric domain structure at nanoscale[16–18]. In this method, the cantilever tip is coated with highly conducting material such as platinum, gold, tungsten etc. is brought in contact to the surface of a ferroelectric or piezoelectric material. As *ac* bias is applied to the tip, deformation is generated in the material through converse piezoelectric effect (CPE). As a result, the cantilever deflects which is recorded through standard photodiode detector. The schematic diagram of a PFM set up is shown in Figure 2.11.

2.3.3 MAGNETIC MEASUREMENT TECHNIQUES

2.3.3.1 VIBRATING SAMPLE MAGNETOMETER (VSM)

Vibrating sample magnetometer (VSM) is widely used to measure magnetic properties of materials[19,20]. It can measure incredibly small magnetic moment up to an order of 10^{-5}

emu. First, the sample is placed in a constant magnetic field (H). Next the sample is vibrated sinusoidally such that the resulting variation of magnetic flux induces the pickup coils. Following Faraday's law of induction, an electromotive force (EMF) is generated across the pickup coils having N identical loops and a cross-sectional area of A. The EMF is given by,

$$V = -NA\frac{dB}{dt} \tag{2.7}$$

If the coil is placed in a constant magnetic field (H), the magnetic flux (B) is given by,

$$B = \mu_0 H \tag{2.8}$$

Where μ_0 is the free space permeability.

If the sample possess a magnetization of M, then the magnetic flux around the vibrating sample is,

$$B = \mu_0(H + M) \tag{2.9}$$

Therefore, the change in magnetic flux due to the presence of the sample is,

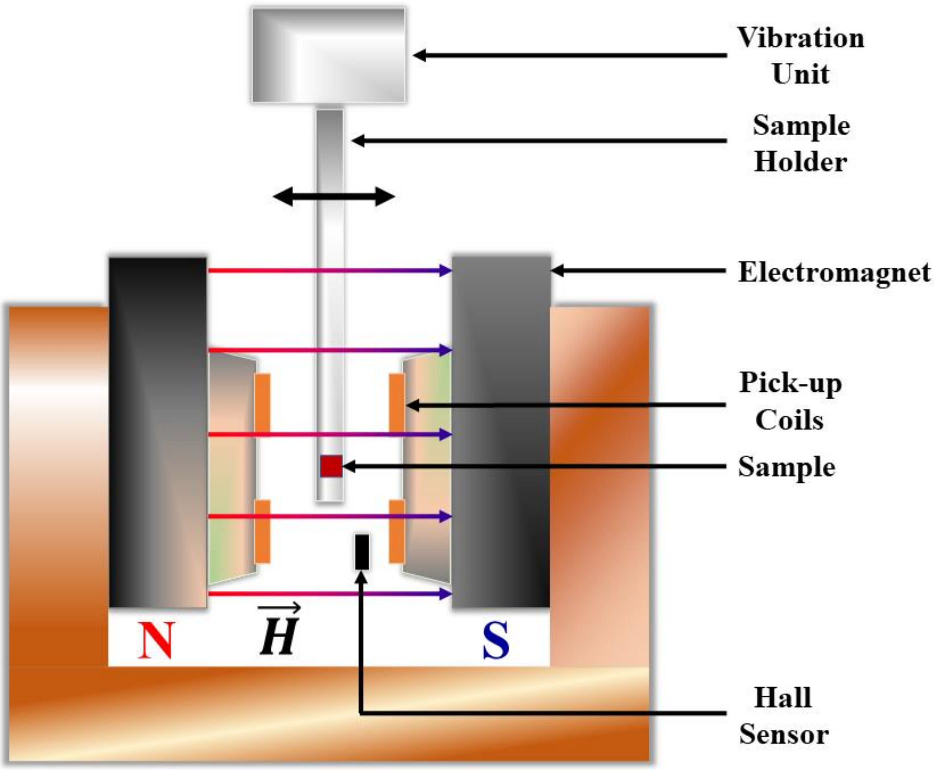

Figure 2.12 Schematic diagram of a vibrating sample magnetometer unit

$$\Delta B = \mu_0 M \tag{2.10}$$

The induced force on the pick-up coil is therefore given by,

$$Vdt = -\mu_0 NAM \tag{2.11}$$

This output signal is recorded and used to calculate the magnetic moment of the sample.

The schematic diagram of a VSM unit is shown in Figure 2.12. The parts that are used in VSM are,

Water cooled electromagnet and power supply: The water-cooled electromagnet, along with the power supply, are used to generate the constant magnetic field to magnetize the sample.

Vibration unit and sample holder: The sample holder rod is attached to the vibration exciter, and the end of it is placed at the central region between the electromagnets. The vibration unit moves the sample up and down at a particular frequency.

Pick-up coils: The EMF force produced by the vibrating sample generates an alternating current in the pick-up coils at the same frequency as the vibrating frequency of the sample. The signal generated contains the information about the magnetization of the sample.

A part of the magnetic readings provided in this dissertation are investigated with the use of a vibrating sample magnetometer (VSM, Lakeshore, model 7144). The model generates a maximum of 1.6 T magnetic field. The low temperature measurement (moment versus temperature and isothermal hysteresis loops) can be performed within the temperature range from 80 K to 400 K using a cryogenic system (Liquid N_2) and the high temperature measurement can be performed within the temperature range of 300 K to 1173 K with a temperature stability of ± 0.2 K and temperature resolution of 0.001 K. In needs, a Physical Property Measurement System (PPMS) from Quantum Design, model – DYNACOOL is used. In this system, the magnetic field can be extended up to 14 T. The low temperature measurement can be performed for a temperature range of 1.8 K to 400 K whereas the high temperature measurement can be done for a temperature range of 300 K to 1000 K.

2.3.3.2 MAGNETIC FORCE MICROSCOPY (MFM)

Magnetic force microscope is an essential tool to know the magnetic domain structure of a sample. In this method, a cantilever coated with small coercive magnetic material such as Ni, Co etc., is used to probe the sample surface[21]. The schematic diagram of a MFM system is shown in Figure 2.13.

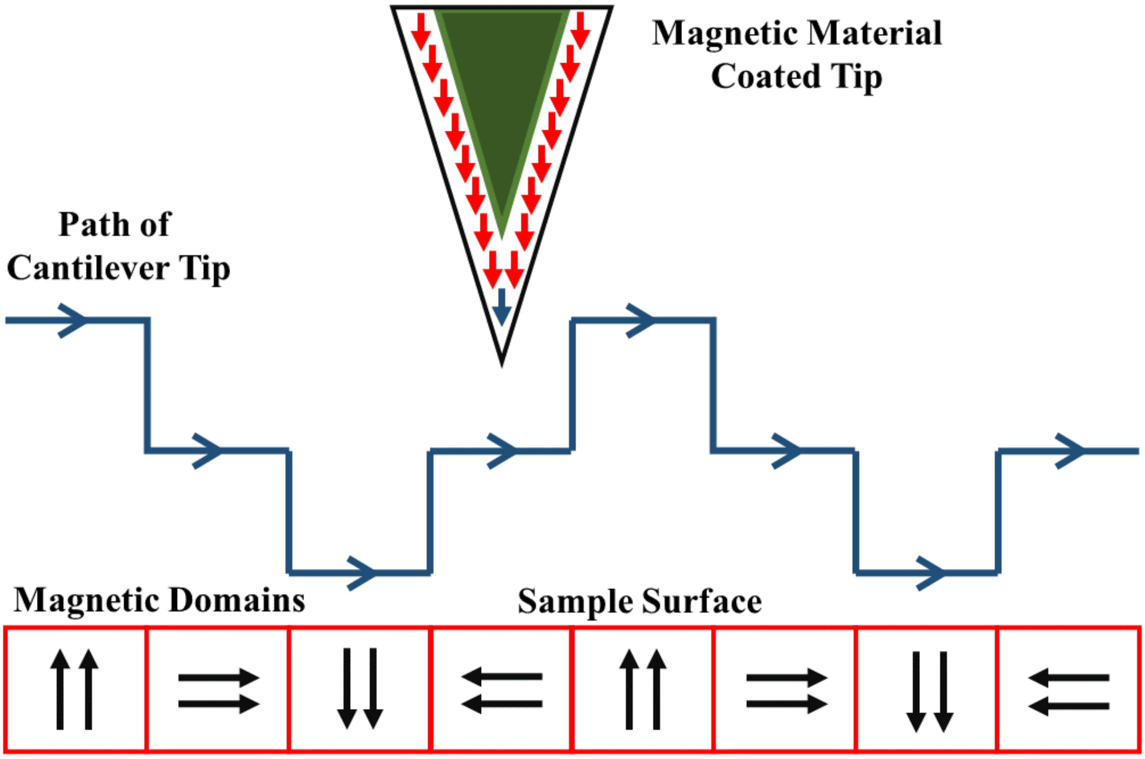

Figure 2.13 Schematic diagram of magnetic force microscope

Here the coercivity of the magnetic material is chosen to be very low as the tip is magnetised and the does not change throughout the measurement. The magnetic tip only interacts with the out-of-plane component of the magnetic domains. In this method, the 1-dimensional scanning of the cantilever is recorded twice. At first step the topographical image is recorded using the AFM tapping mode and at second step, this information of at what distance the cantilever should be kept is used to keep the cantilever at certain distance during MFM image capture. The distance of the cantilever is known as "Lift Height" and can be modified if needed. Typical resolution can be achieved when Lift Height is about 30 nm, although resolutions as low as 10 to 20 nm are attainable. During scanning the magnetic tip is deflected according to the direction of stray field of the material creating the dark and bright spots.

2.3.4 MICROWAVE MEASUREMENT TECHNIQUE - VECTOR NETWORK ANALYZER

In the context of measuring the parameters of electrical networks, the vector network analyser (VNA) is indispensable because it measures both amplitude and phase properties. Reflection and transmission of electrical networks are simple and accurate to measure at high frequencies, so S-parameters are typically measured by network analysers. VNAs can be used on networks with any number of ports, but this article will only discuss a two-port network system[22]. The VNA, which is an automatic network analyser, is widely utilized for radio frequency (RF) and microwave design applications and characterizations for both passive and active networks in terms of network scattering parameters, i.e., S parameters.

A simplified block diagram of a vector network analyser is shown in the accompanying figure, Figure 2.14. This diagram illustrates the fundamental components of a typical 2-port VNA. Port 1 (P1) and port 2 (P2) represent the two ports of the device under test (DUT). PC1 and PC2 are the precision cables which are connected to the P1 and P2 ports of the VNA, respectively. The RF test frequency is generated by a variable-frequency source, and its power level is controlled by a variable attenuator. The orientation of the switch SW1 determines the path of the test signal through the DUT. Consider initially that SW1 is in position 1, so that the test signal is incident at P1 on the DUT, which is suitable for measuring S11 and S21. The test signal is connected to the common port of splitter 1, with the reference

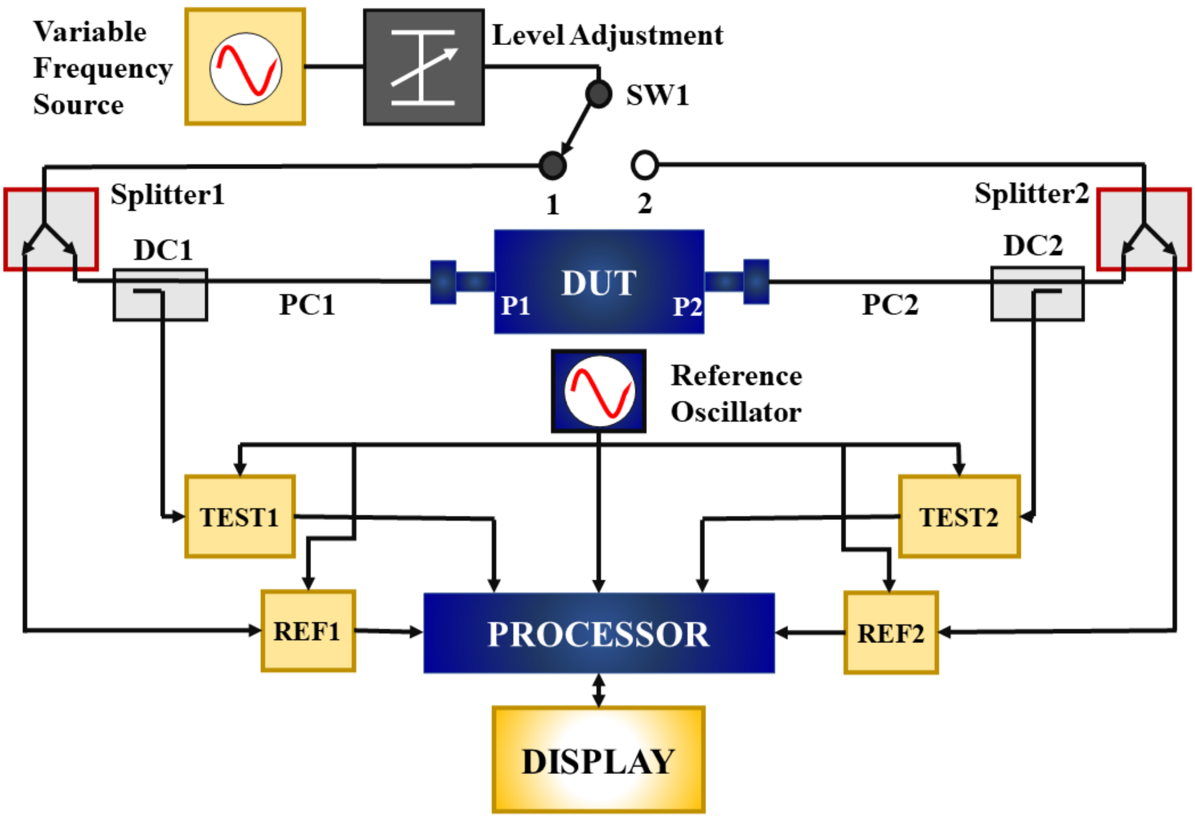

Figure 2.14 Simplified schematic presentation of a vector network analyzer

channel feeding a reference receiver for P1 (REF1) and the test channel connecting to P1 via directional coupler DC1 and cable PC1. The third port of DC1 couples the power reflected from P1 via PC1 to the test receiver 1 (TEST1). Likewise, signals leaving P2 are routed via PC2 and DC2 before reaching TEST2. REF1, TEST1, REF2, and TEST2 are referred to as coherent receivers because they share the same reference oscillator and can measure the amplitude and phase of a test signal at a specific frequency. All complex receiver output signals are fed to a processor, which performs the necessary mathematical operations and displays the selected parameters and format. Despite the fact that the instantaneous value of phase includes both temporal and spatial com ponents, the former is eliminated by using two test channels, one as a reference and the other for measurement. This instrument can readily determine quantities such as standing wave ratio (SWR), return loss, group delay, impedance, etc., and it can also determine the time-domain response of the network. Figure 2.15 depicts the setup for measuring microwave properties in our lab, including all of the necessary equipment. A calibration procedure corrects errors caused by mismatched directional couplers, imperfect directivity, cable loss, and variations in the frequency response of the

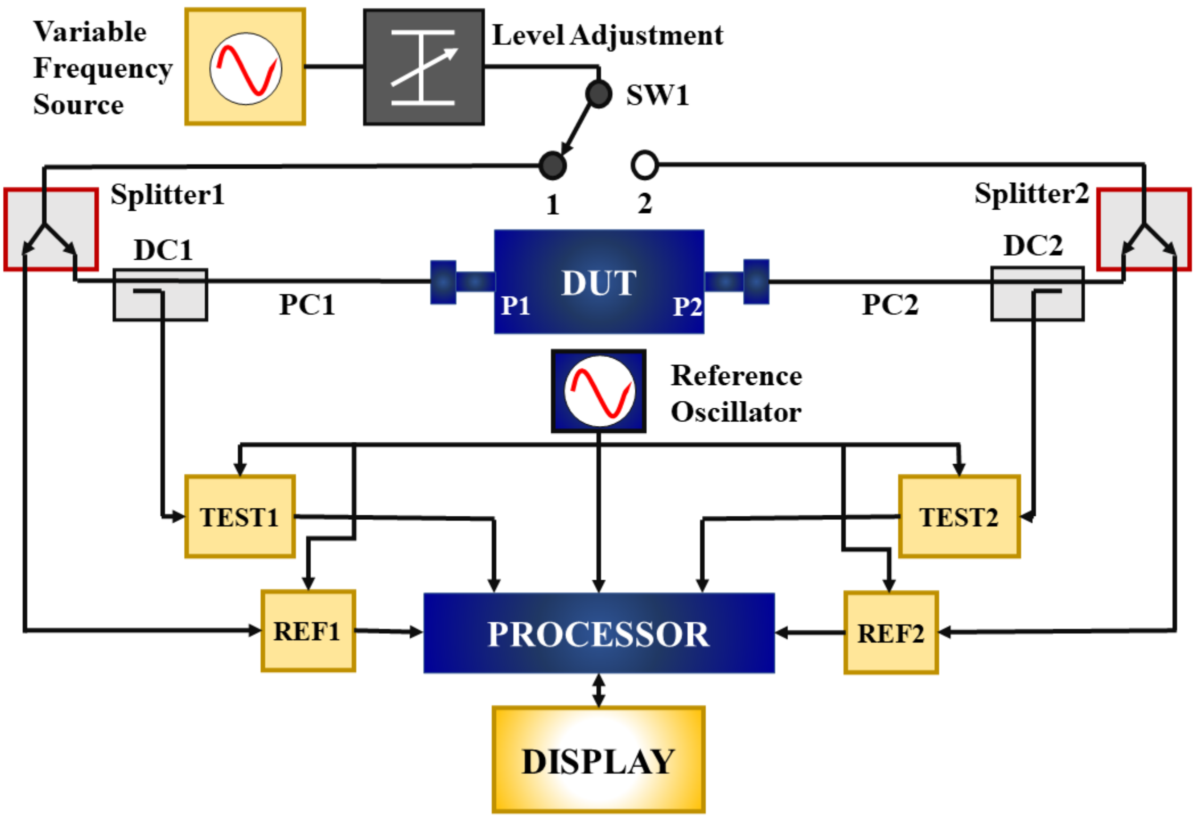

Figure 2.15 Microwave properties measurement set-up in our laboratory

analyser system. The simplest for this purpose is SOLT, which stands for Short, Open, Load, and Through. Modern network analysers store device-related information in a calibration kit.

REFERENCES

[1] C.N. Afonso, J. Gonzalo, R. Serna, J. Solis, Chapter 13 PULSED LASER DEPOSITION FOR FUNCTIONAL OPTICAL FILMS, n.d.

[2] G.Z. Liu, Q.Y. Lei, X.X. Xi, Stoichiometry of SrTiO 3 films grown by pulsed laser deposition, Appl Phys Lett. 100 (2012). https://doi.org/10.1063/1.4717984.

[3] B.D. (Bernard D. Cullity, Elements of x-ray diffraction, Addison-Wesley Publishing Company, Inc, 1978.

[4] A. Hewat, W.I.F. David, L. van Eijck, Hugo Rietveld (1932–2016), J Appl Crystallogr. 49 (2016) 1394–1395. https://doi.org/10.1107/S1600576716012061.

[5] H.M. Rietveld, A profile refinement method for nuclear and magnetic structures, J Appl Crystallogr. 2 (1969) 65–71. https://doi.org/10.1107/S0021889869006558.

[6] D.J. Gardiner, Introduction to Raman Scattering, in: D.J. Gardiner, P.R. Graves (Eds.), Practical Raman Spectroscopy, Springer Berlin Heidelberg, Berlin, Heidelberg, 1989: pp. 1–12. https://doi.org/10.1007/978-3-642-74040-4_1.

[7] Classical Theory of Rayleigh and Raman Scattering, in: The Raman Effect, 2002: pp. 31–48. https://doi.org/https://doi.org/10.1002/0470845767.ch3.

[8] Quantum Mechanical Theory of Rayleigh and Raman Scattering, in: The Raman Effect, 2002: pp. 49–84. https://doi.org/https://doi.org/10.1002/0470845767.ch4.

[9] K. Akhtar, S.A. Khan, S.B. Khan, A.M. Asiri, Scanning Electron Microscopy: Principle and Applications in Nanomaterials Characterization, in: S.K. Sharma (Ed.), Handbook of Materials Characterization, Springer International Publishing, Cham, 2018: pp. 113–145. https://doi.org/10.1007/978-3-319-92955-2_4.

[10] M. Abd Mutalib, M.A. Rahman, M.H.D. Othman, A.F. Ismail, J. Jaafar, Chapter 9 - Scanning Electron Microscopy (SEM) and Energy-Dispersive X-Ray (EDX) Spectroscopy, in: N. Hilal, A.F. Ismail, T. Matsuura, D. Oatley-Radcliffe (Eds.), Membrane Characterization, Elsevier, 2017: pp. 161–179. https://doi.org/https://doi.org/10.1016/B978-0-444-63776-5.00009-7.

[11] B. Fultz, J.M. Howe, eds., The TEM and its Optics, in: Transmission Electron Microscopy and Diffractometry of Materials, Springer Berlin Heidelberg, Berlin, Heidelberg, 2008: pp. 61–118. https://doi.org/10.1007/978-3-540-73886-2_2.

[12] B. Fultz, J.M. Howe, eds., High-Resolution TEM Imaging, in: Transmission Electron Microscopy and Diffractometry of Materials, Springer Berlin Heidelberg, Berlin, Heidelberg, 2008: pp. 517–582. https://doi.org/10.1007/978-3-540-73886-2_10.

[13] F.J. Giessibl, Advances in atomic force microscopy, Rev Mod Phys. 75 (2003) 949–983. https://doi.org/10.1103/RevModPhys.75.949.

[14] G. Binnig, C.F. Quate, Ch. Gerber, Atomic Force Microscope, Phys Rev Lett. 56 (1986) 930–933. https://doi.org/10.1103/PhysRevLett.56.930.

[15] R. Andika, L.O. Husein Zilullah Toresano, M. Hikam, B. Soegijono, A. Sudarmaji, The Electrical Hysteresis Loop and Polarization Value of BaZrxTi1-xO3 Multilayer Films Material at Different Annealing Temperature (x = 0.1 and 0.08) based on Sawyer Tower Circuit, 2014. https://doi.org/10.13140/RG.2.1.2911.1526.

[16] S. v Kalinin, A.N. Morozovska, L.Q. Chen, B.J. Rodriguez, Local polarization dynamics in ferroelectric materials, Reports on Progress in Physics. 73 (2010) 056502. https://doi.org/10.1088/0034-4885/73/5/056502.

[17] P. Güthner, K. Dransfeld, Local poling of ferroelectric polymers by scanning force microscopy, Appl Phys Lett. 61 (1992) 1137–1139. https://doi.org/10.1063/1.107693.

[18] S. v Kalinin, B.J. Rodriguez, S. Jesse, J. Shin, A.P. Baddorf, P. Gupta, H. Jain, D.B. Williams, A. Gruverman, Vector Piezoresponse Force Microscopy, Microscopy and Microanalysis. 12 (2006) 206–220. https://doi.org/DOI: 10.1017/S1431927606060156.

[19] V. Lopez-Dominguez, A. Quesada, J.C. Guzmán-Mínguez, L. Moreno, M. Lere, J. Spottorno, F. Giacomone, J.F. Fernández, A. Hernando, M.A. García, A simple vibrating sample magnetometer for macroscopic samples, Review of Scientific Instruments. 89 (2018) 034707. https://doi.org/10.1063/1.5017708.

[20] W. Burgei, M.J. Pechan, H. Jaeger, A simple vibrating sample magnetometer for use in a materials physics course, Am J Phys. 71 (2003) 825–828. https://doi.org/10.1119/1.1572149.

[21] U. Hartmann, MAGNETIC FORCE MICROSCOPY, Annual Review of Materials Science. 29 (1999) 53–87. https://doi.org/10.1146/annurev.matsci.29.1.53.

[22] D.M. Pozar, J. Wiley, Microwave Engineering Third Edition W WILEY, n.d.

CHAPTER 3

EFFECT OF BARIUM AND YTTRIUM CO-DOPING AT BISMUTH SITE OF BISMUTH FERRITE

This chapter discusses the effect of Barium and Yttrium co-doping at the Bismuth site of single-phase Bismuth Ferrite on electric and magnetic properties. The effect of the same on different morphologies such as bulk, nanoparticle, and thin film are also explored and discussed in this chapter.

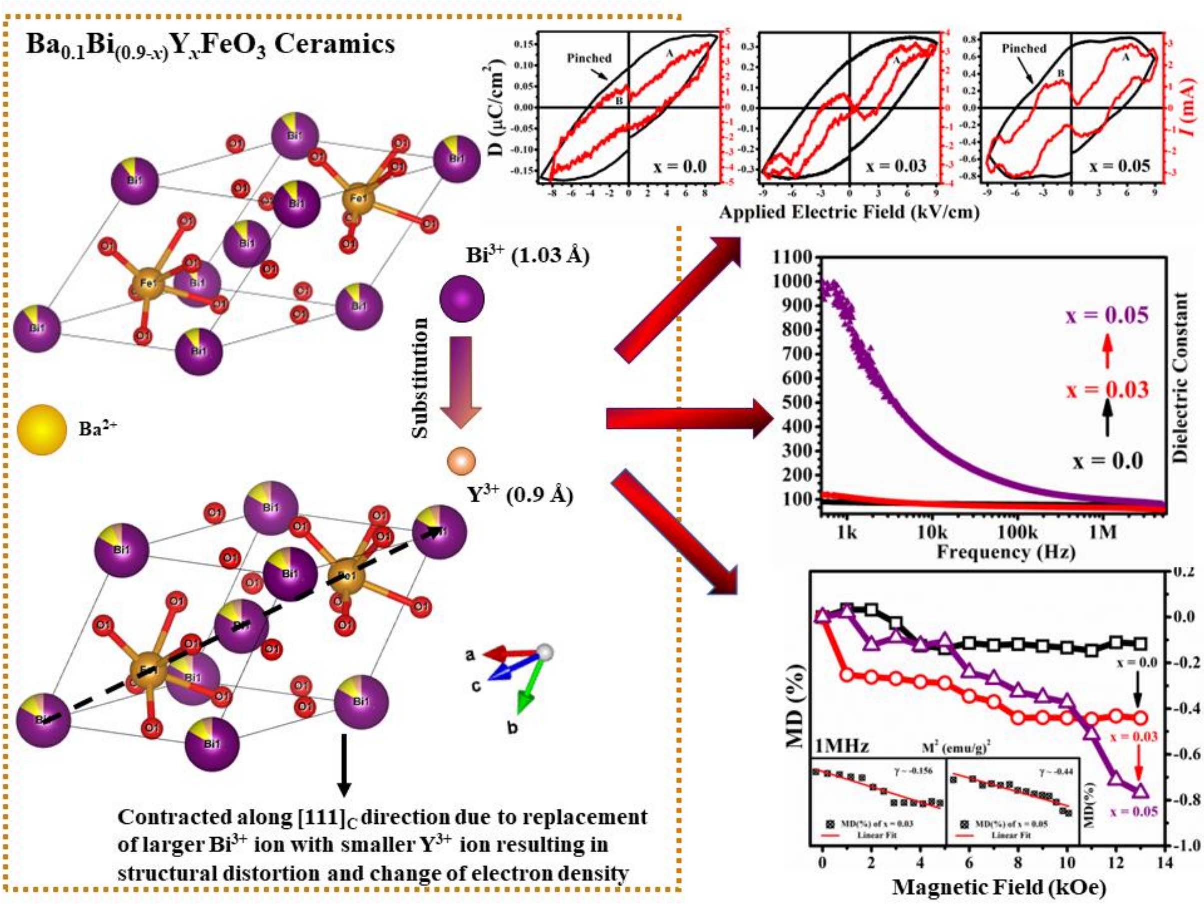

3.1 PREAMBLE

Bismuth Ferrite or $BiFeO_3$ (BFO) exhibits magnetoelectric coupling at room temperature and has a high degree of ferroelectric polarisation, both of which are crucial for its practical use. However, the material's large conductivity and weak magnetism prohibit it from being used for its wide range of applications. A variety of treatments, including changing the synthesis temperature and time, the atmospheric conditions during synthesis, the morphology, etc., have been investigated in an effort to address the shortcomings[1–12]. It has been observed that doping $BiFeO_3$ with the appropriate elements at either the Bi- or Fe-site increases the ferroelectricity and ferromagnetism while decreasing leakage current and conductivity[13–28]. Doping with aliovalent and isovalent elements also offers a lot of information about the carriers in charge of the material's low *dc* resistivity. Understanding the governing carriers makes it easier to manipulate them and increase BFO's *dc* resistivity, which in turn improves its ferroelectric behaviour.

The possible mechanisms of conduction that has been proposed over the years, mainly are,

$$O_O^X \rightarrow \frac{1}{2}O_2 + V_O^{\blacksquare\blacksquare} + 2e' \tag{3.1}$$

$$Bi_{Bi}^X + 3e' \rightarrow Bi_{(g)} + V_{Bi}''' \tag{3.2}$$

$$Fe_{Fe}^X + e' \rightarrow Fe_{Fe}' \tag{3.3}$$

For instance, Qi et al.[29] discovered that partial substitution of Fe^{3+} ions with Ti^{4+} ions increased the material's *dc* resistivity while partial substitution with Ni^{2+} did the opposite, leading them to the conclusion that oxygen vacancies, as per Eq. 3.1, were the governing charge carriers. Formation of bismuth vacancies are one very common phenomenon during the synthesis of BFO due to volatile nature of bismuth according to the mechanism shown in Eq. 3.2[30,31]. In contrast, Dai et al.[32] investigated the formation of BFO under various sintering atmospheres and found that the sample with the highest oxygen vacancies but the lowest Fe^{2+} concentration exhibited the highest resistivity, drawing the conclusion that electrons, not holes, were the primary charge carriers controlling the material's overall conductivity (Eq. 3.3).

It is discovered that isovalent substitution at the Bi-site of BFO is able to lower the non-stoichiometry by the reduction of the concentration of volatile Bi^{3+} ions, despite the fact that aliovalent substitution is observed to increase the resistivity[20,23,29,30,33–36]. As a result, secondary phase production is decreased, *dc* resistivity is increased, and the material's ferroelectric behaviour is subsequently improved. Because non-volatile Y^{3+} ions replace volatile Bi^{3+} ions at the Bi-site of the BFO, it is seen that resistivity steadily rises while secondary phase formation decreases. The material's conduction mechanism can be changed from oxygen vacancies to an electron-dominant one by yttrium doping. Due to structural deformation and a change in the Fe-O-Fe bond angles brought on by the size differences between the Bi^{3+} and Y^{3+} ions, it has been shown that both polarisation and magnetization have increased[30]. In contrast, the neighbouring Fe^{3+} ions in a BFO with a G-type antiferromagnetic structure should align antiparallel to each other. However, in BFO, these spins are not perfectly antiparallel to one another and are slightly canted in the direction of one another, which results in a weak ferromagnetism[37]. The macroscopic magnetism in the bulk form is nevertheless cancelled out by the presence of another long-range spiral structure with a period of 62 nm, which is created as a result of the Dzyaloshinkii-Moriya (DM) interaction. To suppress this spiral structure and improve the magnetoelectric characteristics of BFO, doping with promising elements at the Bi-site or Fe-site is discovered to be very successful. For instance, it has been demonstrated that doping BFO ceramics with alkali and rare-earth elements enhances their ferroelectric and ferromagnetic characteristics[15,38,39]. It has been observed that Fe-site doping with Cr, Mn, Ti, and Co increases the magnetization by suppressing the spin spiral structure. Single-phase Ba-doped BFO ceramics have been found to have enhanced magnetic properties[40–42].

As a result of charge compensation, according to Eq. 3.5, optimum doping of BFO with Ba^{2+} causes the creation of Fe^{4+} ions inducing ferrimagnetic nature in the material[15,43–46],

$$\frac{1}{2}(1-x)Bi_2O_3 + xAO + \frac{1}{2}Fe_2O_3 \rightarrow Bi_{1-x}^{3+}A_x^{2+}Fe^{3+}O_{3-\frac{x}{2}}^{2-} \tag{3.4}$$

$$\frac{1}{2}(1-x)Bi_2O_3 + xAO + \frac{1}{2}Fe_2O_3 \rightarrow Bi_{1-x}^{3+}A_x^{2+}Fe_{1-x}^{3+}Fe_x^{4+}O_3^{2-} \tag{3.5}$$

In order to create a single-phase material with high resistivity, high polarisation, and high magnetization, yttrium and barium are co-doped at the Bi-site of BFO. Initially, the effect of yttrium and barium co-doping on the electric and magnetic properties of bulk form of bismuth ferrite ($Ba_{0.1}Bi_{0.9-x}Y_xFeO_3$) at yttrium doping concentrations of x = 0.1 and 0.2 is investigated. Nonetheless, both co-doped samples exhibit first order field-induced metamagnetic transition near a 0.73 T critical field, which is a fundamental flaw of these samples. As previously established, the antiferromagnetic to ferromagnetic phase change, known as the metamagnetic transition, is caused by ferromagnetic (FM) pinning in the antiferromagnetic (AFM) superlattice. At and above critical pinning fields, the pinned ferromagnetic sublattice in the antiferromagnetic matrix of the particles begins to align and grow rapidly, resulting in metamagnetic transition[47]. The antiferromagnetic interaction, however, is seen to decrease as particle size decreases, and weak ferromagnetism is introduced while decreasing AFM-FM competition and consequently metamagnetic transition. Similar observation is found in size-dependent study of metamagnetic transition in Ba doped BFO nanoparticles[6]. Henceforth, in order to eliminate the observed metamagnetic transition, the same co-doped samples are prepared in nano-structural forms. It is observed that the magnetic characteristics obtained for the corresponding nanoparticles do not display any metamagnetic transition, in contrast to their bulk counterpart, which does. In contrast to their bulk counterparts, the barium and yttrium co-doped $BiFeO_3$ nanoparticles exhibit stronger ferromagnetism at the nanoscale due to uncompensated spins at the surface and a significant surface to volume ratio, which disrupts long-range anti-ferromagnetic order at surfaces. As a result, the residual magnetization of these nanoparticles is considerably greater than that of their bulk counterparts. However, a structural phase transition is observed from rhombohedral to orthorhombic structure for 10 at. wt.% yttrium doping ($Ba_{0.1}Bi_{0.8}Y_{0.1}FeO_3$) in nano-structural form unlike their bulk counterpart and is attributed to the changing phase stabilities due to large surface to volume ratio in nano-structural form. Therefore, the doping concentration of yttrium is decreased from x = 0.1 to x = 0.03 and 0.05 in $Ba_{0.1}Bi_{0.9-x}Y_xFeO_3$ nanoparticles. The magnetic, ferroelectric, and magnetodielectric properties of these co-doped nanoparticles are examined in detail in order to obtain a single-phase material in rhombohedral structure. As discussed in section 1.5.2 of chapter 1 in this thesis, 2D thin film structure is crucial for the practical applications of magnetoelectric materials, as nano-structured thin films allow for additional degrees of freedom and an increase lattice strain, thereby enhancing the magnetoelectric (ME) effect. To examine this, the 5 at. wt.% yttrium doped sample, $Ba_{0.1}Bi_{0.85}Y_{0.05}FeO_3$, which is observed to possess highest dielectric constant, remnant polarization, and magnetodielectric factor with stronger ferroelectric domain switching is taken to fabricate thin film deposited on $SrTiO_3$ (111) substrate using Pulsed Laser Deposition method in order to enhance its magnetoelectric properties.

3.2 EXPERIMENTAL DETAILS

3.2.1 SYNTHESIS

3.2.1.1 BULK

The tartaric acid-assisted sol-gel process is used to synthesize the $Ba_yBi_{1-x-y}Y_xFeO_3$ ceramics for x = 0.0 (BaBYFO-0-Bulk), 0.1 (BaBYFO-10-Bulk), and 0.2 (BaBYFO-20-Bulk) at y = 0.1. In the presence of nitric acid, high purity (more than 99.9%) $Bi(NO_3)_3.5H_2O$, $Fe(NO_3)_3.9H_2O$, $Ba(NO_3)_2.H_2O$, and $Y(NO_3)_3.6H_2O$ is dissolved in double distilled water in the appropriate stoichiometric ratios. As a chelating agent, tartaric acid ($C_6H_6O_7$) is added to the nitrates to finish their combustion. The 3 hour-long vigorous stirring of the yellow, transparent solution is followed by keeping it at 80 °C until it is completely dried. After that, the fluffy dried powder is gathered and grinded in an agate mortar. To produce the required phase, the powders are calcined at 600 °C for two hours. The resultant material is then compressed into pellets with dimensions of 5 mm in diameter and 0.7 mm in thickness. These pellets are then further annealed for 30 minutes at a temperature of 700 °C to produce the bulk form. Using these pellets, all of the typical measurements have been performed.

3.2.1.2 NANOPARTICLE

By modifying the sol gel process with tartaric acid and utilising analytical-grade chemical reagents (Sigma-Aldrich, > 99.9%), Ba and Y co-doped $BiFeO_3$ nanoparticles are synthesized. In water, all the nitrates are dissolved in their respective stoichiometric ratios with the help of dilute HNO_3, while being constantly stirred. The tartaric acid ($C_6H_6O_7$) is then added as a chelating agent to ensure complete combustion of the nitrates. Over a hot plate maintained at 80 ºC, the yellow translucent solution is vigorously agitated at 500 rpm for 24 hours. The fluffy dried powder is then grinded and sintered for 30 minutes at 700 ºC in air. $Ba_{0.1}Bi_{0.9-x}Y_xFeO_3$ nanoparticles for x = 0.0 (BaBYFO-0), 0.03 (BaBYFO-3), 0.05 (BaBYFO-5), and 0.1 (BaBYFO-10) are synthesized under the same experimental circumstances by adding various amounts of $Y(NO_3)_3.6H_2O$.

3.2.1.3 THIN FILM

Using the pulsed laser deposition (PLD) approach in oxygen atmospheres with the KrF excimer laser, $BiFeO_3$ (BFO) and $Ba_{0.1}Bi_{0.85}Y_{0.05}FeO_3$ (BaBYFO) thin films are formed on Nb doped $SrTiO_3$ (111) substrates at 700 ºC. With a fluence of 2 $J.cm^{-2}$ and oxygen pressures of 0.06 mbar, the thin films are formed at a repetition rate of 5 Hz. The polycrystalline $BiFeO_3$ and $Ba_{0.1}Bi_{0.85}Y_{0.05}FeO_3$ powders, which is produced via the sol-gel process, is used to prepare the PLD targets. In a nutshell, the initial reagents are $Bi(NO_3)_3.5H_2O$, $Fe(NO_3)_3.9H_2O$, $Ba(NO_3)_2.H_2O$, and $Y(NO_3)_3.6H_2O$ which are then successively dissolved in double distilled water with their stoichiometric ratios in presence of Nitric acid (HNO_3). The solution is stirred while a suitable amount of tartaric acid is added, and the molar ratio of citric acid to the metal components in the solution is 1:1. The mixture is stirred for 30 minutes to achieve homogeneity and then heated at temperature of 80 ºC until completely dried. The dried powder is grinded, and calcined several times at different temperatures (600 ºC – 1000 ºC) for 12 hours each. To utilise as the PLD target, the powders are transformed into pellets, and the final calcination is performed at 1000 ºC for 12 hours.

3.2.2 CHARACTERIZATION

By recording X-ray diffraction (XRD) at room temperature using a Panalytical X'Pert Pro diffractometer and utilising the Cu-Kα radiation (λ = 1.54 Å) at a scanning rate of 0.6° per minute in the 2θ range of 20° - 90°, the phase and structure of the bulk and nanoparticles are examined. The FullProf Rietveld refinement software is used to analyse the XRD data, and VESTA (Visualisation for Electronic Structural Analysis) is used to visualise the refined data. High-resolution transmission electron microscopy (HRTEM) using a FEG HRTEM (80-200 kV) and an FEI QUANTA FEG250 scanning electron microscope (SEM) with an AMETEK EDAX QUANTA 200 and Element attachment are used to study the size of the nanoparticles and elemental analysis. A spectrometer from LabRam HR Evolution; HORIBA France SAS-532 nm laser is used to capture Raman spectra of the nanoparticles. The Precision Premier II, Precision Materials Analyzer is used to perform the room temperature ferroelectric measurements (Radiant Technologies Inc.) for both bulk and nanoparticles. Using a vibrating sample magnetometer, the field-dependent magnetization at room temperature is investigated (Lakeshore VSM) for all samples including the thin film. The temperature and frequency dependency of the dielectric characteristics of these samples are measured for a frequency range of 500 Hz to 1 MHz and a temperature range of 25 °C to 300 °C using an LCR meter (NF Corporation LCR Meter ZM2376) for the bulk and nanoparticle samples. Atomic force microscopy (AFM), manufactured by Innova, Bruker is used to examine the surface morphology of the thin films. Magnetic force microscopy (MFM) has also been performed to understand the magnetic characteristics of the thin films. Using NanoDrive v8 real-time control & NanoScope Analysis, the piezo-response force microscopy (PFM) data are acquired for the thin films to investigate the ferroelectric properties.

3.3 RESUTLS AND DISCUSSION

3.3.1 STRUCTURE AND MORPHOLOGY

3.3.1.1 BULK

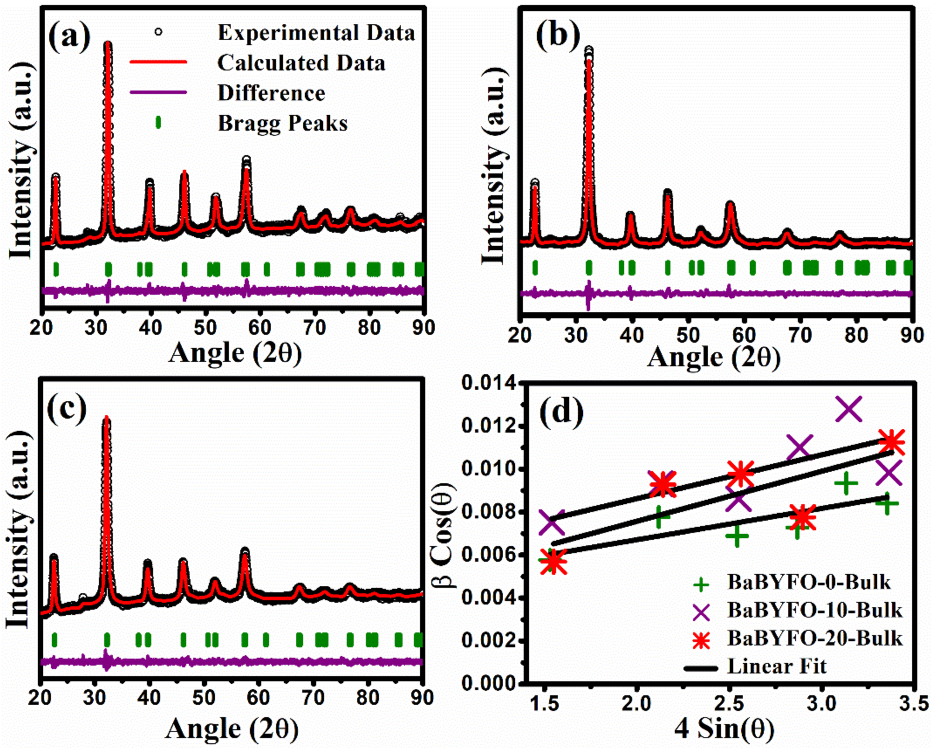

Figure 3.1. XRD data for (a) BaBYFO-0-Bulk, (b) BaBYFO-10-Bulk, and (c) BaBYFO-20-Bulk. (d) W-H plot of all samples

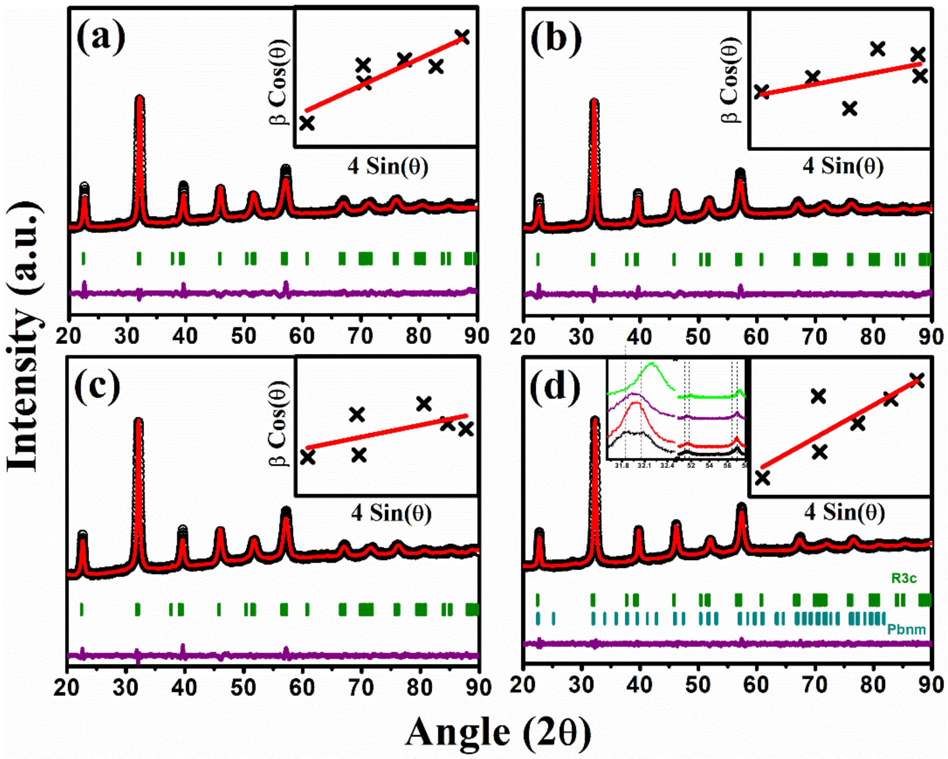

Figure 3.2. XRD plots along with Rietveld refinement result of (a) BaBYFO-0, (b) BaBYFO-3, (c) BaBYFO-5 and (d) BaBYFO-10. Inset of (d) depicts the merging of peaks around 32°, 52° and 57°. All insets indicate the Williamson-Hall plot for the corresponding sample.

Figure 3.1 shows the Rietveld refinement analysis of the X-Ray diffraction (XRD) data for all bulk samples. As demonstrated in Table 3.1, due to the reduced radius of Y^{3+} ions (0.9 Å) compared to Bi^{3+} ions (1.03 Å), the *c/a* ratio and cell volumes drop with increasing Y^{3+} doping concentration. The volume of the unit cell is shown to steadily shrink while the density rises for the same reason. Using the refined unit cell characteristics, the bond length and bond angles are calculated from the visualisation of the refined structure. When Bi ions are replaced with Y ions, it is seen that the distance between Bi and Fe along the $[111]_C$ axis decreases, indicating a compression along the axis, which is also suggested by the shorter length of *c*. The progressive increase in the Fe-O1-Fe bond angle corresponds to a gradual rise in the antiferromagnetic superexchange interaction between nearby Fe ions. The growing bond length between Bi and O1 ions imply weekend bonding between Bi and Y ions as a result of the absence of lone pairs in Y ions. The buckling of Bi-O1-Fe bond angle along with shortening of Bi-Fe bond-length imply a compression along $[111]_C$ axis, implying a reduction in non-centrosymmetric distortion. Stronger bonds between Fe and O ions are indicated by decreased Fe-O1 bond lengths and Bi-O1-Fe bond angles.

Table 3.1 - Cell parameters obtained from Rietveld refinement of XRD data of all samples

Sample Name	**Cell (Å), Volume (Å³), And Density (gm/cm³)**	**Bond Angle (°)**		**Bond Length (Å)**		**R factors**
BaBYFO-0-Bulk	a = 5.5963±0.0007 c = 13.7350±0.0019 V = 375.892±0.083 d = 36.47 e = $-3.65\text{x}10^{-4}$	Fe-O1-Fe O1-Bi-O1 Bi-O1-Fe	123.00 72.55 104.00	Fe-O1 Fe-O2 Bi-O1 Bi-O2 Bi-Fe	2.70 1.78 2.20 2.60 4.00	RF = 0.766 R_B = 0.909 χ^2 = 1.41
BaBYFO-10-Bulk	a = 5.6560±0.0010 c = 13.7199±0.0036 V = 367.978±0.130 d = 30.39 e = $-5.1\text{x}10^{-4}$	Fe-O1-Fe O1-Bi-O1 Bi-O1-Fe	135.40 69.30 102.70	Fe-O1 Fe-O2 Bi-O1 Bi-O2 Bi-Fe	2.44 1.81 2.20 2.70 3.63	RF = 0.413 R_B = 0.454 χ^2 = 1.66
BaBYFO-20-Bulk	a = 5.5582±0.0007 c = 13.5132±0.0127 V = 361.5475±0.0790 d = 47.46 e = $-5.83\text{x}10^{-4}$	Fe-O1-Fe O1-Bi-O1 Bi-O1-Fe	160.11 67.24 87.22	Fe-O1 Fe-O2 Bi-O1 Bi-O2 Bi-Fe	2.07 1.91 2.59 2.46 3.23	RF = 0.773 R_B = 0.998 χ^2 = 2.84

3.3.1.2 NANOPARTICLE

*R*3*c* rhombohedral crystal structure is confirmed by the X-ray diffractogram shown in Figure 3.2. However, at a higher doping concentration, observable changes in the crystal structure are seen. As shown in the inset of Figure 3.2(b), the peaks near 32° (corresponding to the (104) and (110) planes), 52° (corresponding to the (116) and (122) planes), and 57° (corresponding to the (018) and (214) planes) are seen to gradually merge with one another, indicating an increase in internal strain and decrease in crystallite size, as shown in Table 3.2.

Table 3.2 - Cell parameters value obtained from Rietveld refinement and WH analysis of XRD data

Sample Name	Cell Parameters	Bond Angle (°)		Bond Length (Å)		R factors
BaBYFO-0	*R*3*c* a = 5.5901 Å c = 13.835 Å V = 374.411 d = 33.16 nm e = -3.35x10^{-4}	Fe-O1-Fe O1-Bi-O1 Bi-O1-Fe	152.62 73.64 86.79	Fe-O1 Fe-O2 Bi-O1 Bi-O2 Bi-Fe	2.125 1.958 2.332 2.447 3.058,3.852	R_P = 6.13 R_{wp} = 7.23 R_e = 3.08 R_F = 0.415 R_B = 0.921 χ^2 = 5.498
BaBYFO-3	*R*3*c* a = 5.599 Å c = 13.726 Å V = 372.659 d = 27.83 nm e = -2.06x10^{-4}	Fe-O1-Fe O1-Bi-O1 Bi-O1-Fe	150.63 66.67 89.25	Fe-O1 Fe-O2 Bi-O1 Bi-O2 Bi-Fe	1.945 2.148 2.395 2.355 3.068,3.796	R_P = 5.83 R_{wp} = 6.66 R_e = 3.36 R_F = 0.234 R_B = 0.581 χ^2 = 3.935
BaBYFO-5	*R*3*c* a = 5.581 Å c = 13.772 Å V = 371.521 d = 26.5 nm e = -7.18x10^{-4}	Fe-O1-Fe O1-Bi-O1 Bi-O1-Fe	149.51 69.2 88.55	Fe-O1 Fe-O2 Bi-O1 Bi-O2 Bi-Fe	2.032 2.069 2.389 2.343 3.097,3.789	R_P = 4.77 R_{wp} = 5.25 R_e = 3.19 R_F = 0.11 R_B = 0.304 χ^2 = 2.711
BaBYFO-10	*R*3*c* (53.44%) a = 5.5791 Å c = 13.6621 Å V = 368.284 d = 42.78 nm e = -7.93x10^{-4}	*R*3*c* : Fe-O1-Fe O1-Bi-O1 Bi-O1-Fe	 160.03 73.51 83.53	Fe-O1 Fe-O2 Bi-O1 Bi-O2 Bi-Fe	2.11 1.895 2.432 2.51 3.035,3.798	R_P = 11.1 R_{wp} = 9.65 R_e = 7.57 R_F = 0.212 R_B = 0.609 χ^2 = 1.62
	Pbnm (46.56%) a = 5.6211 Å b = 5.5769 Å c = 7.8996 Å V = 247.633	*Pbnm*: Fe-O1-Fe Fe-O2-Fe	 147.12 148.22	Fe-O1 Fe-O2 Bi-O1 Bi-O2	2.059 2.054 2.477 2.527	R_P = 10.82 R_{wp} = 8.27 R_e = 7.04 R_F = 0.378 R_B = 0.597 χ^2 = 1.54

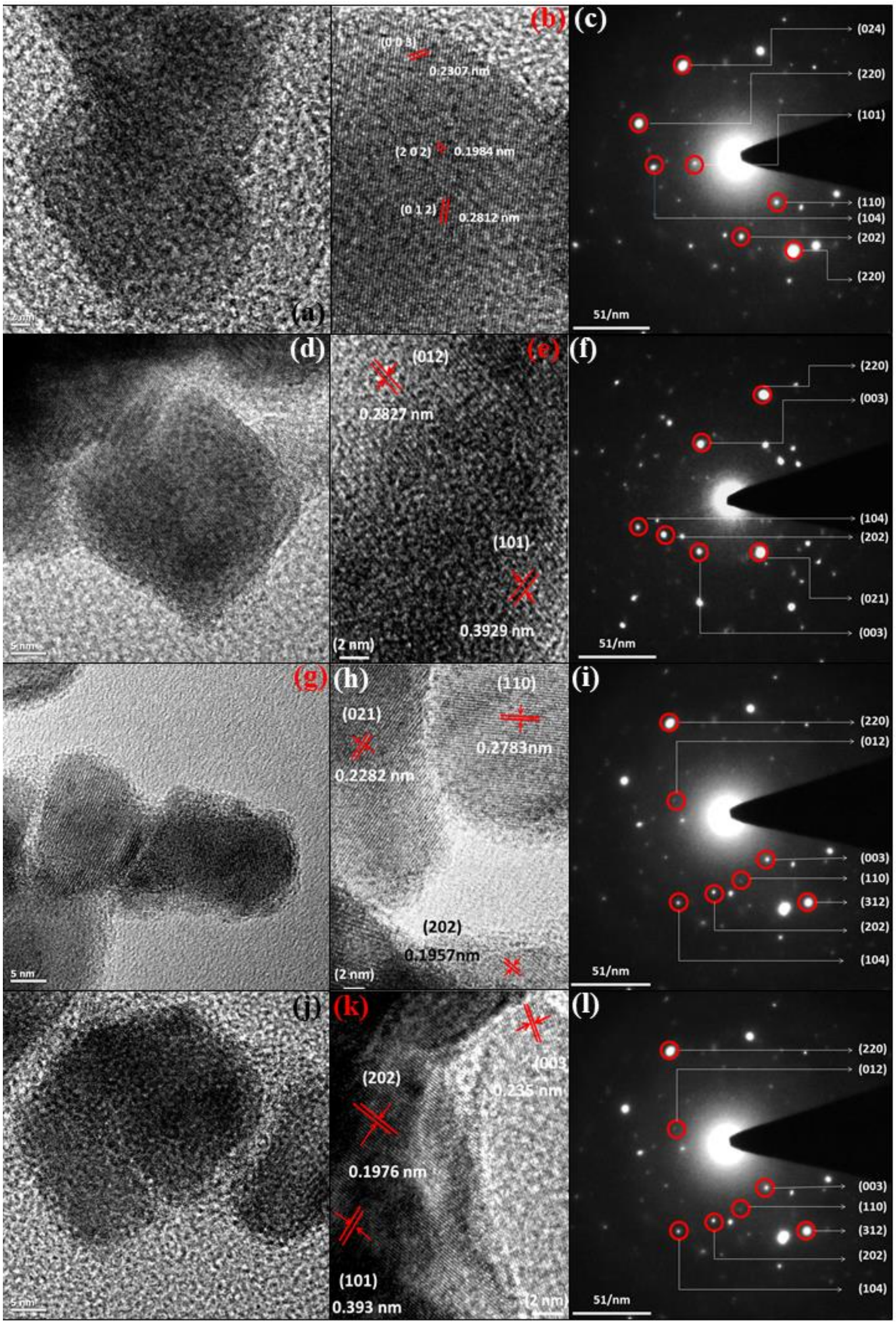

Figure 3.3 (a, d, g, j) depicts TEM at 5nm scale, (b, e, h, k) shows HRTEM, (c, f, i, l) depicts SAED data of BaBYFO-0, BaBYFO-3, BaBYFO-5 and BaBYFO-10 respectively.

According to similar works, the strain for BaBYFO-10 is sufficient to cause a structural change from the *R*3*c* to orthorhombic (*Pbnm*) phase. While the rhombohedral structure of BaBYFO-0, 3, and 5 is confirmed by Rietveld refinement using FullProf software, the refinement of BaBYFO-10 produced lower values of *R* parameters by assuming a combination of rhombohedral *R*3*c* group and orthorhombic *Pbnm* space group [Table 3.2].

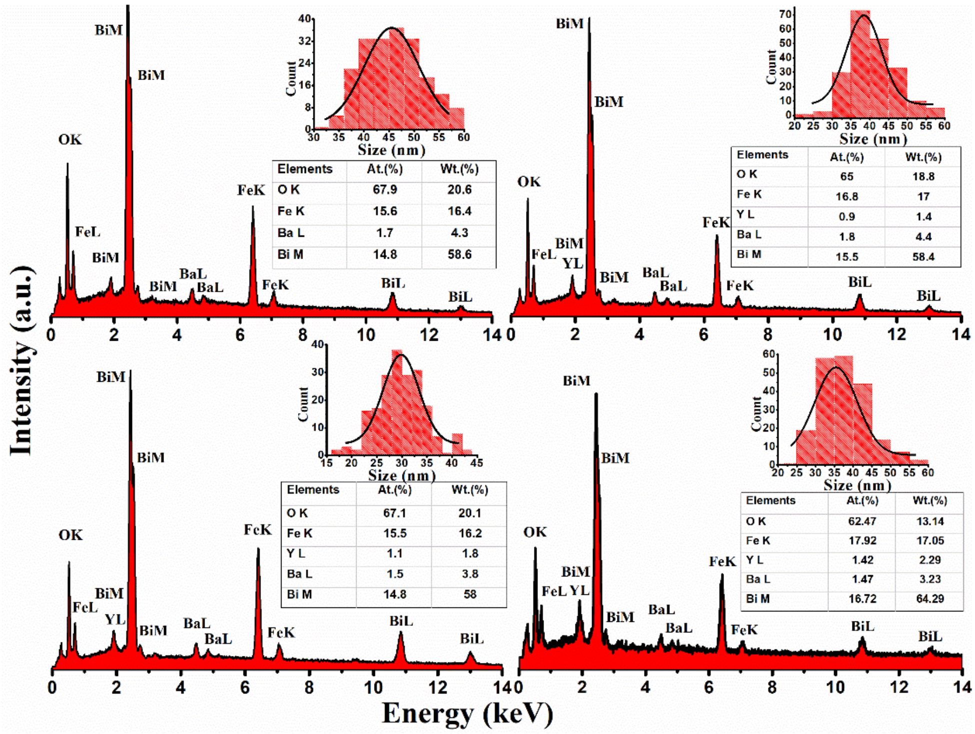

Figure 3.4 The EDAX data of (a) BaBYFO-0, (b) BaBYFO-3, (c) BaBYFO-5, and (d) BaBYFO-10 are shown. The insets of the images indicate the particle size distribution.

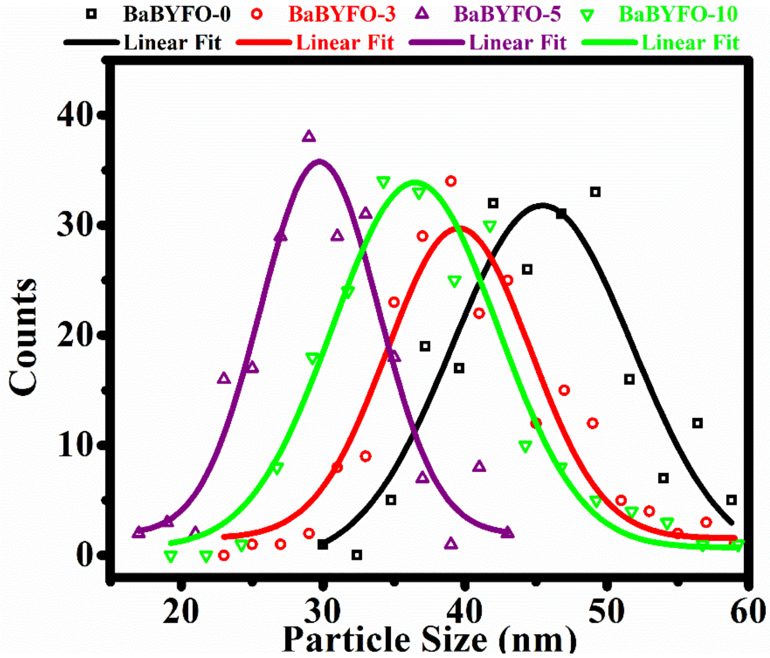

Figure 3.5 Particle size distribution of all nanoparticles

The formula for the octahedral tilt is, $\omega = \frac{1}{2}(\pi - \langle Fe - O - Fe \rangle)$, where $\langle Fe - O - Fe \rangle$ is the bond angle of Fe-O1-Fe. Decrease in Fe-O1-Fe angle up to 5 at. wt. % doped sample therefore indicates an increase in octahedral tilt. On the other hand, a cavity is generated at the FeO_6 octahedron due to the substitution of the larger Bi^{3+} ion with the smaller Y^{3+} ion, which is filled by the movement of Fe ions towards the Bi ion, hence lowering the O1-Bi-O1 and Fe-O1-Fe bond angles. The greater length of the Bi-O bond, which denotes a decreased bond strength, is caused by the absence of the $6s^2$ lone pair in the less electronegative Y ion. Increased Bi-Fe and Bi-O1-Fe angle suggests a strain along the unit cell's $[111]_C$ axis. A much smaller change in cell parameters, bond angles and bond lengths are observed with increasing doping concentrations of yttrium in bulk (Table 3.1) and nanoparticles (Table 3.2) which is attributed to lower doping concentrations of yttrium in nanoparticles.

Table 3.3 - Data from particle size distribution

Sample Name	Sample Size	Mean Size (nm)	Median (nm)	Standard Deviation (nm)
BaBYFO-0	204	45.7	45.7	5.9
BaBYFO-3	208	40.7	39.8	6.1
BaBYFO-5	203	30	29.7	4.8
BaBYFO-10	205	37.5	36.9	6.4

Using ImageJ software, the particle size distribution of each sample is assessed using a sample size of 200 particles obtained utilizing TEM (Figure 3.3(a, d, g, j)), and the results are displayed in the insets of Figure 3.4(a-d) to demonstrate the mean particle size. BaBYFO-0, 3, 5, and 10 are observed to have a mean particle size of 45.7 ± 5.9 nm, 39.8 ± 6.1 nm, 29.7 ± 4.8 nm, and 36.9 ± 6.4 nm, respectively. As can be observed from Figure 3.5, there is an overall shift in particle size distribution towards lower particle size with increasing doping concentration up to 5 at. wt.%. Although the histogram of BaBYFO-0 and BaBYFO-3 is partly overlapping attributed to the low doping concentration, the mean and median of both histograms are distinctly separated from each other [Table 3.3]. The median of the histograms implies that for BaBYFO-3, 50% of particles has size ranging below 39.8 nm while for BaBYFO-5, 50% of particles has size ranging above 45.7 nm. On the other hand, the histogram of BaBYFO-5 is quite distinctly situated from that of BaBYFO-0 indicating an obvious decrease in particle size with increasing doping concentration. Since the synthesis temperature and time is the same for all samples, the reason behind the change in particle size is attributed to the changing doping concentration and can be described using Kirkendall effect. However, the increase in particle size with farther doping in BaBYFO-10 has been attributed to the changed nucleation as a result of phase transformation from rhombohedral to orthorhombic phase. The lattice fringe values corresponding to (012), (110), (202), and (003) planes of BFO are observed using HRTEM image portrayed in Figure 3.3(b, e, h, k). In the BaBYFO-0 sample, the EDAX [Figure 3.4(a-d)] shows the presence of barium, bismuth, iron, and oxygen as elements, while the co-doped sample supports yttrium replacement at the Bi^{3+} site in desired atomic percentage. On the other hand, the SAED pattern shown in Figure 3.3(c, f, i, l) suggests that the samples are polycrystalline and contain peaks associated with the rhombohedral structure of BFO, such as (104), (110), etc.

In order to learn more about the structural transformation and local distortion, room-temperature Raman scattering spectra are obtained for all the nanoparticles. As shown in Figure 3.6, it is possible to determine the precise Raman peak positions within the 50-600 cm^{-1} range through fitting the observed spectra and deconvoluting the fitted curves. Purified BFO

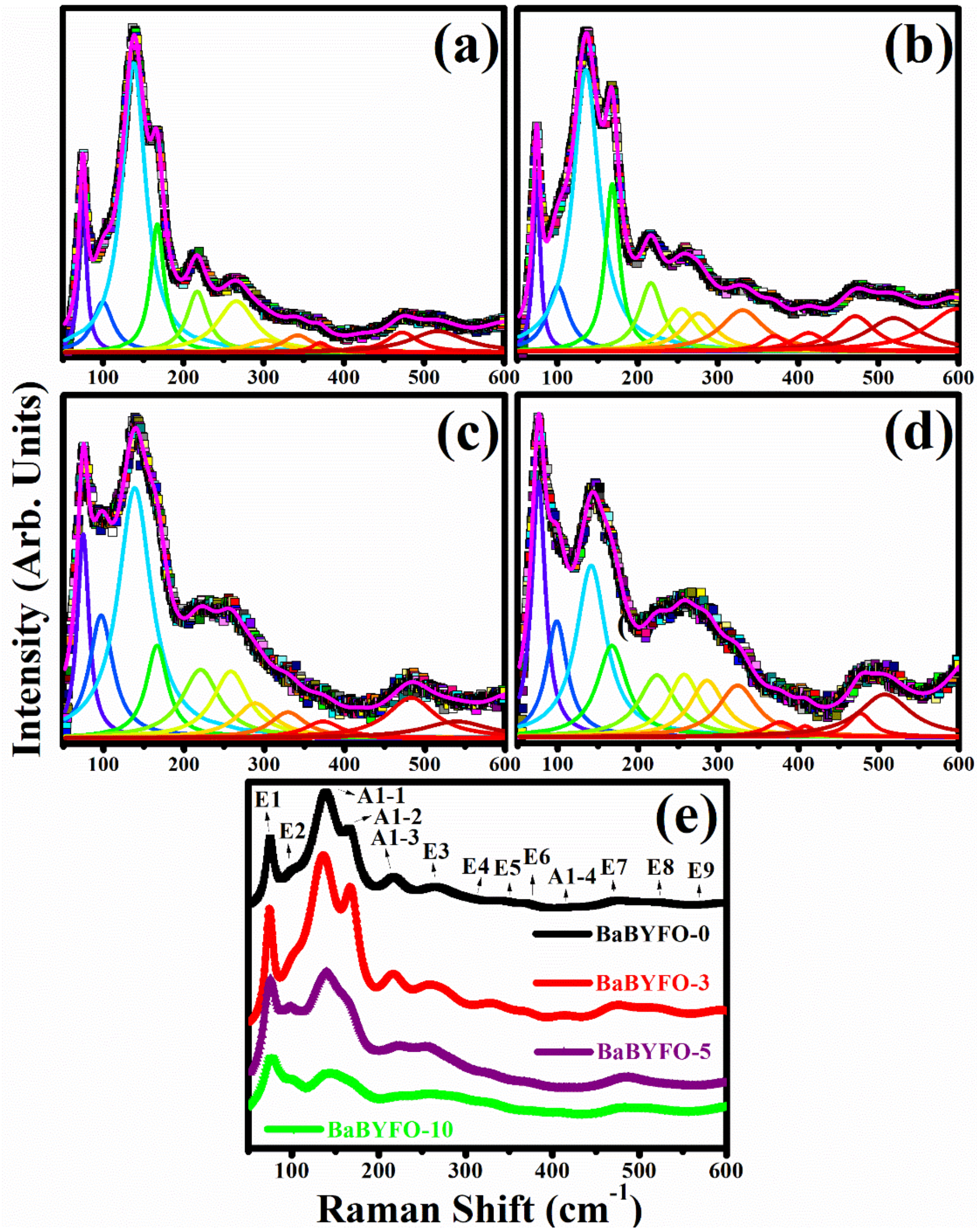

Figure 3.6 Raman spectra of (a) BaBYFO-0, (b) BaBYFO-3, (c) BaBYFO-5 and (d) BaBYFO-10. Figure (e) represents a comparative plot of Raman data for all samples in order to understand the mode shift due to doping.

shows 18 (4A1 + 5A2 + 9E) modes, according to the group theory study of the lattice vibrations in the $R3c$ structure, as shown by the following formula:

$$\Gamma_{R3c} = 4A_1(z, x^2 + y^2, z^2) + 5A_2(-) + 9E(x, y, x^2 - y^2, xy, yz, xz) \quad (3.6)$$

The irreducible representation, = 4A1 + 9E, summarises the aforementioned expression because the A2 modes are silent. E modes (doubly degenerate) are polarised along the XY plane, while A1 modes are polarised along the Z axis[50].

For BFO, it has been found that the modes below 167 cm^{-1} are mostly contributed to by the Bi-O covalent bonds, while the modes between 152 cm^{-1} and 262 cm^{-1} are contributed by Fe atoms. The modes for the vibrational motion of oxygen atoms are seen at frequency 262 cm^{-1}. Thus, the Bi-O bonds that control the strong scattering intensity of the A1-1, A1-2, and A1-3 modes, the weak scattering intensity of the A1-4 mode, and the medium scattering intensity of the nine E modes all contribute to the origin of these modes. The E-1, E-2, E-3, E-4, E-6, E-7, E-8, and E-9 modes are entitled to the peaks positioned at 74.62, 99.55, 265.96, 302.49, 342.42, 370.45, 472.75, and 516.87 cm^{-1} correspondingly. It is noticed that the A1-1, A1-2, A1-3, and A1-4 modes can be designated to the peaks situated at 138.3,

Table 3.4 - Peak positions obtained from Raman spectral analysis along with reported peak positions

TO Modes	BFO Ceramic at 300K [48]	Kothari et al. at 300K [49]	BaBYFO-0	BaBYFO-3	BaBYFO-5	BaBYFO-10
E-1	71.9	71	74.62	74.12	74.5	75.95
E-2	99.4	98	99.55	100.34	97.17	96.03
A1-1	134.6	135	138.3	135.74	138.78	141.58
A1-2	170.3	167	167.57	168.31	167.48	167.38
A1-3	228.0	218	216.98	217.2	220.83	223.68
E-3	262.8	255	265.96	254.81	258.5	257.43
E-4	310.5	283	302.49	274.19	288.67	285.92
E-5	345.1	321	342.42	330.64	329.53	324.14
E-6	369.2	351	370.45	370.11	373.19	377.11
A1-4	433.1	430	420.86	412.89	417.72	408.25
E-7	472.5	467	472.75	471.23	483.06	476.95
E-8	521.1	526	516.87	518.85	539.58	507.53
E-9	554.9	598	603.07	598.26	605.27	616.86

167.57, 216.98, and 420.86 cm^{-1} respectively. Table 3.4 lists all of the Raman modes for pure BFO that have been measured experimentally and in the literature. According to the equation below, the drop in mass caused by the substitution of the heavier Bi^{3+} ion with the lighter Y^{3+} ion is what is responsible for the A1-1, A1-2, and A1-3 peaks shifting towards higher frequency.

$$\nu = \frac{1}{2\pi c}\sqrt{\frac{K}{\mu}} \tag{3.7}$$

Where, v is the wavenumber, c is the speed of light, K is the force constant of the bond, and μ is the effective mass given by,

$$\mu = \frac{M_O \times (0.1 \times M_{Ba} + x \times M_Y + (0.9 - x) \times M_{Bi})}{M_O + [0.1 \times M_{Ba} + x \times M_Y + (0.9 - x) \times M_{Bi}]} \tag{3.8}$$

where the atomic weights of oxygen, bismuth, yttrium, and barium are, respectively, M_O, M_{Bi}, M_Y, and M_{Ba}. The reduction in stretching or bending vibration brought on by the shortening of the Fe-O bond length is what is responsible for the red shift of the E-3, E-4, and E-5 peaks. On the other hand, the increasing intensity of the peaks above 262 cm^{-1} is considered to be a result of the rise in oxygen vacancies in BaBYFO-5 and BaBYFO-10. The structural transition from the *R*3*c* to the *Pbnm* phase is readily obvious in the BaBYFO-10 Raman spectra, which is corroborated by the XRD data. There is also a considerable broadening and increase in peak intensity.

3.3.1.3 THIN FILM

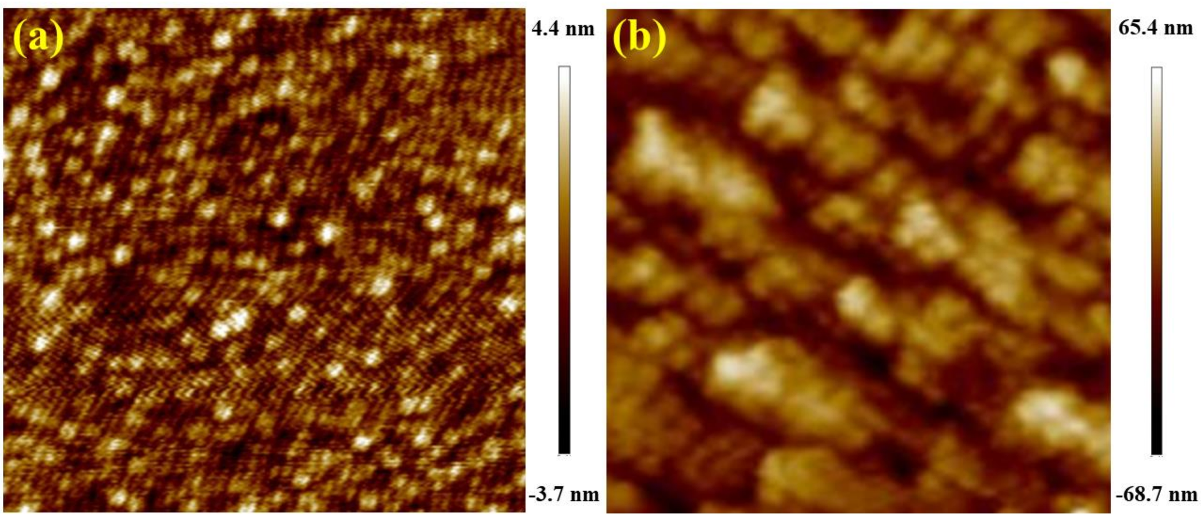

Figure 3.7 1 × 1 μm^2 micrograph showing topographical images of (a) BFO and (b) BaBYFO thin film.

Atomic force microscopy (AFM) analysis of all the films were carried out to investigate the morphology of the films deposited on the Nb:STO substrates. Figure 3.7 shows the morphology of the film examined by AFM under ambient condition. The images indicate larger grain size to be observed in the BaBYFO thin film with higher surface roughness. However, the overall morphological structure of the films depicts uniform and compact distribution of grains over long range.

3.3.2 ELECTRICAL PROPERTIES

3.3.2.1 BULK

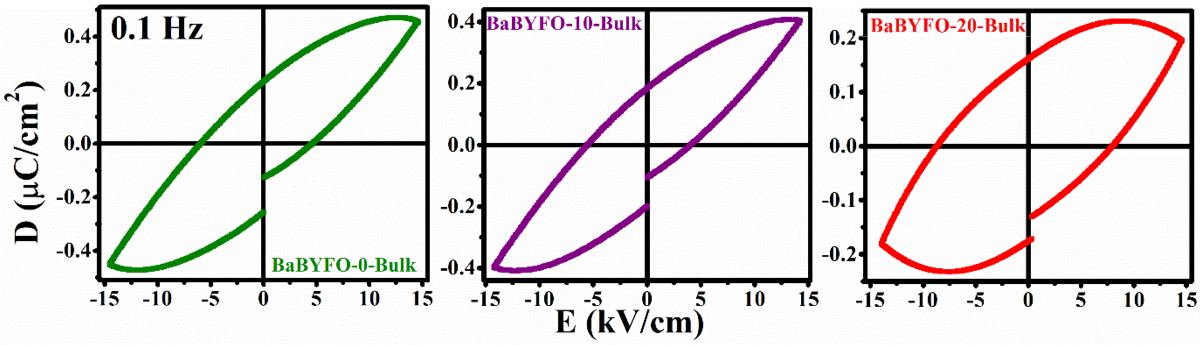

Figure 3.8 Electric Displacement (D) – Electric Field (E) hysteresis loop of all samples

Figure 3.8 displays the electric displacement (*D*) - electric field (*E*) hysteresis loop measurements at a frequency of 0.1 Hz. Electric conductivity (D_1), ferroelectric polarisation due to domain switching (*P*), and dielectric displacement ($D_2 = \varepsilon_0 \varepsilon_r E$), where ε_r is the relative permittivity of the material and ε_0 is the free space permittivity, are all included in the measured electric displacement (*D*). With increasing Yttrium doping concentration, it is seen that the remnant polarisation from the *D*-*E* hysteresis loop steadily decreases, which may be explained by the materials' lower conductivity. However, the rounded *D*-*E* loop observed in the BaBYFO-20-Bulk, which indicates a lossy nature, suggests that the sample has higher conductivity.

3.3.2.2 NANOPARTICLE

Figure 3.9 illustrates the current (*I*) - electric field (*E*) loop and the electric displacement (*D*) - electric field (*E*) hysteresis loop to explain the presence of ferroelectricity in the nanoparticles. It is noted that for BaBYFO-0, the current peak during domain switching, as represented by point "A", is smaller than that at the highest applied electric field, despite the saturated nature of the *D*-*E* hysteresis loop. The peak at point "A" coincides with the coercive field, indicating that there is ferroelectric contribution owing to domain wall switching.

However, the electrical conductivity is also strong enough to contribute to the polarisation. Since the current for BaBYFO-3 does not exceed that at the domain switching when the maximal electric field is applied, this sample's ferroelectric contribution is significantly greater. The coercivity of the *D-E* hysteresis loop correlates well with the domain switching peak location ("A") for this sample. The saturated *D-E* hysteresis loop of BaBYFO-5, however, shows that the domain switching peak is unique and that the current during domain switching is significantly larger than that at the maximum applied electric field. The presence of ferroelectric polarisation in the sample is confirmed by the position of the domain switching peak acquired from the *I-E* loop, which is in good agreement with the coercivity obtained from the *D-E* loop. "B" denotes the presence of an additional peak that is seen in the

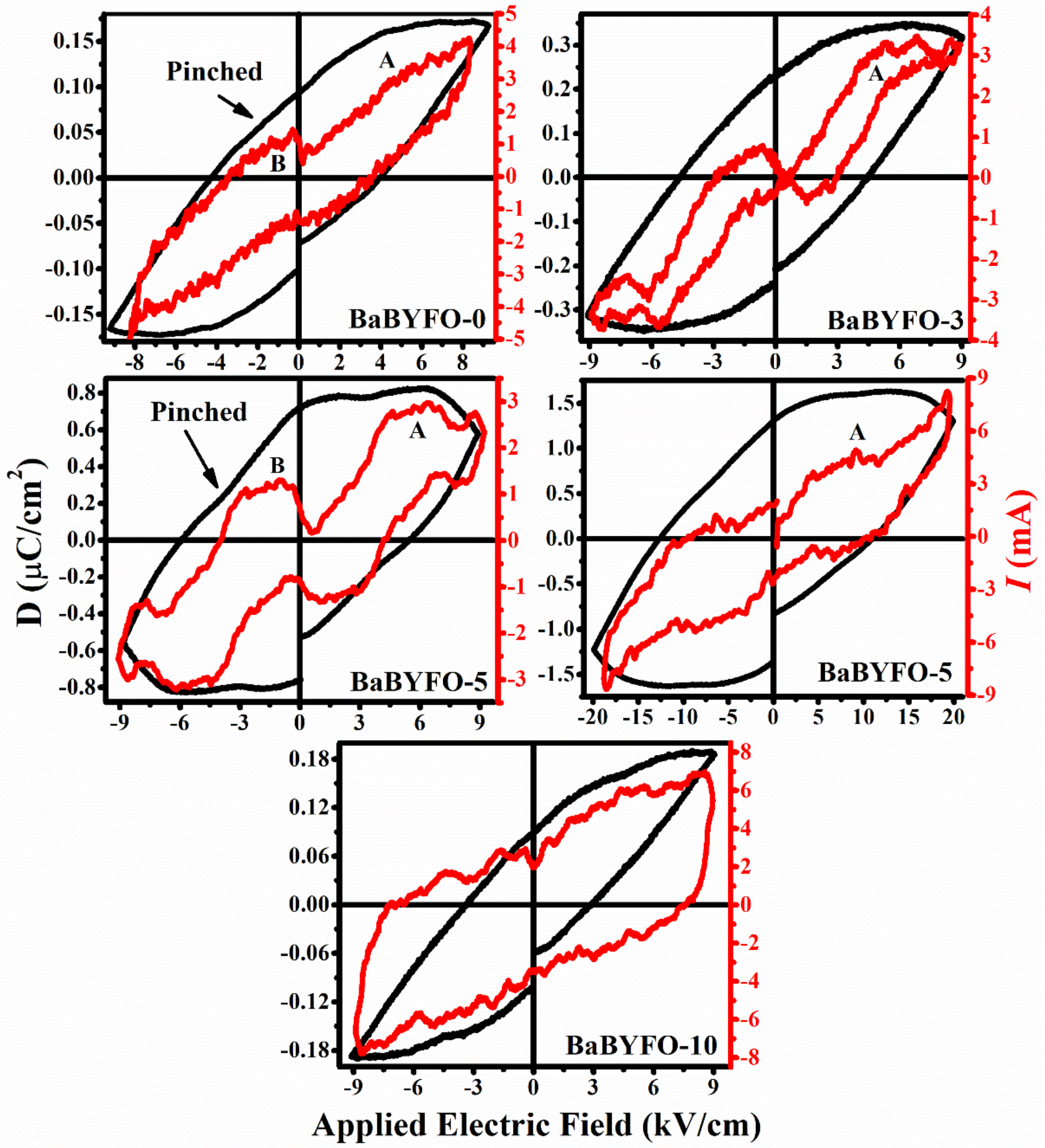

Figure 3.9 the electric displacement – electric field (*D-E*) and current – electric field (*I-E*) hysteresis loops of all samples at 20 Hz

I-E loop for BaBYFO-0 and 5 under low applied electric field. This peak is caused by the switching of oxygen vacancy dipoles, which is what causes pinched *D-E* loops to form as shown in BaBYFO-0 and 5 [39]. The *I-E* curves for BaBYFO-10 show no ferroelectric domain switching peak, supporting the paraelectric character of the orthorhombic phase.

Electrical conductivity and dielectric permittivity both contribute to the electric displacement, which results in the unsaturated *D-E* loop observed for this sample. The local piezo-response phase and amplitude hysteresis loops obtained to further demonstrate the

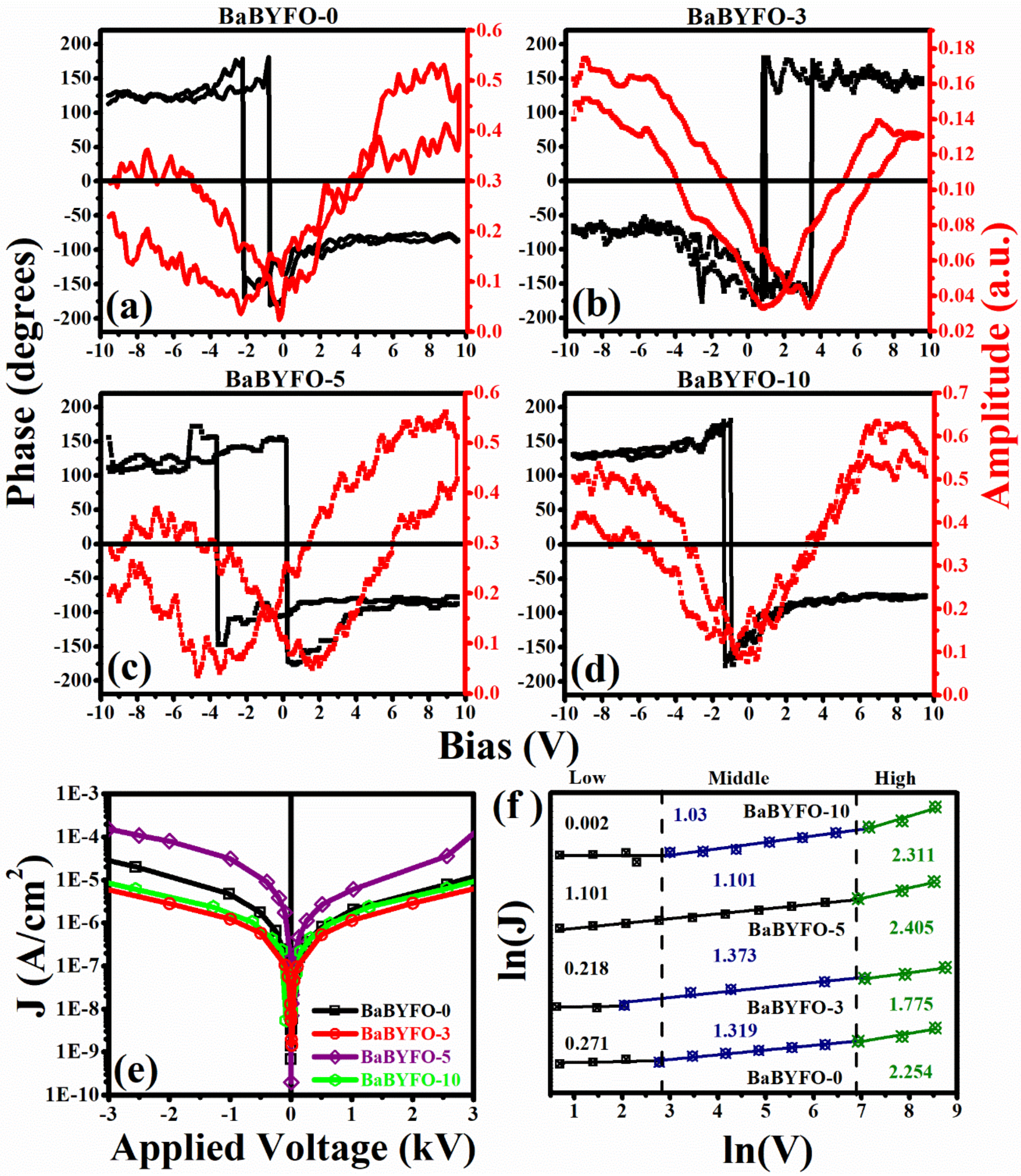

Figure 3.10 (a-d) the piezo-response force microscope (PFM) phase and amplitude hysteresis loops, (e) field dependent leakage current, (f) the fitted plot of log(J) with log(V) indicating the conduction mechanism followed by the samples.

presence of ferroelectric characteristics in the materials are shown in Figure 3.10(a-d). Sweeping the *dc* bias voltage from +10 V to -10 V produces the phase and amplitude hysteresis loops for the out-of-plane piezo-response force microscope (PFM). Local surface polarisation and electromechanical strain are correlated by the PFM phase and amplitude loops, respectively. BaBYFO-0, 3, and 5 samples with coercive voltages of 0.76, 1.3, and 1.9 V respectively exhibit well-defined ferroelectric hysteresis loops of phase and butterfly-like strain, demonstrating the presence of ferroelectricity in these samples[51]. Hysteresis loop

displacements from the origin of voltage axis point to local random fields, trapped charges, and favoured polarisation orientations at the electrode-ceramic interface[52–54]. In addition to the clearly defined electromechanical strain hysteresis loop and the ferroelectric hysteresis loop, BaBYFO-10 also exhibits a weak ferroelectric phase as well as a thin phase hysteresis loop and a V-shaped strain hysteresis loop.

The enormous ferroelectricity of $BiFeO_3$[55] is due to the anisotropic character of the $6s^2$ lone pair in BFO, which forms a space-filling localised lobe. This anisotropy causes the relative motions of the Bi and Fe ions in the $[111]_C$ direction. It is believed that the absence of a lone pair in the Y ion reduces this distortion while also diminishing its ferroelectric properties. However, it has been found that substituting a smaller, less electronegative Y ion lengthens the Bi-O bond and reduces the O-Bi-O bond angle, bringing the oxygen ions together. These structural deformations increase ferroelectricity by redistributing the cell's electron density and causing a larger off-centering displacement along the Bi-Fe axis ($[111]_C$ axis). This type of behaviour has already been observed in Yttrium-doped BFO, leading

Table 3.5 - Data of remnant and saturation polarization from hysteresis measurement, leakage currents at zero and high field, slope obtained from fitting of log(J) and log(V) plot are listed

Sample Name	**Hysteresis Loop (Applied electric field = 9 kV/cm)**		**Zero Field Leakage Current (A/cm^2)**	**High Field Leakage Current (A/cm^2)**	**Slope of log(J)-log(V)**		
	P_r ($\mu C/cm^2$)	**P_S ($\mu C/cm^2$)**			**Low**	**Middle**	**High**
BaBYFO-0	0.1	0.21	6.721×10^{-10}	2.76×10^{-5}	0.271	1.319	2.254
BaBYFO-3	0.23	0.35	1.466×10^{-9}	6.092×10^{-6}	0.218	1.373	1.775
BaBYFO-5	0.73 1.28 at 20kV/cm	0.8 1.63 at 20kV/cm	1.859×10^{-10}	1.5×10^{-4}	1.101	1.101	2.405
BaBYFO-10	0.1	--	5.749×10^{-9}	8.4×10^{-6}	0.002	1.03	2.311

researchers to conclude that doping with smaller ionic size elements can significantly shift BFO in the $[111]_C$ direction even in the absence of lobe-like lone pair electrons[56]. The decreased ferroelectric character of BaBYFO-10 is caused by the existence of paraelectric orthorhombic phase.

To comprehend the lossy nature of BaBYFO-5, as demonstrated by the analysis of leakage current, a comprehensive examination of the conduction mechanism generating it and the dielectric properties has been conducted. Figure 3.10(e) displays how the applied electric field affects the leakage current across all samples. At a high applied voltage of roughly 3 kV, the BaBYFO-5 exhibits the maximum leakage current of $1.5\text{x}10^{-4}$ A.cm^{-2}, whereas the BaBYFO-3 exhibits the lowest leakage current of $6.092\text{x}10^{-6}$ A.cm^{-2}. Numerous potential mechanisms for leakage current are discussed in the literature for BFO and other ferroelectric perovskite oxides that are similar, including space-charge-limited conduction (SCLC), ohmic conduction, Poole-Frenkel (PF) emission, interface limited Schottky emission, and grain boundary limited conduction (GBLC)[57]. These samples are, however, primarily controlled by three different types of conduction mechanisms. The first one is the SCLC mechanism where the current density is given by,

$$J_{SCLC} = \frac{9\mu\varepsilon_0 K}{8}\frac{V^2}{d^3} \tag{3.9}$$

Where, μ = carrier mobility, K = dielectric constant, ε_0 = free space permittivity, d = sample thickness, V = field voltage. Eq. 3.9 can be written as,

$$\log(J_{SCLC}) = \log(AV) \tag{3.10}$$

Where, A = $\sqrt{\frac{9\mu\varepsilon_0 K}{8d^3}}$.

The second one is Ohmic conduction where the current density is directly proportional to the applied field voltage,

$$J \propto V \tag{3.11}$$

The third type is Grain Boundary Limited Conduction (GBLC), where the current is almost independent of the applied electric field since it is restricted to the grain boundaries due to a significant difference in resistance between the grain and the grain boundaries[58]. In Figure 3.10(f), the fitted data for log(*J*) versus log(*V*) are displayed. "Low" refers to the voltage range below 20 V (3 kV/cm), whereas "Middle" refers to the voltage range between 20 V and

400 V. "High" refers to an area where the voltage is greater than 400V (or 7 kV/cm). BaBYFO-5 demonstrates no change in slope between the "Low" and "Middle" regions, with a value close to 1.101, indicating that Ohmic conduction governs the sample's conduction mechanism for voltages below 400 V, where the current is derived solely from free charge carriers in the bulk[59]. In contrast, the slope is nearly 2 in the "High" region, indicating SCLC conduction, which occurs when the density of injected free carriers from electrodes exceeds the material's free charge carrier density and current is primarily driven by these injected free charge carriers from electrodes. In all three locations for the remaining three samples, there are three distinct slopes. Although these samples follow SCLC and Ohmic conduction mechanisms at the "High" and "Middle" regions, respectively, the "Low" region's current is nearly independent of the applied field and has a slope significantly lower than 1, suggesting that the region is controlled by GBLC mechanism. The study of dielectric characteristics leading to an understanding of grain and grain boundary resistances becomes required since the GBLC mechanism predominates when there is a significant difference in resistances between grains and grain boundaries.

3.3.2.3 THIN FILM

Ferroelectric switching of the films was studied by piezoresponse force microscopy, in terms of the local hysteresis loop and mapping. Figure 3.11(a-c) and (d-f) depict the PFM amplitude mapping image and phase mapping image on a scanning area of 1.8 x 1.8 μm surface of the BFO thin film at different bias fields, respectively. The BFO film contains ferroelectric domains with diameters ranging from a few dozens to several hundreds of nanometers. For example, a relatively small ferroelectric domain (diameter of 60 nm) is measured by switching spectroscopy shown in Figures 3.11(a) and 3.11(b). The switching electric fields of the phase and amplitude loops are the same, at -2.77 and 3.15 V, respectively, resulting in a shift of approximately 0.19 V in the positive direction as illustrated in Figure 3.12 (a) and (b) respectively. Charge injection at one-side interface may account for the shift of the loops. Similar amplitude and phase mapping images are also displayed for thin BaBYFO film, demonstrated in Figure 3.14(a) and (b) respectively. In this case however, the PFM images represented in Figure 3.13 depicts that the ferroelectric domains are much larger in size than the ones in BFO film and spread over long range of distance. The switching spectroscopy for the same implies a switching field of -1.49 V and 4.94 V with a positive shift of 1.72 V.

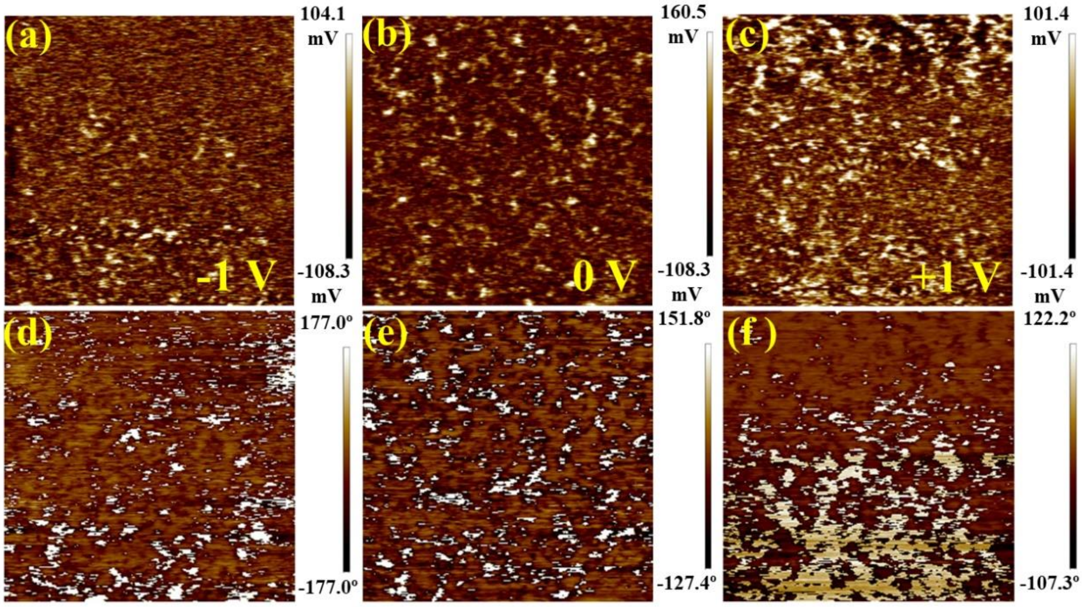

Figure 3.11 The piezoresponce force microscopy data is shown for BFO thin film at a bias field of (a) -1 V, (b) 0 V, and (c) +1 V. The piezoresonce phase is as well shown for bias fields (d) -1 V, (e) 0 V, and (f) +1 V.

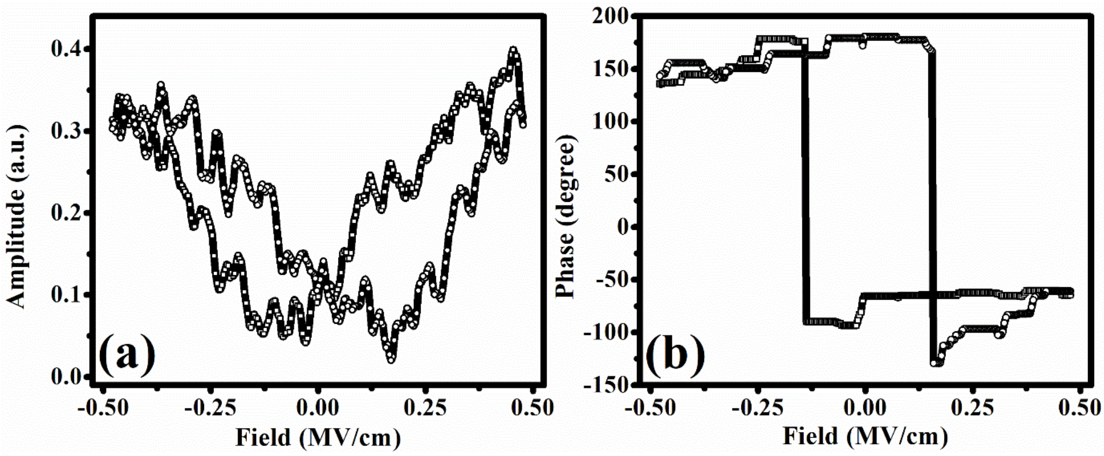

Figure 3.12 The piezoresponse force microscope (PFM) (a) amplitude and (b) phase hysteresis loops of BFO thin film.

The *dc* bias is changed from -1V to +1V in BFO thin film and from -6V to +6V in BaBYFO thin film (Figure 3.13) in order to demonstrate clear change in the phase of ferroelectric domains over same area. It is observed that the switching is much more prominent in the BaBYFO thin film having larger ferroelectric domains.

3.3.3 DIELECTRIC PROPERTIES

3.3.3.1 BULK

To comprehend the type of conductivity of the samples influencing the nature of the observed *D-E* loop, additional research into the dielectric characteristics of the samples has been conducted. The frequency-dependent dielectric constant (ε′) is shown in Figure 3.15 (a, c, and e) in the frequency range of 500 Hz to 1 MHz, and the temperature dependence of the

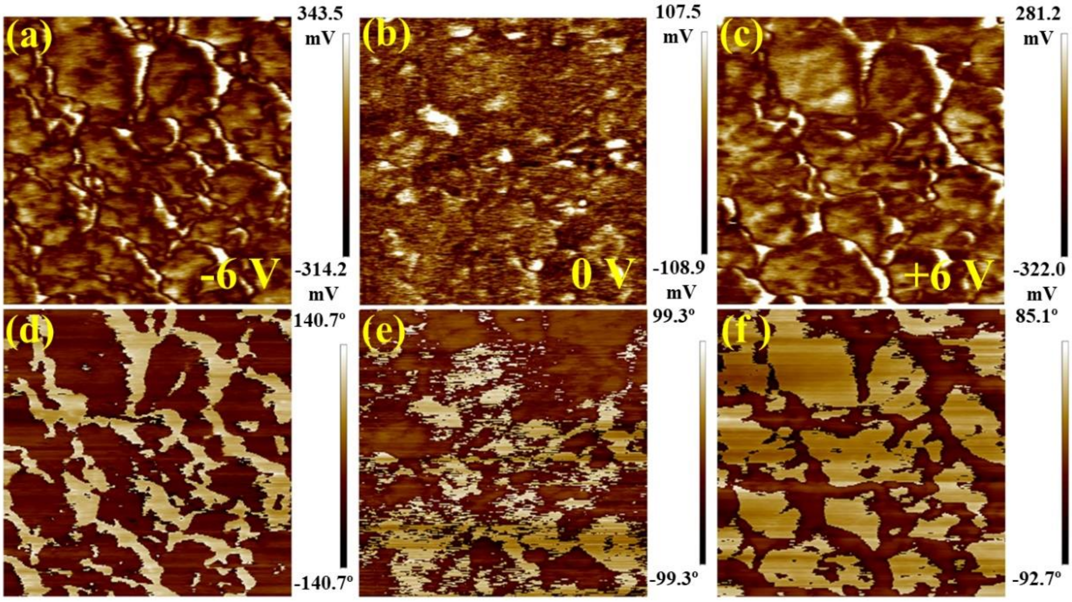

Figure 3.13 The piezoresponce force microscopy data is shown for BaBYFO thin film at a bias field of (a) -6 V, (b) 0 V, and (c) +6 V. The piezoresonce phase is as well shown for bias fields (d) -6 V, (e) 0 V, and (f) +6 V.

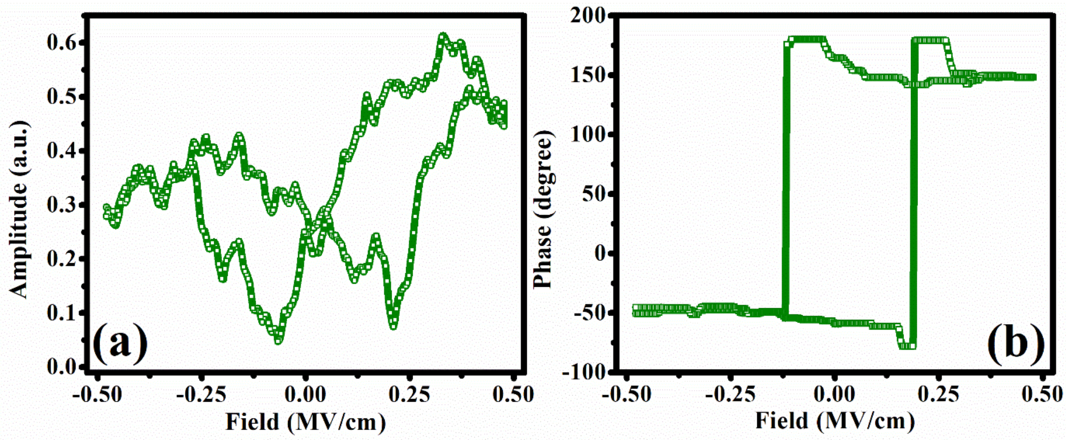

Figure 3.14 The piezoresponse force microscope (PFM) (a) amplitude and (b) phase hysteresis loops of BaBYFO thin film.

dielectric loss is shown in Figure 3.15 (b, d, and f) for a temperature range of 25 °C to 300 °C. It is found that at low temperatures (less than 150 °C), the thermal energy of the dipoles is insufficient to match the frequency of the applied field, which results in the frequency independence of the signal. Higher values of ε′ come from the dipole moments being better able to follow the applied electric field at higher temperatures (> 150 °C). Dielectric materials of all kinds often have one of five fundamental forms of electric polarizations: (a) electronic polarisation; (b) atomic or ionic polarisation; (c) dipolar polarisation; (d) interface or space charge polarisation; and (e) spontaneous polarisation[60]. The amount of overall polarisation relies on the frequency of the electric field since each type of polarisation takes time to

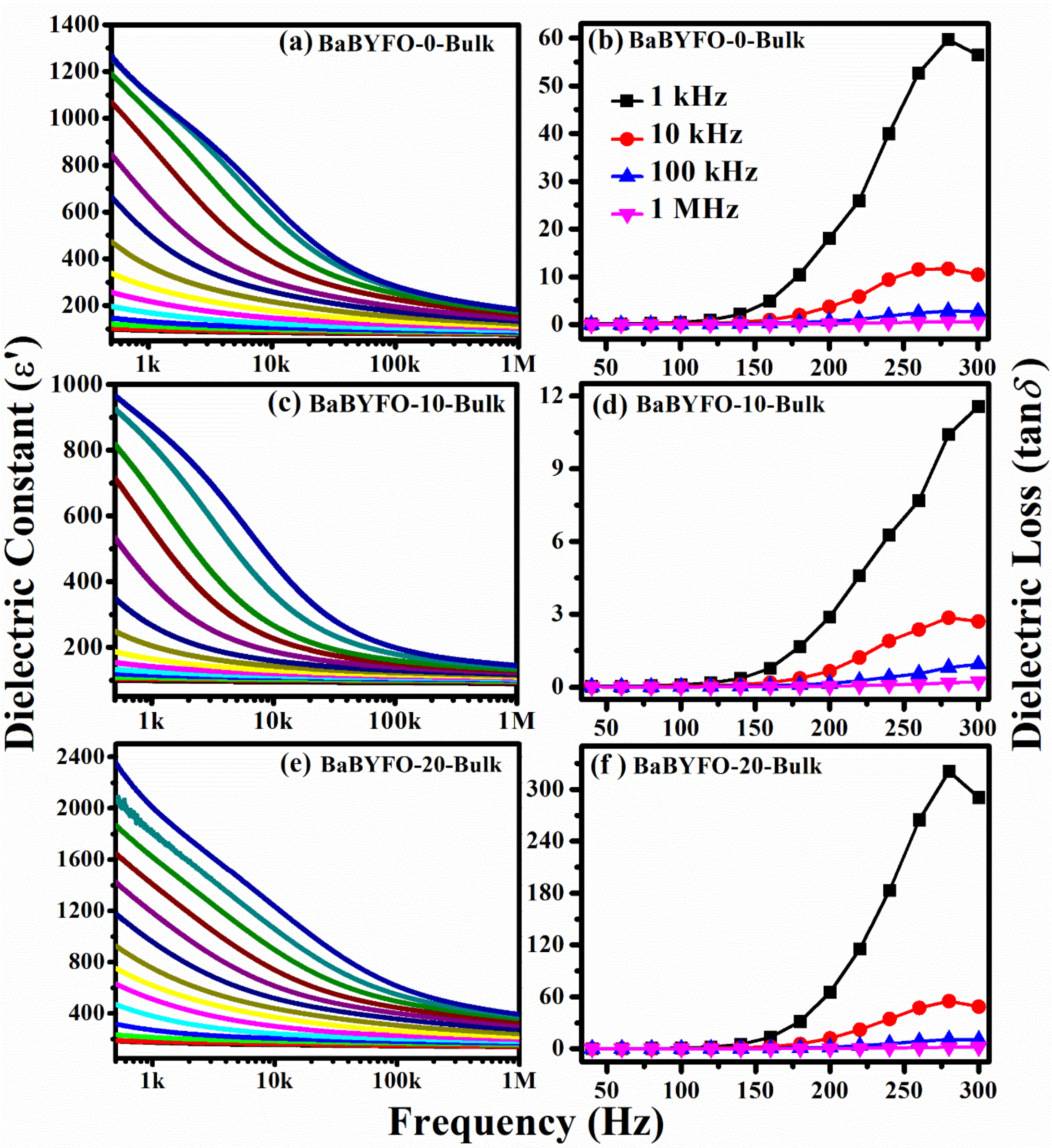

Figure 3.15 (a, c, e) depict the frequency dependence of real part of dielectric permittivity for BaBYFO-0-Bulk, BaBYFO-10-Bulk and BaBYFO-20 Bulk respectively. (b, d, f) demonstrates the temperature dependence of dielectric loss of all samples.

complete. For instance, space charge polarisation predominates at frequencies below 10^3 Hz, but dipolar polarisation, also known as orientational polarisation, predominates in the sub-infrared frequency range of 10^3 Hz - 10^9 Hz[34]. Ionic polarisation rules at frequencies between 10^9 Hz and 10^{12} Hz, while electronic polarisation rules at frequencies higher than 10^{12} Hz. The dipolar and space charge polarisation is consequently the largest contributor to the observed polarisation for the frequency range of 500 Hz - 1 MHz at which the samples are analysed. The dielectric constant for BaBYFO-0-Bulk varies from 90 to 77 for frequencies between 500 Hz and 1 MHz. The dielectric constant for BaBYFO-10-Bulk changes from 100 to 89 between 500 Hz and 1 MHz. Additionally, for BaBYFO-20-Bulk it varies from 185 to 138. Therefore, it is clear that BaBYFO-10-Bulk has the best frequency stability and least space-charge impact on the sample's dielectric constant indicating a decrease in conducitvity of the material as a result of Y^{3+} ion doping[61–64]. On the other hand, the dielectric loss study suggests that BaBYFO-20-Bulk posses the highest levels of dielectric loss.

Figure 3.16 (left panels) depicts nyquist plots of the imaginary (Z'') and real (Z') components of the complex impedance. At low temperatures, the steep slope and nearly straight-line curves reveal the excellent insulating properties of the materials. As the temperature rises, the curves bend toward the Z′-axis and create warped semicircles. The decreasing radii of the semicircles with increasing temperature indicate a decrease in the resistivity of the material, which clearly demonstrates the non-metallic nature of the material, just as the intercept of the curves at the Z′-axis indicates the material's resistivity. According to the ideal equivalent circuit with resistance and capacitance due to grain and interfacial grain boundary contribution, the complex impedance of an inhomogeneous system are given by,

$$Z' = \frac{R_g}{1+(\omega R_g C_g)^2} + \frac{R_{gb}}{1+(\omega R_{gb} C_{gb})^2} \tag{3.12}$$

$$Z'' = \frac{\omega R_g^2 C_g}{1+(\omega R_g C_g)^2} + \frac{\omega R_{gb}^2 C_{gb}}{1+(\omega R_{gb} C_{gb})^2} \tag{3.13}$$

Where R_g, C_g, R_{gb}, and C_{gb} stand for, respectively, grain resistance, capacitance, grain boundary resistance, and capacitance. These equations have been derived in the section 1.3.3 of the chapter 1 of this thesis. Figure 3.17(a) displays the frequency variation of the real part of the complex impedance combined with the fitted values. Table 3.6 lists the values of R_g, C_g, R_{gb}, and C_{gb} derived from this fitting using Eq. 3.13.

The R_g and R_{gb} values are further fitted using Arrhenius equation,

$$R_g = A e^{\frac{E_g}{k_B T}} \tag{3.14}$$

$$R_{gb} = B e^{\frac{E_{gb}}{k_B T}} \tag{3.15}$$

By fitting $\ln(R_g)$ and $\ln(R_{gb})$ with $\frac{1}{k_B T}$ in accordance with the aforementioned formulae, the values of E_g and E_{gb}, listed in Table 3.6, are obtained [Figures 3.17(b, c)]. The fact that the grain boundaries of all samples have higher activation energies suggests that the charge carriers at grain boundaries are more sensitive to temperature than those at the grains. The panels on the right side of Figure 3.16 show the frequency variation of total conductivity at different temperatures. The value of σ(ω) has been calculated using following formula,

$$\sigma(\omega) = \omega\varepsilon'\varepsilon_0 tan\delta \qquad (3.16)$$

Where, the value of ε_0 is taken as 8.854×10^{-12} *F/m*. The increase in $\sigma(\omega)$ with increasing

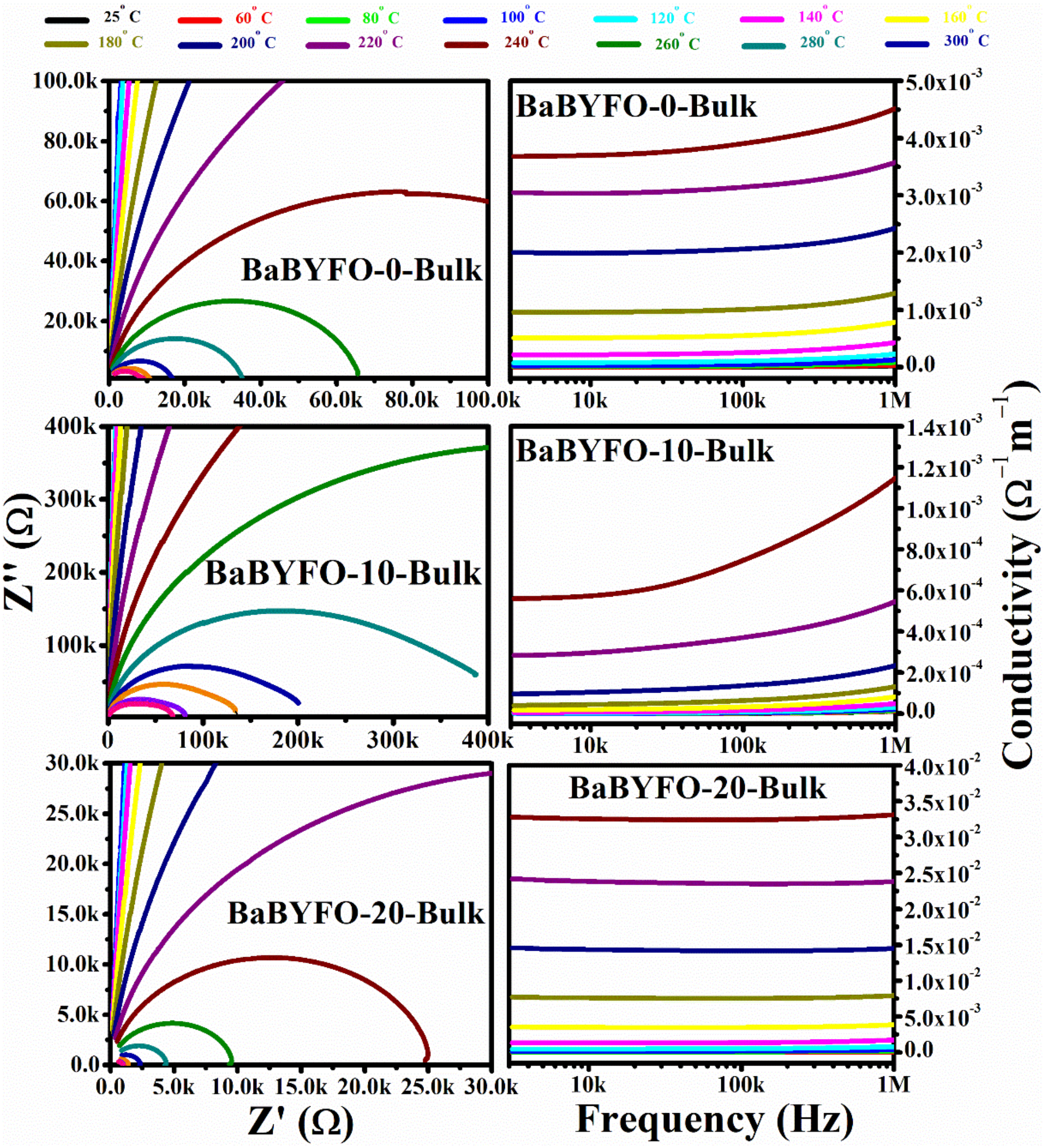

Figure 3.16 (left) The Nyquist plots of BaBYFO-0-Bulk, BaBYFO-10-Bulk, BaBYFO-20-Bulk respectively for a temperature range from 25 to 300. (Right) The conductivity of the samples with varying frequency are depicted.

temperature and frequency indicates the increase in hopping of charge carriers through the grains. This conductivity ($\sigma(\omega)$) can be studied using "Jonscher's Universal Power Law"[65], which are described as sum of the frequency-independent part, σ_{DC} and frequency-dependent part, σ_{AC}:

$$\sigma(\omega) = \sigma_{DC} + \sigma_{AC} \tag{3.17}$$

$$\sigma_{AC} = A\omega^{S} \tag{3.18}$$

And,

$$\sigma_{DC} = \sigma_0 e^{-\frac{E_a}{k_B T}} \tag{3.19}$$

E_a is the activation energy of conductance, or the amount of energy a charge must overcome to move through a material, and σ_0 is the conductivity at an infinitely high temperature. The fitted values of $\ln(\sigma_{DC})$ vs. $\frac{1}{k_B T}$ for all samples are displayed in Figure 3.17(d). The values of activation energies E_a for all samples are given by the slope of the fitted data [Table 3.6]. The activation energy of *dc* conductivity and the activation energy of dielectric relaxation are

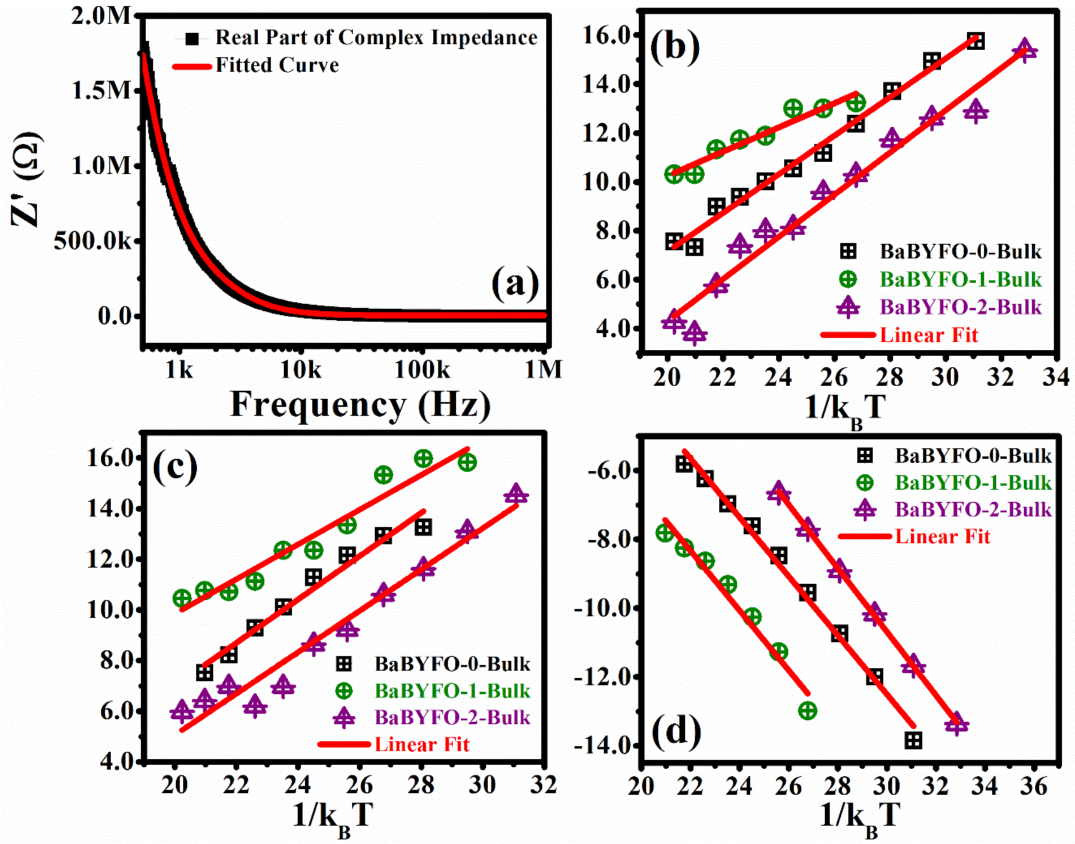

Figure 3.17 (a) fitted plot of real part of complex impedance (Z') with frequency. (b, c, d) refers to fitted plot of logarithm of grain and grain boundary resistance, dc conductivity with $1/k_B$ T respectively.

reasonably in agreement.

It has been found that the BaBYFO-10-Bulk exhibits a substantial rise in grain and grain boundary resistivity, whereas the BaBYFO-20-Bulk exhibits a marked decrease. The conductivity of the materials can be seen to be clearly influenced by the type of grain and grain boundary resistivities in Table 3.6. While the mobility of vacancies is significantly influenced by temperature, the flow of electrons is not significantly impacted. Therefore, the existence of more vacancies on the grain boundaries than in the grains is implied by the greater activation energy of grain boundaries for BaBYFO-0-Bulk and BaBYFO-10-Bulk. When compared to other materials, BaBYFO-20-Bulk exhibits contradictory grain and grain boundary resistivities and conductivities because the grains contain more vacancies than the grain boundaries. The lower activation energies of the grain and grain boundaries of BaBYFO-10-Bulk compared to BaBYFO-0-Bulk, on the other hand, show that the vacancies are reduced in this sample as a result of the replacement of 10 at. wt.% of the volatile bismuth with non-volatile yttrium. Thus, electrons are the predominant charge carriers in this sample. The reduction in activation energies therefore leads to the conclusion that with 10 at. wt.% yttrium doping, the vacancies are decreased at both grain and grain boundaries. The decrease in vacancies also increases resistance at the grain and grain boundaries, which lowers the total conductivity.

Table 3.6 - The values of R_g, R_{gb}, C_g, and C_{gb} along with total conductivity and the activation energies depicted from Arrhenius equations are listed below

Sample Name	R_g (kΩ)	R_{gb} (kΩ)	C_g (nF)	C_{gb} (nF)	E_g (eV)	E_{gB} (eV)	Conductivity ($\Omega^{-1}m^{-1}$)	E_a (eV)
BaBYFO-0-Bulk	39	25	0.35	2.2	0.788	0.855	6.2×10^{-7}	0.868
BaBYFO-10-Bulk	450	460	0.28	1.1	0.495	0.696	7.55×10^{-8}	0.858
BaBYFO-20-Bulk	3.44	5.7	3.15	0.7	0.862	0.816	1.52×10^{-6}	0.921

However, with additional yttrium doping, as in BaBYFO-20-Bulk, the vacancies are once more augmented in both the grains and the grain boundaries. This means that the grains have a larger vacancy concentration as seen by their higher activation energy than the grain boundaries. As the formation of bismuth vacancies (Eq. 3.2) decreases drastically, the electrons generated during oxygen vacancy formations (according to Eq. 3.1) are used up to increase the formation of Fe^{2+} as per Eq. 3.3. It has been established in the past that a material can exhibit extremely low conductivity even when it has a very high concentration of oxygen vacancies if the concentration of Fe^{2+} is much lower, suggesting that the effect of electrons as charge carriers is much more dominant than that of the vacancies. The high concentration of Fe^{2+} ions in BaBYFO-20-Bulk therefore operate as charge carriers and result in highly conducting grains and grain boundaries.

3.3.3.2 NANOPARTICLE

Similar studies are also performed for the nanoparticles to understand the governing conduction mechanisms in these samples. Figure 3.18(a-d) shows that the real parts of the dielectric permittivity (ε') for BaBYFO-0, 3, 5, and 10 are, respectively, 93, 120, 212, and 95 at room temperature. The temperature dependency of the dielectric loss for each sample is depicted in the insets of Figure 3.18(a-d). For BaBYFO-5, the maximum values of the dielectric constant and loss is measured. This sample also demonstrates a significant effect from space charge polarisation at lower frequency region, with the maximum frequency

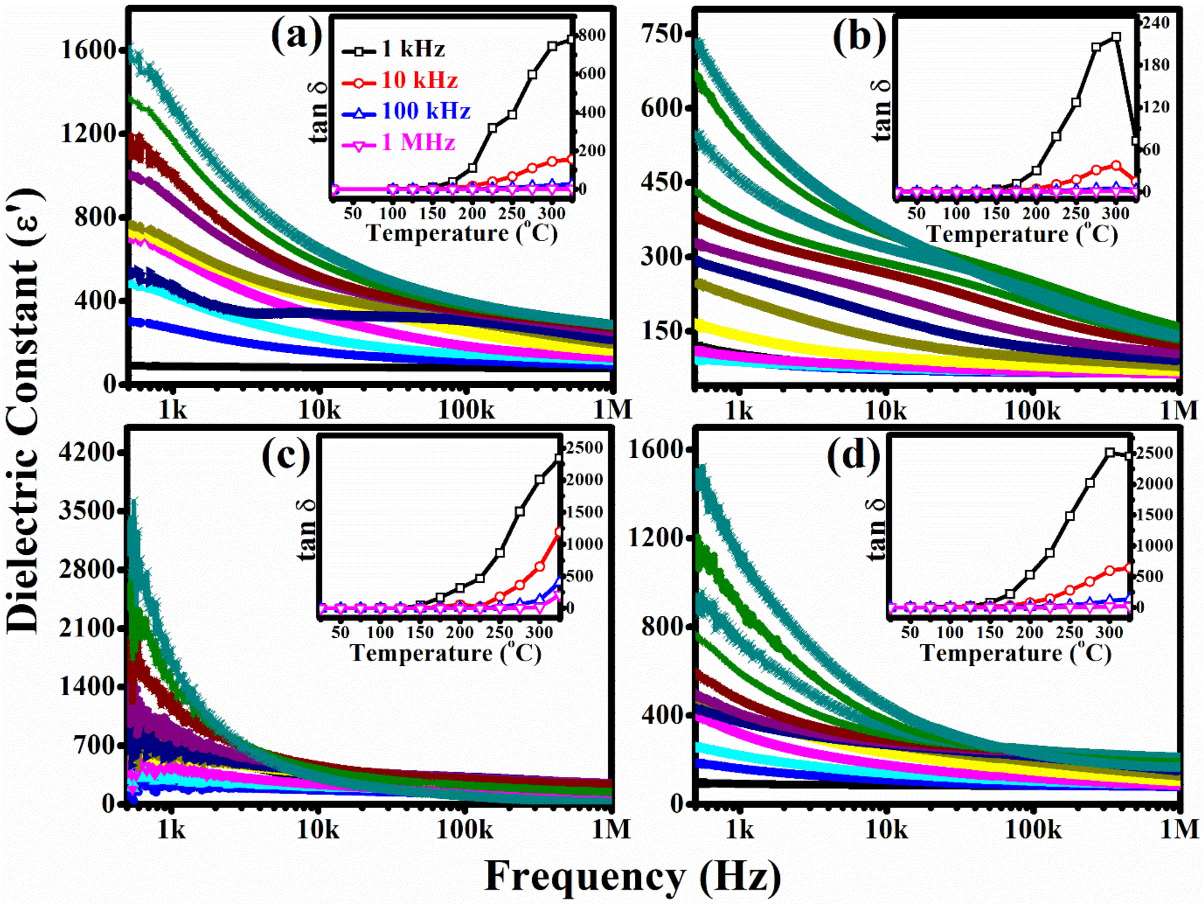

Figure 3.18 Frequency dependence of real part of dielectric permittivity for (a) BaBYFO-0, (b) BaBYFO-3, (c) BaBYFO- 5, and (d) BaBYFO-10 respectively. In inset the temperature dependence of loss tangent for different frequencies is depicted.

dispersion of the dielectric constant dropping from 212 to 65 due to a shift in frequency from 500 Hz to 1 MHz.

Figure 3.19(a) displays the frequency fluctuation of the real part of complex impedance combined with the fitted values. Table 3.7 contains the values of R_g, C_g, R_{gb}, and C_{gb} that are determined by fitting the measured Z′ data with Eq. 3.13. The increase in conductivity, σ(ω) with increasing temperature and frequency, shown in Figures 3.19(e-h),

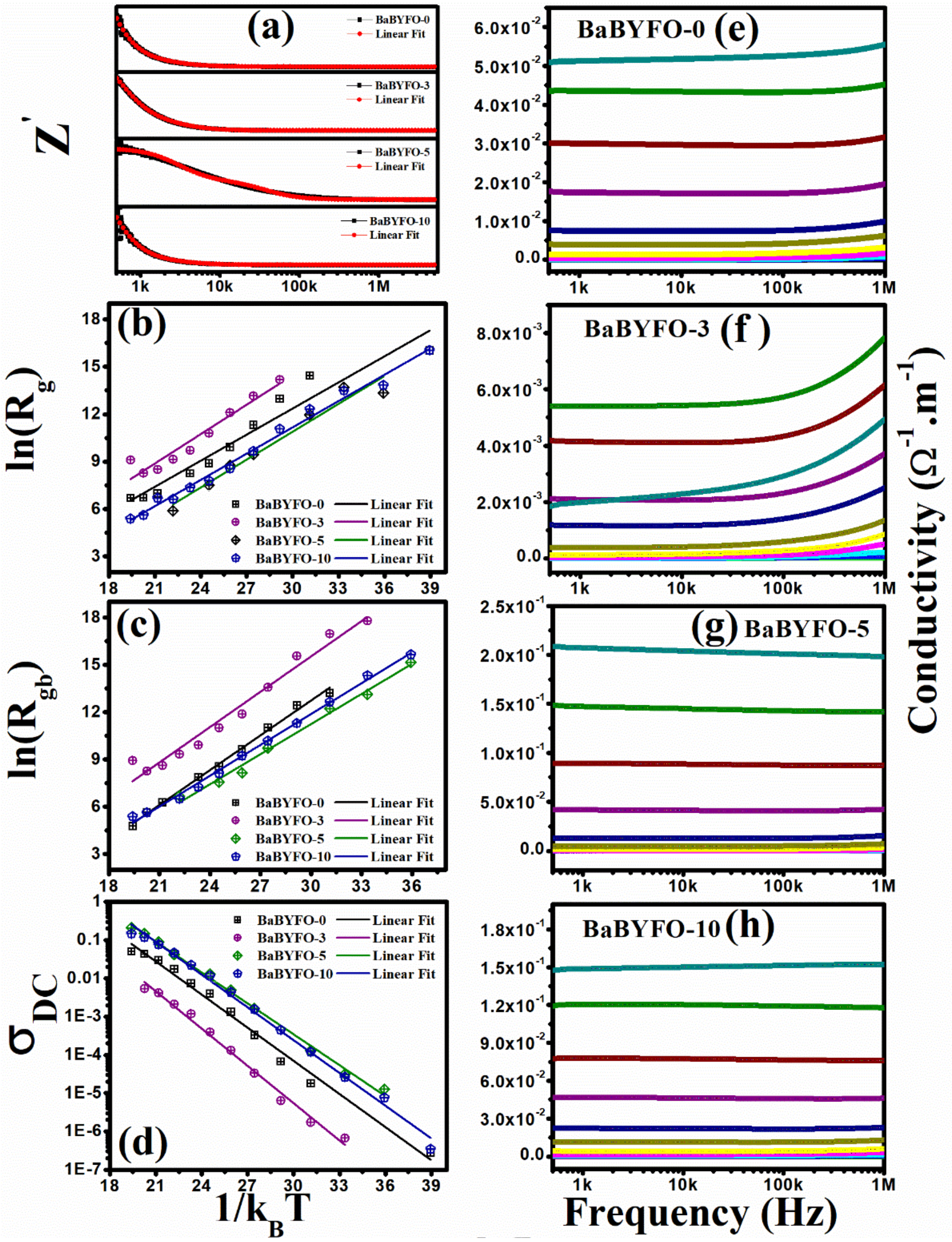

Figure 3.19 (a) fitted plot of real part of complex impedance (Z') with frequency. (b, c, d) refers to fitted plot of logarithm of grain and grain boundary resistance, *dc* conductivity with $1/k_BT$ respectively. (e-h) show plot of *ac* conductivity with frequency.

indicates the increase in hopping of charges inside the grains.

The fitted values of $\ln(\sigma_{DC})$ vs. $\frac{1}{k_B T}$ for all samples are displayed in Figure 3.19(d). The activation energy of *dc* conductivity and the activation energy of dielectric relaxation are reasonably in agreement. The fact that grain boundaries in all samples have greater activation energies suggests that distinct types of charge carriers are causing the conduction in grains and grain boundaries. However, according to Eq. 3.3, the activation energy values indicate that the electrons are the predominant charge carriers. The total conductivity of the materials is caused by the electrons at the grain boundaries and the grains themselves. The BaBYFO-5 sample, on the other hand, exhibits similar types of charge carriers in its grain and grain boundaries, which is supported by the sample's close values of grain and grain resistivity, which results in high conductivity, and which is explained by the smallest difference between the activation energies of the grain and grain boundary.

Table 3.7 - Data of grain resistance and capacitance, grain boundary resistance and capacitance, conductivity along with activation energies of grain and grain boundaries

Sample Name	R_g (MΩ)	R_{gb} (MΩ)	C_g (nF)	C_{gb} (nF)	E_g (eV)	E_{gb} (eV)	σ ($\times 10^{-7}$S)	E_a (eV)
BaBYFO-0	9.2	0.22	0.43	1.53	0.23895	0.31922	2.791	0.28874
BaBYFO-3	9.2	0.91	0.31	0.19	0.2694	0.32398	6.714	0.32478
BaBYFO-5	0.22	0.12	1.5	0.21	0.25523	0.27617	127.3	0.2691
BaBYFO-10	9.3	0.25	0.31	1.04	0.24056	0.28282	3.472	0.28545

In polycrystalline materials, grain and grain boundary structures are key microstructure components that may have a substantial effect on the electrical characteristics. Different activation energies determine the characteristics of charge carriers. Finding activation energies between 0.2 eV and 0.3 eV in $LuFe_2O_4$ and $YFeO_3$ suggests that conduction is governed by charge carrier hopping between Fe^{2+} and Fe^{3+} within the grain[66,67]. While activation energies between 0.6 eV and 0.9 eV can result in heterogeneous microstructure at grain boundaries[68,69]. The value above 0.9 eV is attributed to the diffusion of doubly charged oxygen vacancies[68,70]. Therefore, in the bulk material, the inhomogeneity of microstructure caused by grain boundaries and diffusion of oxygen vacancies govern the conductivity of the sample. However, the conductivity of nanoparticles is entirely determined by the hopping of charge carriers between Fe^{2+} and Fe^{3+} within grains.

3.3.4 MAGNETIC PROPERTIES

3.3.4.1 BULK

The magnetic hysteresis loop at ambient temperature for all samples, as shown in Figure 3.20(a), suggests that all of our co-doped samples exhibit a first order metamagnetic transition. The negative slope seen in the Arrott plots (Figure 3.20(b)) for all samples confirms the first order field-induced magnetic transition, also known as the metamagnetic transition, in accordance with the Banerjee criterion[71]. According to numerous studies on doped BFO, the metamagnetic transition—where a field-induced change from an antiferromagnetic to a ferromagnetic state occurs—occurs at a critical magnetic field of roughly $H_p \sim 0.6$ T[72]. Recently, Dmitry Sokolov and colleagues explained how competition between two magnetic sublattices may result in a structure where the spins are arranged in some locations in an antiferromagnetic manner and in others in a ferromagnetic

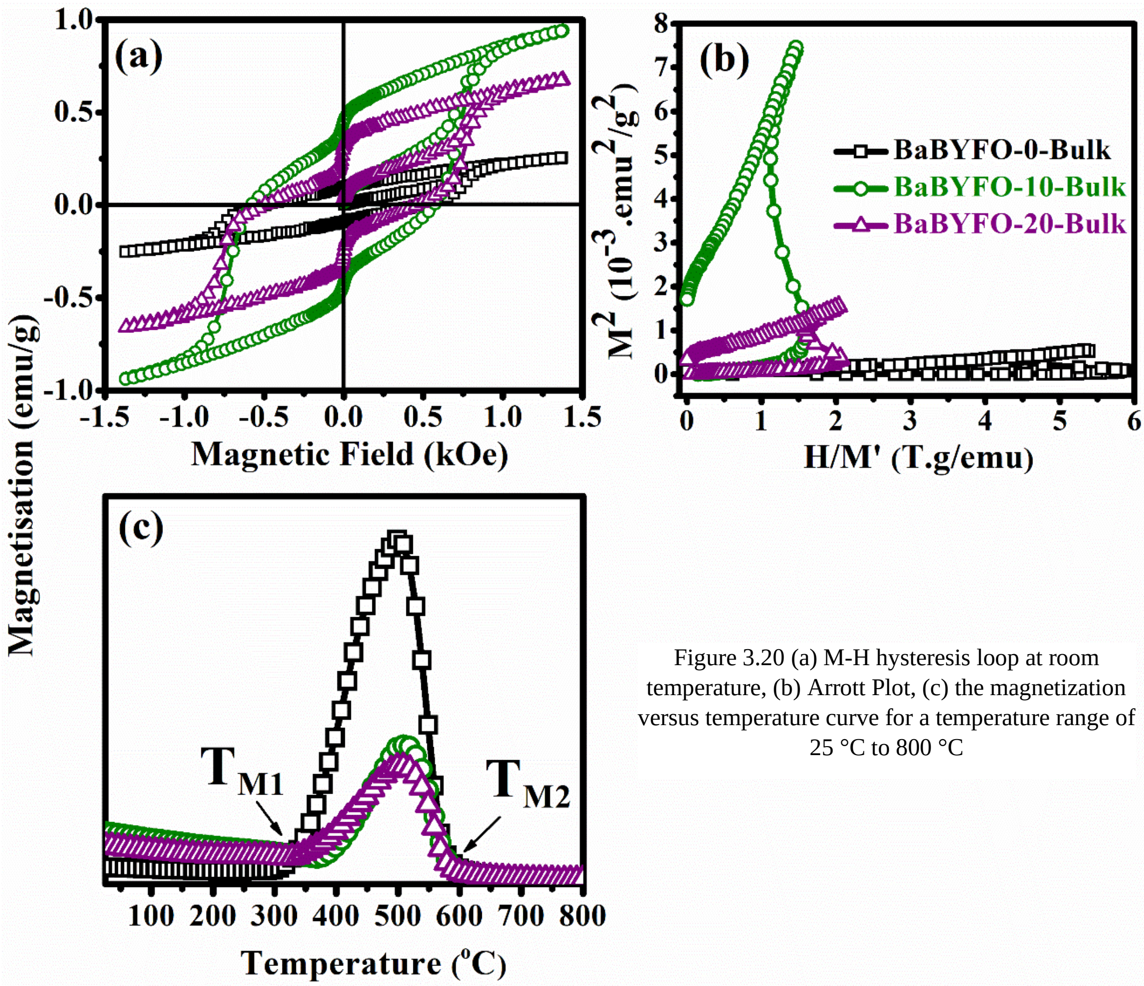

Figure 3.20 (a) M-H hysteresis loop at room temperature, (b) Arrott Plot, (c) the magnetization versus temperature curve for a temperature range of 25 °C to 800 °C

manner[47]. All of these spins have the ability to orient in the direction of the applied field if a sufficient magnetic field is present, exhibiting a first order metamagnetic transition. According to Eq. 3.5, the charge compensation brought on by the substitution of Ba^{2+} ions with Fe^{4+} ions cause the lattice to become ferrimagnetic. Keeping the barium doping concentration constant, the Fe-O1-Fe bond angle increases while the Fe-O1 bond length decreases as the Y concentration rises. Due to yttrium doping, the Fe-O1-Fe bond angle is increased, implying stronger antiferromagnetic properties. Because of this, the co-doped samples display the observed metamagnetic transition as a result of struggle between stronger antiferromagnetic sublattice brought on by yttrium substitution and pre-existing ferrimagnetic sublattice.

Figure 3.20(c) implies that all samples show an antiferromagnetic to a ferromagnetic or ferrimagnetic transition at temperatures, T_{M1} ~ 310 ^{o}C, 368 ^{o}C and 327 ^{o}C [Table 3.8] for BaBYFO-0, BaBYFO-1 and BaBYFO-2 respectively. This is in accordance with the reported remnant magnetizations for BaBYFO-0-Bulk, BaBYFO-10-Bulk, and BaBYFO-20-Bulk of 0.1 emu/g, 0.47 emu/g, and 0.31 emu/g. The co-doped samples' greater magnetism indicates an enhanced ferromagnetic domain that raises the ferromagnetic to antiferromagnetic Neel temperature.

Table 3.8 - Values of remnant polarisation, remnant magnetisation, T_{M1} and T_{M2} values of all samples

Sample Name	Remnant Polarisation, P_r (μC/cm^2)	Remnant Magnetisation, M_r (emu/g)	T_{M1} (^{o}C)	T_{M2} (^{o}C)
BaBYFO-0-Bulk	0.054 - -0.0545	0.093	310	600
BaBYFO-10-Bulk	0.0806 - -0.1131	0.47	368	600
BaBYFO-20-Bulk	-0.0012 - -0.0071	0.32	327	600

3.3.4.2 NANOPARTICLE

The magnetic hysteresis loop at room temperature is shown in Figure 3.21(a) for each sample. As was already noted, the charge compensation necessary as a result of the doping of the Ba^{2+} ion at the site of the Bi^{3+} ion in BFO causes the change in magnetic characteristics in the Ba doped sample. The magnetic properties have been reported to be improved as a result of the incorporation of Fe^{4+} ions, which transform the magnetic spin structure from antiferromagnetic to ferrimagnetic. But in these samples, the Ba doping level is held constant while the Y level is raised, preventing any additional incorporation of Fe^{4+} ions. As a result, these samples' magnetic characteristics show no discernible change. On the other hand, the Fe (3*d*) - O1 (2*p*) orbital overlap is enhanced by a decrease in the length of the Fe-O1 bond, but the opposite is true for the Fe-O1-Fe bond angle. The magnitude of the super-exchange interactions between the nearby Fe spins is determined by the amount of net orbital overlap. Fe-O1 bond length and Fe-O1-Fe bond angle are seen to decrease in all samples, although there isn't a discernible change in magnetic characteristics. For the same reason, while the drop in coercivity is consistent with the smaller particle size, the change in Neel temperature determined from the minimum of the dM/dT curve shown in Figure 3.21(b) is similarly negligible [Table 3.9].

The variation of dielectric constant in presence of magnetic field at room temperature is measured to calculate the magnetodielectric factor measured at 1 MHz. The magnetodielectric factor (MD) is given by,

$$MD(\%) = \frac{\varepsilon'(H) - \varepsilon'(0)}{\varepsilon'(0)} \times 100\% \tag{3.20}$$

The magnetodielectric factor for applied magnetic fields ranging from 0 to 13 kOe is shown

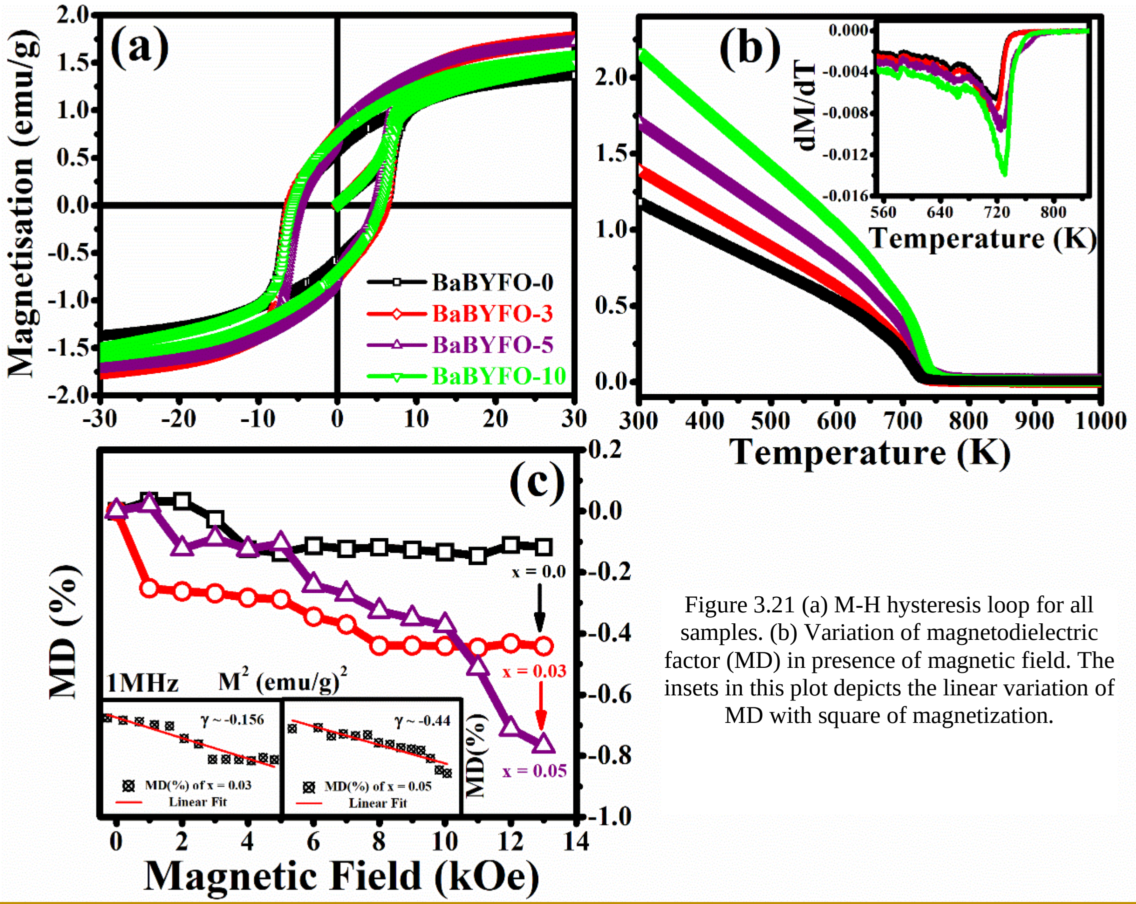

Figure 3.21 (a) M-H hysteresis loop for all samples. (b) Variation of magnetodielectric factor (MD) in presence of magnetic field. The insets in this plot depicts the linear variation of MD with square of magnetization.

in Figure 3.21(c). BaBYFO-5 exhibits the maximum magnetodielectric factor of roughly 0.8 percent at an applied magnetic field of 13 kOe, as seen in the figure. This figure is consistent with previously reported values on comparable BFO co-doping[50,73–75]. This sample has the highest remaining polarisation and magnetization. Additionally, the magnetoelectric coupling nature and the DM interaction of BFO, which is seen to be strongest in this sample, are directly impacted by the octahedral tilt. Therefore, it can be concluded that Y ion doping has the ability to affect the Fe-O1-Fe super-exchange mechanism and the Bi-O hybridization in a way that causes the coupling to increase for this sample.

At nanoscale, the surface to volume ratio becomes large and long-range anti-ferromagnetic order is interrupted at surfaces resulting in weak ferromagnetism due to uncompensated spins at the surface of $BiFeO_3$ nanoparticles in contrast to the bulk counterparts[4,76]. As a result, these nanoparticles reported in present study show much higher remnant magnetisation than its bulk counterparts. The metamagnetic transition or magnetic field induced antiferromagnetic to ferromagnetic phase transition is observed due to ferromagnetic (FM) pinning in antiferromagnetic (AFM) superlattice. At and above the critical pinning field, the pinned ferromagnetic areas in the antiferromagnetic matrix of particles begin to quickly align and develop, culminating in metamagnetic transition[47]. However, as the particle size is reduced, the AFM super exchange interaction is reduced and weak FM is introduced while reducing the AFM-FM interaction as well as metamagnetic transition. Similar observation is found in size dependent study of metamagnetic transition in Ba doped BFO nanoparticles[72]. Therefore, it is evident that the nanoparticles in the present study do not show any metamagnetic transition while their bulk counterpart shows metamagnetic transition.

The thermodynamic potential φ for a multiferroic material can be expressed as,

$$\varphi = \varphi_0 + \alpha P^2 + \frac{\beta}{2} P^4 - PE + \alpha' M^2 + \frac{\beta'}{2} M^4 - MH + \gamma P^2 M^2 \qquad (3.21)$$

Table 3.9 - Remnant (M_r), saturation magnetisation (M_S) and coercivity (H_C) of all samples

Sample Name	**Remnant Magnetisation (emu/g)**	**Saturation Magnetisation (emu/g)**	**Coercivity (Oe)**	**T_N (K)**
BaBYFO-0	0.58	1.39	610	717
BaBYFO-3	0.73	1.72	601	717
BaBYFO-5	0.78	1.77	480	727
BaBYFO-10	0.72	1.57	586	729

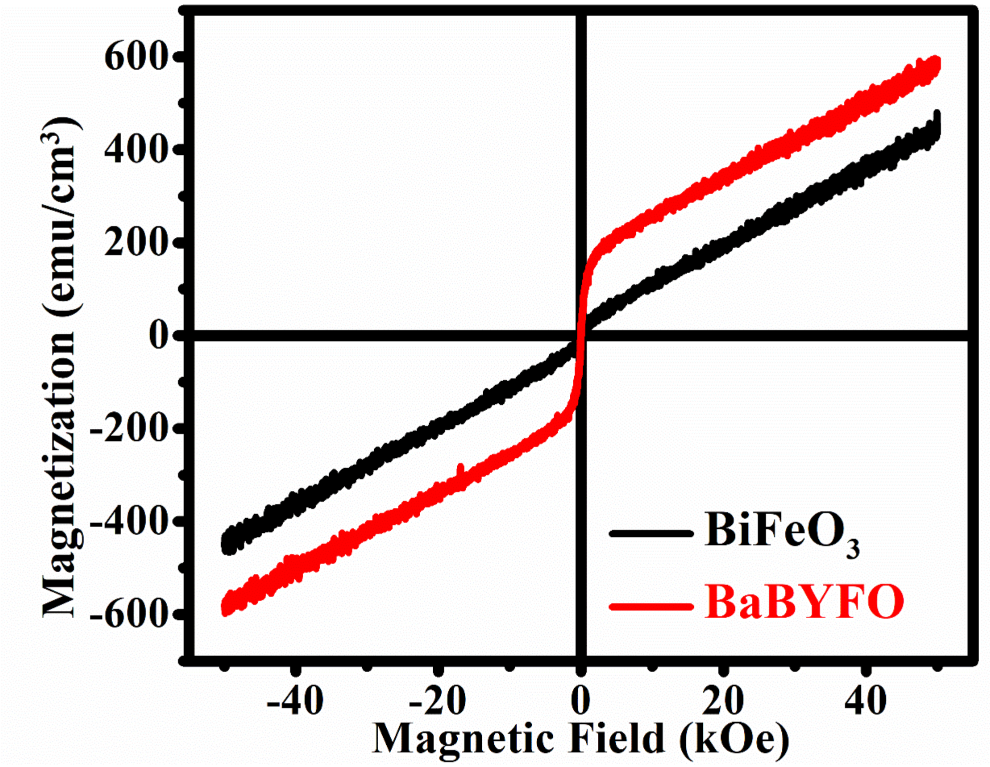

Figure 3.22 demonstrates magnetic hysteresis loop of BFO and BaBYFO thin films measured at room temperature

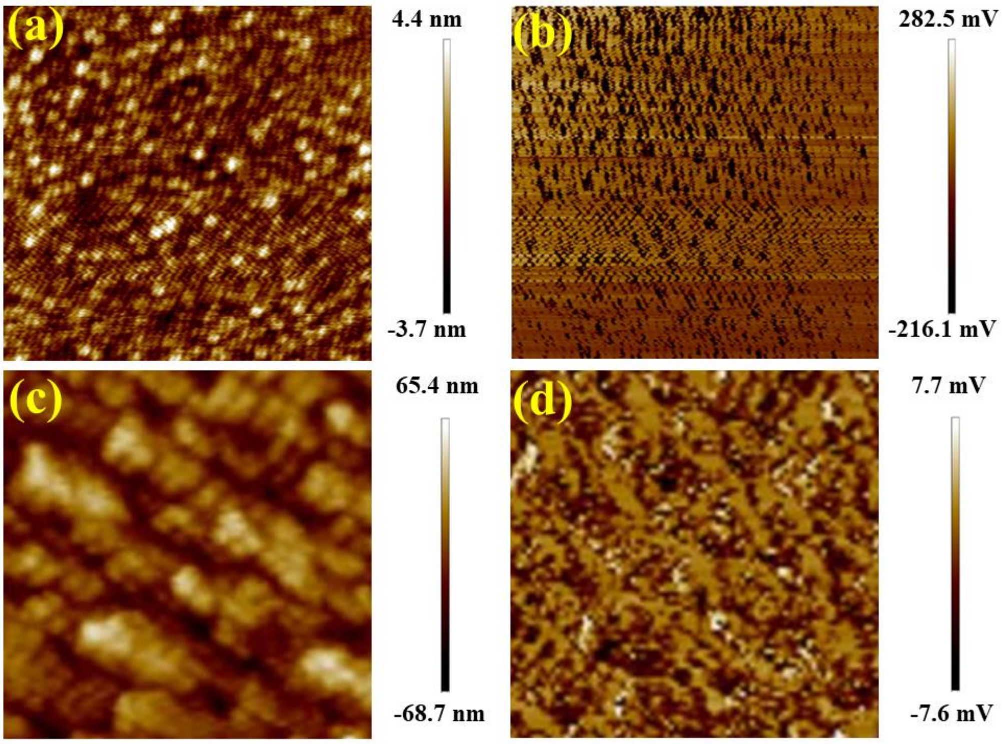

Figure 3.23 1 × 1 μm^2 micrograph showing topographical images of (a) BFO and (c) BaBYFO thin film along with their MFM images demonstrating magnetic domain structures of (b) BFO and (d) BaBYFO thin film.

where, α, β, α′, β′, and γ are coupling coefficients. *P* and *M* are electric polarization and magnetization respectively. The P^2M^2 term represents the coupling between electrical and magnetic ordering. The magnetodielectric factor (MD) is proportional to M^2, as demonstrated by research by Kimura et al. on the magnetic ordering in dielectric materials[77]. The inset of figure 3.21(c) demonstrates that the MD is proportional to M^2. Numerous other multiferroic materials have documented the existence of a similar linear relationship[50,78–80]. The slope of the linear fitting of the MD–M^2 graph can be used to calculate the linear magnetoelectric coupling coefficient (γ). The existence of magnetoelectric coupling in the co-doped samples is confirmed by the linear change in relative permittivity with the square of magnetism.

3.3.4.3 THIN FILM

The magnetic properties (M–H curve) of BFO and BaBYFO thin films produced on STO substrates are tested at room temperature under maximum perpendicular magnetic field of 45 kOe, and the resultant hysteresis loops are shown in Figure 3.22. Under the same applied field, BaBYFO thin film display well-defined (M–H) loops and demonstrate enhanced magnetization compared to undoped BFO thin films. In order to examine the magnetic domain structure of the films, MFM scanning was also done. Figure 3.23(b, d) shows the MFM pictures and the corresponding AFM structures demonstrated in Figure 3.23(a, c) respectively for BFO and BaBYFO thin film acquired at room temperature. Both films reveal a periodic magnetic structure and closely related to its topographical structure. The BaBYFO thin film also demonstrates larger magnetic domains.

3.4 CONCLUSION

In conclusion, the influence of yttrium and barium co-doping on the electric and magnetic characteristics of bismuth ferrite ($Ba_{0.1}Bi_{0.9-x}Y_xFeO_3$) at doping concentrations of x = 0.1 and 0.2 is studied. Although co-doping improved electric and magnetic characteristics such as high dielectric constant, large grain and grain boundary resistances, and high remnant and saturation magnetization, both co-doped samples exhibit first order field-induced metamagnetic transition at a 0.73 T critical field. To eliminate the observed metamagnetic transition, identical nano-structured co-doped samples are created. It is discovered that the magnetic properties of the similarly doped nanoparticles do not exhibit any metamagnetic transition, unlike the bulk equivalent, which does. In contrast to their bulk counterparts, the co-doped barium and yttrium $BiFeO_3$ nanoparticles display enhanced ferromagnetism on the nanoscale. Although the existence of ferroelectric properties could not be proven in bulk equivalents, they are detected in nanoparticles. In general, the magnetic, ferroelectric, and magnetodielectric characteristics of these co-doped nanoparticles are investigated in depth and found to be significantly enhanced. The 5 at. wt. % yttrium doped sample, $Ba_{0.1}Bi_{0.85}Y_{0.05}FeO_3$, is shown to have the greatest dielectric constant, remnant polarization, and magnetodielectric factor, along with stronger ferroelectric domain switching. In order to further improve the magnetoelectric characteristics, this composition has been chosen for the fabrication of epitaxial thin films on $SrTiO_3$ (111) substrate. The successfully manufactured thin film of the Ba and Y co-doped BFO exhibits bigger and stronger ferroelectric domains, as well as enhanced ferromagnetic characteristics and larger magnetic domains, in comparison to the undoped BFO thin film.

REFERENCES

[1] X.M. Liu, S.Y. Fu, C.J. Huang, Synthesis and magnetic characterization of novel CoFe2O 4-BiFeO3 nanocomposites, Mater Sci Eng B Solid State Mater Adv Technol. 121 (2005) 255–260. https://doi.org/10.1016/j.mseb.2005.04.009.

[2] P.R. Vanga, R. V. Mangalaraja, M. Ashok, Sol-gel synthesis and characterisation of (Nd, Cr) co-doped BiFeO3 nanoparticles, J Exp Nanosci. 11 (2016) 1348–1359. https://doi.org/10.1080/17458080.2016.1218556.

[3] L. Sun, X. Yi, X. Ren, al -, X. Ning, J. Huang, L. Li, W. Jingqin, Z. Ying, K. Huiling -, Rhombohedral R3c to orthorhombic Pnma phase transition induced by Y-doping in BiFeO 3 You may also like Synthesis and Electrochemical Performances of Y-Doped Lithium-Rich Layered Li[Li 0.2 Ni 0.2 Mn 0.6]O 2 Cathode Material Enhanced electronic transport in Y-doped TiO 2 branched nanorod array thin film electrodes Study on properties of AgSnO 2 contact materials doped with rare earth Y, (2018). https://doi.org/10.1088/1361-648X/aac74f.

[4] T.J. Park, G.C. Papaefthymiou, A.J. Viescas, A.R. Moodenbaugh, S.S. Wong, Size-dependent magnetic properties of single-crystalline multiferroic BiFeO3 nanoparticles, Nano Lett. 7 (2007) 766–772. https://doi.org/10.1021/NL063039W/SUPPL_FILE/NL063039WSI20061224_021839.PDF.

[5] N. Sheoran, M. Saini, A. Kumar, V. Kumar, T. Kumar, M. Sheoran, Size dependent morphology, magnetic and dielectric properties of BiFeO3 nanoparticles, MRS Advances 2019 4:28. 4 (2019) 1659–1665. https://doi.org/10.1557/ADV.2019.167.

[6] M. Hasan, M.A. Hakim, M.A. Basith, M.S. Hossain, B. Ahmmad, M.A. Zubair, A. Hussain, M.F. Islam, Size dependent magnetic and electrical properties of Ba-doped nanocrystalline BiFeO3, AIP Adv. 6 (2016) 035314. https://doi.org/10.1063/1.4944817.

[7] S. Chaturvedi, R. Das, P. Poddar, S. Kulkarni, Tunable band gap and coercivity of bismuth ferrite-polyaniline core-shell nanoparticles: the role of shell thickness, (2015). https://doi.org/10.1039/c5ra00933b.

[8] S.M. Yusuf, P.K. Manna, M.M. Shirolkar, S.K. Kulkarni, R. Tewari, G.K. Dey, A study of exchange bias in BiFeO3 core/NiFe2O 4 shell nanoparticles, in: J Appl Phys, 2013. https://doi.org/10.1063/1.4803549.

[9] N. Kumar, A. Shukla, N. Kumar, R.N.P. Choudhary, A. Kumar, Structural, electrical, and multiferroic characteristics of lead-free multiferroic: Bi(Co0.5Ti0.5)O3-BiFeO3 solid solution, RSC Adv. 8 (2018) 36939–36950. https://doi.org/10.1039/c8ra02306a.

[10] N. Kumar, A. Shukla, R.N.P. Choudhary, Structural, dielectric, electrical and magnetic characteristics of lead-free multiferroic: Bi(Cd0.5Ti0.5)O3–BiFeO3 solid solution, J Alloys Compd. 747 (2018) 895–904. https://doi.org/10.1016/j.jallcom.2018.03.114.

[11] C. Behera, R.N.P. Choudhary, P.R. Das, Structural and electrical properties of La-modified BiFeO3–BaTiO3 composites, Journal of Materials Science: Materials in Electronics. 25 (2014) 2086–2095. https://doi.org/10.1007/s10854-014-1844-z.

[12] S. Dash, R.N.P. Choudhary, P.R. Das, A. Kumar, Effect of KNbO3 modification on structural, electrical and magnetic properties of BiFeO3, Applied Physics A. 118 (2015) 1023–1031. https://doi.org/10.1007/s00339-014-8862-9.

[13] P. Uniyal, K.L. Yadav, Pr doped bismuth ferrite ceramics with enhanced multiferroic properties, Journal of Physics: Condensed Matter. 21 (2009) 405901. https://doi.org/10.1088/0953-8984/21/40/405901.

[14] A. Chaudhuri, K. Mandal, Enhancement of ferromagnetic and dielectric properties of lanthanum doped bismuth ferrite nanostructures, Mater Res Bull. 47 (2012) 1057–1061. https://doi.org/10.1016/j.materresbull.2011.12.034.

[15] V.A. Khomchenko, D.A. Kiselev, M. Kopcewicz, M. Maglione, V. V. Shvartsman, P. Borisov, W. Kleemann, A.M.L. Lopes, Y.G. Pogorelov, J.P. Araujo, R.M. Rubinger, N.A. Sobolev, J.M. Vieira, A.L. Kholkin, Doping strategies for increased performance in BiFeO3, J Magn Magn Mater. 321 (2009) 1692–1698. https://doi.org/10.1016/J.JMMM.2009.02.008.

[16] J. Wei, R. Haumont, R. Jarrier, P. Berhtet, B. Dkhil, Nonmagnetic Fe-site doping of BiFeO3 multiferroic ceramics, Appl Phys Lett. 96 (2010) 102509. https://doi.org/10.1063/1.3327885.

[17] D. Kothari, V.R. Reddy, A. Gupta, C. Meneghini, G. Aquilanti, Eu doping in multiferroic BiFeO3 ceramics studied by Mossbauer and EXAFS spectroscopy, Journal of Physics Condensed Matter. 22 (2010). https://doi.org/10.1088/0953-8984/22/35/356001.

[18] A. Mukherjee, S. Basu, P.K. Manna, S.M. Yusuf, M. Pal, Enhancement of multiferroic properties of nanocrystalline BiFeO3 powder by Gd-doping, J Alloys Compd. 598 (2014) 142–150. https://doi.org/10.1016/j.jallcom.2014.01.245.

[19] N. Kumar, A. Shukla, N. Kumar, R.N.P. Choudhary, Structural, electrical and magnetic properties of eco-friendly complex multiferroic material: Bi(Co0.35Ti0.35Fe0.30)O3, Ceram Int. 45 (2019) 822–831. https://doi.org/10.1016/j.ceramint.2018.09.249.

[20] N. Kumar, A. Shukla, N. Kumar, S. Sahoo, S. Hajra, R.N.P. Choudhary, Structural, electrical and ferroelectric characteristics of Bi(Fe0.9La 0.1)O3, Ceram Int. 44 (2018) 21330–21337. https://doi.org/10.1016/j.ceramint.2018.08.185.

[21] N. Kumar, A. Shukla, R.N.P. Choudhary, Development of lead-free multifunctional materials Bi(Co0.45Ti0.45Fe0.10)O3, Progress in Natural Science: Materials International. 28 (2018) 308–314. https://doi.org/10.1016/j.pnsc.2018.01.012.

[22] N. Kumar, A. Shukla, C. Behera, R.N.P. Choudhary, Structural, electrical and magnetic properties of Bi(Ni0.45Ti0.45Fe0.10)O3, J Alloys Compd. 688 (2016) 858–869. https://doi.org/10.1016/j.jallcom.2016.07.009.

[23] L. Thansanga, A. Shukla, N. Kumar, R.N.P. Choudhary, Studies of structural, electrical and ferroelectric characteristics of gadolinium and yttrium modified bismuth ferrite, Mater Chem Phys. 263 (2021). https://doi.org/10.1016/j.matchemphys.2021.124359.

[24] N. Kumar, A. Shukla, R.N.P. Choudhary, Structural, electrical and magnetic properties of (Cd, Ti) modified BiFeO3, Physics Letters, Section A: General, Atomic and Solid State Physics. 381 (2017) 2721–2730. https://doi.org/10.1016/j.physleta.2017.06.012.

[25] A. Shukla, N. Kumar, C. Behera, R.N.P. Choudhary, Structural and electrical characteristics of (Co, Ti) modified BiFeO3, Journal of Materials Science: Materials in Electronics. 27 (2016) 7115–7123. https://doi.org/10.1007/s10854-016-4674-3.

[26] S. Pattanayak, B.N. Parida, P.R. Das, R.N.P. Choudhary, Impedance spectroscopy of Gd-doped BiFeO3 multiferroics, Applied Physics A. 112 (2013) 387–395. https://doi.org/10.1007/s00339-012-7412-6.

[27] S. Pattanayak, R.N.P. Choudhary, P.R. Das, Effect of Gd-substitution on phase transition and conduction mechanism of BiFeO3, Journal of Materials Science: Materials in Electronics. 24 (2013) 2767–2771. https://doi.org/10.1007/s10854-013-1168-4.

[28] S. Pattanayak, R.N.P. Choudhary, P.R. Das, Effect of Sm-substitution on structural, electrical and magnetic properties of BiFeO3, Electronic Materials Letters. 10 (2014) 165–172. https://doi.org/10.1007/s13391-013-3050-1.

[29] X. Qi, J. Dho, R. Tomov, M.G. Blamire, J.L. MacManus-Driscoll, Greatly reduced leakage current and conduction mechanism in aliovalent-ion-doped BiFeO3, Appl Phys Lett. 86 (2005) 1–3. https://doi.org/10.1063/1.1862336.

[30] N. Ilić, J.D. Bobić, B. Stojadinovic, A. Džunuzović, M.M. Vijatović Petrović, Z. Dohčević-Mitrović, B. Stojanović, Improving of the electrical and magnetic properties of BiFeO3 by doping with yttrium, Mater Res Bull. 77 (2016) 60–69. https://doi.org/10.1016/j.materresbull.2016.01.018.

[31] N.I. Ilić, A.S. Džunuzović, J.D. Bobić, B.S. Stojadinović, P. Hammer, M.M. Vijatović Petrović, Z.D. Dohčević-Mitrović, B.D. Stojanović, Structure and properties of chemically synthesized BiFeO3. Influence of fuel and complexing agent, Ceram Int. 41 (2015) 69–77. https://doi.org/10.1016/j.ceramint.2014.08.020.

[32] H.Y. Dai, Z.P. Chen, T. Li, R.Z. Xue, J. Chen, Structural and electrical properties of bismuth ferrite ceramics sintered in different atmospheres, J Supercond Nov Magn. 26 (2013) 3125–3132. https://doi.org/10.1007/s10948-013-2130-7.

[33] A. Chaudhuri, K. Mandal, Study of structural, ferromagnetic and ferroelectric properties of nanostructured barium doped Bismuth Ferrite, J Magn Magn Mater. 353 (2014) 57–64. https://doi.org/10.1016/j.jmmm.2013.09.049.

[34] S.K. Pradhan, B.K. Roul, Electrical behavior of high resistivity Ce-doped BiFeO 3 multiferroic, Physica B Condens Matter. 407 (2012) 2527–2532. https://doi.org/10.1016/j.physb.2012.03.061.

[35] L. Thansanga, A. Shukla, N. Kumar, R.N.P. Choudhary, Studies of structural, dielectric and electrical characteristics of Bi(Fe0.85Y0.15)O3 ceramics, Phase Transitions. 94 (2021) 47–61. https://doi.org/10.1080/01411594.2021.1876234.

[36] N. Kumar, A. Shukla, N. Kumar, P. Chaitanya, R.N.P. Choudhary, The structural and dielectric properties of Bi(Fe0.95Sm0.05)O3 ceramic, Ferroelectrics. 588 (2022) 10–17. https://doi.org/10.1080/00150193.2022.2034434.

[37] C. Ederer, N.A. Spaldin, Weak ferromagnetism and magnetoelectric coupling in bismuth ferrite, Phys Rev B. 71 (2005) 060401. https://doi.org/10.1103/PhysRevB.71.060401.

[38] V.A. Khomchenko, D.A. Kiselev, J.M. Vieira, L. Jian, A.L. Kholkin, A.M.L. Lopes, Y.G. Pogorelov, J.P. Araujo, M. Maglione, Effect of diamagnetic Ca, Sr, Pb, and Ba substitution on the crystal structure and multiferroic properties of the BiFeO3 perovskite, J Appl Phys. 103 (2008) 024105. https://doi.org/10.1063/1.2836802.

[39] Y. Yao, W. Liu, Y. Chan, C. Leung, C. Mak, B. Ploss, Studies of Rare-Earth-Doped BiFeO3 Ceramics, Int J Appl Ceram Technol. 8 (2011) 1246–1253. https://doi.org/10.1111/j.1744-7402.2010.02577.x.

[40] J.B. Li, G.H. Rao, J.K. Liang, Y.H. Liu, J. Luo, J.R. Chen, Magnetic properties of Bi(Fe1-xCrx)O3 synthesized by a combustion method, Appl Phys Lett. 90 (2007). https://doi.org/10.1063/1.2720349.

[41] X.J. Xi, S.Y. Wang, W.F. Liu, H.J. Wang, F. Guo, X. Wang, J. Gao, D.J. Li, Enhanced magnetic and conductive properties of Ba and Co co-doped BiFeO3 ceramics, J Magn Magn Mater. 355 (2014) 259–264. https://doi.org/10.1016/j.jmmm.2013.12.036.

[42] M. Azuma, H. Kanda, A.A. Belik, Y. Shimakawa, M. Takano, Magnetic and structural properties of BiFe1-xMnxO3, J Magn Magn Mater. 310 (2007) 1177–1179. https://doi.org/10.1016/j.jmmm.2006.10.287.

[43] G.F. Cheng, Y.H. Huang, J.J. Ge, B. Lv, X.S. Wu, Effects of local structural distortion on magnetization in BiFeO3 with Pr, Ba co-doping, J Appl Phys. 111 (2012) 07C707. https://doi.org/10.1063/1.3673821.

[44] X. Zhang, Y. Sui, X. Wang, J. Tang, W. Su, Influence of diamagnetic Pb doping on the crystal structure and multiferroic properties of the BiFeO3 perovskite, J Appl Phys. 105 (2009) 07D918. https://doi.org/10.1063/1.3079770.

[45] D.H. Wang, W.C. Goh, M. Ning, C.K. Ong, Effect of Ba doping on magnetic, ferroelectric, and magnetoelectric properties in mutiferroic BiFeO3 at room temperature, Appl Phys Lett. 88 (2006) 212907. https://doi.org/10.1063/1.2208266.

[46] R. Das, K. Mandal, Magnetic, ferroelectric and magnetoelectric properties of Ba-doped BiFeO 3, J Magn Magn Mater. 324 (2012) 1913–1918. https://doi.org/10.1016/j.jmmm.2012.01.022.

[47] D.A. Sokolov, N. Kikugawa, T. Helm, H. Borrmann, U. Burkhardt, R. Cubitt, J.S. White, E. Ressouche, M. Bleuel, K. Kummer, A.P. Mackenzie, U.K. Rößler, Metamagnetic texture in a polar antiferromagnet, Nature Physics 2019 15:7. 15 (2019) 671–677. https://doi.org/10.1038/s41567-019-0501-0.

[48] S. Kamba, D. Nuzhnyy, M. Savinov, J. Šebek, J. Petzelt, J. Prokleška, R. Haumont, J. Kreisel, Infrared and terahertz studies of polar phonons and magnetodielectric effect in multiferroic BiFe O3 ceramics, Phys Rev B Condens Matter Mater Phys. 75 (2007). https://doi.org/10.1103/PhysRevB.75.024403.

[49] D. Kothari, V. Raghavendra Reddy, V.G. Sathe, A. Gupta, A. Banerjee, A.M. Awasthi, Raman scattering study of polycrystalline magnetoelectric BiFeO3, J Magn Magn Mater. 320 (2008) 548–552. https://doi.org/10.1016/j.jmmm.2007.07.016.

[50] C.A. Wang, H.Z. Pang, A.H. Zhang, M.H. Qin, X.B. Lu, X.S. Gao, M. Zeng, J.M. Liu, Room temperature multiferroic and magnetodielectric properties in Sm and Sc co-doped BiFeO3 ceramics, J Phys D Appl Phys. 48 (2015). https://doi.org/10.1088/0022-3727/48/39/395302.

[51] C.S. Chen, P.Y. Chen, W.S. Chang, C. Blaise, L.H. Yi, R.R. Chien, V.H. Schmidt, Y.S. Jou, C.S. Tu, Evolution of domain structure and ferroelectric polarization in praseodymium doped BiFeO3 ceramics, Mater Res Bull. 133 (2021). https://doi.org/10.1016/j.materresbull.2020.111054.

[52] R.K. Vasudevan, Y.C. Chen, H.H. Tai, N. Balke, P. Wu, S. Bhattacharya, L.Q. Chen, Y.H. Chu, I.N. Lin, S. v. Kalinin, V. Nagarajan, Exploring topological defects in epitaxial BiFeO3 thin films, ACS Nano. 5 (2011) 879–887. https://doi.org/10.1021/nn102099z.

[53] P. Maksymovych, N. Balke, S. Jesse, M. Huijben, R. Ramesh, A.P. Baddorf, S. v. Kalinin, Defect-induced asymmetry of local hysteresis loops on BiFeO3 surfaces, J Mater Sci. 44 (2009) 5095–5101. https://doi.org/10.1007/s10853-009-3697-z.

[54] S. Dunn, Strain behavior of thin film PbZr0.3Ti0.7O 3 (30/70) examined through piezoforce microscopy, J Appl Phys. 94 (2003) 5964–5968. https://doi.org/10.1063/1.1611635.

[55] G.W. Watson, S.C. Parker, G. Kresse, Ab initio calculation of the origin of the distortion of-PbO, (n.d.).

[56] Z. Zhang, P. Wu, L. Chen, J. Wang, Systematic Variations in Structural and Electronic Properties of BiFeO3 by A-Site Substitution, Appl Phys Lett. 96 (2010) 12905. https://doi.org/10.1063/1.3279137.

[57] G.W. Pabst, L.W. Martin, Y.H. Chu, R. Ramesh, Leakage mechanisms in BiFe O3 thin films, Appl Phys Lett. 90 (2007). https://doi.org/10.1063/1.2535663.

[58] C.-C. Lee, J.-M. Wu, Studies on Leakage Mechanisms and Electrical Properties of Doped BiFeO[sub 3] Films, Electrochemical and Solid-State Letters. 10 (2007) G58. https://doi.org/10.1149/1.2745123.

[59] T. Rojac, M. Kosec, D. Damjanovic, Large Electric-Field Induced Strain in BiFeO3 Ceramics, Journal of the American Ceramic Society. 94 (2011) 4108–4111. https://doi.org/https://doi.org/10.1111/j.1551-2916.2011.04861.x.

[60] K.C. Kao, Electric Polarization and Relaxation, Dielectric Phenomena in Solids. (2004) 41–114. https://doi.org/10.1016/B978-012396561-5/50012-8.

[61] V. Kumar, A. Gaur, N. Sharma, J. Shah, R.K. Kotnala, High temperature dielectric and magnetic response of Ti and Pr doped BiFeO3 ceramics, Ceram Int. 39 (2013) 8113–8121. https://doi.org/10.1016/j.ceramint.2013.03.084.

[62] Reetu, A. Agarwal, S. Sanghi, Ashima, Rietveld analysis, dielectric and magnetic properties of Sr and Ti codoped BiFeO3 multiferroic, J Appl Phys. 110 (2011). https://doi.org/10.1063/1.3646557.

[63] J. Liu, M. Li, L. Pei, J. Wang, B. Yu, X. Wang, X. Zhao, Structural and multiferroic properties of the Ce-doped BiFeO3 thin films, J Alloys Compd. 493 (2010) 544–548. https://doi.org/10.1016/j.jallcom.2009.12.152.

[64] B. Stojadinović, Z. Dohčević-Mitrović, N. Paunović, N. Ilić, N. Tasić, I. Petronijević, D. Popović, B. Stojanović, Comparative study of structural and electrical properties of Pr and Ce doped BiFeO3 ceramics synthesized by auto-combustion method, J Alloys Compd. 657 (2016) 866–872. https://doi.org/10.1016/j.jallcom.2015.09.235.

[65] A.K. Jonscher, The 'universal' dielectric response, Nature. 267 (1977) 673–679. https://doi.org/10.1038/267673a0.

[66] N. Ikeda, H. Ohsumi, K. Ohwada, K. Ishii, T. Inami, K. Kakurai, Y. Murakami, K. Yoshii, S. Mori, Y. Horibe, H. Kitô, Ferroelectricity from iron valence ordering in the charge-frustrated system LuFe2O4, Nature 2005 436:7054. 436 (2005) 1136–1138. https://doi.org/10.1038/nature04039.

[67] S. Hunpratub, P. Thongbai, T. Yamwong, R. Yimnirun, S. Maensiri, Dielectric relaxations and dielectric response in multiferroic BiFeO 3 ceramics, (2009). https://doi.org/10.1063/1.3078825.

[68] S.F. Shao, J.L. Zhang, P. Zheng, Microstructure and electrical properties of ceramics ARTICLES YOU MAY BE INTERESTED IN, J. Appl. Phys. 99 (2006) 84106. https://doi.org/10.1063/1.2191447.

[69] J.L. Zhang, P. Zheng, C.L. Wang, M.L. Zhao, J.C. Li, J.F. Wang, Dielectric dispersion of Ca Cu3Ti4O12 ceramics at high temperatures, Appl Phys Lett. 87 (2005) 1–3. https://doi.org/10.1063/1.2077864.

[70] G. Singh, V.S. Tiwari, P.K. Gupta, Role of oxygen vacancies on relaxation and conduction behavior of ceramic ARTICLES YOU MAY BE INTERESTED IN, J. Appl. Phys. 107 (2010) 64103. https://doi.org/10.1063/1.3309745.

[71] B.K. Banerjee, On a generalised approach to first and second order magnetic transitions, Physics Letters. 12 (1964) 16–17. https://doi.org/https://doi.org/10.1016/0031-9163(64)91158-8.

[72] M. Hasan, M.A. Hakim, M.A. Basith, Size dependent magnetic and electrical properties of Ba-doped nanocrystalline BiFeO 3 ARTICLES YOU MAY BE INTERESTED IN, AIP Adv. 6 (2016) 35314. https://doi.org/10.1063/1.4944817.

[73] F. Pedro-García, L.G. Betancourt-Cantera, A.M. Bolarín-Miró, C.A. Cortés-Escobedo, A. Barba-Pingarrón, F. Sánchez-De Jesús, Magnetoelectric coupling in multiferroic BiFeO 3 by co-doping with strontium and nickel, Ceram Int. 45 (2019) 10114–10119. https://doi.org/10.1016/j.ceramint.2019.02.058.

[74] H. Hemanta Singh, H. Basantakumar Sharma, Investigation on electrical, magnetic and magneto-dielectric properties of yttrium and cobalt co-doped bismuth ferrite nanoparticles, Indian Journal of Physics. 94 (2020) 1561–1572. https://doi.org/10.1007/s12648-019-01611-7.

[75] G. Singh, H.P. Bhasker, R.P. Yadav, S.K. Mandal, A. Kumar, B. Khan, A. Kumar, M.K. Singh, Dielectric, magnetic and magneto-dielectric properties of (La, Co) co-doped BiFeO3, Phys Scr. 94 (2019). https://doi.org/10.1088/1402-4896/ab354a.

[76] M. Hasan, M.F. Islam, R. Mahbub, M.S. Hossain, M.A. Hakim, A soft chemical route to the synthesis of BiFeO3 nanoparticles with enhanced magnetization, Mater Res Bull. 73 (2016) 179–186. https://doi.org/10.1016/J.MATERRESBULL.2015.09.007.

[77] T. Kimura, S. Kawamoto, I. Yamada, M. Azuma, M. Takano, Y. Tokura, Magnetocapacitance effect in multiferroic BiMnO3, Phys Rev B Condens Matter Mater Phys. 67 (2003) 180401. https://doi.org/10.1103/PhysRevB.67.180401.

[78] J. Kolte, A.S. Daryapurkar, M. Agarwal, D.D. Gulwade, P. Gopalan, Magnetoelectric properties of microwave sintered BiFeO3 and Bi0.90La0.10Fe0.95Mn0.05O3 nanoceramics, Mater Chem Phys. 193 (2017) 253–259. https://doi.org/10.1016/j.matchemphys.2017.02.037.

[79] A. Kumar, K.L. Yadav, The effect of Ni substitution on magnetic, dielectric and magnetoelectric properties in BiFe1-xNixO3 system, Physica B Condens Matter. 405 (2010) 4650–4654. https://doi.org/10.1016/j.physb.2010.08.054.

[80] A. Kumar, K.L. Yadav, J. Rani, Low temperature step magnetization and magnetodielectric study in Bi 0.95La 0.05Fe 1-xZr xO 3 ceramics, Mater Chem Phys. 134 (2012) 430–434. https://doi.org/10.1016/j.matchemphys.2012.03.013.

CHAPTER 4

STUDY OF ELECTRIC AND MAGNETIC PROPERTIES OF COMPOSITES

In this chapter we have synthesized composites of Gallium Ferrite and Sodium Bismuth Titanate – Strontium Titanate solid solution with Gadolinium Gallium Garnet and Yttrium Iron Garnet and studied their electric and magnetic properties.

COMPOSITES

$$ME = \frac{Magnetic}{Electric} = \frac{Magnetic}{Mechanical} \times \frac{Mechanical}{Electric}$$

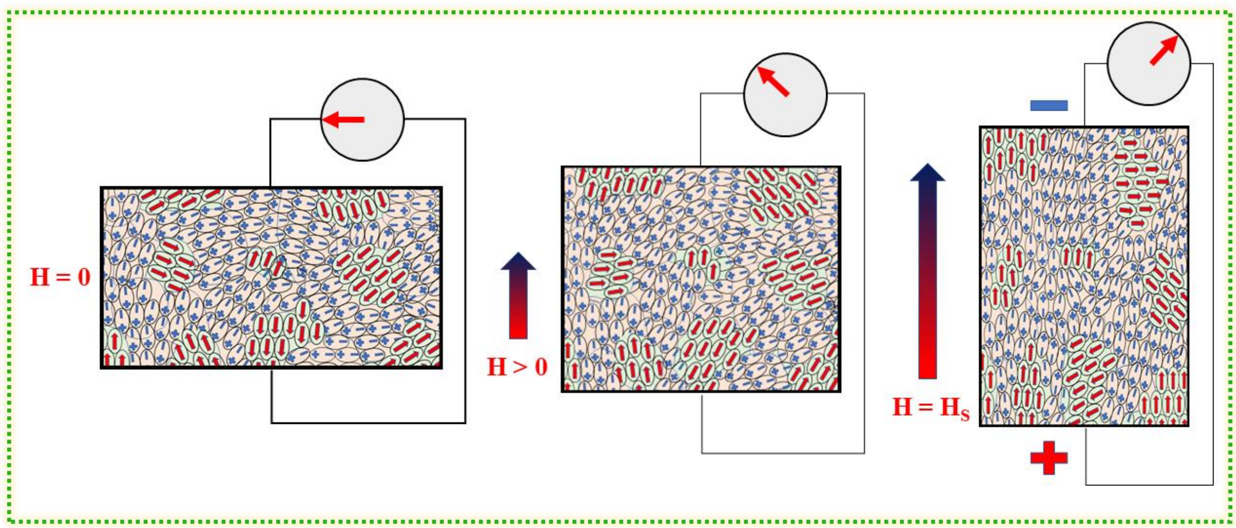

4.1 PREAMBLE

Each phase in multiferroic composites carries distinct ferroic orders, primarily ferromagnetic and ferroelectric. When an electric field is applied, the ferroelectric phase, which is also piezoelectric, produces strain that changes the magnetic characteristics of the magneto-strictive phase and vice versa. As a result, the magnetoelectric (ME) effect is described as a multiplication of piezoelectricity from the ferroelectric phase and magneto-striction from the magnetic phase[1–4].

$$ME = \frac{Magnetic}{Mechanical} \times \frac{Mechanical}{Electric}$$

The two phases can be arranged in a number of different geometries, including (1) 0-3 particulate composite, where particles (0) of one phase are embedded in a matrix (3) of another phase, (2) 2-2 bi-layer composite, where thin layer of one phase is deposited on top of the layer of another phase, and (3) 1-3 composite, where nanotube pillar of one phase is embedded in the matrix of another phase. The best results, however, are shown in the 0-3 particle composite phase, whereas 2-2 geometry is constrained by the clamping effect between layers and 1-3 geometry is constrained by the high conductivity brought on by the connected magnetic phase[5–8].

A well-known multiferroic that has been thoroughly researched for years is bismuth ferrite. Magnetoelectric Gallium Ferrite is one of the very few materials that exhibits multiferroic coupling at room temperature, and higher magnetoelectric coupling (10^{-11} s/m at 4.2 K)[9,10]. Although this material possesses ferroelectricity in its thin film structure, its bulk form exhibits room temperature piezoelectricity and low temperature ferrimagnetism, making it a promising candidate for further study. In addition, $Ga_{2-x}Fe_xO_3$ (GFO) maintains a stable crystallographic phase throughout a broad range of x ($0.7 \leq x \leq 1.2$), which facilitates the properties of the substance. On the other hand, the material's Curie temperature (T_C), or the transition temperature from ferrimagnetic (fM) to paramagnetic (PM) phase, is particularly sensitive to the compositions of the material and the Ga:Fe ratio, making it easy to tune the Curie temperature above ambient temperature. One unit cell of GFO, which has a space group of *Pc*21*n*, has gallium and iron ions that are octahedrally coupled to nearby oxygen ions (Ga2, Fe1, and Fe2), as well as four Gallium ions that are tetrahedrally connected to nearby oxygen ions (Ga1). Fe1 and Fe2 differ based on the antiparallel orientations of their magnetic moments. The ferrimagnetic property of this material improves when a Fe ion substitutes a Ga2 ion due to similar ionic radii, and ferromagnetic interaction with one of the neighboring Fe ions, also known as site-disorder. On the other hand, the material becomes polarized as a result of the centrosymmetric symmetry being broken by the distortion in the tetrahedrons and octahedrons. High leakage and a low magnetic transition temperature, however, prevent this material from being used in practical applications. Numerous possible solutions have been proposed, such as doping, the development of composites, and the modification of atmospheric conditions during synthesis. There are still a number of areas to investigate in order to enhance this material's multiferroic properties.

Numerous studies have been conducted on composites of magnetic ferrites with ferroelectric materials ($BiFeO_3$, $BaTiO_3$, and PZT), and the results are encouraging in terms of improving magnetoelectric coupling. High magneto-strictive $CoFe_2O_4$ and other magnetic ferrites with high conductivities have been found to improve the magnetoelectric coupling but increase the conductivity and dielectric loss of composite materials as well which is detrimental to their practical application[11–16]. In this chapter, Gadolinium Gallium Garnet (GGG) and Yttrium Iron Garnet (YIG), both having high density and high resistivity, are used to synthesize composite materials with Gallium Ferrite ($Ga_{0.8}Fe_{1.2}O_3$, GFO). As previously mentioned, the ability of $Ga_{2-x}Fe_xO_3$ to increase ferrimagnetism while raising the magnetic Curie temperature (T_C) can be greatly aided by increasing the Fe:Ga ratio. Therefore, x = 1.2 composition of $Ga_{2-x}Fe_xO_3$ is chosen for the formation of composites in this chapter. Although GGG is paramagnetic in room temperature, a significant enhancement in dielectric, and magnetodielectric properties along with a reduction in leakage current by four orders of magnitude have been achieved in GFO-GGG composites due to surrounding of GFO grains with highly resistive GGG particles and grain size reduction. On the other hand, YIG being room temperature ferromagnet having magneto-strictive property (-3 ppm), significant improvement in magnetic characteristics of the GFO-YIG composites along with an increment of Curie temperature beyond room temperature has been achieved.

As previously mentioned, GFO is piezoelectric at room temperature, but bismuth sodium titanate ($Na_{0.5}Bi_{0.5}TiO_3$, also known as NBT) is another interesting material to study due to its strong room temperature ferroelectricity and high ferroelectric Curie temperature of 320 °C. At ambient temperature, it is a perovskite *R*3*c* structure; but, beyond 225 °C, it transitions into a tetragonal phase. However, the high conductivity of the material makes *D-E* measurements of this material challenging. In the past, solid solutions of NBT containing many perovskites have been investigated in an effort to get characteristics appropriate for technological applications[17–24]. However, due to the high Curie temperature of NBT and the other perovskite materials employed for the solid solution, the majority of the compounds ultimately had high Curie temperatures[25]. In order to create the solid solution and lower the Curie temperature to a level that is adequate for technological applications, $SrTiO_3$, which has a phase transition temperature from cubic to tetrahedral at 105 K, is utilized[26–29]. At ambient temperature, Sr^{2+}, whose ionic radii are between Na^{1+} and Bi^{3+}, settles in the Na/Bi sites of the NBT-ST solid solution and modifies the crystal structure of NBT[30]. It has been determined that the concentration of x = 0.5 has a transition temperature that is sufficiently close to room temperature (300 K at 3 kHz) and a high enough dielectric constant at low frequency (~560) when compared to other concentrations of $SrTiO_3$ in the $Sr_x(Na_{0.5}Bi_{0.5})_{1-x}TiO_3$ solid solution ($0.25 \leq x \leq 0.75$)[17]. This sample is appropriate for use as microwave absorption materials since it also demonstrates significant microwave absorption (MAMs). In this study, 0–3 particulate composite is created by embedding ferromagnetic Yttrium Iron Garnet (YIG) particles in a matrix of Bismuth Sodium Titanate–Strontium Titanate ($Sr_{0.5}Bi_{0.25}Na_{0.25}TiO_3$, SNBT50) solid solution. These composites exhibit improved ferroelectric and magnetodielectric characteristics and presence of enhanced coupling between magnetic and electric properties.

4.2 EXPERIMENTAL METHODS

4.2.1 SYNTHESIS

4.2.1.1 $Ga_{0.8}Fe_{1.2}O_3$ – $Gd_3Ga_5O_{12}$

The (1-x) GFO – x GGG ceramics are synthesised using the sol-gel method for two different GGG concentrations (x = 0.1 and 0.2) while maintaining a constant final sintering temperature of 1300 ºC and for two different sintering temperatures (1300 ºC and 1350 ºC) while maintaining a constant GGG concentration of x = 0.2. The samples are designated as Sample[0,1300], Sample[0.1,1300], Sample[0.2,1300], and Sample[0.2,1350], with the first parameter inside the bracket denoting the concentration of GGG present in the composite and the second parameter denoting the annealing temperature in degrees Celsius. Two varying parameters determine the properties of the synthesised samples.

$Ga(NO_3)_3.H_2O$ (99.9% trace metal basis), $Gd(NO_3)_3.6H_2O$ (99.9% trace metal basis), and $Fe(NO_3)_3.9H_2O$ (99.95%) are taken in accordance with the stoichiometric ratios and dissolved in double distilled water first. The resulting mixture is continually mixed and heated for 24 hours at 80 °C. The dried brown powder is then subjected to an 8-hour calcination process at 600 °C in air, followed by 55 MPa pressure pressing to form pellets with similar masses, diameters (5 mm), and thicknesses (1 mm). Sample[0,1300], Sample[0.1,1300], and Sample[0.2,1300] pellets are annealed at 1300 ºC, and Sample[0.2,1350] pellet is annealed at 1350 ºC for 4 hours to get the final crystalline form. On these pellets, all measurements are made while they are at room temperature.

4.2.1.2 $Ga_{0.8}Fe_{1.2}O_3$ – $Y_3Fe_5O_{12}$

$Ga_{0.8}Fe_{1.2}O_3$ (GFO), $0.95Ga_{0.8}Fe_{1.2}O_3$–$0.05Y_3Fe_5O_{12}$ (GFO-5YIG), and $0.9Ga_{0.8}Fe_{1.2}O_3$–$0.1Y_3Fe_5O_{12}$ (GFO-10YIG) ceramics are synthesized using the sol-gel technique. $Ga(NO_3)_3.H_2O$, $Y(NO_3)_3.6H_2O$, and $Fe(NO_3)_3.9H_2O$ are taken according to their stoichiometric ratios and dissolved in double distilled water. The resulting solution is heated at 80 °C until entirely dried and calcined at 600 °C for 8 h afterward. Next, the calcined powder is pressed into pellets of equal mass, diameter, and thickness and finally annealed at 1300 ^oC for 4 hours.

4.2.1.3 $Sr_{0.5}(Na_{0.5}Bi_{0.5})_{0.5}TiO_3$ – $Y_3Fe_5O_{12}$

The solid-state reaction approach was used to synthesize (1-x) $Sr_{0.5}Bi_{0.25}Na_{0.25}TiO_3$ (SNBT50) – x $Y_3Fe_5O_{12}$ (YIG) composites with x = 0.0, 0.1, and 0.2. In an acetone medium, the stoichiometric concentrations of high purity Bi_2O_3 (99 % pure, Loba Chemie), TiO_2 (98 % pure, Loba Chemie), Na_2CO_3 (99.5 % pure, Loba Chemie), and $SrCO_3$ (reagent grade, Loba Chemie) were well combined. To synthesize the composites with varying amounts of YIG, Y_2O_3 and Fe_3O_4 (> 99 %, Sigma-Aldrich) were added in appropriate proportions. After 8 h of grinding in an agate mortar, the mixture was calcined in an alumina crucible at 1173 K for 12 h in air before being cooled to room temperature at a rate of 80 K/h. To prevent bismuth loss, the calcined samples were pelletized into a 5-mm-diameter disk, sintered at 1223 K for 4 hours in closed alumina crucibles, and cooled to ambient temperature at a rate of 1 K/min.

4.2.2 CHARACTERIZATION

The Rigaku SmartLab X-Ray diffractometer uses Cu-K_α radiation with a wavelength of 1.5406 Å to record X-ray diffraction (XRD) patterns. Visualization for Electronic Structural Analysis (VESTA) software is used to visualise Rietveld refinement performed using MAUD software for all samples in order to determine the unit cell parameters. Energy dispersive x-ray analysis (EDAX) is performed on each sample with a scanning electron microscope (SEM) equipped with an AMETEK EDAX QUANTA 200. Using a vibrating sample magnetometer, magnetic measurements are made (VSM, LakeShore model 665). Using the Precision Premier II, Precision Materials Analyzer, electrical polarizations and leakage current densities are measured (Radiant Technologies Inc.). The dielectric characteristics of the samples are determined using an LCR metre (NF Corporation LCR Meter ZM2376). Pellets with a contact area of 0.2 cm^2 on both sides of the synthesized pellets are created using silver paste (Sigma-Aldrich, 99.9 %) for the measurements of ferroelectric and dielectric characteristics.

4.3 RESULTS AND DISCUSSION

4.3.1. STRUCTURE AND MORPHOLOGY

4.3.1.1 $Ga_{0.8}Fe_{1.2}O_3$ – $Gd_3Ga_5O_{12}$

Figure 4.1 shows the X-Ray diffraction results for each sample. To comprehend the phase and crystal structures of the materials, Rietveld refinement analysis and Williamson-Hall analysis are also carried out, and the results are presented in Figure 4.1. In order to verify the presence of the necessary orthorhombic (*Pc*21*n*) gallium ferrite (GFO) phase and gadolinium gallium garnet ($Gd_3Ga_5O_{12}$, GGG), respectively, the ICDD card numbers 761005 and 9013458 are used. The coexistence of the two phases in the composites without the presence of any other phases or compounds supports their chemical compatibility for forming composite. As anticipated, increasing concentration gradually strengthens the diffraction peak at 32.19° that corresponds to GGG phase, whereas increasing annealing temperature has no effect on the intensity of the peak as the concentration of GGG remains same. The parameters in Table 4.1, which are derived from the Rietveld refinement analysis and the Williamson-Hall (W-H) analysis, include lattice distance, unit cell volume, bond length, bond angles, crystallite size, and strain. The compressive strain has grown with increasing GGG content and annealing temperature. The average bond length of Ga1-O, Ga2-O, Fe1-O, and Fe2-O are determined to be 1.776 Å, 2.127 Å, 1.971 Å, and 2.149 Å, respectively.

These values are in good agreement with theoretical values and neutron diffraction studies[10,31]. With increasing GGG concentrations, it is seen that the Fe1-O bond grows while the Ga2-O and Fe2-O gradually shrink. Fe1-O is seen to decrease while Ga1-O, Ga2- O, and Fe2-O increase with increasing annealing temperature while keeping the GGG concentration constant. Increased orthorhombic distortion of the GFO unit cells in the composite materials is implied by the increase in the value of $\sqrt{2}c/b$. The FESEM studies in Figure 4.2 demonstrate a steady reduction in grain size with increasing GGG concentration, which can be explained by the Zener model. The Smith-Zener

Table 4.1 - Lattice Parameters of all samples calculated from Rietveld refinement and Williamson-Hall analysis

Sample Name	**Lattice Parameters (Å), Volume (Å^3), Crystallite Size (nm) and Strain**	**Bond Length (Å) and Distortion**	**Bond Angles (º)**
Sample[0,1300]	c/a = 0.5815 $\sqrt{2}$c/b = 0.7629 V = 417.45 d = 52.69 ± 4.1 e = -3.91E-4	Ga1-O = 1.776 Ga2-O = 2.127 Fe1-O = 1.971 Fe2-O = 2.149	Ga1-O2-Ga2 = 116.62 Ga1-O6-Fe2 = 128.69 Ga2-O4-Ga1 = 120.51 Fe2-O4-Ga1 = 124.11 Fe1-O1-Ga2 = 177.51 Fe1-O2-Ga2 = 112.09 Fe1-O3-Ga2 = 117.06
Sample[0.1,1300]	c/a = 0.5807 $\sqrt{2}$c/b = 0.7642 V = 413.63 d = 50.96 ± 3.45 e = -5.01E-4	Ga1-O = 1.801 Ga2-O = 2.061 Fe1-O = 1.989 Fe2-O = 2.114	Ga1-O2-Ga2 = 111.78 Ga1-O6-Fe2 = 122.48 Ga2-O4-Ga1 = 125.69 Fe2-O4-Ga1 = 120.33 Fe1-O1-Ga2 = 171.05 Fe1-O2-Ga2 = 110.62 Fe1-O3-Ga2 = 126.86
Sample[0.2,1300]	c/a = 0.5800 $\sqrt{2}$c/b = 0.7638 V = 415.75 d = 43.58 ± 3.74 e = -6.47E-4	Ga1-O = 1.725 Ga2-O = 2.06 Fe1-O = 2.099 Fe2-O = 2.085	Ga1-O2-Ga2 = 116.94 Ga1-O6-Fe2 = 114.78 Ga2-O4-Ga1 = 132.4 Fe2-O4-Ga1 = 111.43 Fe1-O1-Ga2 = 165.35 Fe1-O2-Ga2 = 100.45 Fe1-O3-Ga2 = 121.25
Sample[0.2,1350]	c/a = 0.5809 $\sqrt{2}$c/b = 0.7647 V = 415.59 d = 40.06 ± 3.74 e = -5.99E-4	Ga1-O = 1.815 Ga2-O = 2.166 Fe1-O = 2.081 Fe2-O = 2.103	Ga1-O2-Ga2 = 116.64 Ga1-O6-Fe2 = 133.46 Ga2-O4-Ga1 = 139.2 Fe2-O4-Ga1 = 123.6 Fe1-O1-Ga2 = 158.35 Fe1-O2-Ga2 = 109.28 Fe1-O3-Ga2 = 122.35

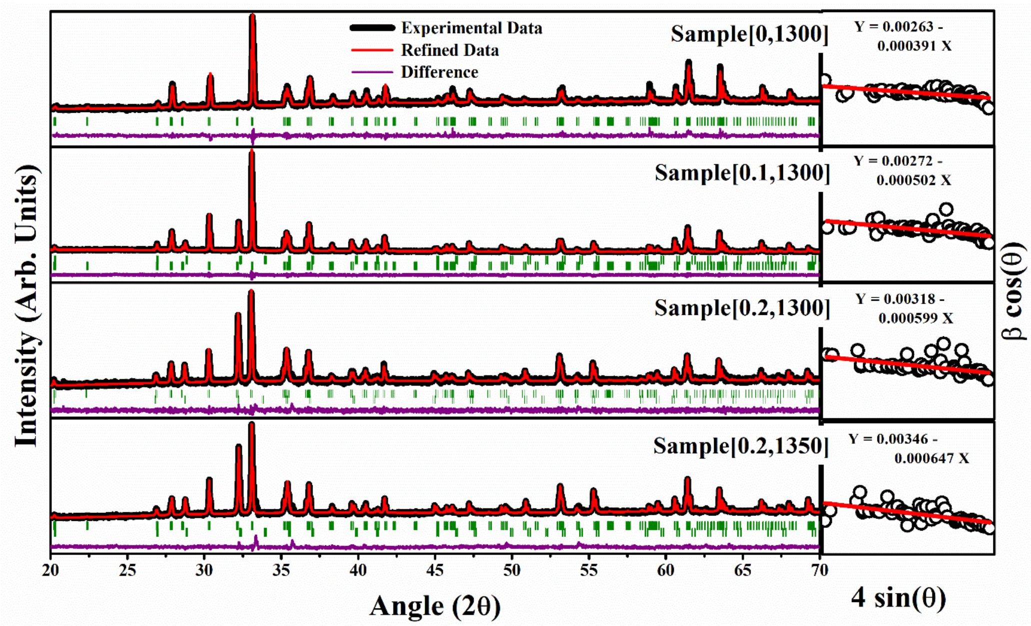

Figure 4.1 (Left) The room temperature XRD data for all samples along with their Rietveld Refinement data are shown. On the right side of each image, the Williamson-Hall analysis of the corresponding samples are plotted depicting the crystallite size and strain of the samples.

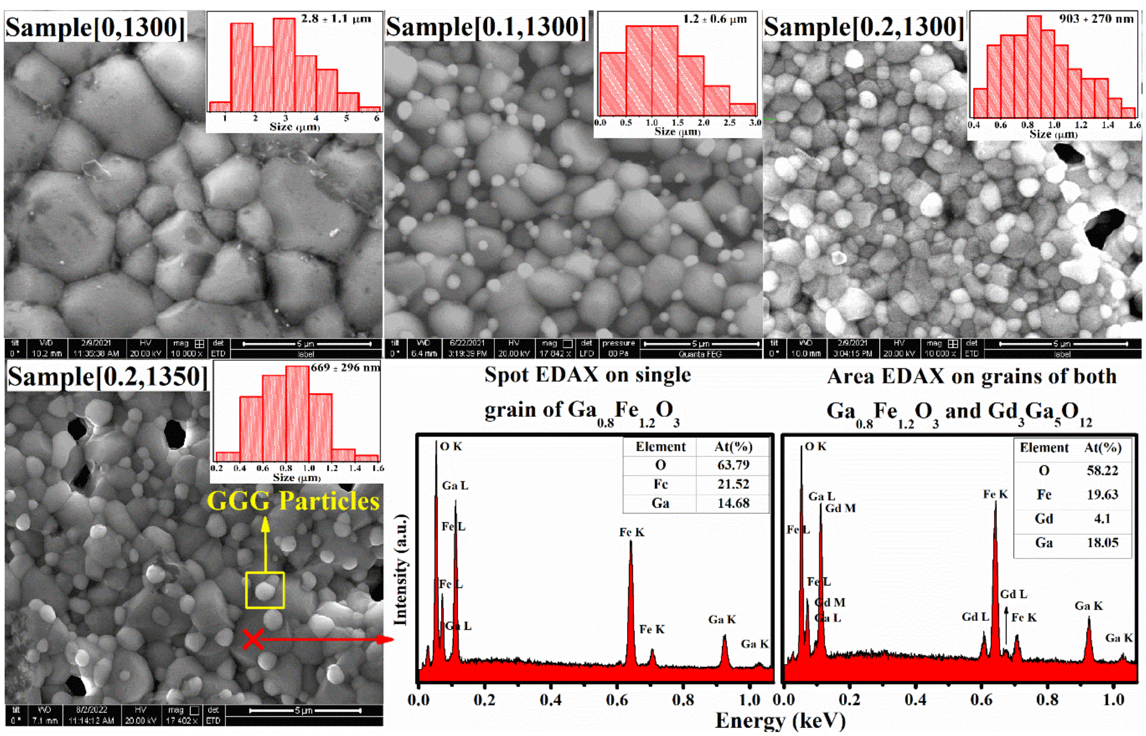

Figure 4.2 FESEM images of all samples along with spot and area EDAX analysis of Sample[0.2,1350] indicating the presence of expected elements in the composites in desired ratio.

equation, can be used to express the grain size as follows[32],

$$\frac{D}{r} = \frac{4}{3f} \quad (4.1)$$

Here, D stands for the grain size, r for second phase particle radius, and f for second phase particle volume fraction. As a result, the grain size decreases when increasing GGG proportion is used as a second material in composites. As a result of a reduction in pore size, raising the annealing temperature in Sample[0.2,1350] to 1350 ºC further reduces the grain size to 669 nm [Table 4.1].

Figure 4.2 shows the EDAX data for Sample[0.2,1350]. The area analysis has been performed on an area of grains including both $Ga_{0.8}Fe_{1.2}O_3$ and GGG particles, as opposed to the spot analysis, which has been performed on a single grain of $Ga_{0.8}Fe_{1.2}O_3$. The spot analysis confirms that only Ga, Fe, and O ions are present, with a Ga:Fe:O ratio of 0.8:1.173:3.476. In the spot analysis, no further peaks that correlate to Gd are seen. However, the area analysis reveals the desired atomic percentages of Gd, Ga, Fe, and O in the material. As a result, our investigation validates the existence of GGG particles embedded in a continuous media of gallium ferrite.

4.3.1.2 $Ga_{0.8}Fe_{1.2}O_3$ – $Y_3Fe_5O_{12}$

The orthorhombic (*Pc*21*n*) GFO phase and cubic (*Ia* -3*d*) YIG are confirmed by the XRD data of all samples using the JCPDS card numbers 00-070-0439 and 10898182, respectively. The composites created by the breakdown of YIG contain a minor amount of $YFeO_3$ (Card no.

Table 4.2 - Lattice Parameters, grain size and magnetic parameters of all samples

Sample Name	Phase Percentages	Lattice Parameters	R Parameters
GFO	100 % GFO	a = 8.83 b = 9.41 c = 5.075 V = 421.49	R_{wp}=2.73 R_b=1.94 R_{exp}=0.43
GFO-5YIG	94.6% GFO 4.7 % YIG 0.66% $YFeO_3$	a = 8.80 b = 9.41 c = 5.090 V = 421.61	R_{wp}=2.86 R_b=2.12 R_{exp}=0.41
GFO-10YIG	87% GFO 11 % YIG 2% $YFeO_3$	a = 8.78 b = 9.44 c = 5.095 V = 422.12	R_{wp}=2.49 R_b=1.92 R_{exp}=0.44

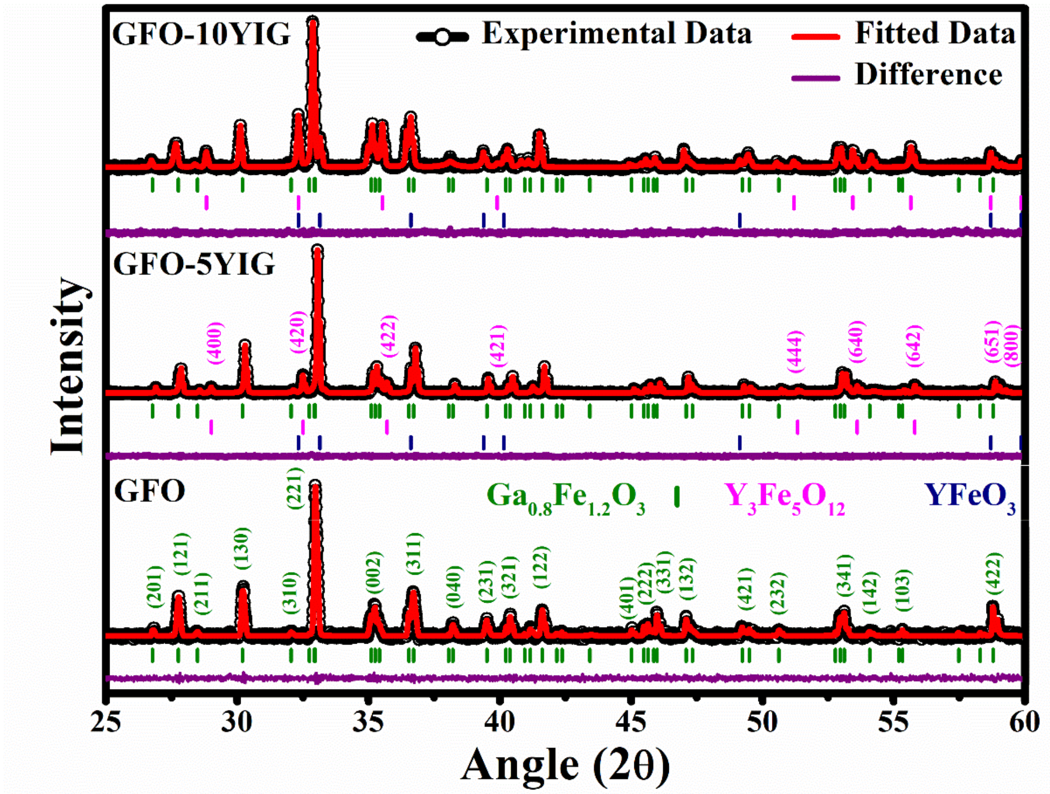

Figure 4.3 (a) depicts Room temperature XRD data along with Rietveld refinement analysis

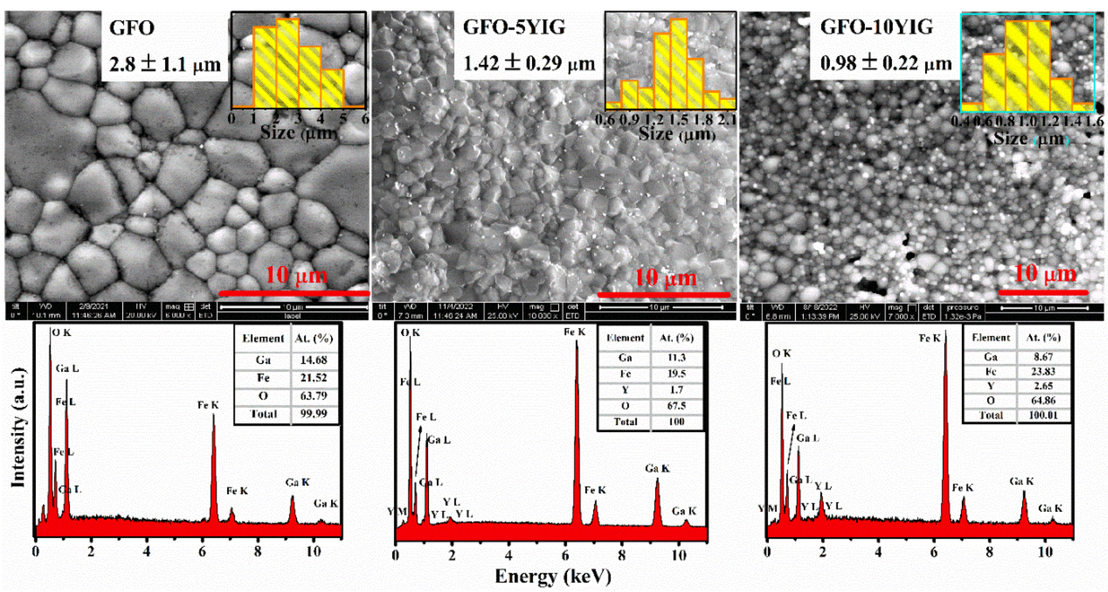

Figure 4.4 represents FESEM images along with EDAX spectroscopy. The insets of FESEM images depicts size distribution of the grains.

10860171), tabulated in Table 4.2.

According to the FESEM data illustrated in Figure 4.4, the Zener model [Eq. 4.1] can be used to explain how grain size gradually decreases as YIG concentration rises. The Ga:Fe:O ratio in

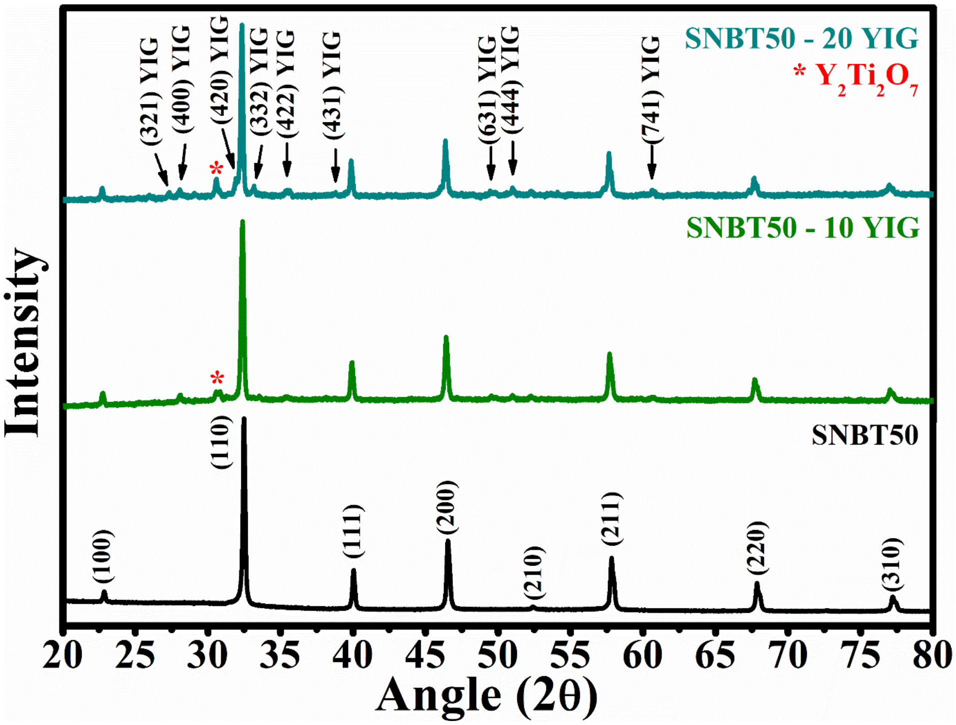

Figure 4.5 The room temperature X-Ray diffraction data for all samples are depicted.

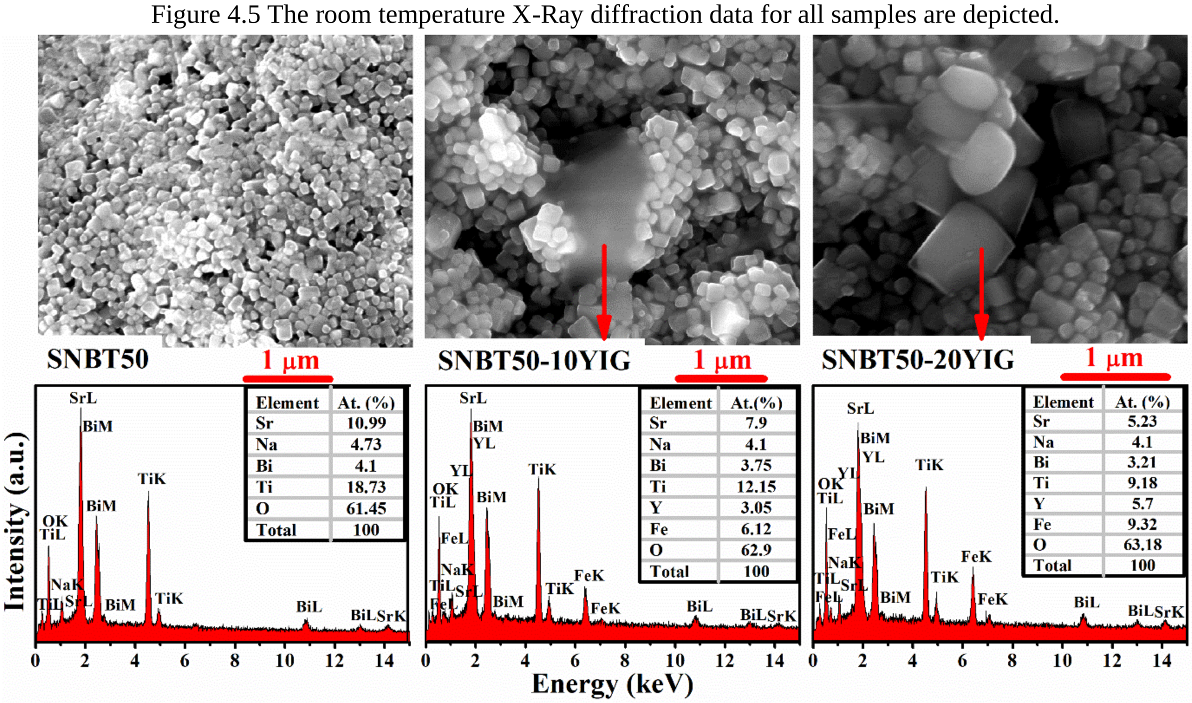

Figure 4.6 The FESEM data demonstrates the formation of 0-3 particulate composites. The EDAX spectroscopy of all samples are also shown along with the tabulated atomic percentage of elements present in the materials.

GFO, according to the EDAX data, is 0.8:1.173:3.476, which corresponds to the intended Ga:Fe ratio of $Ga_{0.8}Fe_{1.2}O_3$. The presence of Y, Ga, Fe, and O in their predicted ratio is also confirmed by the tabulated atomic percentages of each element together with the EDAX spectra of the composites.

4.3.1.3 $Sr_{0.5}(Na_{0.5}Bi_{0.5})_{0.5}TiO_3$ – $Y_3Fe_5O_{12}$

Figure 4.5 displays the XRD results for each sample. The reflection at 30.67° on the XRD profile of the composites confirms the existence of a minor amount of the parasitic phase, $Y_2Ti_2O_7$ (ICDD Card No. 00-042-0413). The interaction of SNBT50 and YIG at the interfaces results in the production of this parasitic phase.

Figure 4.6 depicts FESEM images of YIG particles that are separated from other YIG particles at a considerable distance and surrounded by smaller SNBT50 particles. This aids in the formation of composites composed of 0–3 particles. In addition to the tabulated atomic percentages of all the elements present in the samples, the EDAX spectra of each sample are collected and displayed in Figure 4.6. EDAX analysis found the Sr:Bi:Na:Ti:O ratio for SNBT50 to be 0.58:0.25:0.22:1:3.28. This ratio verifies the oxygen content and expected elemental ratios of the samples. However, the ratio of Sr:Bi:Na:Ti:Y:Fe:O for 0.9($Sr_{0.5}Bi_{0.25}Na_{0.25}TiO_3$) - 0.1($Y_3Fe_5O_{12}$) and 0.8($Sr_{0.5}Bi_{0.25}Na_{0.25}TiO_3$) - 0.2($Y_3Fe_5O_{12}$) is 0.65:0.34:0.31:1:0.25:0.51:5.2 and 0.57:0.45:0.35:1:0.62:1.02:6.88 respectively confirming enriched amount of oxygen in all the samples.

4.3.2 ELECTRIC POLARIZATION

4.3.2.1 $Ga_{0.8}Fe_{1.2}O_3$ – $Gd_3Ga_5O_{12}$

High leakage current is a major factor that prevents GFO from having a broad range of practical applications, making the research of leakage current particularly significant[12,13]. As a result, Figure 4.7 shows the variation of the leakage current density (J) with an applied electric field (E) for all samples. With the steady reduction of grain size, which results in an increase in the number of grain boundaries, it is seen that the leakage current steadily decreases in consistency. In Sample[0.2,1350], leakage current is reduced by four order of magnitude at an applied electric field of roughly 41 kV/cm. The following part will explore and further examine the log(J) versus log(V) plots in order to better understand the process underlying the decrease in leakage current.

The Space Charge Limited Conduction (SCLC) mechanism, where the current is dominated by the movement of charges injected from the electrodes and the current density is provided by [33,34],

$$\log(J_{SCLC}) = 2\log(AV) \qquad (4.2)$$

where,

$$A = \sqrt{\frac{9\mu\varepsilon_0 K}{8d^3}} \qquad (4.3)$$

For Ohmic conduction where the leakage current is mainly governed by the intrinsic charges present in the sample and the current density is directly proportional to the applied field voltage[35],

$$J \propto V \qquad (4.4)$$

For the Grain Boundary Limited Conduction (GBLC), where the current is essentially independent of the applied field and the slope value is significantly less than 1. The initial flow of leakage current in Sample[0,1300] and Sample[0.1,1300] is governed by ohmic conduction and space charge restricted conduction, according to the log(J) - log(V) figure shown in Figure 4.7. Due to the high leakage current of Sample[0,1300], the maximum applied voltage is only 256 V. This sample exhibits a rounded polarisation hysteresis loop (*D*-*E*) for the same reason. Up to an applied voltage of around 500 V, the leakage is marginally reduced for Sample[0.1,1300] and is controlled by a combination of the ohmic and SCLC mechanisms. As the applied voltage is increased further, the leakage current increases dramatically, and the trap-mediated SCLC mechanism takes control and regulates the flow of charges[35]. This happens because there are partially-occupied trap states between the equilibrium Fermi level and conduction band. Up to an applied voltage of 2000 V, the current flow of Sample[0.2,1300] is dominated by ohmic conduction, which accounts for the sample's lower leakage current readings. However, it is discovered that the conduction for Sample[0.2,1350] is initially controlled by the Grain Boundary Limited Conduction (GBLC) mechanism, which accounts for the least leakage current found in this sample. As the applied voltage rises, the grain boundaries degrade and the flow of charge carriers suddenly increases, combining the ohmic and SCLC mechanisms. As

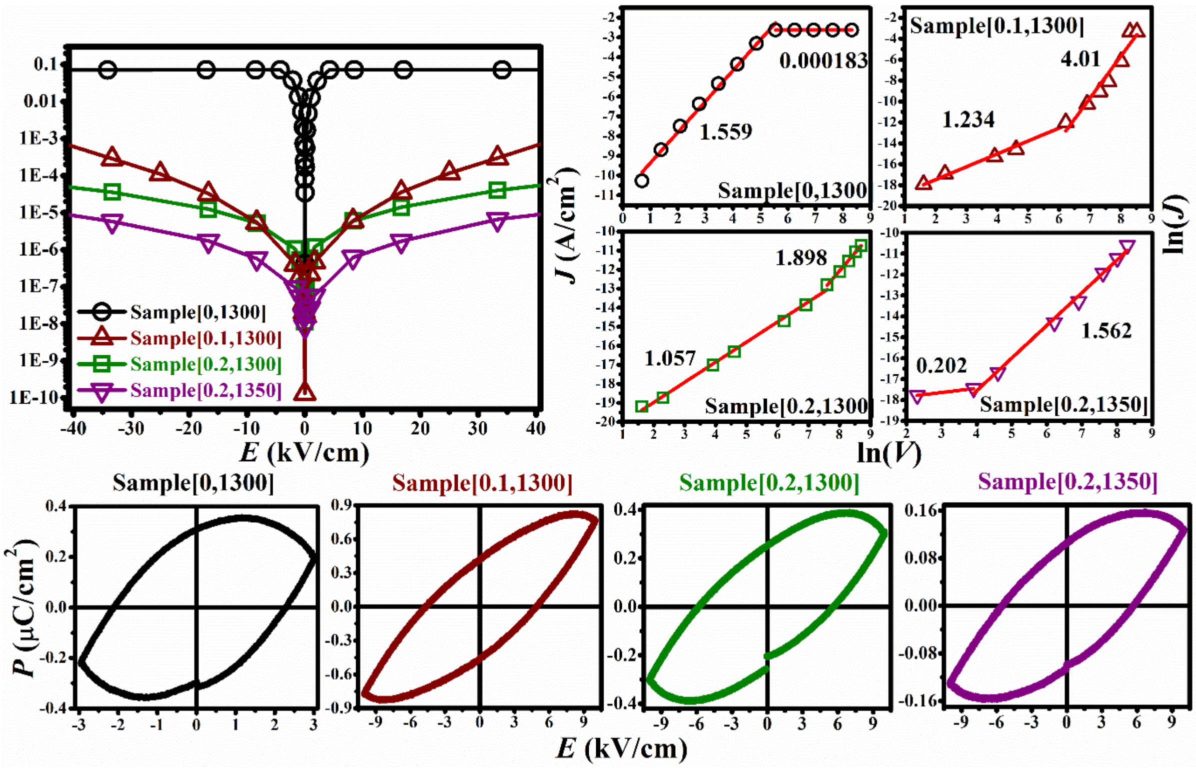

Figure 4.7 Leakage current measurements of all samples along with the slope values of ln(J) versus ln(V) plot are shown on top indicating the governing conduction mechanisms. The figures at the bottom depict the polarisation hysteresis loop for all samples.

leakage current is reduced, the form of the *D-E* hysteresis loops gradually becomes less rounded and the measured polarisation values gradually fall. The dielectric characteristics of all samples are examined in more detail in the following part in order to comprehend the nature of charge carriers and the resistivities of the grains and grain boundaries that result in the observed conduction processes.

4.3.2.2 $Ga_{0.8}Fe_{1.2}O_3 – Y_3Fe_5O_{12}$

The D-E hysteresis loops for each sample are shown in Figure 4.8. The hysteresis loop of GFO,

Table 4.3 - Ferroelectric analysis of all samples along with grain size data from FESEM analysis

Sample Name	Average Grain Size (μm)	Slope value and Conduction Mechanism at Room Temperature		Low Field Current (A/cm^2)	High Field Current (A/cm^2)
Sample[0,1300]	2.8	1.56	Ohmic + SCLC	4.24×10^{-7}	0.1
Sample[0.1,1300]	1.2	1.24	Ohmic + SCLC	1.32×10^{-10}	6.6×10^{-4}
Sample[0.2,1300]	0.903	1.06	Ohmic	1.16×10^{-8}	5.1×10^{-5}
Sample[0.2,1350]	0.669	0.202	GBLC	8.62×10^{-9}	8.51×10^{-6}

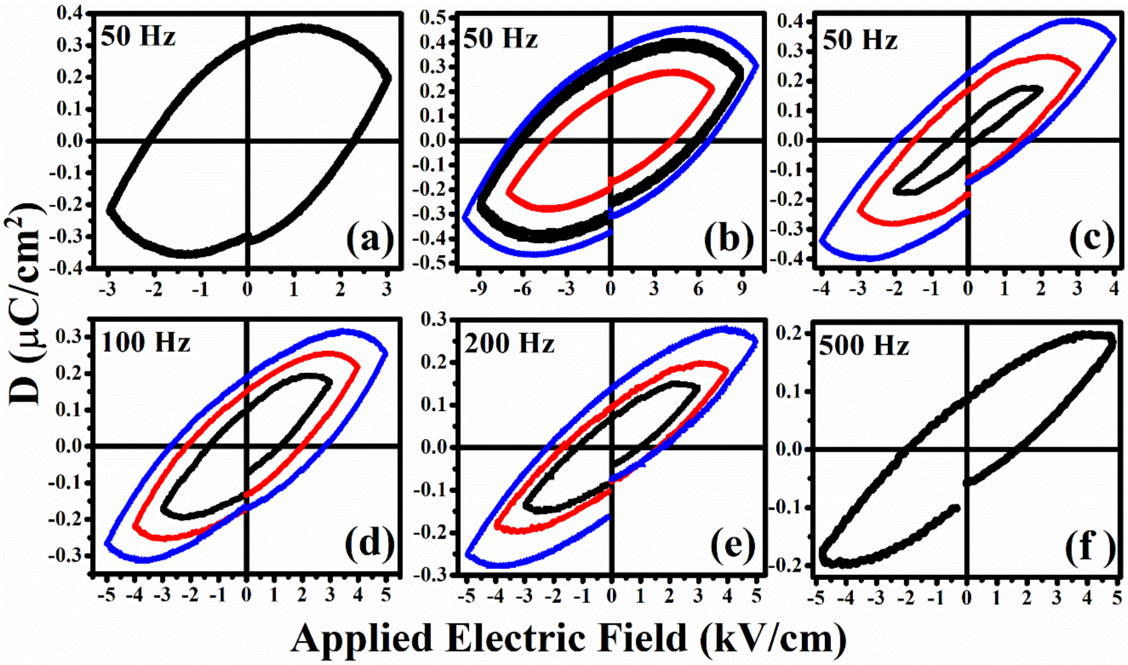

Figure 4.8 Room temperature D-E Hysteresis loop of (a) GFO, (b) GFO-5YIG, and (c) GFO-10YIG obtained at 50 Hz frequency. The D-E hysteresis loop obtained for GFO-10YIG for frequencies (d) 100 Hz, (e) 200 Hz, and (f) 500 Hz.

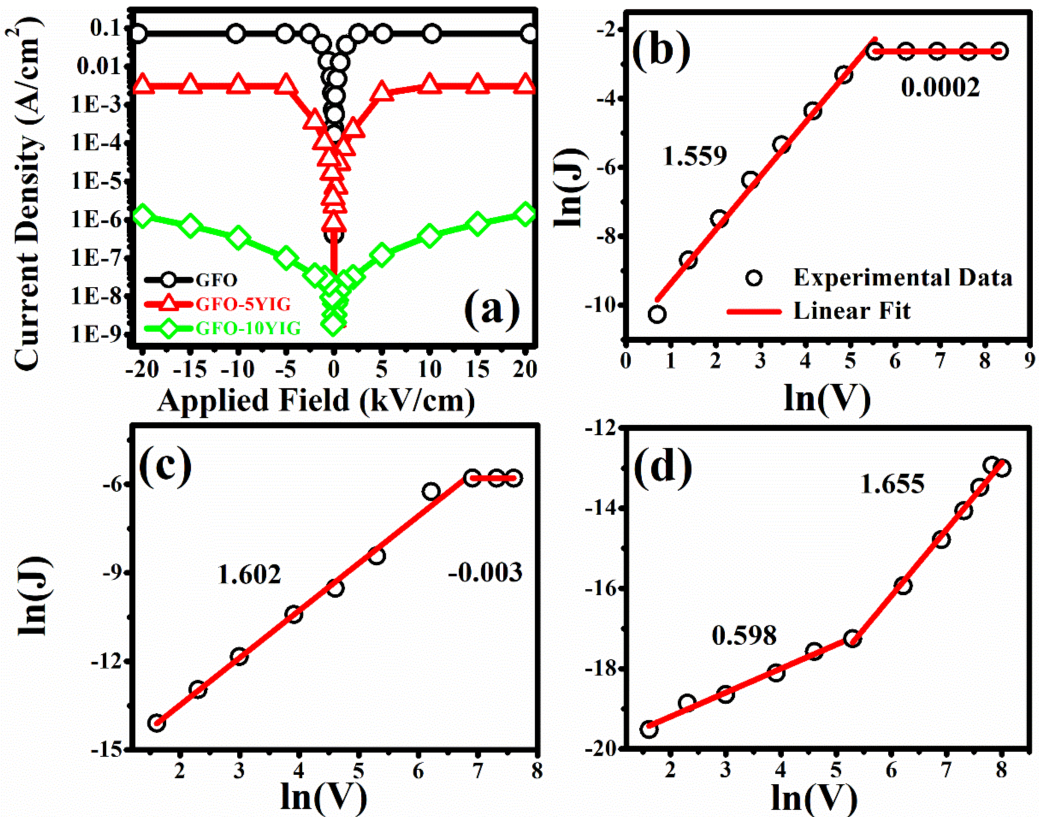

Figure 4.9 (a) The variation of leakage current density (J) with applied electric field (kV/cm) for all samples. The ln(J) versus ln(V) plots along with the slope values from linear fit shown for (b) GFO, (c) GFO-5YIG, and (d) GFO-10YIG.

seen in Figure 4.8(a), is found to be very loopy. However, as the concentration of YIG increases, the hysteresis loops measured at 50 Hz become considerably more square in GFO-5YIG (Figure 4.8(b)) and GFO-10YIG (Figure 4.8(c)) as the value of electric displacement (*D*) decreases due to the materials' lowering conductivity and leakage current. The best nature of the hysteresis loops is observed in GFO-10YIG. With increasing frequency of applied electric field the contribution from leakage to the observed polarization can be reduced. Therefore, the D-E hysteresis loops for GFO-10YIG have been obtained for increasing frequencies from 50Hz to 500 Hz and illustrated in Figures 4.8(c-f). The hysteresis loops of the sample retain the square shape with increasing frequency while the decreasing value of electric displacement confirms the reduced contribution from leakage current. The leakage current density (*J*) versus applied electric field (*E*) is further studied to quantify the reduction in leakage current due to the formation of composite and the underlying mechanism governing the leakage conduction. Figure 4.9(a) demonstrates the change in leakage current density with increasing electric field and confirms a gradual reduction in leakage current with increasing concentration of YIG. GFO-10YIG undergoes a reduction in leakage current by five orders of magnitude at an applied electric field of 20 kV/cm. The ln(*J*) versus ln(*V*) are plotted and represented in Figures 4.9 (b), (c), and (d) for GFO, GFO-5YIG, and GFO-10YIG respectively. It can be observed that for both GFO and GFO-10YIG, the leakage is governed by both SCLC and Ohmic conduction and then breaks down beyond a particular field.

The breakdown voltage is ~ 300 V or 3 kV/cm for GFO, whereas the same for GFO-5YIG is ~ 1000 V or 10 kV/cm, indicating an enhanced resistivity in GFO-5YIG. However, GFO-10YIG is observed to be governed by GBLC mechanism up to an applied electric field ~ 200 V or 2 kV/cm. With further application of electric field, both Ohmic and SCLC mechanism governs the leakage conduction in the sample and retains the same for the studied applied

Table 4.4 - Ferroelectric analysis of all samples along with grain size data from FESEM analysis

Sample Name	**Average Grain Size (μm)**	**Slope value and Conduction Mechanism at Room Temperature**		**Low Field Current (A/cm^2)**	**High Field Current (A/cm^2)**
GFO	2.8 ± 1.1	1.559	Ohmic + SCLC	4.24 x 10^{-7}	0.1
GFO-5YIG	1.42 ± 0.29	1.602	Ohmic + SCLC	2.45 x 10^{-9}	0.003
GFO-10YIG	0.98 ± 0.22	0.598	GBLC	1.89 x 10^{-9}	1.2 x 10^{-6}

voltage of ~ 3000 V or 30 kV/cm. The sample undergoes breakdown beyond this applied voltage of 3000 V. The enhanced breakdown voltage along with the reduced slope values observed in GFO-10YIG explains the observed reduction of leakage current by five orders of magnitude.

4.3.2.3 $Sr_{0.5}(Na_{0.5}Bi_{0.5})_{0.5}TiO_3 – Y_3Fe_5O_{12}$

The *D-E* hysteresis loops for each sample have been measured and are shown in Figures 4.10 and 4.11. Figure 4.10(a) depicts the *D-E* hysteresis loop of the SNBT50 sample measured at 0.05 Hz and demonstrates a saturated *D-E* hysteresis loop. However, the *I-E* characteristic curve of the sample reveals a highly resistive nature, with charge conductivity contributing significantly

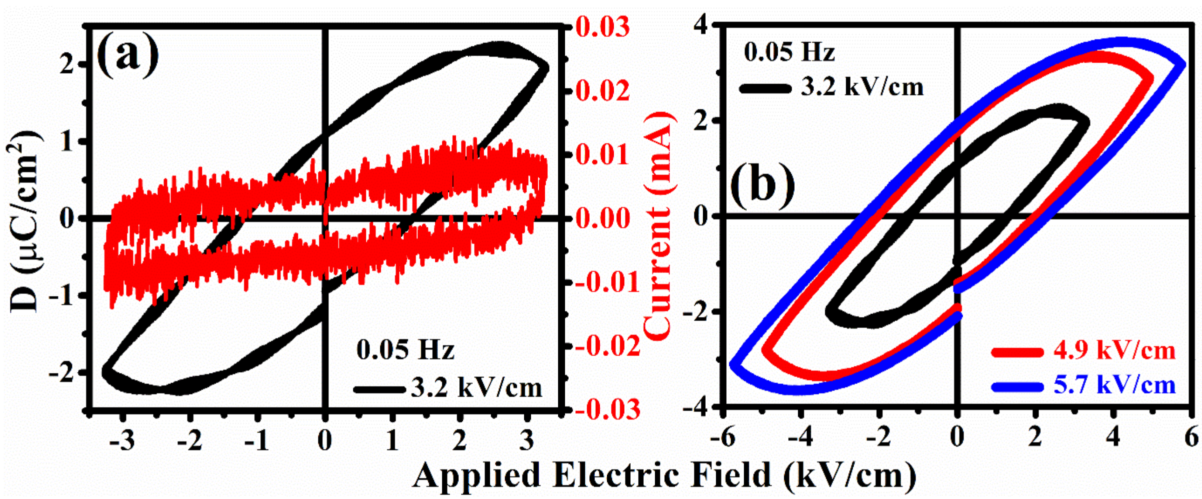

Figure 4.10 (a) The *D-E* characteristic of SNBT50 at an applied electric field of 3.2 kV/cm, (b) The *D-E* characteristics of SNBT50 with increasing electric field from 3.2 kV/cm to 5.7 kV/cm.

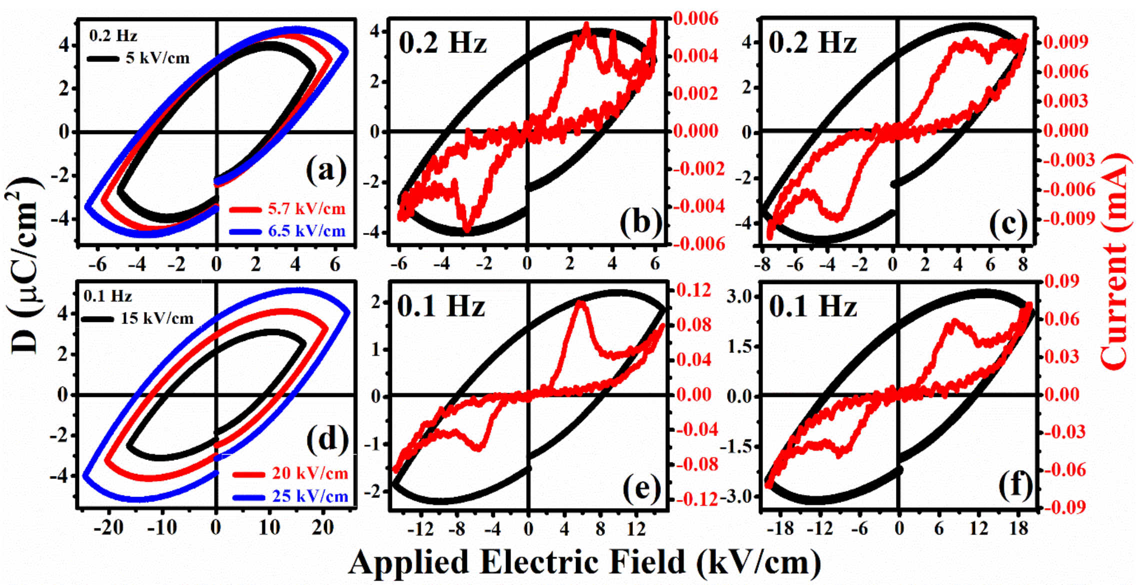

Figure 4.11 The room temperature *D-E* Hysteresis loops and *I-E* characteristic graphs for (a-c) SNBT50-10YIG and (d-f) SNBT50-20YIG obtained at different applied electric field.

to the polarization. Consequently, the *I-E* curve for this sample is incapable of proving the occurrence of domain switching. However, the remnant polarization can be computed from the *D-E* hysteresis loop by using the value of the intercept at zero applied field if, as seen in Figure 4.10(b), the value of the intercept at the *y*-axis remains unchanged as the applied electric field increases. Despite an increase in the applied field from 3.2 kV/cm to 5.7 kV/cm, the remnant polarization varies from 3.2 kV/cm to 4.9 kV/cm but then remains unchanged. The SNBT50 sample possess a remnant polarization of approximately 2.1 μC/cm^2 and a saturation polarization of 3.9 μC/cm^2. However, the sample's strong conductivity prevents the applied electric field from exceeding 5.7 kV/cm. The *D-E* loops of the composites, on the other hand, exhibit good insulating ability to withstand increasing applied electric field up to 25 kV/cm in SNBT50-20YIG, as shown in Figure 4.11. While the contribution from domain wall switching resulting from ferroelectricity becomes higher with increasing YIG concentrations, the *I-E* characteristic curves for both composites confirm an increasingly less conducting nature. Figure 4.11(a) shows the saturated nature of the *D-E* loops for the SNBT50-10YIG, whereas Figure 4.11(b) shows the remnant polarization with an applied electric field of 6.5 kV/cm and a value of 3.5 μC/cm^2. Up to 8 kV/cm of applied electric field is raised [Figure 4.11(c)]. In addition, it possesses excellent *I-E* features, with well-aligned domain wall switching peaks and coercivity. Figure 4.11(d) demonstrates that the maximum residual or saturation polarization for SNBT50-20YIG could not be obtained despite extending the applied electric field to 25 kV/cm while maintaining a saturated *D-E* loop characteristic. As demonstrated by the application of an augmented electric field up to 25 kV/cm, a sharp domain switching is observed in this sample, which is attributed to a decreased contribution from conductivity.

4.3.3 DIELECTRIC STUDY

4.3.3.1 $Ga_{0.8}Fe_{1.2}O_3 – Gd_3Ga_5O_{12}$

The real part of dielectric permittivity (ε') depicted in Figure 4.12 implies that the values of dielectric constant at room temperature are 57, 153, 134, and 172 for Sample[0,1300], Sample[0.1,1300], Sample[0.2,1300], and Sample[0.2,1350] respectively. The higher interfacial polarisation caused by a rise in grain boundaries is accounted for the observed increase in dielectric permittivity. Increased grain boundary resistances brought on by the surrounding of GFO grains with highly resistant GGG grains are also seen to result in a decrease in dielectric

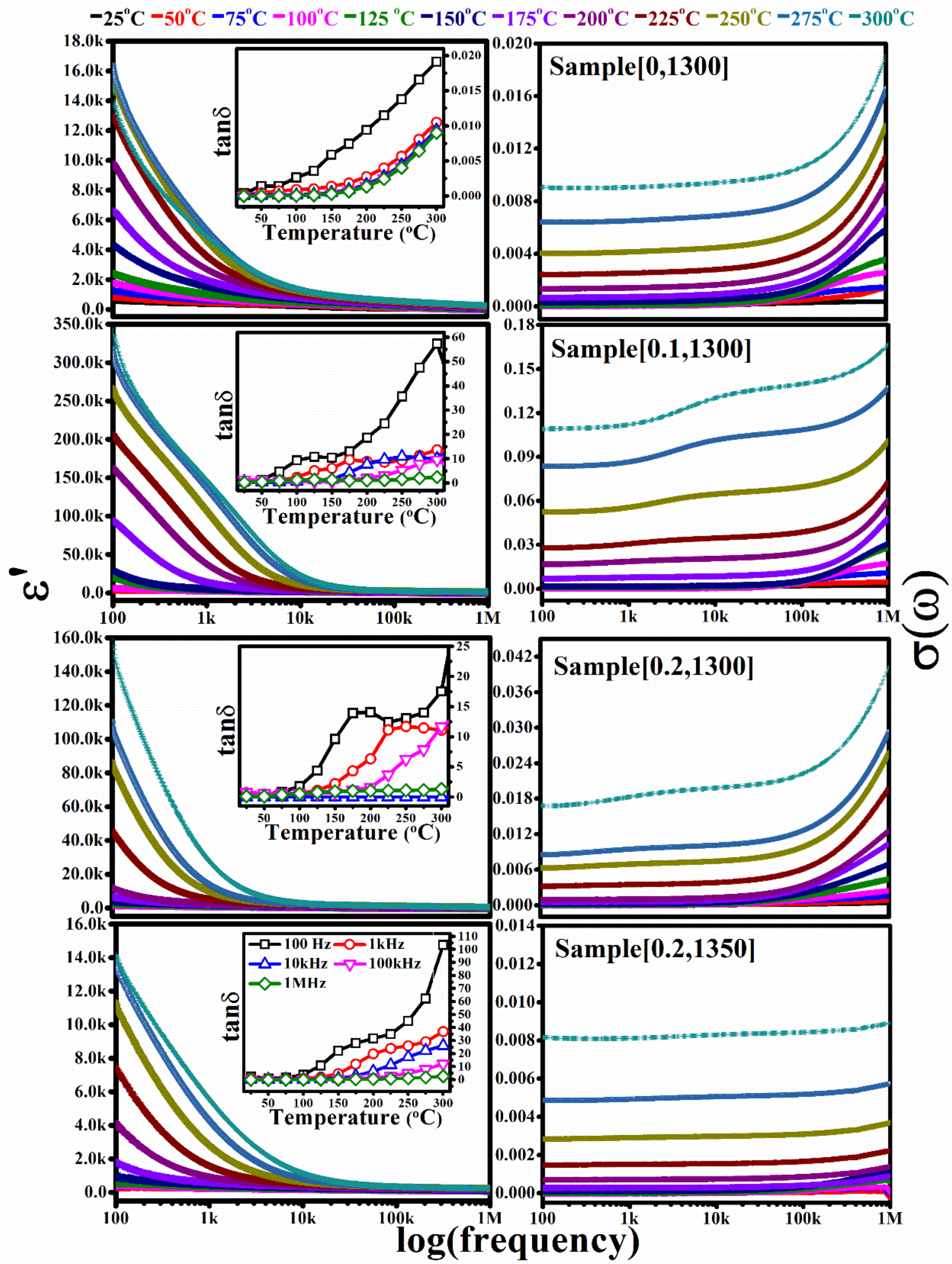

Figure 4.12 (left) panels depict the frequency dependence of real part of complex permittivity for all samples while the tangent loss with varying temperature is shown in the insets of corresponding sample. (right) panels depict the variation of total conductivity with frequency for a temperature range of 25 °C to 300 °C.

loss ($tan\delta$), which represents the energy dissipation of the dielectric system. The insets of the relevant samples display the temperature-dependent dielectric loss observed at various frequencies. The plot of dielectric loss vs. temperature shows a clear peak that is seen to move with increasing frequency towards higher temperatures. Rezlescu's model[36] states that this peak is seen when the frequency of hopping electrons present at various lattice sites coincides with the frequency of the applied field, causing resonance and the highest amount of dielectric loss. The shift of the peak to a higher frequency with rising temperature is correlated with an increase in the mobility of the charge carriers. For Sample[0.2,1300] and Sample[0.2,1350] the dielectric loss peak is observed at low frequencies appears more or less at the same temperatures (~ 175 ^{o}C at 100 Hz) whereas the same for Sample[0.1,1300] and Sample[0,1300] occurs at lower temperature (~ 120 ^{o}C and ~ 50 ^{o}C at 100 Hz respectively) concluding that the increase in concentration of GGG decreases the hopping such that it needs more thermal energy to take place. On the other hand, Sample[0.2,1350] is observed to have much reduced peak intensity implying reduction in number of hopping charges with increasing annealing temperature in consistence with reduced leakage in this sample.

Following Maxwell's equivalent circuit including grain and grain boundary resistances and capacitances the complex impedance of inhomogeneous system is expressed by following equations, derived in section 1.3.3 of chapter 1 (Eq. 1.23 and 1.24),

$$Z' = \frac{R_g}{1+(\omega R_g C_g)^2} + \frac{R_{gb}}{1+(\omega R_{gb} C_{gb})^2} \tag{4.5}$$

$$Z'' = \frac{\omega R_g^2 C_g}{1+(\omega R_g C_g)^2} + \frac{\omega R_{gb}^2 C_{gb}}{1+(\omega R_{gb} C_{gb})^2} \tag{4.6}$$

Where, R_g, C_g, R_{gb}, and C_{gb} are the grain resistance and capacitance, grain boundary resistance and capacitance respectively. Using Eq. 4.5, the frequency variation of the real part of the

Table 4.5 - Dielectric parameters from dielectric analysis of all samples

Sample Name	ε_r	tanδ	R_g (MΩ)	R_{gb} (MΩ)	C_g (pF)	C_{gb} (pF)	σ	E_g	E_{gb}	E_a
Sample[0,1300]	57	0.45	1.64	7.44	0.819	0.0123	58.29	0.2037	0.2121	0.2098
Sample[0.1,1300]	153	0.5	1.38	11.13	0.015	0.903	240.4	0.2398	0.2404	0.2349
Sample[0.2,1300]	134	0.13	1.198	9.53	0.442	0.0131	32.56	0.2686	0.2261	0.2499
Sample[0.2,1350]	172	0.04	5.76	72.88	0.0197	0.0144	18.07	0.2832	0.2685	0.2496

impedance is fitted, and the fitted data and frequency variation are displayed in Figure 4.13(a). Table 4.5 lists the values of R_g, C_g, R_{gb}, and C_{gb} subtracted from the fitting. The significant variation in grain and grain boundary resistances accounts for the GBLC mechanism seen in Sample[0,1350].

The obtained R_g and R_{gb} values are further fitted using Arrhenius equation to calculate the activation energies, E_g and E_{gb} tabulated in Table 4.5,

$$R_g = Ae^{\frac{E_g}{k_B T}} \tag{4.7}$$

$$R_{gb} = Be^{\frac{E_{gb}}{k_B T}} \tag{4.8}$$

The frequency dependence of total conductivity shown in Figure 4.12, at different temperatures is calculated using following formula[37],

$$\sigma(\omega) = \omega\varepsilon'\varepsilon_0 tan\,\delta \tag{4.9}$$

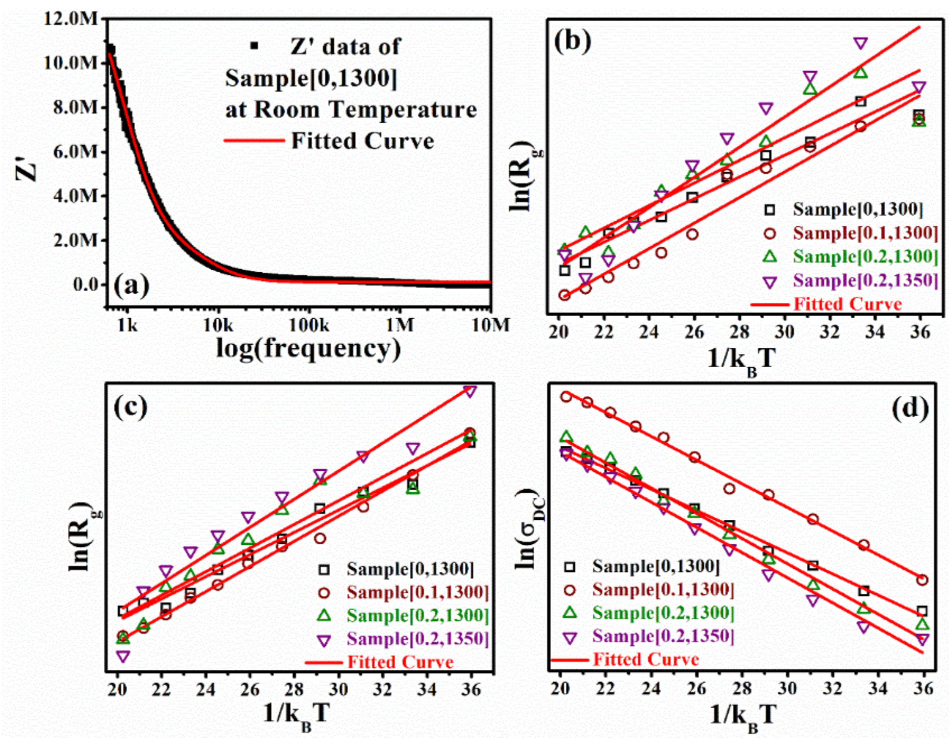

Figure 4.13 The fitted curve of real part (Z') of complex impedance with frequency is shown in (a). (b-d) depicts the fitted data of ln(R_g), ln(R_{gb}) and ln(σ_{DC}) with 1/ k_BT respectively in order to calculate the activation energies of the samples.

Where, the value of ε_0 is taken as 8.854x10^{-12} *F/m*. And the *dc* conductivity is extrapolated from the σ(ω) using "Jonscher's Universal Power Law" (Eq. 4.10) and further fitted using the Arrhenius equation (Eq. 4.8) in order to get the values of activation energy of conductance (E_g):

$$\sigma(\omega) = \sigma_{DC} + \sigma_{AC} \tag{4.10}$$

$$\sigma_{DC} = \sigma_0 e^{-\frac{E_a}{k_B T}} \tag{4.11}$$

The fitted values of ln(σ_{DC}) vs $\frac{1}{k_B T}$ for all samples are displayed in Figure 4.13(d). The activation energy of *dc* conductivity and the activation energy of dielectric relaxation are reasonably in agreement. The dielectric loss peak and the activation energies estimates suggest that electrons hopping between distinct lattice sites are the dominant charge carriers driving the observed conduction in the samples.

4.3.2.2 $Ga_{0.8}Fe_{1.2}O_3$ – $Y_3Fe_5O_{12}$

The low dielectric constant of YIG is shown to have significantly decreased the dielectric permittivity of the composites in Figure 4.14(a)[16,38]. The composite has much less conductivity and dielectric loss combined. The GFO-10YIG greatly reduced the intensity of the loss peak, which was caused by the hopping of electrons at various lattice sites, showing a decrease in the charge hopping transport phenomena[36]. The Cole-Cole plots for all samples are displayed in Figure 4.14(e-g) to help in understanding the change in resistivity implied by increased impedance [Figure 4.14(c)]. While the same slope for GFO is a visible semi-circle, the slopes for composites tend to become practically straight lines, showing increased resistivity of the composites.

The real portion of complex impedance, Z′ has been fitted using Eq. 4.5, to provide a

Table 4.6 - Dielectric parameters from room temperature dielectric analysis

Sample Name	ε_r	tanδ	Z(MΩ)	σ(Ω^{-1}.m^{-1})	R_g(kΩ)	R_{gb}(MΩ)	C_g(nF)	C_{gb}(nF)
GFO	274	3.4	6.13	3.23x10^{-4}	73	0.034	3.16	0.35
GFO-5YIG	69	1.82	5.48	3.93x10^{-5}	270	0.42	0.46	0.30
GFO-10YIG	13	0.38	0.13	2.22x10^{-5}	461	2.1	0.065	0.29

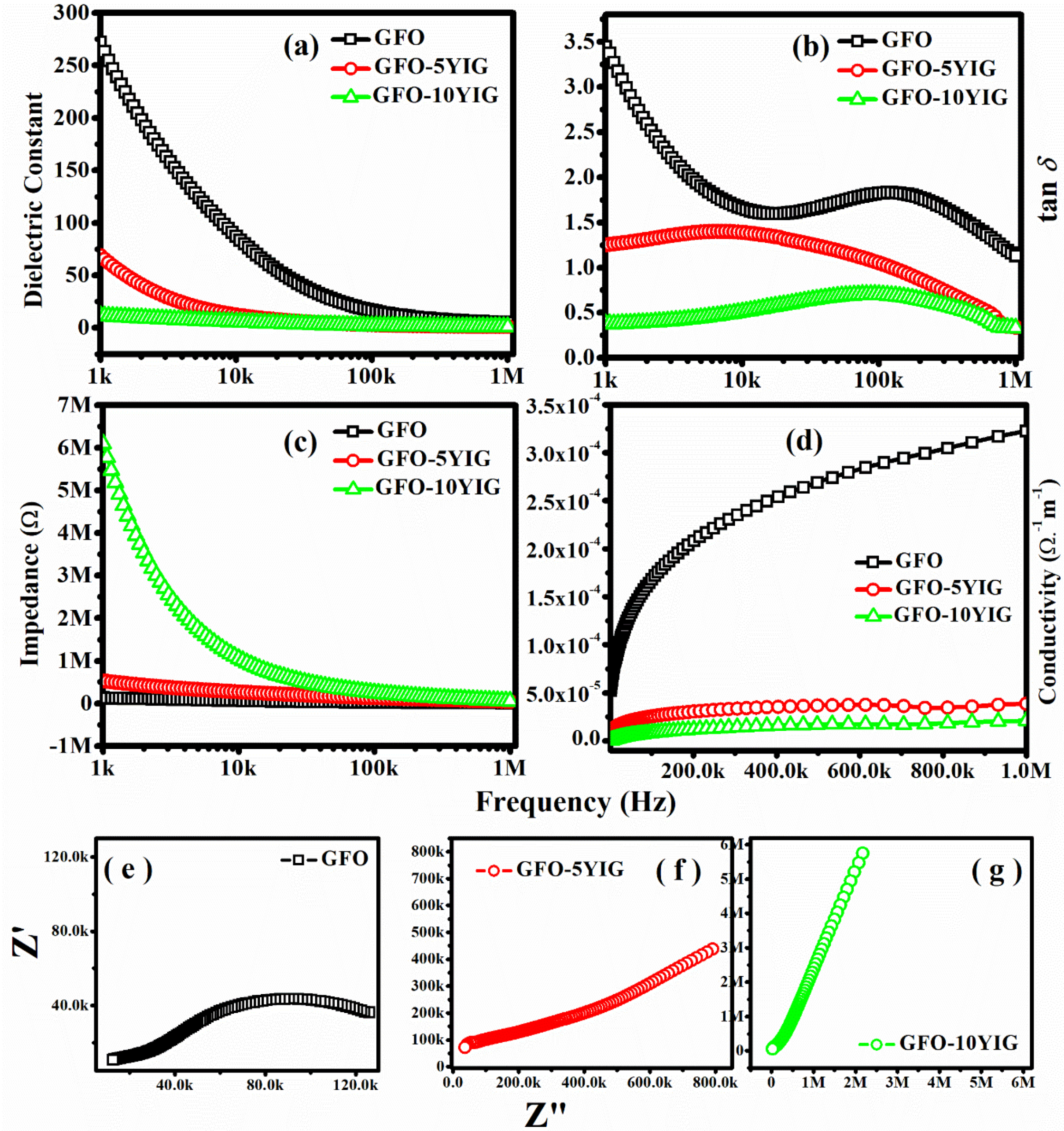

Figure 4.14(a) depicts the frequency variation of the dielectric constant, (b) loss, (c) impedance, (d) conductivity. (e-g) represents the cole-cole plot of all samples.

quantitative understanding of the grain and grain boundary resistances. Table 4.6 lists the extrapolated grain (C_g) and grain boundary (C_{gb}) capacitances as well as the acquired grain (R_g) and grain boundary (R_{gb}) resistances from the fitting with Eq. 4.13. The values of the resistances at the grain and grain boundary in comparison to those of the GFO reveal that the development of a composite with a high resistive YIG is capable of significantly increasing the resistivity in the GFO while lowering the conductivity and dielectric loss.

4.3.4 MAGNETIC AND MAGNETODIELECTRIC PROPERTIES

4.3.4.1 $Ga_{0.8}Fe_{1.2}O_3$ – $Gd_3Ga_5O_{12}$

The variation of dielectric constant, also known as magnetodielectric factor (MD), due to the variation of magnetic field from 0 – 15 kOe measured at a frequency of 10 kHz is calculated using the following equation,

$$MD(\%) = \frac{\varepsilon'(H) - \varepsilon'(0)}{\varepsilon'(0)} \times 100\% \qquad (4.12)$$

The coupling between the electric and magnetic parameters of samples is measured by the change in dielectric parameters caused by the application of a magnetic field. According to Figure 4.15, the magnetodielectric factor values for Sample[0,1300], Sample[0.1,1300], Sample[0.2,1300], and Sample[0.2,1350] are 2.02%, 3.07%, 7.03%, and 5.01%, respectively. Up to around 10 kOe of applied magnetic field, a noticeable shift is seen. Beyond that point, the change is practically constant, suggesting that all of the magnetic spins have aligned, and beyond that, the change in magnetic configuration decreases due to saturation.

To comprehend the impact of magnetostriction, piezo-magnetism, and other phenomena on the fluctuation of the dielectric constant when a magnetic field is applied, the MD - M^2 graphs are displayed. The MD only depends linearly on the square of magnetization for all samples at low M^2 values, which correspond to low applied magnetic fields, it has been shown. Therefore,

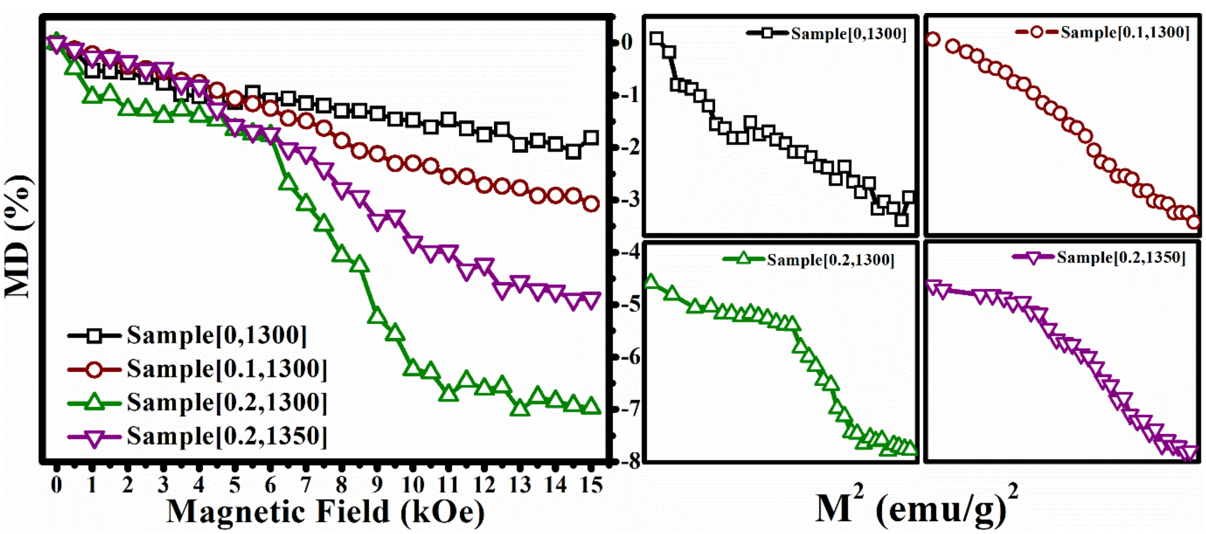

Figure 4.15 The figure on the left side shows the variation of magnetodielectric constant (MD) with changing applied magnetic field. The figures on the right depicts the linear variation of MD with square of magnetisation for all samples indicating the presence of magnetoelectric coupling

the square magnetization model (SqMM), in which strain is linearly proportional to M^2, cannot fully explain the change in the magnetodielectric factor. Gualdi et al.[39] have thought about this phenomenon in depth and come to the conclusion that in order to fully describe the total strain of a magneto-strictive material surrounded by non-magnetic media such as the 0-3 composite systems, it is also necessary to take into account the strain caused by stress, piezo-magnetism, and magnetostriction[40]. They proposed a stress magnetization model (SMM) in which the total strain of the system is proportional to the applied stress, magnetic field, and magnetization square. It has been noted that the magneto-strictive characteristics of ferromagnetic materials are significantly impacted by grain size reduction[41]. High internal stress typically develops at the grain boundaries of polycrystals. Along with a high elastic energy density, the high density of anisotropy usually accumulates near the grain boundaries. As a result, substantial internal stress is produced across the grains with an accumulation of magnetic charges at the grain boundaries as grain size decreases and the grain boundaries gradually richer. The internal stress in these samples grows stronger as the grain size decreases with rising GGG concentration and increasing sintering temperature, further deviating the linearity of the MD-M^2 graphs as a result of magnetostriction brought on by grain size reduction.

4.3.4.2 $Ga_{0.8}Fe_{1.2}O_3$ – $Y_3Fe_5O_{12}$

The high anisotropy of the octahedral sites (Ga2, Fe1, and Fe2) and the weak anisotropy of the tetrahedral Ga1 site, which act as hard and soft magnetic phases, respectively, was previously linked to the pinched waist feature of the magnetic hysteresis loop of the GFO shown in Figure 4.16(a)[42,43]. This pinched shape, however, is not present in any of the composites, indicating that the material's anisotropy has significantly changed in its composite forms. Strain is applied in the magneto-strictive YIG when an external magnetic field is introduced, which causes stress on the grains of GFO. As a result, GFO undergoes an inverse magnetostriction or magnetoelastic action.

Through magnetostriction, an applied external force or an internal stress that exists in a direction different from the applied field can shift the magnetization's direction. When a clear direction of magnetization is established, applied stress can lead to anisotropy. Where σ is the saturation magnetostriction and is the applied stress, $K_{u\sigma} = \frac{3}{2}\sigma\lambda_s$, λ_s gives the magnitude of the stress-induced anisotropy. It can be concluded that the movement of moments has increased in the direction of application of magnetic field as a result of the rising influence from YIG based on the observed increasing sharpness of the dM/dT curves [Figure 4.16(b)] with increasing concentration of magneto-strictive YIG. Previous extensive research has been done on the influence of stress or the inverse magneto-strictive effect on the geometry of the magnetic hysteresis loops of magnetic materials that affect remnant, saturation magnetization, and coercivity[44–49]. With this effort, the remnant magnetization was increased from 0.211 emu/g for GFO to 2.82 emu/g for the GFO-10YIG composite. The inversely proportional dependency of coercivity with grain size observed in polycrystalline materials, explained by domain-wall pinning at grain boundaries, is responsible for the coercivity's decrease with increasing grain size [Table 4.7][50–52]. The minima of the dM/dT versus temperature plot of the field-cooled magnetization data are used to determine the ferrimagnetic to paramagnetic phase transition temperature. The effect of the improved alignments of magnetic moments increasing the

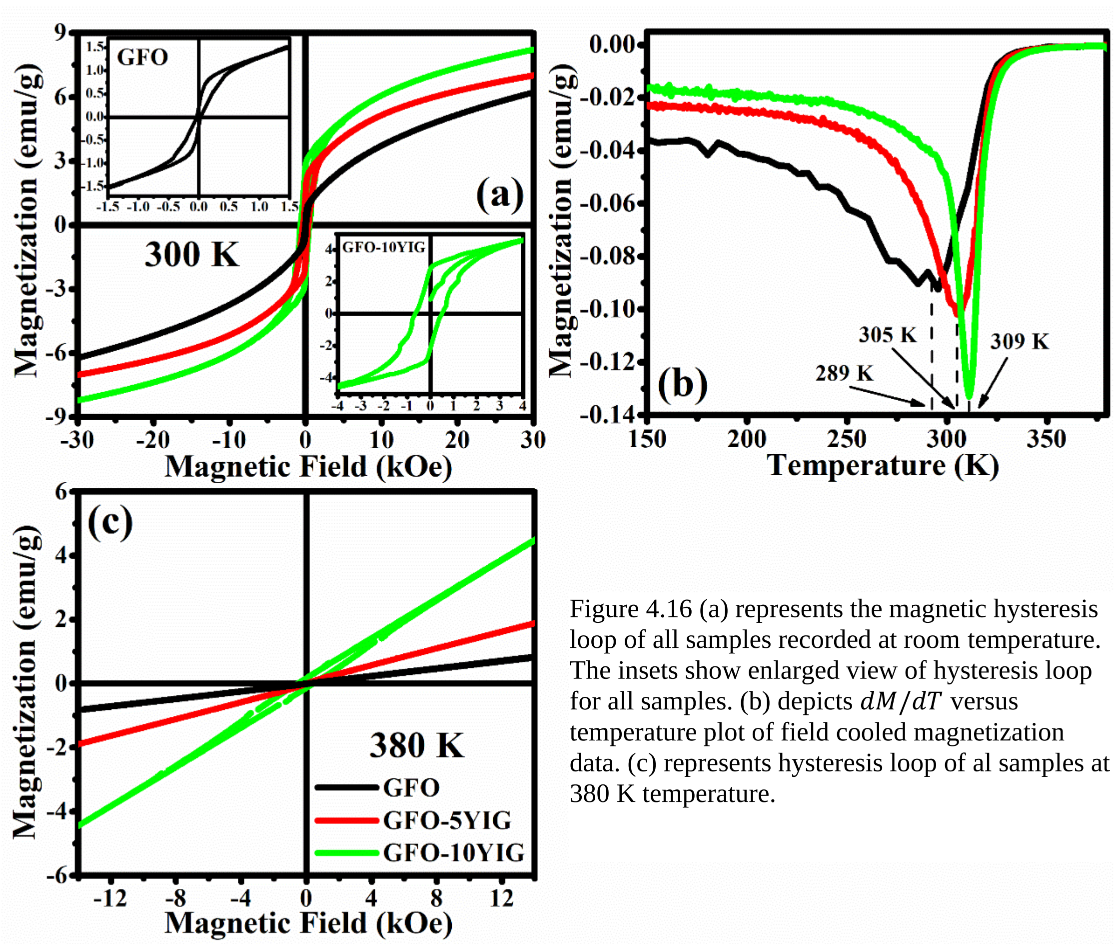

Figure 4.16 (a) represents the magnetic hysteresis loop of all samples recorded at room temperature. The insets show enlarged view of hysteresis loop for all samples. (b) depicts dM/dT versus temperature plot of field cooled magnetization data. (c) represents hysteresis loop of al samples at 380 K temperature.

magnetic domain volume along the easy magnetization direction due to the application of magneto-strictive YIG may explain the observed steady increase in T_C beyond room temperature [Figure 4.16(b)]. The magnetic hysteresis loop is shown in Figure 4.16(c) at a temperature of 380 K, which is far higher than the T_C of any of the samples. The minor remnant magnetization shown in the composites is solely attributable to the presence of ferromagnetic YIG, which is to be expected given that the M-H loop of GFO is paramagnetic.

A ferroelectric or piezoelectric material and a magneto-strictive material are combined to form a magnetoelectric composite. Consequently, strain is produced in the magneto-strictive material when a magnetic field is applied. This strain creates an electric field that changes the piezoelectric material's electrical characteristics. To determine the strength of magnetoelectric coupling, it is possible to study the change in electrical characteristics such as capacitance, dielectric loss, etc. in the presence of a magnetic field. In order to determine whether magnetoelectric coupling exists, the following formulas are used to calculate magneto-capacitance (MC(%)), magneto-loss (ML(%)), magneto-impedance (MI(%)), and magneto-phase

(Mϕ(%))[53–55].

$$MC(\%) = \frac{C(H,T)-C(0,T)}{C(0,T)} \times 100\% \tag{4.14}$$

$$ML(\%) = \frac{tan\ \delta(H,T)-tan\ \delta(0,T)}{tan\ \delta(0,T)} \times 100\% \tag{4.15}$$

$$MI(\%) = \frac{Z(H,T)-Z(0,T)}{Z(0,T)} \times 100\% \tag{4.16}$$

Table 4.7 - Magnetic properties such as remnant, saturation magnetization, coercivity and Curie temperature tabulated for all samples

	GFO	**GFO-5YIG**	**GFO-10YIG**
Remnant Magnetization (emu/g)	0.211	1.57	2.82
Saturation Magnetization (emu/g)	6.25	7.02	8.2
Coercivity (Oe)	30	330	650
Curie Temperature (K)	289	305	309

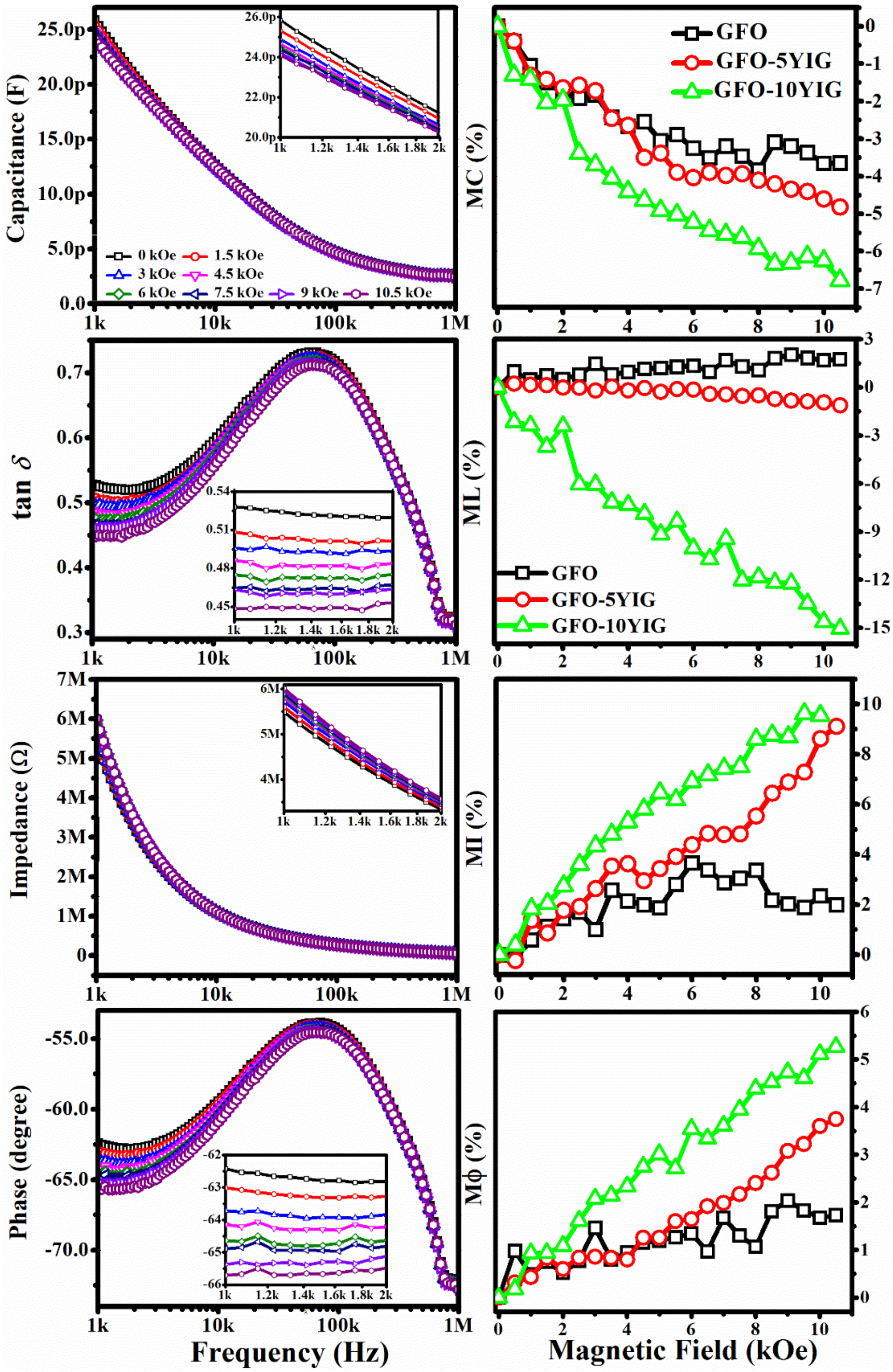

Figure 4.17 (left) magneto – capacitance, -dielectric loss, -impedance and -phase at different frequencies shown only for the GFO-10YIG composite. (right) the comparative study of magneto-capacitance, loss, impedance and phase of GFO and the composites at 1 kHz

$$M\Phi(\%) = \frac{\Phi(H,T) - \Phi(0,T)}{\Phi(0,T)} \times 100\% \tag{4.17}$$

Figure 4.17 shows that the values obtained for MC(%), ML(%), MI(%), and Mϕ(%) are approximately -3.5%, 1.5%, 2%, and 1.7% respectively for GFO, -5%, -1.5%, 9%, and 3.9% respectively for GFO-5YIG, and -7%, -15%, 9.5%, and 5.4% respectively for GFO-10YIG. The stronger link between magnetic and electrical parameters with increased magneto-strictive YIG concentration is confirmed by the bigger changes in electrical parameters upon the application of magnetic field in the composite.

4.3.4.2 $Sr_{0.5}(Na_{0.5}Bi_{0.5})_{0.5}TiO_3$ – $Y_3Fe_5O_{12}$

Figure 4.18(a) illustrates the magnetic hysteresis loops generated at ambient temperature. Despite the fact that SNBT50 was originally a dielectric material, the magnetic property of composites rises as the concentration of ferromagnetic YIG increases, as seen in the inset of Figure 4.18(a). However, none of the magnetic hysteresis phases displayed evidence of saturation, which may be attributable to the presence of the dielectric SNBT50 phase in greater quantities.

The Eq. 4.12 is used to measure and analyze the change in dielectric constant for three distinct frequencies (1 kHz, 10 kHz, and 100 kHz) in order to comprehend how the magnetic field affects the electric parameters. The dielectric nature of the material is to blame for the magnetodielectric factor of SNBT50, which is distributed evenly along the x-axis and indicates an average of zero change in dielectric constant with regard to increasing applied magnetic field, as seen in the inset of Figure 4.18(b). However, for the composites, as shown in Figure 4.19(b-d), the dielectric constant rises with increasing applied magnetic field, indicating a positive coupling coefficient. The spin pair correlation between the adjacent spins and the coupling constant are the two factors that determine whether the coefficient is negative or positive. The magnetodielectric factor reports to be 9.22% for SNBT50-10YIG and SNBT50-20YIG, respectively, at an applied magnetic field of 5 kOe, 7.34% at 1 kHz, 2.82% and 1.42% at 10 kHz, and 1.06% and 0.12% at 100 kHz. Due to the formation of SNBT50-YIG magnetoelectric composites, this increase demonstrates the existence of connection between electric and magnetic characteristics.

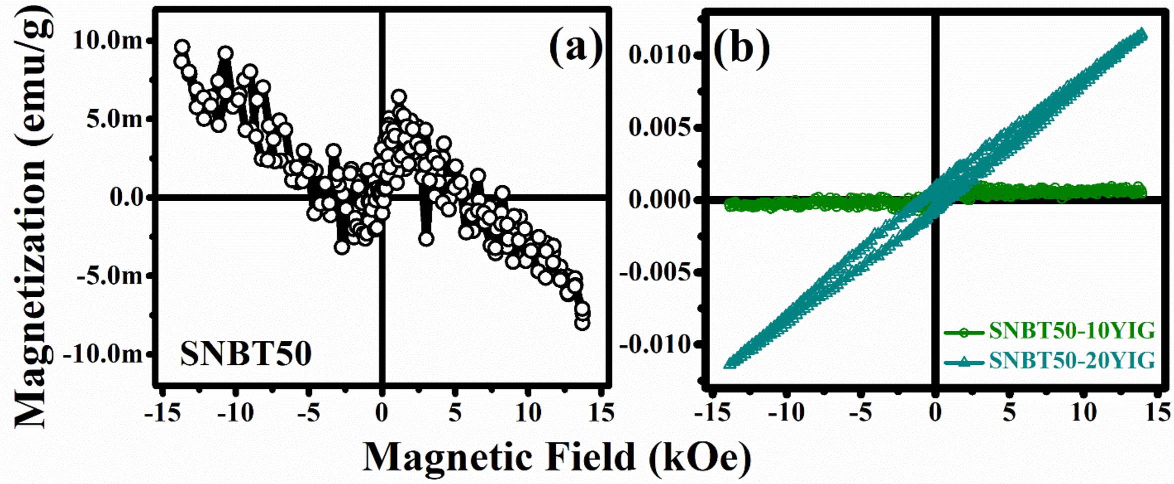

Figure 4.18 The room temperature magnetic hysteresis loop of (a) SNBT50, and (b) SNBT50-10YIG and SNBT50-20YIG

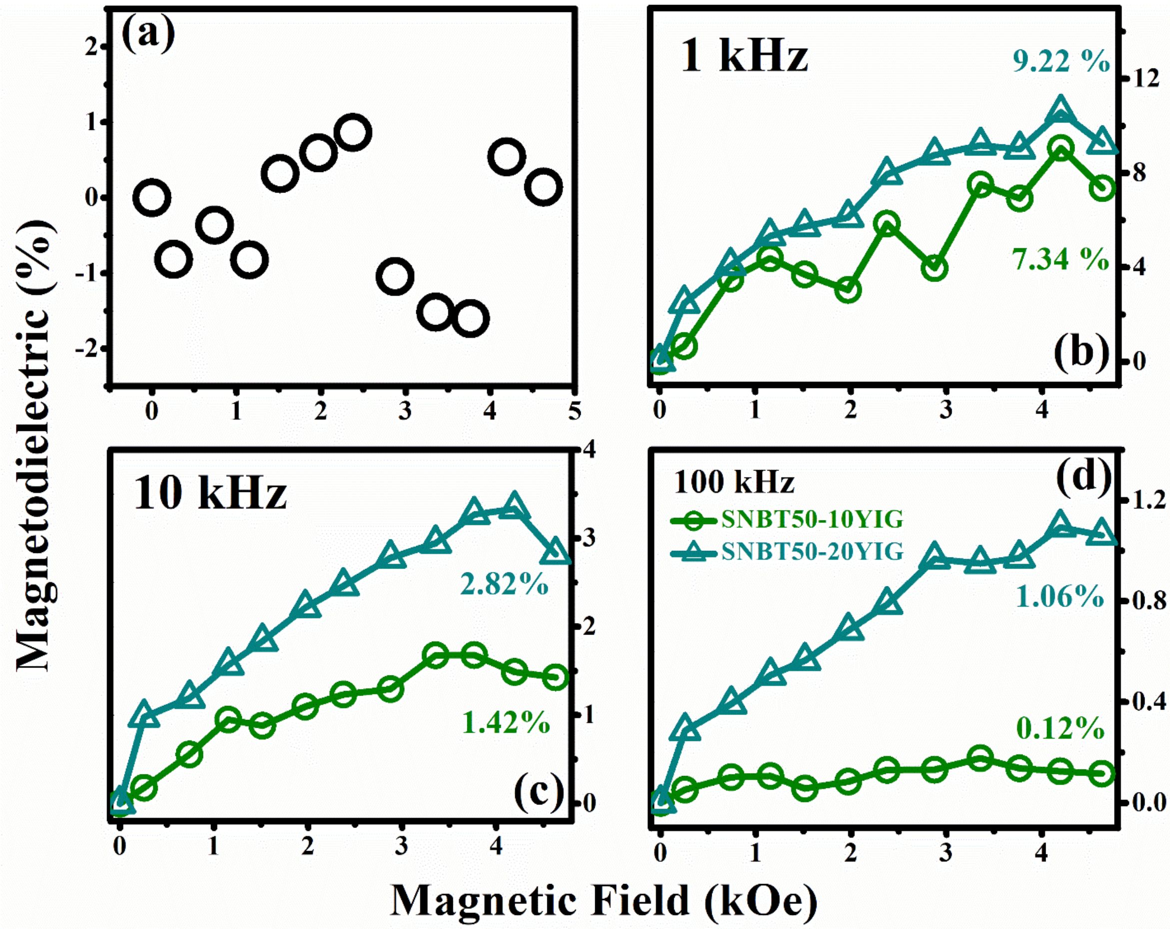

Figure 4.19 The room temperature magnetodielectric factor for (a) SNBT50 sample. The same is shown for both SNBT50-10YIG and SNBT50-20YIG for (b) 1 kHz, (c) 10 kHz, and (d) 100 kHz frequencies.

4.4 CONCLUSION

(1-x)$Ga_{0.8}Fe_{1.2}O_3$ – x$Ga_5Gd_3O_{12}$ composites are observed to achieve a reduction in leakage current by four orders of magnitude to 1.38 x 10^{-5} A/cm^2 recorded at an applied electric field as high as 45 kV/cm. High resistive $Ga_5Gd_3O_{12}$ enhances the dielectric constant of the composite while reducing the dielectric loss of the samples as well. The conductivity of the material has as well reduced along with a significant enhancement in grain and grain boundary resistances of the composites. The magnetodielectric coupling is also enhanced in all the composites reporting improved magnetoelectric coupling. On the other hand, composites of $Ga_{0.8}Fe_{1.2}O_3$ with $Y_3Fe_5O_{12}$ is observed to reduce the leakage current by five orders of magnitude at an applied electric field of 30 kV/cm. Further increment in applied electric field could not be possible due to electrical breakdown. In addition to that, unlike $Ga_5Gd_3O_{12}$ increasing the concentration of $Y_3Fe_5O_{12}$ could not be possible due to agglomeration of the material at the interfaces. However, the ferromagnetic nature along with magnetostriction significantly improved the magnetic properties of the composites increasing the Curie temperature beyond room temperature at the same time. The magnetodielectric properties also significantly enhanced in (1-x)$Ga_{0.8}Fe_{1.2}O_3$ – x$Y_3Fe_5O_{12}$ composites compared to that of (1-x)$Ga_{0.8}Fe_{1.2}O_3$ – x$Ga_5Gd_3O_{12}$ composites. The comparative literature study with other doping or composites of $Ga_{2-x}Fe_xO_3$ is shown in Table 4.8. It can be observed that formation of (1-x)$Ga_{0.8}Fe_{1.2}O_3$ – x$Y_3Fe_5O_{12}$ and (1-x)$Ga_{0.8}Fe_{1.2}O_3$ – x$Ga_5Gd_3O_{12}$ composites are able to reduce the leakage current to the lowest possible value to the best of our knowledge. The breakdown voltage is also significantly larger in these composites. Even at an applied electric field as high as 40 kV/cm and 30 kV/cm, the leakage current of these composites are quite low. On the other hand, although the magnetic properties of (1-x)$Ga_{0.8}Fe_{1.2}O_3$ – x$Y_3Fe_5O_{12}$ are not as high as GFO@SiO_2[63] and (1-x) $GaFeO_3$ - (x)$Co_{0.5}Zn_{0.5}Fe_2O_4$[11], they are quite significant.

The composite between high ferroelectric $Sr_{0.5}(Na_{0.5}Bi_{0.5})_{0.5}TiO_3$ (SNBT50) and room-temperature ferromagnet Yttrium Iron Garnet (YIG) exhibits enhanced ferroelectric polarization. With increasing concentration of ferromagnet YIG, the domain switching is observed to become more apparent as characterized by *I-E* plots. Therefore, unlike $Ga_{0.8}Fe_{1.2}O_3$ system, which does not exhibit any ferroelectric properties in its bulk form, the effect of YIG on the ferroelectric domain switching is studied in SNBT50-YIG composites. Implementation of YIG in the

Table 4.8 – Comparative literature study of leakage current and magnetic properties of different doping and composites of Gallium Ferrite with the present works

Sample Name	**Leakage Current (A/cm²)**	**Magnetic** Parameters **at RT**
$Ga_{0.8}Fe_{1.2}O_3$[56]	~ 10^{-2} at 15 kV/cm	Paramagnetic
$GaFe_{0.9}Cr_{0.1}O_3$[57]	~ 1 x 10^{-4} at 1 kV	Paramagnetic
In doped GFO[58]	-	Paramagnetic
Ni doped GFO[59]	~ 5.94 x 10^{-7} at 10 kV/cm	M_r ~ 0.62 emu/g
Al doped GFO[60]	-	M_r ~ 2 emu/g
Mn doped GFO[56]	~ 2 x 10^{-6} at 15 kV/cm	M_r ~ 6.73 emu/g
Zn doped GFO	~ 4 x 10^{-4} at 5 kV/cm[61]	M_r ~ 2.74 emu/g M_S ~ 8.5 emu/g[62]
GFO@SiO_2[63]	~ 5.5 x 10^{-7} at 2 kV/cm	M_S ~ 14 emu/g
(1-x) $GaFeO_3$ - (x)$Co_{0.5}Zn_{0.5}Fe_2O_4$[11]	~ 1 x 10^{-7} at 5 kV	M_S ~ 30.6 emu/g
Zr doped GFO[61]	~ 0.1 at 10 V/cm	-
(1-x) $Ga_{0.8}Fe_{1.2}O_3$ – $xGa_5Gd_3O_{12}$	~ 1.38 x 10^{-5} at 40 kV/cm ~ 8.8 x 10^{-7} at 10 kV/cm ~ 6.6 x 10^{-8} at 1 kV/cm	-
(1-x) $Ga_{0.8}Fe_{1.2}O_3$ – $xY_3Fe_5O_{12}$	~ 1.34 x 10^{-6} at 20 kV/cm ~ 2.76 x 10^{-7} at 10 kV/cm ~ 2.24 x 10^{-8} at 1 kV/cm	Mr ~ 2.82 M_S ~ 8.2

diamagnetic matrix of SNBT50 is able to introduce ferromagnetic nature in the composites. For the same reason, although the magnetodielectric factor of SNBT50 is zero on average, the composites exhibit high magnetodielectric factor confirming the formation of coupling between magnetic and electric parameters.

In conclusion, this chapter reports successful formations of composites as a means to improve electrical characteristics, magnetic properties, and magnetoelectric coupling. In $Ga_{0.8}Fe_{1.2}O_3$, which is severely hindered by its high leakage current, the formation of composite with suitable material is capable of reducing the leakage current significantly higher than previously reported solutions. Enhancing its magnetic Curie temperature beyond room temperature, it is able to improve magnetic parameters such as magnetization, magnetostriction, anisotropy, and magnetoelectric coupling. In addition, the formation of composites between a highly ferroelectric and a room temperature ferromagnet results in a material which exhibits strongly enhanced ferroelectric domain switching and magnetoelectric coupling.

REFERENCES

[1] C.W. Nan, M.I. Bichurin, S. Dong, D. Viehland, G. Srinivasan, Multiferroic magnetoelectric composites: Historical perspective, status, and future directions, J Appl Phys. 103 (2008). https://doi.org/10.1063/1.2836410.

[2] J. Ma, J. Hu, Z. Li, C.W. Nan, Recent progress in multiferroic magnetoelectric composites: From bulk to thin films, Advanced Materials. 23 (2011) 1062–1087. https://doi.org/10.1002/adma.201003636.

[3] Y. Wang, J. Hu, Y. Lin, C.W. Nan, Multiferroic magnetoelectric composite nanostructures, NPG Asia Mater. 2 (2010) 61–68. https://doi.org/10.1038/asiamat.2010.32.

[4] C.A.F. Vaz, J. Hoffman, C.H. Ahn, R. Ramesh, Magnetoelectric coupling effects in multiferroic complex oxide composite structures, Advanced Materials. 22 (2010) 2900–2918. https://doi.org/10.1002/adma.200904326.

[5] D.K. Pradhan, V.S. Puli, S. Kumari, S. Sahoo, P.T. Das, K. Pradhan, D.K. Pradhan, J.F. Scott, R.S. Katiyar, Studies of phase transitions and magnetoelectric coupling in PFN-CZFO multiferroic composites, Journal of Physical Chemistry C. 120 (2016) 1936–1944. https://doi.org/10.1021/acs.jpcc.5b10422.

[6] J.S. Andrew, J.D. Starr, M.A.K. Budi, Prospects for nanostructured multiferroic composite materials, Scr Mater. 74 (2014) 38–43. https://doi.org/10.1016/j.scriptamat.2013.09.023.

[7] D.K. Pradhan, V.S. Puli, S. Narayan Tripathy, D.K. Pradhan, J.F. Scott, R.S. Katiyar, Room temperature multiferroic properties of Pb(Fe0.5Nb 0.5)O3-Co0.65Zn0.35Fe 2O4 composites, J Appl Phys. 114 (2013). https://doi.org/10.1063/1.4847595.

[8] Y. Li, Z. Wang, J. Yao, T. Yang, Z. Wang, J.M. Hu, C. Chen, R. Sun, Z. Tian, J. Li, L.Q. Chen, D. Viehland, Magnetoelectric quasi-(0-3) nanocomposite heterostructures, Nat Commun. 6 (2015). https://doi.org/10.1038/ncomms7680.

[9] J.P. Remeika, GaFeO3: A Ferromagnetic-Piezoelectric Compound, J Appl Phys. (1960). https://doi.org/10.1063/1.1984690.

[10] T. Arima, D. Higashiyama, Y. Kaneko, J.P. He, T. Goto, S. Miyasaka, T. Kimura, K. Oikawa, T. Kamiyama, R. Kumai, Y. Tokura, Structural and magnetoelectric properties of Ga2-xFe xO3 single crystals grown by a floating-zone method, Phys Rev B Condens Matter Mater Phys. 70 (2004). https://doi.org/10.1103/PhysRevB.70.064426.

[11] A. Ghani, S. Yang, S.S. Rajput, S. Ahmed, A. Murtaza, C. Zhou, Y. Zhang, X. Song, X. Ren, Enhanced multiferroic properties of lead-free (1-x)GaFeO3-(x)Co0.5Zn0.5Fe2O4 composites, J Appl Phys. 124 (2018) 154101. https://doi.org/10.1063/1.5044675.

[12] R.S. Kharat, M. Saleem, N. Kaurav, H.S. Dagar, A study of structural, optical and electrical studies of the composites of ZnFe2O4, BiFeO3 and GaFeO3 compounds, AIP Conf Proc. 2369 (2021) 020223. https://doi.org/10.1063/5.0061846.

[13] R.S. Kharat, M. Saleem, N. Kaurav, H.S. Dagar, Composites of ZnFe2O4 and GaFeO3: Structural, optical bandgap and morphology studies, AIP Conf Proc. 2369 (2021) 020165. https://doi.org/10.1063/5.0061848.

[14] F.P. Gheorghiu, A. Ianculescu, P. Postolache, N. Lupu, M. Dobromir, D. Luca, L. Mitoseriu, Preparation and properties of (1 − x)BiFeO3–xBaTiO3 multiferroic ceramics, J Alloys Compd. 506 (2010) 862–867. https://doi.org/10.1016/J.JALLCOM.2010.07.098.

[15] H. Yang, Q. Ke, H. Si, J. Chen, 0.7BiFeO3-0.3BaTiO3-Y3Fe5O 12 composites with simultaneously improved electrical and magnetic properties, J Appl Phys. 111 (2012). https://doi.org/10.1063/1.3677944.

[16] G. Schileo, C. Pascual-Gonzalez, M. Alguero, I.M. Reaney, P. Postolache, L. Mitoseriu, K. Reichmann, A. Feteira, Yttrium Iron Garnet/Barium Titanate Multiferroic Composites, Journal of the American Ceramic Society. 99 (2016) 1609–1614. https://doi.org/10.1111/JACE.14131.

[17] K. Sakata, Y. Masuda, Ferroelectric and Antiferroelectric Properties of (Na0.5 Bi0.5)TiO3-SrTiO3 Solid Solution Ceramics, Ferroelectrics. 7 (1974) 347–349. https://doi.org/10.1080/00150197408238042.

[18] B.-J. Chu, D.-R. Chen, G.-R. Li, Q.-R. Yin, Electrical properties of Na 1/2 Bi 1/2 TiO 3-BaTiO 3 ceramics, n.d. www.elsevier.com/locate/jeurceramsoc.

[19] J. Suchanicz, J. Kusz, H. Bö Hm, Structural and electric characteristics of (Na 0.5 Bi 0.5) 0.50 Ba 0.50 TiO 3 and (Na 0.5 Bi 0.5) 0.20 Ba 0.80 TiO 3 ceramics, n.d. www.elsevier.com/locate/mseb.

[20] X. Wang, H. Lai-Wa Chan, C. Choy, Piezoelectric and dielectric properties of CeO 2-added (Bi 0.5 Na 0.5) 0.94 Ba 0.06 TiO 3 lead-free ceramics, n.d. www.elsevier.com/locate/ssc.

[21] O. Elkechai, M. Manier, J.P. Mercurio, Na0.5Bi0.5TiO3-K0.5Bi 0.5TiO3 (NBT-KBT) system: A structural and electrical study, Physica Status Solidi A Appl Res. 157 (1996) 499–506. https://doi.org/10.1002/pssa.2211570234.

[22] H. Yang, S.-H. Cho, Y. Yun, al -, S. Tatsumi, Y. Sasaki, S. Toyoda, X. Yuan, Y. Sakurai, S. Kondo, Lead-Free Piezoelectric Ceramics of (Bi 1/2 Na 1/2)TiO 3-KNbO 3-1/2(Bi 2 O 3 ·Sc 2 O 3) System You may also like Eight-year Simultaneous Monitoring Observations of H 2 O and SiO Masers toward V627 Cas Planar electro-optic deflector using KTa 1x Nb x O 3 for low-power-consumption operation Effect of Ni doping on the electro-optic property in K(Ta 0.6 Nb 0.4)O 3 films, 1998.

[23] A. Ali Khan, S. Ahmad Arbab, A. Manan, al -, A. Sasaki, T. Chiba, Y. Mamiya, E. Otsuki, Dielectric and Piezoelectric Properties of (Bi 0.5 Na 0.5)TiO 3-(Bi 0.5 K 0.5)TiO 3 Systems Inorganic dielectric materials for energy storage applications: a review Anina Anju Balaraman and Soma Dutta-Dielectric and Piezoelectric Properties of (Bi 0.5 Na 0.5)TiO 3-(Bi 0.5 K 0.5)TiO 3 Systems, 1999.

[24] J. Yun Yi, J.-K. Lee, P. Chen, C. Yang, J. Cai, al -, T. Wada, K. Toyoike, Y. Imanaka, Y. Matsuo, Dielectric and Piezoelectric Properties of (A 0.5 Bi 0.5)TiO 3-ANbO 3 (A=Na, K) Systems You may also like Stabilized antiferroelectric phase in lanthanum-doped (Na Inorganic dielectric materials for energy storage applications: a review Anina Anju Balaraman and Soma Dutta-Dielectric and Piezoelectric Properties of (A 0.5 Bi 0.5)TiO 3-ANbO 3 (A = Na, K) Systems morphotropic phase boundary, 2001.

[25] J. Suchanicz, Behaviour of Na 0.5 Bi 0.5 TiO 3 ceramics in the a.c. electric field , Ferroelectrics. 209 (1998) 561–568. https://doi.org/10.1080/00150199808018070.

[26] Soft Modes in Ferroelectrics and Antiferroelectrics, n.d. http://iopscience.iop.org/0031-9112/27/3/038.

[27] R.A. Cowley, Structural phase transitions I. Landau theory, Adv Phys. 29 (1980) 1–110. https://doi.org/10.1080/00018738000101346.

[28] M. Fischer, A.M. Lahmar Maglione, A. San Miguel, J.P. Itic, A. Polian, F. Baudelet, Local disorder studied in SrTi03 at low temperature by EXAFS spectroscopy, 1994.

[29] H. Unoki, T. Sakudo, Electron Spin Resonance of Fe3+ in SrTiO3 with Special Reference to the 110°K Phase Transition, J Physical Soc Japan. 23 (1967) 546–552. https://doi.org/10.1143/JPSJ.23.546.

[30] A. Dutta, A. Gorai, D. Mandal, K. Mandal, Dielectric and microwave absorption properties of Na0.5Bi0.5TiO3–SrTiO3 system, Ferroelectrics. 583 (2021) 252–263. https://doi.org/10.1080/00150193.2021.1980324.

[31] V.B. Naik, R. Mahendiran, Electrical, magnetic, magnetodielectric, and magnetoabsorption studies in multiferroic GaFeO3, J Appl Phys. 106 (2009). https://doi.org/10.1063/1.3271391.

[32] K. Okada, T. Sakuma, The Role of Zener's Pinning Effect on the Grain Growth in Al2O3-ZrO2, n.d.

[33] G.W. Pabst, L.W. Martin, Y.H. Chu, R. Ramesh, Leakage mechanisms in BiFe O3 thin films, Appl Phys Lett. 90 (2007). https://doi.org/10.1063/1.2535663.

[34] B.S. Simpkins, M.A. Mastro, C.R. Eddy, J.K. Hite, P.E. Pehrsson, Space-charge-limited currents and trap characterization in coaxial AlGaN/GaN nanowires, J Appl Phys. 110 (2011). https://doi.org/10.1063/1.3622145.

[35] C.C. Lee, J.M. Wu, Studies on leakage mechanisms and electrical properties of doped BiFe O3 films, Electrochemical and Solid-State Letters. 10 (2007). https://doi.org/10.1149/1.2745123.

[36] N. Rezlescu, E. Rezlescu, Abnormal dielectric behaviour of copper containing ferrites, Solid State Commun. 14 (1974) 69–72. https://doi.org/10.1016/0038-1098(74)90234-8.

[37] A. Mukherjee, Sk.M. Hossain, M. Pal, S. Basu, Effect of Y-doping on optical properties of multiferroics BiFeO3 nanoparticles, Appl Nanosci. 2 (2012) 305–310. https://doi.org/10.1007/s13204-012-0114-8.

[38] Y.J. Wu, Y. Gao, X.M. Chen, ARTICLES YOU MAY BE INTERESTED IN, Appl. Phys. Lett. 91 (2007) 92912. https://doi.org/10.1063/1.2780116.

[39] A.J. Gualdi, F.L. Zabotto, D. Garcia, A.J.A. de Oliveira, Stress magnetization model for magnetostriction in multiferroic composite, J Appl Phys. 114 (2013). https://doi.org/10.1063/1.4816785.

[40] A.J. Gualdi, F.L. Zabotto, D. Garcia, A. Bhalla, R. Guo, P.C. de Camargo, A.J.A. de Oliveira, Understanding the dynamic magnetization process for the magnetoelectric effect in multiferroic composites, J Appl Phys. 119 (2016). https://doi.org/10.1063/1.4944889.

[41] C.C. Hu, Z. Zhang, T.N. Yang, Y.G. Shi, X.X. Cheng, J.J. Ni, J.G. Hao, W.F. Rao, L.Q. Chen, Phase field simulation of grain size effects on the phase coexistence and magnetostrictive behavior near the ferromagnetic morphotropic phase boundary, Appl Phys Lett. 115 (2019). https://doi.org/10.1063/1.5118927.

[42] W. Kim, J.H. We, S.J. Kim, C.S. Kim, Effects of cation distribution for AFe O3 (A=Ga,Al), in: J Appl Phys, 2007. https://doi.org/10.1063/1.2712819.

[43] T.C. Han, T.Y. Chen, Y.C. Lee, Grain size effect on site-disorder and magnetic properties of multiferroic GaFeO3 nanoparticles, Appl Phys Lett. 103 (2013). https://doi.org/10.1063/1.4838057.

[44] Y. Zhu, X. Yang, N.M. Wereley, Research on hysteresis loop considering the prestress effect and electrical input dynamics for a giant magnetostrictive actuator, Smart Mater Struct. 25 (2016). https://doi.org/10.1088/0964-1726/25/8/085030.

[45] A. Jakubas, K. Chwastek, A simplified sablik's approach to model the effect of compaction pressure on the shape of hysteresis loops in soft magnetic composite cores, Materials. 13 (2020). https://doi.org/10.3390/ma13010170.

[46] B.C. K HEAps, The Effect of Strain on Magnetostriction and Magnetization in Nickel, 1894.

[47] A. Zhukov, M. Ipatov, J.M. Blanco, P. Corte-León, J. Olivera, J. Gonzalez, V. Zhukova, Engineering of magnetic properties of magnetic microwires, in: Acta Phys Pol A, Polish Academy of Sciences, 2018: pp. 321–328. https://doi.org/10.12693/APhysPolA.133.321.

[48] V.S. Severikov, A.M. Grishin, V.S. Ignahin, Study of inverse magnetostrictive effect in metallic glasses Fe80-xCoxP14B6, in: J Phys Conf Ser, Institute of Physics Publishing, 2017. https://doi.org/10.1088/1742-6596/929/1/012049.

[49] M.J. Sablik, T. Yonamine, F.J.G. Landgraf, Modeling plastic deformation effects in steel on hysteresis loops with the same maximum flux density, IEEE Trans Magn. 40 (2004) 3219–3226. https://doi.org/10.1109/TMAG.2004.832763.

[50] A. Mager, Über den Einfluß der Korngröße auf die Koerzitivkraft, Ann Phys. 446 (1952) 15–16. https://doi.org/https://doi.org/10.1002/andp.19524460104.

[51] R.H. Yu, S. Basu, Y. Zhang, A. Parvizi-Majidi, J.Q. Xiao, Pinning effect of the grain boundaries on magnetic domain wall in FeCo-based magnetic alloys, J Appl Phys. 85 (1999) 6655–6659. https://doi.org/10.1063/1.370175.

[52] N. Choudhary, S. Sharma, M.K. Verma, N.D. Sharma, D. Singh, Comparative Study of Nano- and Bulk La0.5Sr0.5Ti0.5Co0.5O3 Perovskite: Structural, Magnetic, and Transport Properties, J Supercond Nov Magn. 31 (2018) 3269–3275. https://doi.org/10.1007/s10948-018-4575-1.

[53] P. Uniyal, K.L. Yadav, Pr doped bismuth ferrite ceramics with enhanced multiferroic properties, Journal of Physics: Condensed Matter. 21 (2009) 405901. https://doi.org/10.1088/0953-8984/21/40/405901.

[54] V.R. Palkar, D.C. Kundaliya, S.K. Malik, S. Bhattacharya, Magnetoelectricity at room temperature in the <span class="aps-inline-formula"><math xmlns="http://www.w3.org/1998/Math/MathML" display="inline"><mrow><msub><mrow><mi mathvariant="normal">Bi</mi></mrow><mrow><mn>0.9</mn><mi>−</mi><mi>x</mi></mrow></msub></mrow><mrow><msub><mrow><mi mathvariant="normal">Tb</mi></mrow><mrow><mi>x</mi></mrow></msub></mrow><mrow><msub><mrow><mi mathvariant="normal">La</mi></mrow><mrow><mn>0.1</mn></mrow></msub></mrow><mrow><msub><mrow><mi mathvariant="normal">FeO</m, Phys Rev B. 69 (2004) 212102. https://doi.org/10.1103/PhysRevB.69.212102.

[55] G. Catalan, Magnetocapacitance without magnetoelectric coupling, Appl Phys Lett. 88 (2006) 102902. https://doi.org/10.1063/1.2177543.

[56] S. Dugu, S. Kumari, D.K. Pradhan, C. Zuluaga Gómez, M. Holcomb, R.S. Katiyar, Tuning the magnetic phase transition above room temperature through Fe and Mn modification in gallium ferrite with reduced leakage current, J Phys D Appl Phys. 53 (2020). https://doi.org/10.1088/1361-6463/ab795c.

[57] N. Sharma, A.K. Mall, R. Gupta, A. Garg, S. Kumar, Significant reduction in the leakage current of Cr-doped GaFeO3 synthesized by sol–gel method, Appl Phys A Mater Sci Process. 123 (2017). https://doi.org/10.1007/s00339-017-1159-z.

[58] C. Song, X. Yan, Q. Liu, J.X. Sui, H.S. Zhao, S. Xu, F. Yuan, Y.Z. Long, Magnetic and ferroelectric properties of Indium-doped gallium ferrite, J Magn Magn Mater. 469 (2019) 8–12. https://doi.org/10.1016/j.jmmm.2018.08.032.

[59] A. Ghani, S. Yang, S.S. Rajput, S. Ahmed, A. Murtaza, C. Zhou, Z. Yu, Y. Zhang, X. Song, X. Ren, Electric modulation of conduction in multiferroic Ni-doped GaFeO3 ceramics, J Phys D Appl Phys. 51 (2018). https://doi.org/10.1088/1361-6463/aaba34.

[60] T.C. Han, Z.Y. Tu, Y.T. Huang, Enhanced magnetic and magnetodielectric properties of Al-doped gallium ferrite nanoparticles, AIP Adv. 10 (2020). https://doi.org/10.1063/1.5130051.

[61] V. Singh, K. Brajesh, S. Sahu, A. Garg, R. Gupta, Control of electrical leakage in magneto-electric gallium ferrite via aliovalent substitution, Journal of the American Ceramic Society. 102 (2019) 7414–7427. https://doi.org/10.1111/jace.16626.

[62] K. Mukhopadhyay, A.S. Mahapatra, P.K. Chakrabarti, Enhanced magneto-electric property of GaFeO3 in Ga (1-x)ZnxFeO3 (x=0, 0.05, 0.10), Physica B Condens Matter. 448 (2014) 214–218. https://doi.org/10.1016/j.physb.2014.03.053.

[63] A. Ghani, S. Yang, S. Rajput, S. Ahmed, A. Murtaza, C. Zhou, Z. Yu, Y. Liu, X. Song, Tuning the conductivity and magnetism of silicon coated multiferroic $GaFeO_3$ nanoparticles, J Solgel Sci Technol. 92 (2019) 224–230. https://doi.org/10.1007/s10971-019-05096-y.

CHAPTER 5

MICROWAVE APPLICATIONS

This chapter discusses the applications of multiferroic materials as a microwave absorbing material or MAM.

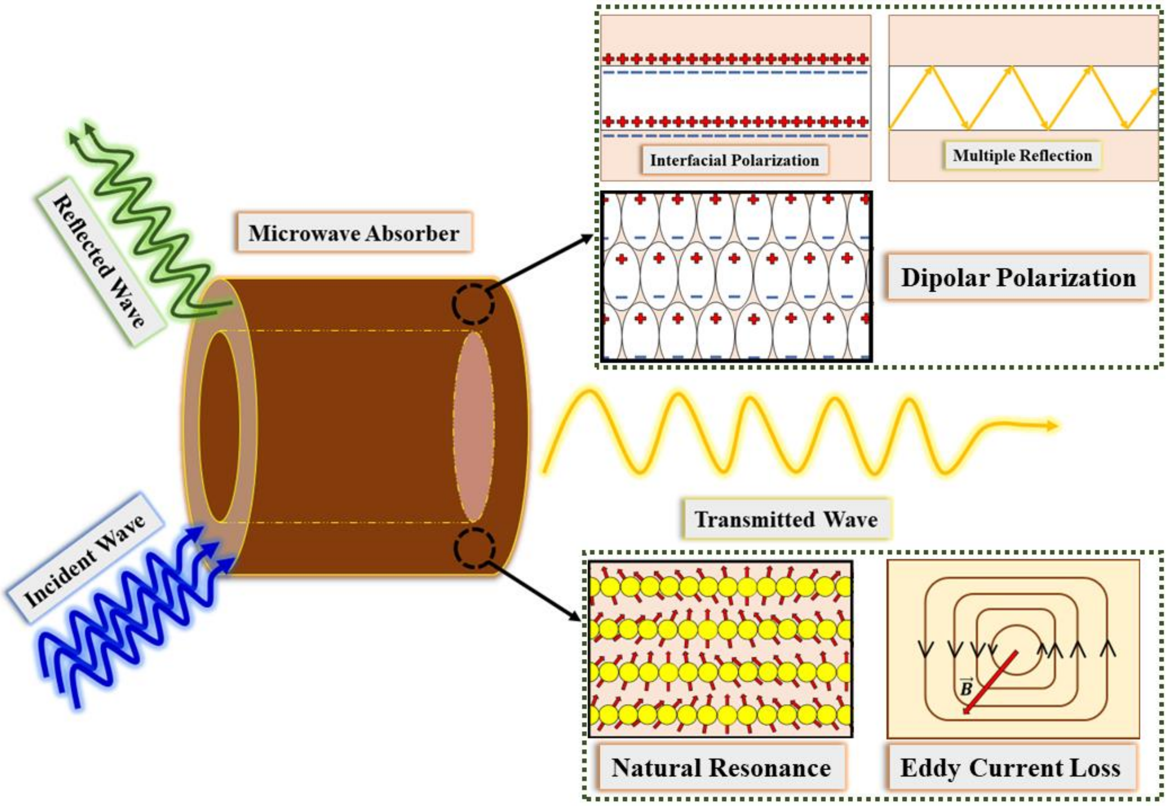

5.1 PREAMBLE

High prevalence of electromagnetic interferences in daily life has become dangerous as a perilous result of recent advances in modern technology[1]. Therefore, research into and development of lightweight, inexpensive materials that can absorb a significant amount of microwave energy have garnered a great deal of interest in the quest to eliminate electromagnetic pollution. As a result, a variety of materials, namely resistor[2], dielectric[3], magnetic[4] and mixed type materials, have been studied in recent years. Ferrites that possess both magnetic and dielectric properties have distinguished themselves as being particularly promising in absorbing significant microwave radiation[5]. Additionally, multiferroic ferrites with magnetoelectric (ME) coupling and magnetic and electric properties, such as bismuth ferrite ($BiFeO_3$), are another option that is advantageous for blocking electromagnetic radiation in the microwave frequency range[6].

One of the very few room-temperature multiferroic materials, $BiFeO_3$ (BFO) exhibits ferroelectricity as well as modest ferromagnetism and coupling at ambient temperature. As an alternative, gallium ferrite ($Ga_{2-x}Fe_xO_3$ or GFO) is another intriguing multiferroic material with near-room temperature ferrimagnetism and a considerable magnetoelectric coupling coefficient (10^{-11} s/m at 4.2 K)[7]. In GFO, it is observed that increasing the Fe:Ga ratio is very useful in increasing its ferrimagnetic property while increasing the magnetic phase transition temperature simultaneously. To the best of our knowledge, this material's microwave properties have not yet been investigated. Therefore, in this work, the microwave properties of $Ga_{2-x}Fe_xO_3$ for x = 1.2 is studied in detail due to its room temperature ferrimagnetic property[8] and the difference in microwave properties of gallium ferrite and bismuth ferrite based on their structural differences is reported.

On the other hand, numerous techniques have been used to increase the microwave absorption and bandwidth of single-phase bismuth ferrite, including modifying the particle size, the synthesis conditions, and doping with the appropriate elements[9,10]. In a Holmium doped BFO, for instance, improved impedance matching by increased magnetization led to an improvement in the minimum reflection loss (RL_{min}) from -8.5 dB to -11 dB and an improved bandwidth (BW) from 0 to 1 GHz[11]. In a lanthanum doped BFO, matching of the magnetic loss ($tan\delta_\mu$) and the dielectric loss ($tan\delta_\varepsilon$) is observed to enhance the RL_{min} from -12 dB to -30 dB and increase the BW from 0.9 to 1.1 GHz[12]. Nd-doped BFO[13], claiming an RL_{min} of -42 dB and BW of 3 GHz, also exhibits a similar phenomenon. In BFO-coated Fe nano capsules, the absorption is observed to be enhanced by natural resonance and increased polarization at the interface of the core-shell structure[14]. Phase boundary manipulation in the coexisting *R*3*c* and *P*4*mm* phases of calcium-doped BFO is also carried out, with improved microwave absorption reported[10]. However, there is still considerable scope of investigating a single-phase BFO which is able to simultaneously have a significant absorption and a wide bandwidth. In chapter 3, we have reported that Ba and Y co-doping at the Bi-site of BFO nanoparticles can improve its ferroelectric, dielectric, and magnetodielectric properties. Up to 5 at. wt.% doping of Y, the phase structure of the nanoparticles remains in their ferroelectric rhombohedral phase. Further increment in doping concentration transforms the phase into a paraelectric orthorhombic phase. In this work, our motive is to study the applicability of Ba and Y co-doped BFO nanoparticles as microwave absorption materials (MAMs) up to the doping percentage of 5 at. wt.% in which it retains its ferroelectricity and magnetoelectric characteristics.

Previously, the microwave properties of Bismuth Sodium Titanate – Strontium Titanate ($Sr_{0.5}Bi_{0.25}Na_{0.25}TiO_3$, SNBT50) solid solution has been reported to exhibit good microwave absorption and bandwidth[15]. However, SNBT50 is a very strong ferroelectric exhibiting diamagnetism at room temperature whereas the 0-3 composite of SNBT50 with highly resistive ferromagnet, Yttrium Iron Garnet (YIG) is a magnetoelectric material having good magnetic and magnetodielectric properties. Additionally, high applicability of YIG at high frequency region makes this composite a very interesting magnetoelectric material to study for the purpose of application as MAMs. In chapter 4 of this thesis, we have shown that although SNBT50 is diamagnetic in nature and do not exhibit any coupling, SNBT50-YIG composites possess strong coupling between magnetic and electric parameters at room temperature. In this work, the microwave properties of 0-3 composite of Yttrium Iron Garnet (YIG) embedded in matrix of Bismuth Sodium Titanate – Strontium Titanate ($Sr_{0.5}Bi_{0.25}Na_{0.25}TiO_3$) solid solution is studied in detail and reported to exhibit enhanced microwave absorption.

5.2 EXPERIMENTAL METHOD

5.2.1 SYNTHESIS

5.2.1.1 $BiFeO_3$ and $Ga_{0.8}Fe_{1.2}O_3$

Powders of $BiFeO_3$ and $Ga_{0.8}Fe_{1.2}O_3$ are made using the sol-gel technique. Nitrates of the necessary chemicals are taken in the appropriate stoichiometric ratios and dissolved in double-distilled water to create BFO and GFO. The dried brown powders of BFO and GFO are produced by heating the solutions for 24 hours at a temperature of 80 °C. These powders are then grinded for hours in an agate mortar. For two hours, the ground-up BFO powder is calcined at 600 °C to create the appropriate crystal structure whereas, the ground-up GFO powder is first calcined at 600 °C for 8 hours, then sintered at 1300 °C for 4 hours to achieve the desired crystal structure. The prepared samples are grown in a matrix of epoxy resin with a 50% concentration in the shape of a hollow cylinder with an outside diameter of 3.5mm and an inner diameter of 1.5mm in order to perform microwave measurements.

5.2.1.2 Barium and Yttrium co-doped Bismuth Ferrite Nanoparticles

Using the tartaric acid-assisted sol-gel process, the $Ba_yBi_{1-x-y}Y_xFeO_3$ (x = 0.0 at y = 0.0 and x = 0.0, 0.03, 0.05 at y = 0.1) nanoparticles are created. In the presence of nitric acid, $Bi(NO_3)_3.5H_2O$, $Fe(NO_3)_3.9H_2O$, $Ba(NO_3)_2.H_2O$, and $Y(NO_3)_3.6H_2O$, all raw materials with high purity (more than 99.9%), are dissolved in the appropriate stoichiometric ratios. As a chelating agent, tartaric acid ($C_6H_6O_7$) is added to the nitrates to finish their combustion. The yellow, transparent solution is stirred vigorously and kept at a temperature 80 °C until it is completely dried. After that, the fluffy dried powder is gathered and grinded in an agate mortar. To produce the nanoparticles, the powders are calcined at 700 °C for 30 minutes. The samples are grown in a matrix of epoxy resin with a 25% concentration in order to collect microwave data. A hollow cylinder with an outside diameter of 3.5mm and an inner diameter of 1.5mm is formed from the composite materials.

5.2.1.3 $Sr_{0.5}(Na_{0.5}Bi_{0.5})_{0.5}TiO_3$ – $Y_3Fe_5O_{12}$

To prepare the (1-x) $Sr_{0.5}Bi_{0.25}Na_{0.25}TiO_3$ (SNBT50) – x $Y_3Fe_5O_{12}$ (YIG) composites for x = 0.0, 0.1 and 0.2, solid state reaction method has been followed. The stoichiometric amounts of high purity Bi_2O_3 (99% pure, Loba Chemie), TiO_2 (98%, Loba Chemie), Na_2CO_3 (99.5%, Loba Chemie), and $SrCO_3$ (reagent grade, Loba Chemie) are thoroughly mixed in the acetone medium. Y_2O_3 and Fe_3O_4 (> 99%, Sigma Aldrich) is added in respective ratio for the preparation of composites of different YIG concentrations. After grinding the mixture for 8 h using agate mortar, the mixtures are calcined in an alumina crucible at 1173 K for 12 h in air and brought to room temperature by cooling at the rate of 80 K/h. The calcined samples are pelletized into a disk (diameter 5 mm) and sintered at 1223 K for 4 h in closed alumina crucibles to avoid bismuth loss and cooled down to room temperature by cooling at the rate of 1 K/min. The final samples are mixed with resin with a cocnentration of 25% and shaped into a hollow cylinder of inner diameter of 1.5mm and outer diameter of 3.5mm in order to perform microwave measurements.

5.2.2 CHARACTERIZATION

X-Ray Diffraction (XRD) of all samples is carried out with a Rigaku Smart Lab diffractometer and Cu-K$_\alpha$ radiation with a wavelength of 1.5406 Å; Rietveld refinement of the resultant XRD data is conducted using FullProf software. VESTA software is used to plot the improved structures in order to visualize the unit cell structures. The diameters of the synthesized nanoparticles are measured using a FEG high-resolution transmission electron microscope (HRTEM) (80-200 kV). Utilizing a scanning electron microscope (SEM) equipped with an AMETEK EDAX QUANTA 200 and Element, energy dispersive x-ray analysis (EDAX) is investigated for all samples. All of the tests in this work are conducted at 300 K, depicted as room temperature (RT). The Lakeshore Vibrating Sample Magnetometer is utilized to analyze the magnetic hysteresis loops for all samples at room temperature (VSM). The resin composite formed with the samples in the shape of hollow cylinders with inner diameter of 1.5mm and outer diameter of 3.5mm to fit into the coaxial airline are used to study their microwave properties. The microwave experiments are performed using an Anritsu MS46122B vector network analyser and a coaxial airline (Maury Microwaves 8043S6).

5.3 RESULTS AND DISCUSSION

5.3.1 STRUCTURAL STUDY

5.3.1.1 $BiFeO_3$ and $Ga_{0.8}Fe_{1.2}O_3$

Figure 5.1(a) depicts the XRD diffractograms of all of the samples. Rhombohedral structure of BFO is observed in all the materials along with one impurity peak at 27.5^o attributed to the existence of a small quantity of $Bi_2Fe_4O_9$ (Card Number: 01-020-0836). For GFO with an orthorhombic structure, pure phase is attained, as indicated by Card Number: 00-062-0890 [Figure 5.1(b)]. Using a Williamson-Hall analysis, the crystallite size and strain of the

Table 5.1 - Lattice parameters of $BiFeO_3$ and $Ga_{0.8}Fe_{1.2}O_3$ powders obtained from Rietveld Refinement and Williamson-Hall analysis of XRD data

Sample Name	*a(Å)*	*b(Å)*	*c(Å)*	*V(Å³)*	*Crystallite Size (nm)*	*Strain (ε)*
$BiFeO_3$	5.636	5.636	14.033	384.38	42.9	-6.48E-4
$Ga_{0.8}Fe_{1.2}O_3$	8.757	9.408	5.088	419.01	52.7	-3.91E-4

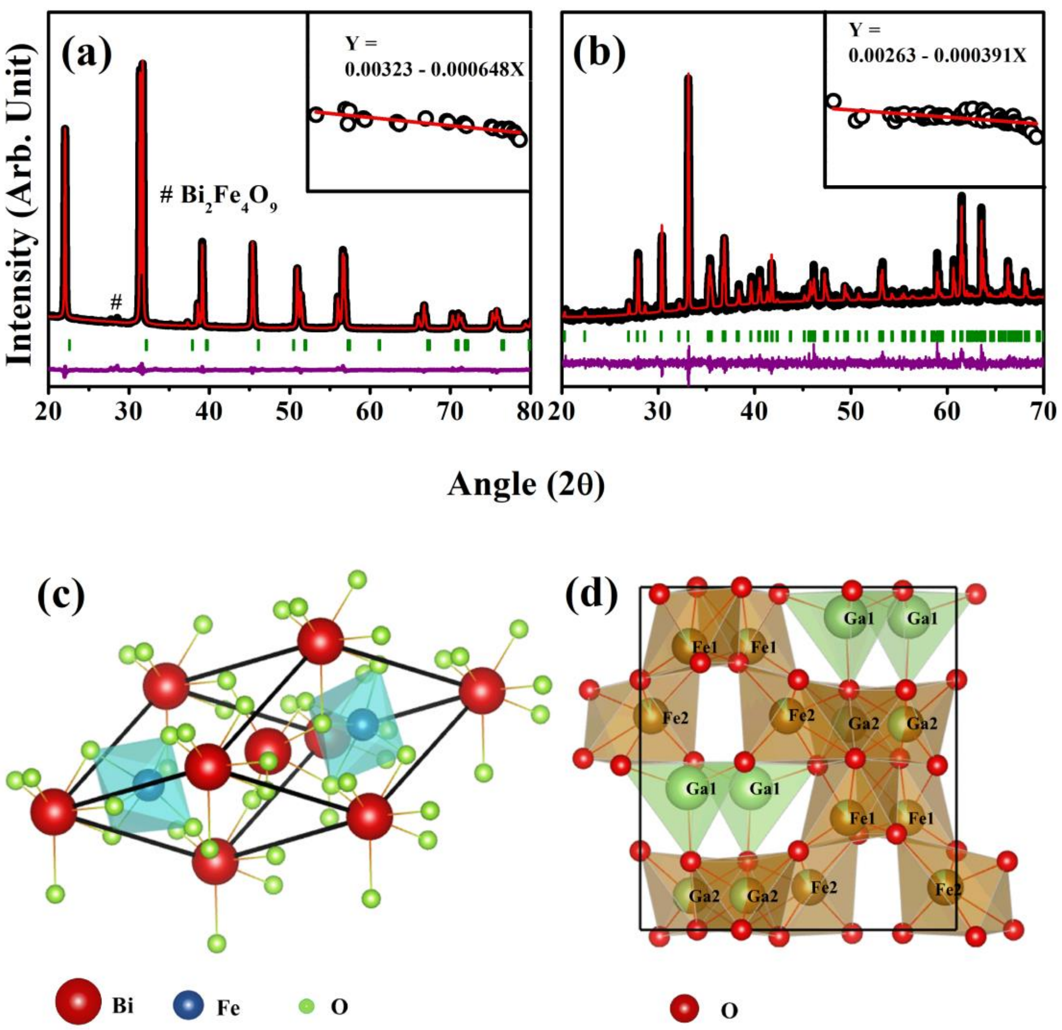

Figure 5.1 (a) X-Ray Diffraction analysis of $BiFeO_3$ and (b) $Ga_{0.8}Fe_{1.2}O_3$ depicting the single-phase nature of the samples. (c) Rhombohedral lattice structure of $BiFeO_3$ (d) Orthorhombic lattice structure of $Ga_{0.8}Fe_{1.2}O_3$.

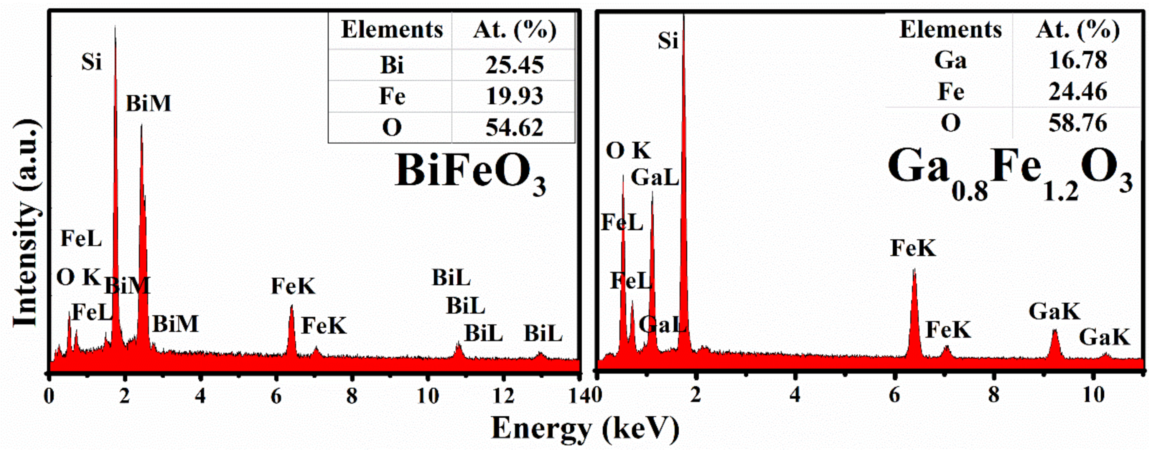

Figure 5.2 EDAX spectra confirming the presence and atomic percentage of different elements in the samples.

samples are determined; the results are displayed in the insets of Figures 5.1(a) and 5.1(b) for the BFO and GFO, respectively. Using VESTA, Figure 5.1(c) illustrates a unit cell of BFO with a single FeO_6 octahedron, which determines the magnetic properties of BFO, and a pseudocubic lattice structure distorted along the $[111]_C$ direction, which disrupts the lattice's centrosymmetry and results in ferroelectricity in the sample. In addition, one GFO unit cell, shown in Figure 5.1(d), has four different types of cations: Ga1, Ga2, Fe1, and Fe2. Based on the polyhedrons that the various cations make with the close-by oxygen anions, Ga1 forms tetrahedrons, while Ga2, Fe1, and Fe2 form octahedrons. The placement of Ga2 ions with Fe ions due to the similarity in their ionic radii causes the ferrimagnetic nature of the sample, known as site-disorder, whereas the distortion of the unit cell is responsible for the observation of polarisation. This is because the Fe1, Fe2 are antiferromagnetically coupled to one another.

Ga:Fe:O and Bi:Fe:O ratios as determined by the analysis are 0.80:1.17:3.47 and 1.4:1.1:3.0, respectively, which are near to the ideal ratios of 0.8:1.2:3 and 1:1:3, respectively, according to EDAX data for $Ga_{0.8}Fe_{1.2}O_3$ and $BiFeO_3$ samples shown in Figure 5.2.

5.3.1.2 Barium and Yttrium co-doped Bismuth Ferrite Nanoparticles

Figure 5.3 depicts the X-Ray diffractograms of all $Ba_yBi_{1-x-y}Y_xFeO_3$ nanoparticles with x = 0.0 at y = 0.0 (BFO) and x = 0.0 (BaBYFO-0), 0.03 (BaBYFO-3), and 0.05 (BaBYFO-5) at y

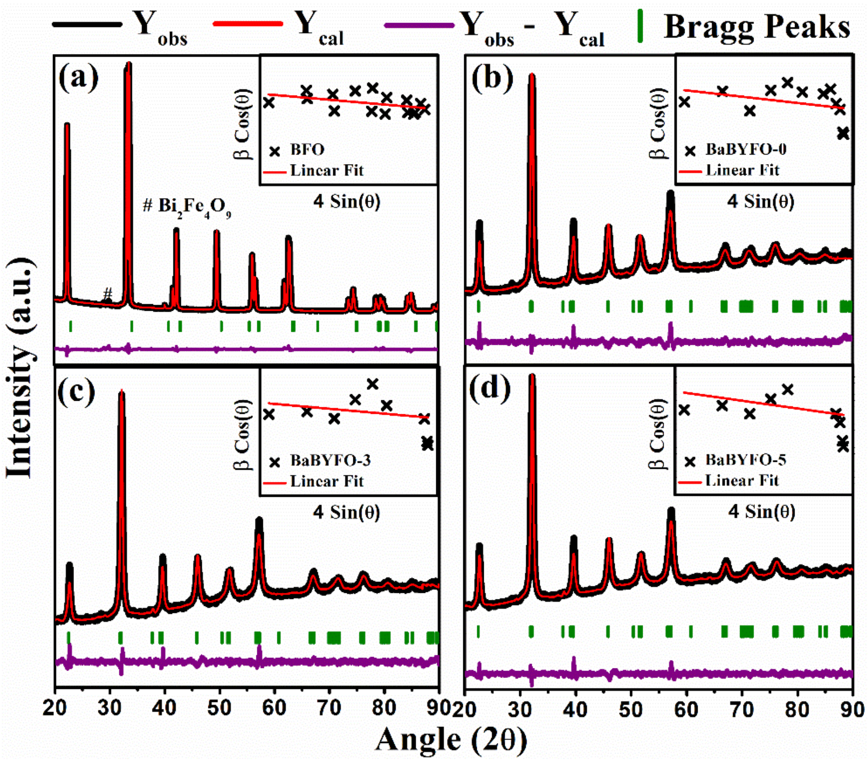

Figure 5.3 Room temperature XRD data of (a) BFO, (b) BaBYFO-0, (c) BaBYFO-3, and (d) BaBYFO-5 along with the Rietveld refinement analysis. The insets depict the Williamson-Hall plots for corresponding sample.

= 0.1. All of the samples exhibit pure rhombohedral structure without any signs of secondary phase. The results of Rietveld refinement are summarized in Table 5.2, which shows that all doped samples have less volume. As a consequence of the substitution of the smaller Bi^{3+} (1.03 Å) ion with the larger Ba^{2+} (1.35 Å), the compressive strain decreases in the Ba2+ doped sample (BaBYFO-0), but rises when the Y^{3+} (0.9 Å) ion is introduced. The recovered bond angles and bond lengths, which are reported in Table 5.2, are visualized in VESTA using the derived refined structures. The Fe-O1-Fe angle gradually decreases as

doping concentration rises. The insets of the TEM image depicted in Figure 5.4(a-d) display the size distribution of the corresponding particles and indicate significantly smaller nanoparticle sizes of the doped samples. For BFO, BaBYFO-0, 3, and 5, the measured mean particle sizes are 126 ± 39 nm, 46 ± 6 nm, 41 ± 6 nm, and 30 ± 5 nm, respectively. This change in particle size can be explained using the Kirkendall effect, which states that an increase in cations is capable of altering diffusion, which changes particle nucleation and reduces particle size. The lattice fringe values corresponding to the (012), (021), (110), (101), and (003) planes of the BFO are seen in all of the samples, according to the HRTEM images of all samples (Figure 5.5(a, c, e, g). The EDAX spectra shown in Figure 5.5(b, d, f, h) confirms the presence of Bi, Fe, and O in BFO ($BiFeO_3$), Ba, Bi, Fe, and O in BaBYFO-0 ($Ba_{0.1}Bi_{0.9}FeO_3$), Bi, Ba, Y, Fe, and O in BaBYFO-3 ($Ba_{0.1}Bi_{0.87}Y_{0.03}FeO_3$) and BaBYFO-5

Table 5.2 - Structural parameters of $Ba_yBi_{1-x-y}Y_xFeO_3$ nanoparticles obtained from Rietveld and Williamson-Hall analysis of room temperature XRD data

Sample Name	Lattice Parameters	Bond Length (Å)	Bond Angle (°)	Crystallite Size (nm) and strain
BFO	*a* = 5.602 Å *c* = 13.86 Å *V* = 384.57 *c/a* = 2.47	3.07 (Bi-Fe) 2.12 (Fe-O1) 1.94 (Fe-O2) 2.32 (Bi-O1)	73.3 (O1-Bi-O1) 156.2 (Fe-O1-Fe) 87.2 (Bi-O1-Fe)	*d* = 42.98 nm *e* = -7.29×10^{-4}
BaBYFO-0	*a* = 5.5901 Å *c* = 13.835 Å *V* = 374.411 *c/a* = 2.48	3.06 (Bi-Fe) 2.13 (Fe-O1) 1.96 (Fe-O2) 2.33 (Bi-O1)	73.64 (O1-Bi-O1) 152.62 (Fe-O1-Fe) 86.8 (Bi-O1-Fe)	*d* = 33.16 nm *e* = -3.35×10^{-4}
BaBYFO-3	*a* = 5.599 Å *c* = 13.726 Å *V* = 372.659 *c/a* = 2.45	3.07 (Bi-Fe) 1.95 (Fe-O1) 2.15 (Fe-O2) 2.4 (Bi-O1)	66.67 (O1-Bi-O1) 150.63 (Fe-O1-Fe) 89.3 (Bi-O1-Fe)	*d* = 27.83 nm *e* = -2.06×10^{-4}
BaBYFO-5	*a* = 5.581 Å *c* = 13.772 Å *V* = 371.521 *c/a* = 2.47	3.1 (Bi-Fe) 2.03 (Fe-O1) 2.07 (Fe-O2) 2.39 (Bi-O1)	69.2 (O1-Bi-O1) 149.51 (Fe-O1-Fe) 88.6 (Bi-O1-Fe)	*d* = 26.5 nm *e* = -7.18×10^{-4}

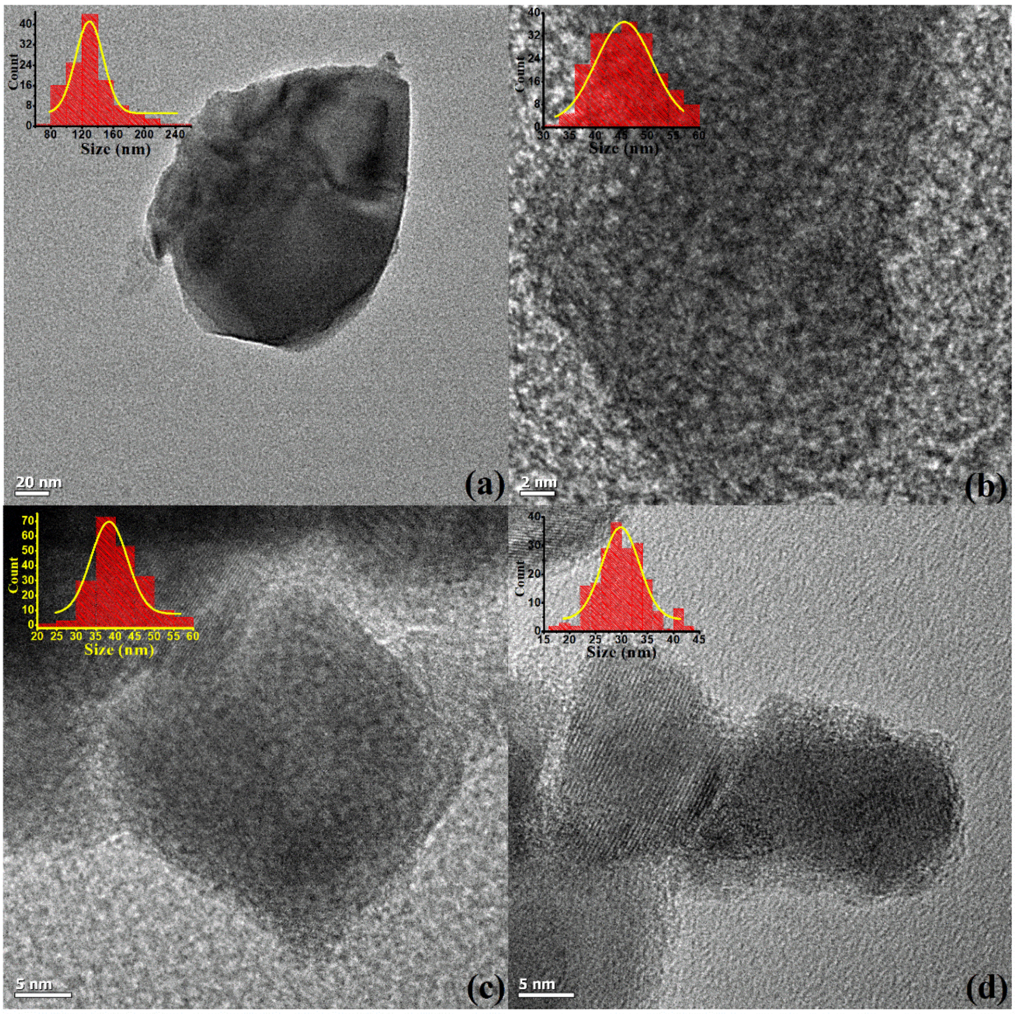

Figure 5.4 (a-d) depicts TEM images of BFO, BaBYFO-0, BaBYFO-3, and BaBYFO-5 respectively. The insets indicate the particle size distribution of the corresponding sample.

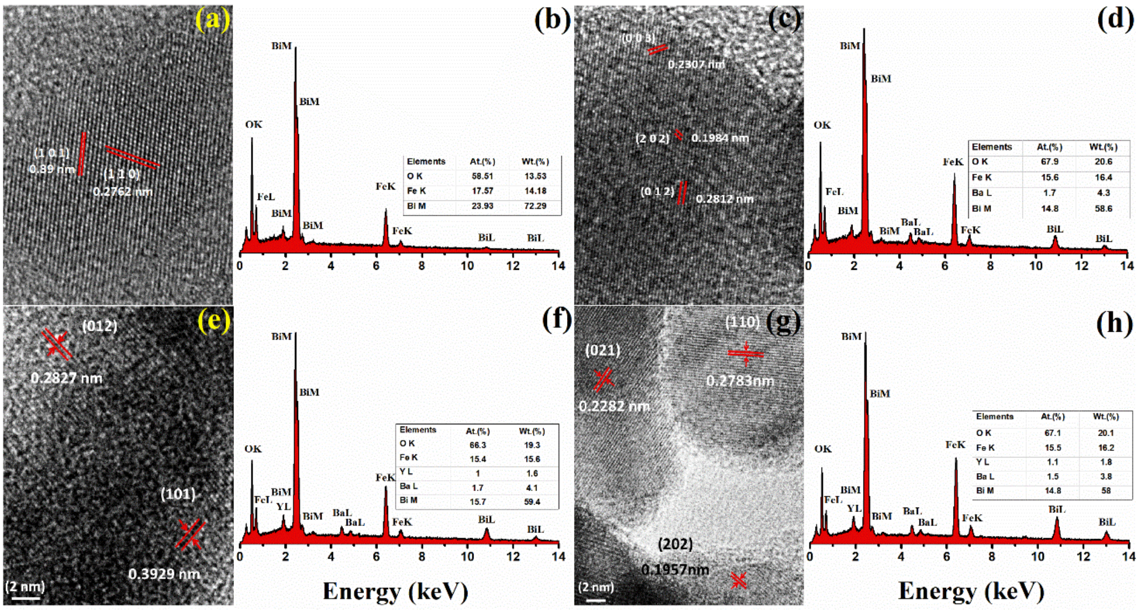

Figure 5.5 (a, c, e, g) depicts HRTEM images and (b, d, f, h) indicates EDAX spectroscopy of BFO, BaBYFO-0, BaBYFO-3, and BaBYFO-5 respectively.

($Ba_{0.1}Bi_{0.85}Y_{0.05}FeO_3$). The atomic and weight percentage of the elements are also in desired ratio as per their stoichiometry.

5.2.1.3 $Sr_{0.5}(Na_{0.5}Bi_{0.5})_{0.5}TiO_3 – Y_3Fe_5O_{12}$

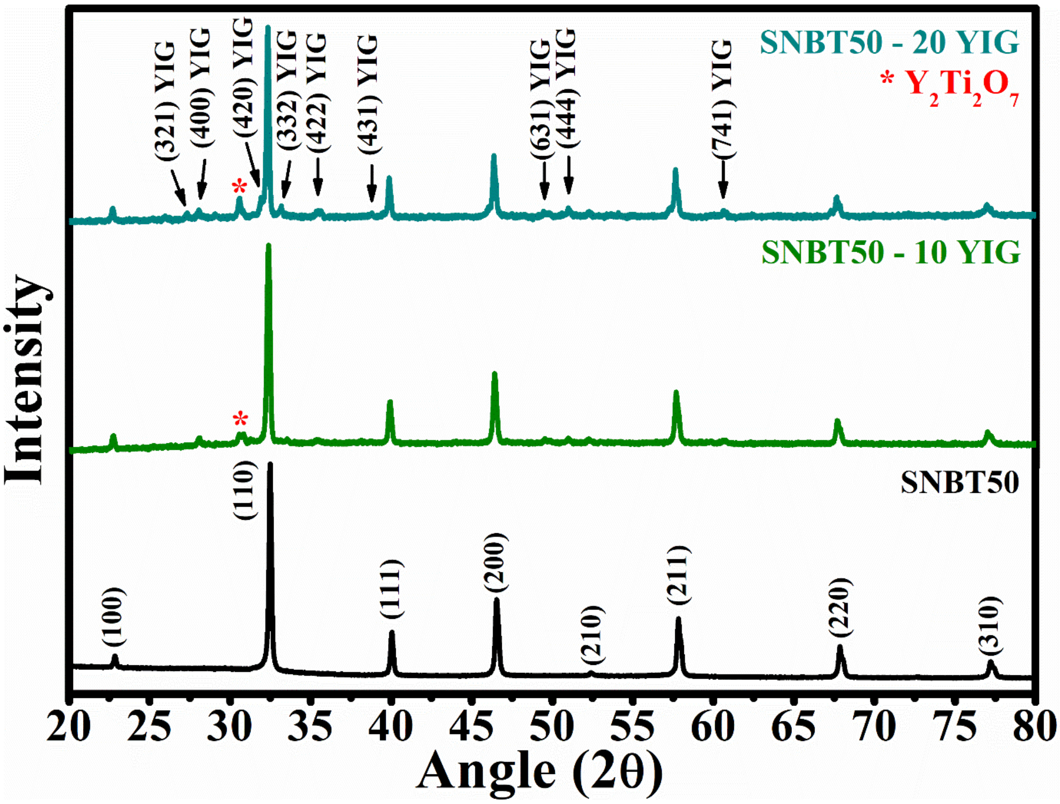

Figure 5.6 depicts the room temperature XRD data for all the samples

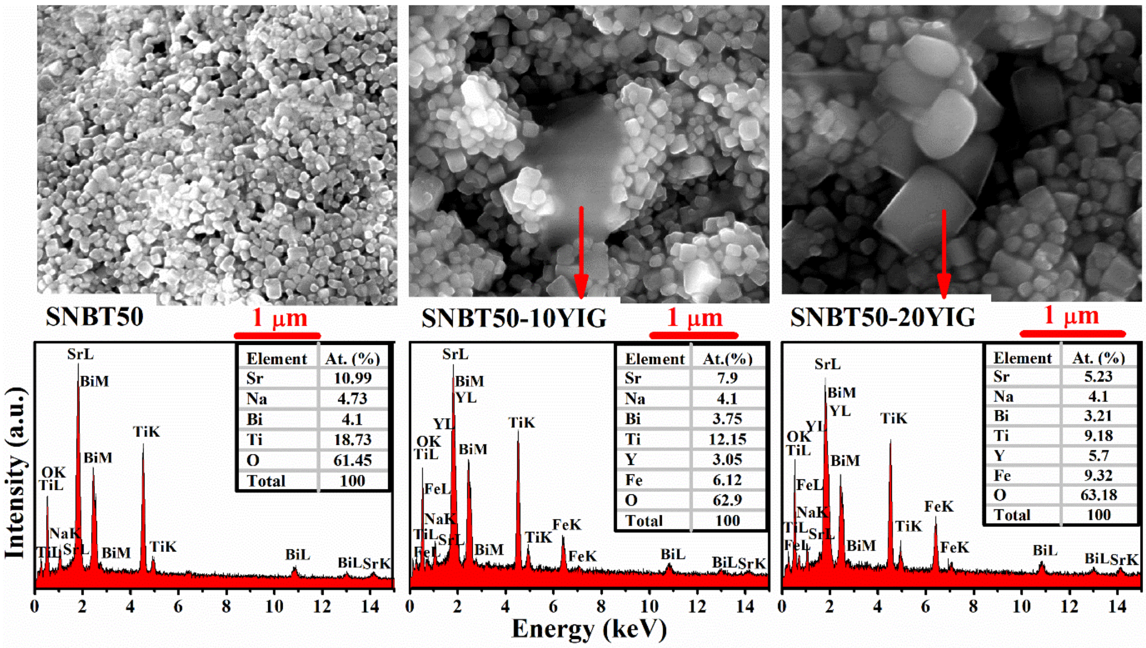

Element	At. (%)
Sr	10.99
Na	4.73
Bi	4.1
Ti	18.73
O	61.45
Total	100

Element	At.(%)
Sr	7.9
Na	4.1
Bi	3.75
Ti	12.15
Y	3.05
Fe	6.12
O	62.9
Total	100

Element	At. (%)
Sr	5.23
Na	4.1
Bi	3.21
Ti	9.18
Y	5.7
Fe	9.32
O	63.18
Total	100

Figure 5.7 depicts the FESEM data of all the samples at a scanning range of 1 µm. The EDAX spectra are also displayed along with the table containing the atomic percentages of all the elements present in the corresponding sample.

Figure 5.6 depicts the XRD data of all the prepared samples obtained at room temperature. It is observed that a small amount of the parasitic phases $Y_2Ti_2O_7$ (PDF no.00-042-0413) is present in the composites, as indicated by the reflection at 30.67° which is attributed to the reaction between SNBT50 and YIG grains occurring at the interfaces. The FESEM images illustrated in Figure 5.7 confirms the presence of YIG particles surrounded with smaller SNBT50 particles and separated from other YIG particles in the long-range confirming the formation of 0-3 particulate composites. The EDAX spectra of all samples is also studied and the atomic percentage of the elements present in the samples are tabulated. The Sr:Bi:Na:Ti:O ratio for SNBT50 as obtained from the EDAX analysis is 0.58:0.25:0.22::1:3.28 confirming the oxygen abundance in the samples. On the other hand, the ratio of Sr:Bi:Na:Ti:Y:Fe:O for 0.9 ($Sr_{0.5}Bi_{0.25}Na_{0.25}TiO_3$) – 0.1 ($Y_3Fe_5O_{12}$) and 0.8 ($Sr_{0.5}Bi_{0.25}Na_{0.25}TiO_3$) – 0.2 ($Y_3Fe_5O_{12}$) are 0.65:0.34:0.31:1:0.25:0.51:5.2 and 0.57:0.45:0.35:1:0.62:1.02:6.88 respectively also confirm the enriched amount of oxygen in all the samples.

5.3.2 ELECTROMAGNETIC PARAMETERS

5.3.2.1 $BiFeO_3$ and $Ga_{0.8}Fe_{1.2}O_3$ BULK

The frequency dependence of the samples' real (ε′) and imaginary (ε′′) components of complex permittivity for a frequency range of 1–18 GHz is shown in Figures 5.8(a) and 5.8(b). In BFO, the *R*3*c* symmetry allows for the emergence of a spontaneous polarisation along the pseudocubic cell's *c*-axis or $[111]_C$ direction. It is consistent with a stereochemically active 6*s* lone pair of Bi^{3+} ions that the Bi, Fe, and O ions are spatially displaced from one another along this threefold axis, with Bi having the biggest displacement. Despite the fact that both Fe and Bi have a formal charge of +3, studies have shown that Bi has a substantially larger displacement than Fe, which increases its contribution to polarisation by about three times [16,17]. Since it is substantially shorter than other Bi-O bonds, the length of the one that runs parallel to the $[111]_C$ direction must have some degree of covalency. The strong covalency of the Bi-O bond along the $[111]_C$ axis, according to a similar observation made from the measurement of electron concentrations inside the unit cell, is the primary factor in the overall polarisation of BFO. According to research, the Ga1-O tetrahedron in GFO has a very low distortion index and an effective coordination number of 4, which is almost identical to that of a conventional tetrahedron. However, the distortion index is sufficiently high for Ga2-O octahedrons to lower the effective coordination number from the desired value of 6. Similar to this, the distortion is

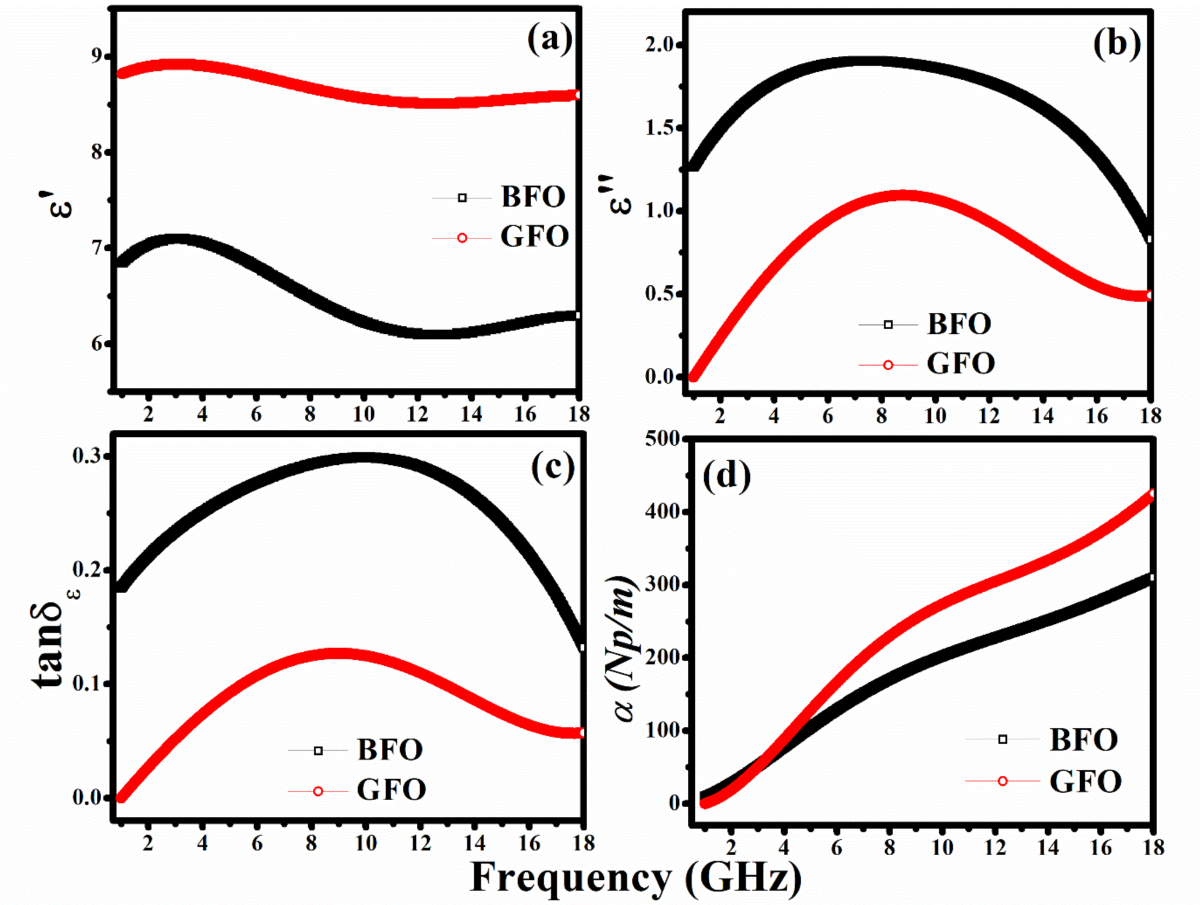

Figure 5.8 Frequency dependent study (1–18 GHz) of (a) real (ε′) (b) imaginary (ε″) parts of complex dielectric constant and (c) dielectric loss (tan δ_ε) (d) attenuation constant (a) of BFO and GFO samples.

substantially worse for Fe1- O and Fe2-O, leading to significantly lower effective coordination numbers[7,8]. This suggests that the cation is largely displaced from its central location for practically all oxygen polyhedrons, leading to substantial non-centrosymmetry of the unit cell. Therefore, the non-centrosymmetry of the unit cell and subsequently the polarisation is determined by the amount of central cation displacement in polyhedrons. Density functional theory research reveals that the interactions between Fe and oxygen ions are primarily ionic, while Ga1-O and Ga2-O bonds exhibit some hybridization, indicating covalency. As a result, it is possible to say that the bindings between oxygen ions and Fe1, Fe2, Ga1, and Ga2 have varying strengths and contribute in diverse ways to the total polarisation. The extremely distorted structure of the unit cell and the high degree of polarisation found in GFO are both attributed to the greater effective charge of Ga1, Ga2, Fe1, and Fe2 cations than the ideal value of +3. According to partial polarisation calculations, Ga1 and Fe1 ions make up the majority of the overall polarisation in GFO.

Within the investigated frequency range, the Cole-Cole plot for both the BFO and the GFO [Figure 5.9] displays distorted semi-circular arcs that point to relaxation processes of the modified Debye type. The more bizarre aspects of the GFO plot, however, imply the existence of various charge carriers and multiple types of dipolar relaxation processes.

$$(\varepsilon' - \frac{\varepsilon_s + \varepsilon_\infty}{2})^2 + (\varepsilon'') = (\frac{\varepsilon_s + \varepsilon_\infty}{2})^2 \quad (5.1)$$

We can conclude from the preceding discussion that the primary dipolar pairings for the dielectric constant of BFO are between the ions Bi and O. Ga1, Fe1, and oxygen ions are the major dipolar pairings for GFO that contribute to greater permittivity.

GFO comprises Ga1, Ga2, Fe1, and Fe2 cations with formal charge +3 while all four cations have distinct effective charges inside the unit cell. BFO contains Bi^{3+} and Fe^{3+} cations with formal charge +3 but with modified effective charges. As seen in Figures 5.8(c) and 5.8(d), GFO comprises Ga2-O, Fe1-O, and Fe2-O octahedrons while BFO only has FeO_6 octahedrons. According to Rietveld refinement [Table 5.1], one orthorhombic unit cell of GFO has a volume of 419.02 Å^3 and includes 8 formula units, whereas one hexagonal unit cell of BFO has a volume of 384.4 Å^3. One unit cell of BFO has six octahedrons, whereas one unit cell of GFO comprises four Ga-O tetrahedrons, four Ga2-O octahedrons, four Fe1-O octahedrons, and four Fe2-O octahedrons.

The type of polyhedron is a crucial consideration because it has a substantial impact on the effective charge of the cation residing inside the polyhedron, which plays a critical part in determining the strength of the dipole moments. It is doubtful that the cation within will contribute to the polarisation as previously discussed if the polyhedrons are symmetric, that is, if the cation is located precisely at the centre of the polyhedron. Although they are more likely to contribute to the overall dipole moment and the greater dielectric constant seen in

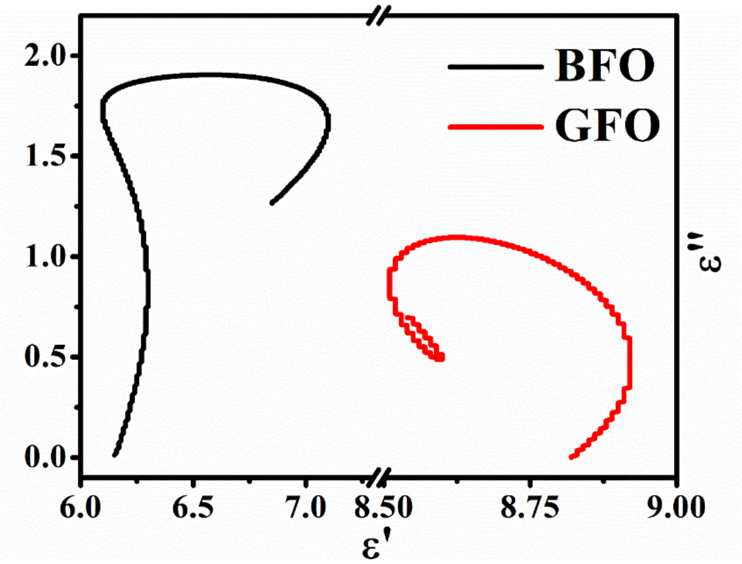

Figure 5.9 Cole-Cole plot of both BFO and GFO within the studied frequency range of 1 GHz – 18 GHz

GFO as illustrated in Figure 5.8(a) if the cations are moved, distorting the polyhedrons and causing structural deformation in the unit cell. However, as dielectric relaxation occurs and the dipoles fall behind the field, the value falls with increasing frequency. Figures 5.8(b) and 5.8(c) show that ε″ and tangent loss are substantially higher in this sample, together with a broad hump in BFO compared to GFO, indicating a higher dielectric loss.

As presented in Figure 5.8(d), attenuation constants (α) indicate the propagation of electromagnetic wave through a sample and is defined as,

$$\alpha = \frac{\sqrt{2}\pi f}{c} \times \sqrt{(\mu''\varepsilon'' - \mu'\varepsilon') + \sqrt{(\mu''\varepsilon'' - \mu'\varepsilon')^2 + (\mu''\varepsilon' + \mu'\varepsilon'')^2}} \quad (5.2)$$

α is observed to be increasing with increasing frequency, relative permittivity and permeability. α is found to be higher in GFO with a maximum of ~ 425 $Np.m^{-1}$.

5.3.2.2 Barium and Yttrium co-doped Bismuth Ferrite Nanoparticles

The variation of the real (ε′) and imaginary (ε″) components of the complex permittivity in the frequency range of 1-17 GHz is shown in Figures 5.10(a) and 5.10(b), respectively. After Ba doping, an immediate decrease in dielectric permittivity is observed. With yttrium doping the permittivity increases and becomes highest in BaBYFO-3. However, once the concentration is increased even further, the permittivity decreases once again as observed in BaBYFO-5. On the other hand, as the doping concentration of both Ba and Y grows up to BaBYFO-3, the imaginary portion of the complex permittivity indicating the charge loss capability gradually declines, before increasing and reaching its maximum in BaBYFO-5.

The inset of Figure 5.10(b) depicts that, with the exception of BaBYFO-3, all samples exhibit a dielectric relaxation peak at about 14 GHz. The development of defect dipoles between Fe^{3+} ions and oxygen vacancies are what causes the emergence of this relaxation peak[18]. Two different kinds of mechanisms are said to occur in BaBYFO-0 as a result of charge compensation[19]. which are

$$\frac{1}{2}(1-x)Bi_2O_3 + xAO + \frac{1}{2}Fe_2O_3 \rightarrow Bi^{3+}_{1-x}A^{2+}_{x}Fe^{3+}O^{2-}_{3-\frac{x}{2}} \quad (5.5)$$

$$\frac{1}{2}(1-x)Bi_2O_3 + xAO + \frac{1}{2}Fe_2O_3 \rightarrow Bi^{3+}_{1-x}A^{2+}_{x}Fe^{3+}_{1-x}Fe^{4+}_{x}O^{2-}_{3} \quad (5.6)$$

Due to the replacement of a larger Ba^{2+} ion (1.35 Å) in the place of a Bi^{3+} ion (1.03 Å), the *c/a* ratio increases [Table 5.2] which rearranges the electron density in the unit cell. On the other hand, the much lower electronegativity of Ba^{2+} (0.9 Å) compared to Bi^{3+} ion (2.02 Å) may as well decrease the total polarization of the sample. It is previously reported that optimal doping of BFO with Ba^{2+} results in the formation of Fe^{4+} ions following Eq. 5.6 which introduces ferrimagnetic nature in the material[19–22]. Therefore, it can be concluded that in BaBYFO-0, the formation of defect dipoles is interrupted due to the formation of Fe^{4+} ions reducing the relaxation peak at 14 GHz and decreasing the overall dielectric loss in this sample. After doping with a small concentration of Y^{3+} in BaBYFO-3, the *c/a* ratio decreases due to replacement with smaller Y^{3+} ions (0.9 Å). On the other hand, Y^{3+} having higher electronegativity (1.22) than Ba^{2+}, rearranges the electron density in such a way that Bi-O bond length increases along with a buckling of O1-Bi-O1 bond angle, which ensures deformation of BiO_6 octahedron. On the other hand, increased Bi-Fe bond length and Bi-O1-Fe bond angle implies an elongation along Bi-Fe axis or $[111]_C$ direction. This distortion in the octahedron and non-centrosymmetric distortion along $[111]_C$ axis may result in the observed enhancement in the overall permittivity of the material whereas significantly increased ε′ is the cause behind the drastic reduction in overall dielectric loss. With higher doping concentration, although the distance between Bi and Fe increases, the buckling of Bi-O1-Fe angle implies a compression along $[111]_C$ direction reducing the overall polarization. This may happen when the absence of lone-pairs in the replaced ions becomes a dominating factor and the off-centering distortion along Bi-Fe axis is reduced. The formation of defect dipoles is again observed in this material due to weakened Fe-O1 bond resulting in the reappearance of the relaxation peak at 14 GHz and high dielectric loss.

5.3.2.3 $Sr_{0.5}(Na_{0.5}Bi_{0.5})_{0.5}TiO_3 – Y_3Fe_5O_{12}$

Figure 5.11 depicts the variation in real (ε′) and imaginary (ε″) parts of the complex dielectric

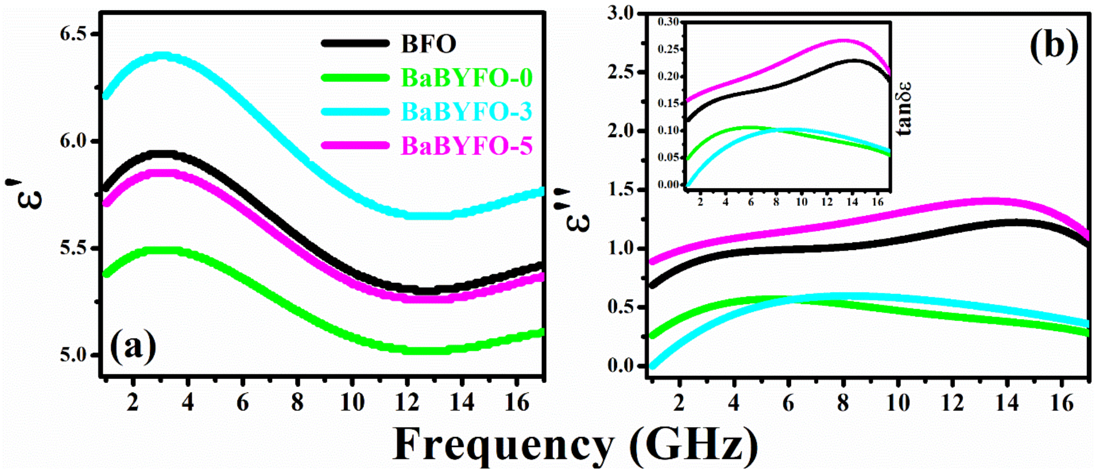

Figure 5.10 The frequency variation of the (a) real (ε′) and (b) imaginary (ε″) part of the samples is depicted. The inset of (b) demonstrates the dielectric loss (tan δ_ε)

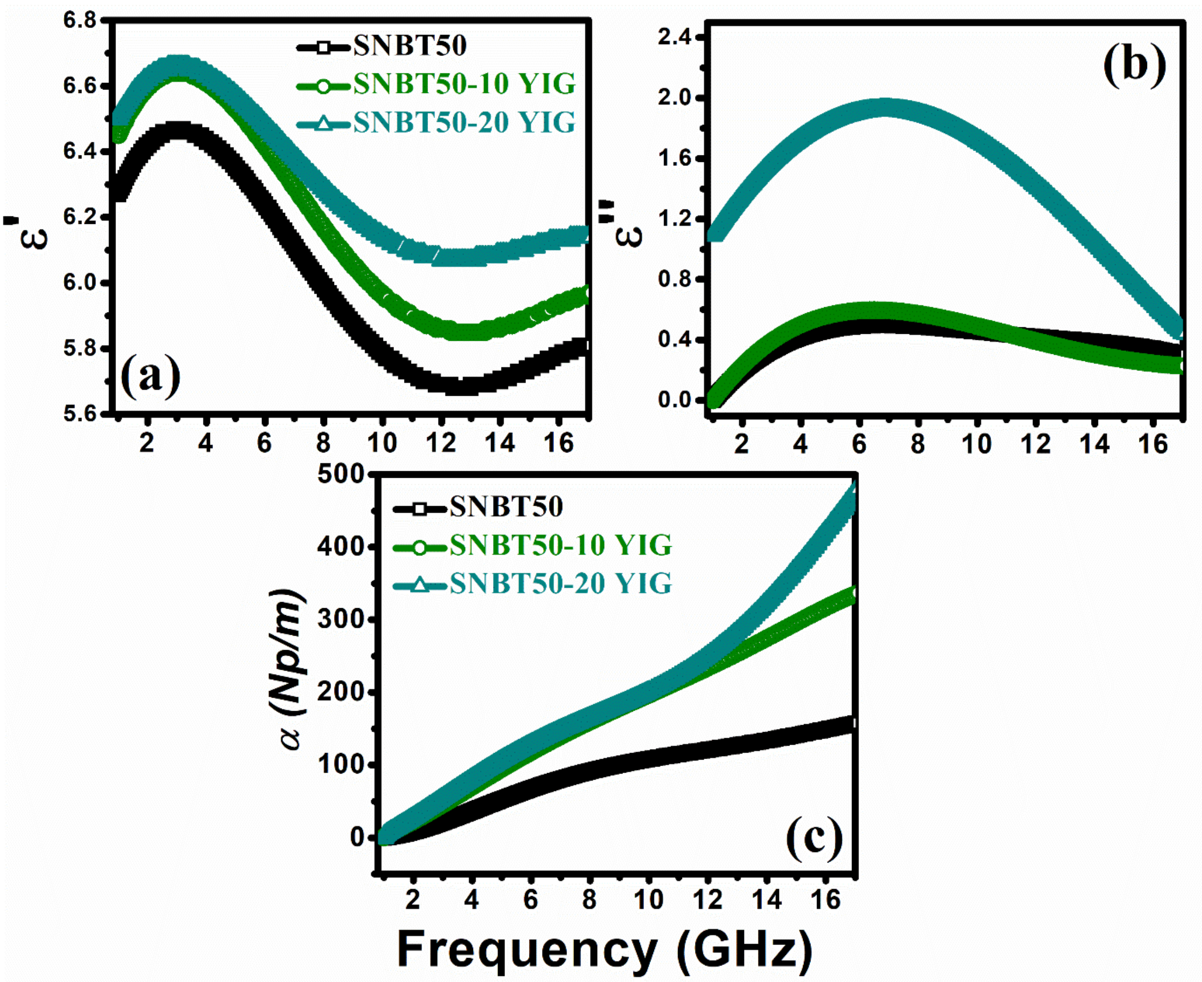

Figure 5.11 The frequency variation of the (a) real (ε′) and (b) imaginary (ε″), and (c) attenuation constant (α) part of the samples is depicted

permittivity of the samples. Figure 5.11 (a) depicts that with increasing concentration of YIG in the composite the real part of dielectric constant is increasing which can be attributed to the increasing interfacial polarization due to the presence of larger amount of YIG particles in the SNBT50 matrix. On the other hand, the imaginary part is observed to remain same for SNBT50 and SNBT50-10YIG samples while increasing significantly in SNBT50-20YIG sample. In perovskite materials, the dielectric loss observed at low frequency is attributed to the presence of leakage conductance, whereas the same at high frequency range is mainly governed by relaxation polarisation and electric conductance. Therefore, it can be concluded that the SNBT50-20YIG sample exhibit higher relaxation mechanisms and subjected to larger electric conductance. This sample also exhibits highest attenuation constant of 467.15 Np m^{-1} whereas the same for SNBT50 and SNBT50-10YIG are 159.88 Np m^{-1} and 337.43 Np m^{-1} respectively. Although this sample has higher dielectric constant and attenuation constant, the high dielectric loss of this sample is detrimental to its application as MAMs. On the other hand, the SNBT50-10YIG sample exhibits low dielectric loss along with a stronger dielectric constant and attenuation constant than the parent sample, SNBT50, making it a promising microwave material for application in many technical fields.

5.3.3 MAGNETIC PARAMETERS

5.3.3.1 $BiFeO_3$ and $Ga_{0.8}Fe_{1.2}O_3$

The real (μ′) and imaginary (μ″) components of complex permeability are shown as a function of frequency in the 1 to 18 GHz range in Figures 5.12(a) and (b). For both samples, μ′ drops until a particular frequency and then nearly stays the same. At a frequency of about 6 GHz, μ″ is seen to have distinctive resonance peaks for both BFO and GFO. Because GFO has a greater magnetization due to its near-room temperature ferrimagnetism whereas BFO has an antiferromagnetic nature at room temperature, the permeability of GFO is significantly higher than that of BFO throughout the examined frequency region. The real components of complex permittivity (ε′) and permeability (μ′) show a material's ability to store electromagnetic energy, whereas the imaginary components (ε″ and μ″) show energy dissipation. Therefore, the larger value of real part of complex permittivity and permeability seen in GFO suggests a greater capacity of the material to store electromagnetic energy.

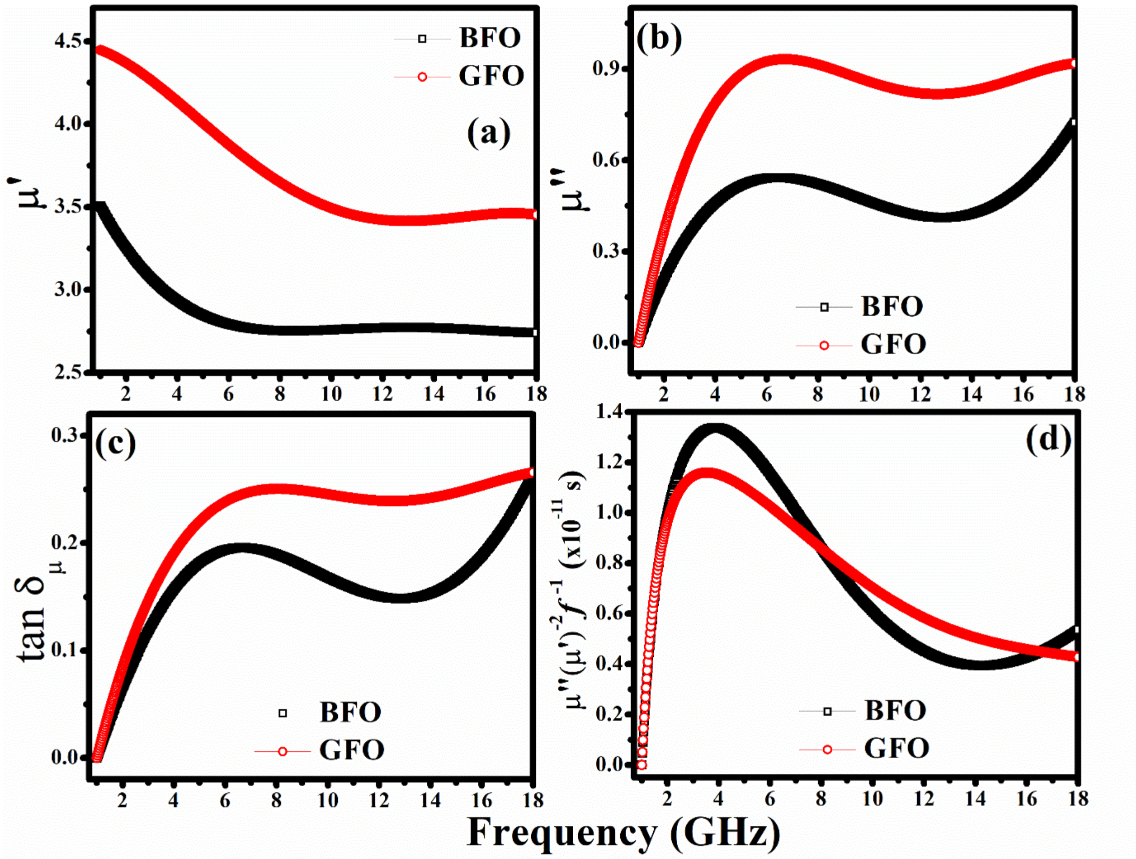

Figure 5.12 Frequency dependent study (1–18 GHz) of (a) real (μ′), (b) imaginary (μ″) parts of complex permeability, (c) magnetic loss (tan δ_μ) and (d) $\mu''(\mu')^{-2}f^{-1}$ of BFO and GFO.

Figure 5.12(c) depicts the frequency dependence of magnetic loss which shows that a broad resonance peak is seen for GFO in the higher frequency range, indicating higher magnetic loss in GFO than BFO. Magnetic hysteresis, eddy current loss, domain wall resonance, and exchange resonance are the principal sources of dynamic magnetic loss. Eddy current loss and exchange resonance can have a dramatic impact on the type of magnetic loss, even while the effects of magnetic hysteresis and domain wall resonance significantly deteriorates in the high frequency area due to the presence of weaker fields[23]. The contribution of eddy current loss to μ'' is expressed by the formula, $\mu'' \sim 2\pi\mu_0\mu'^2(d^2\sigma)f$, where d is the thickness of the composite, σ is the electrical conductivity and μ_0 is the permeability of free space[24]. If μ'' (or $tan\delta_\mu$) is originated entirely from the eddy current loss, then the $\mu''(\mu')^{-2} f^{-1}$ curves will remain uniform with varying frequency[25]. The frequency variation of $\mu''(\mu')^{-2} f^{-1}$ is depicted in Figure 5.12(d) in order to understand the possible origins of magnetic loss in the samples. At 3.8 GHz and 3.5 GHz, respectively, a noticeably sharp peak for the BFO and GFO connected to the sample's magnetic resonance can be seen. Even though the fluctuation is greatly reduced at the higher frequency area, none of the curves are constant. Therefore, the cause of magnetic loss for both BFO and GFO can be partly attributed to the occurrence of eddy current loss at higher frequencies while being mostly attributable to magnetic resonance at low frequencies.

5.3.3.2 Barium and Yttrium Co-doped Bismuth Ferrite Nanoparticles

Figures 5.13(a) and 5.13(b) represent the real and imaginary parts of complex permeability versus frequency plots for all samples. The magnetic ordering in BFO is G-type antiferromagnetic [48], where each Fe^{3+} spin is surrounded by six antiparallel spins of its closest neighbours. However, due to magnetoelectric interaction, the spins are not entirely antiparallel; they form an angle to produce a weak canting moment [47]. Therefore, for an antiferromagnet, the ideal angle between Fe-O1-Fe angle should be 180°, but due to spin canting the angle is shorter. Fig. 3(g) of the main manuscript represents the Fe-O1-Fe bond angle for all samples where each Fe forms FeO_6 octahedra with neighbouring oxygens ions. This buckling of Fe-O1-Fe bond angle has a crucial role in enhancing magnetic properties of BFO. Since the Fe-O-Fe superexchange is antiferromagnetic in nature, the buckling induces canting in the antiferromagnetic sublattice thus giving rise to ferromagnetic nature. It can be observed from the Fig. 3(g) and the data tabulated in Table I that with increasing co-doping,

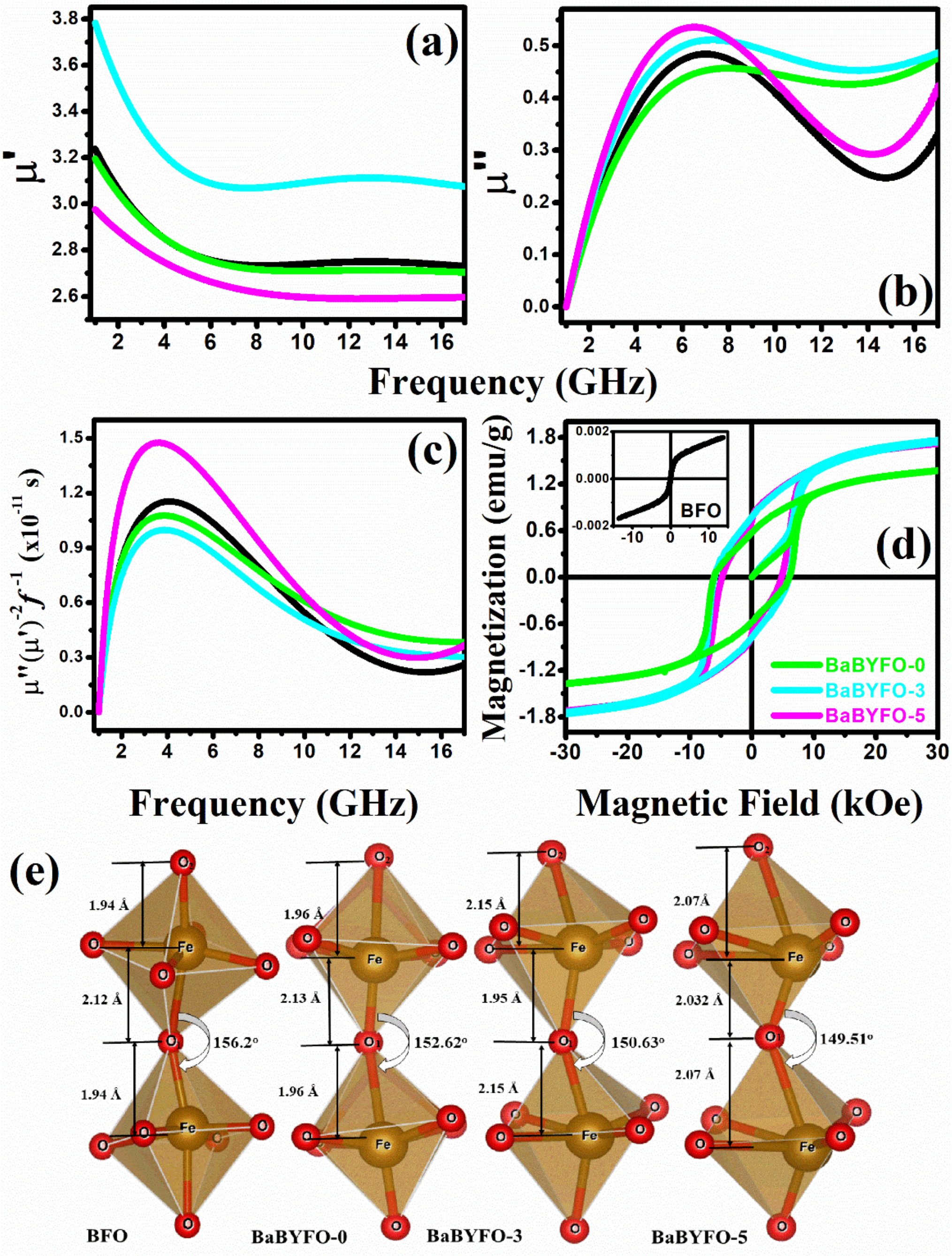

Figure 5.13 Frequency dependence of (a) real (μ′), (b) imaginary (μ″) parts of complex permeability, (c) $\mu''(\mu')^{-2} f^{-1}$, and (d) room temperature magnetic hysteresis loop of all samples. Inset of (d) demonstrates the room temperature M-H hysteresis loop for Bismuth ferrite nanoparticles. (e) shows the two FeO_6 octahedrons depicting Fe-O-Fe bond angles and Fe-O bond lengths of all samples.

this angle gradually reduces modifying octahedral tilting behaviour of the samples, and therefore inducing more canting and subsequently enhancing the magnetization [21,22].

The superexchange mechanism also depends on the bond strength between Fe and O atoms as well. The shorter the bond length, the stronger the antiferromagnetic superexchange mechanism. Therefore, the final state of magnetisation will depend on the resultant of these two effects.

The real part of magnetic permeability decreases with increasing frequency due to the inability of the magnetic dipoles to follow the increasingly changing magnetic field, as evident in all samples shown in Figure 5.13(a). For BFO and BaBYFO-0, the similar values of Fe-O bond parameters (Table 1) are the reason behind the similar frequency-dependence of their magnetic dipoles in an alternating magnetic field having frequency within the microwave range. In BaBYFO-3, the Fe-O1 bond length is smallest, while Fe-O2 becomes even larger (2.15 Å) than the total ionic radii of Fe^{3+} and O^{2-} ions (2.13 Å) implying a weaker antiferromagnetic superexchange interaction. As a result, the effect of canting becomes dominant, increasing the overall magnetic permeability. However, in BaBYFO-5, the Fe-O1 increases and Fe-O2 decreases becoming almost similar to each other which makes the FeO_6 octahedron an almost symmetric one. As a result, although the Fe-O1-Fe bond is smallest in this sample, the regained strength of antiferromagnetic superexchange interaction due to shorter Fe-O bond lengths reduces the overall magnetic permeability of the material.

The magnetic loss value is similar for all samples with resonance peaks observed at around 7 GHz. The reason behind magnetic loss in a material can lie in magnetic hysteresis, eddy current loss, domain wall resonance, and magnetic exchange resonance. However, in such a high-frequency region with low magnetic field strength, the effect of magnetic hysteresis and domain wall resonance significantly reduces[23]. Therefore, the possible reasons behind the observed magnetic loss in the reported frequency range could be eddy current loss and exchange resonance. As previously mentioned, the contribution of eddy current loss can be established if the $\mu'' (\mu')^{-2} f^{-1}$ remains independent of varying frequency since, the imaginary part of permeability (μ'') entirely originates from eddy current loss, expressed as $\mu'' \sim 2\pi\mu_0 (\mu')^2(d^2\sigma) f$, where d is the thickness of the composite, σ is the electrical conductivity and μ_0 is the free space permeability[26]. As can be observed from Figure 5.13(c), all the samples show a peak at a lower frequency indicating a loss due to magnetic resonance. But at higher frequency regions, BaBYFO-0 and BaBYFO-3 become almost invariant with changing frequency compared to BFO and BaBYFO-5. Therefore, it can be stated that although at lower frequency regions the magnetic loss of all samples has a contribution from magnetic resonance, at higher frequency (> 10 GHz) the magnetic loss in BaBYFO-0 and BaBYFO-3 has a primary contribution from eddy current loss while BFO and BaBYFO-5 have other contributions than only eddy current causing the observed magnetic loss[25]. The formation of Fe^{4+} ions due to charge compensation upon doping with

Ba^{2+} can as well be proved by the magnetic hysteresis loop shown in Figure 5.13(d). BFO is antiferromagnetic, as can be contemplated from the hysteresis loop shown in the inset of Figure 5.13(d). Upon doping with 10 wt.% Ba at the Bi-site shows enhanced remnant and saturation magnetization. But, as the doping concentration of Y^{3+} is enhanced keeping the doping concentration of Ba^{2+} fixed at y = 0.1, no significant change in magnetization is observed, attributed to no further incorporation of Fe^{4+} ions.

5.3.2.3 $Sr_{0.5}(Na_{0.5}Bi_{0.5})_{0.5}TiO_3$ – $Y_3Fe_5O_{12}$

Figure 5.14 illustrates the dependence of the real (μ′) and imaginary (μ′′) part of magnetic permeability on frequency. It is observed that with increasing concentration of ferromagnetic YIG in the composite, it firstly increases for SNBT50-10YIG, but then decreases for SNBT50-20YIG. This reduction in magnetic permeability can be attributed to the formation of the nonmagnetic parasitic phase $Y_2Ti_2O_7$ surrounding the magnetic YIG particles at the interfaces of YIG and SNBT50 grains reducing the response of magnetic spins in ferromagnetic YIG upon externally applied magnetic field. No significant change is observed

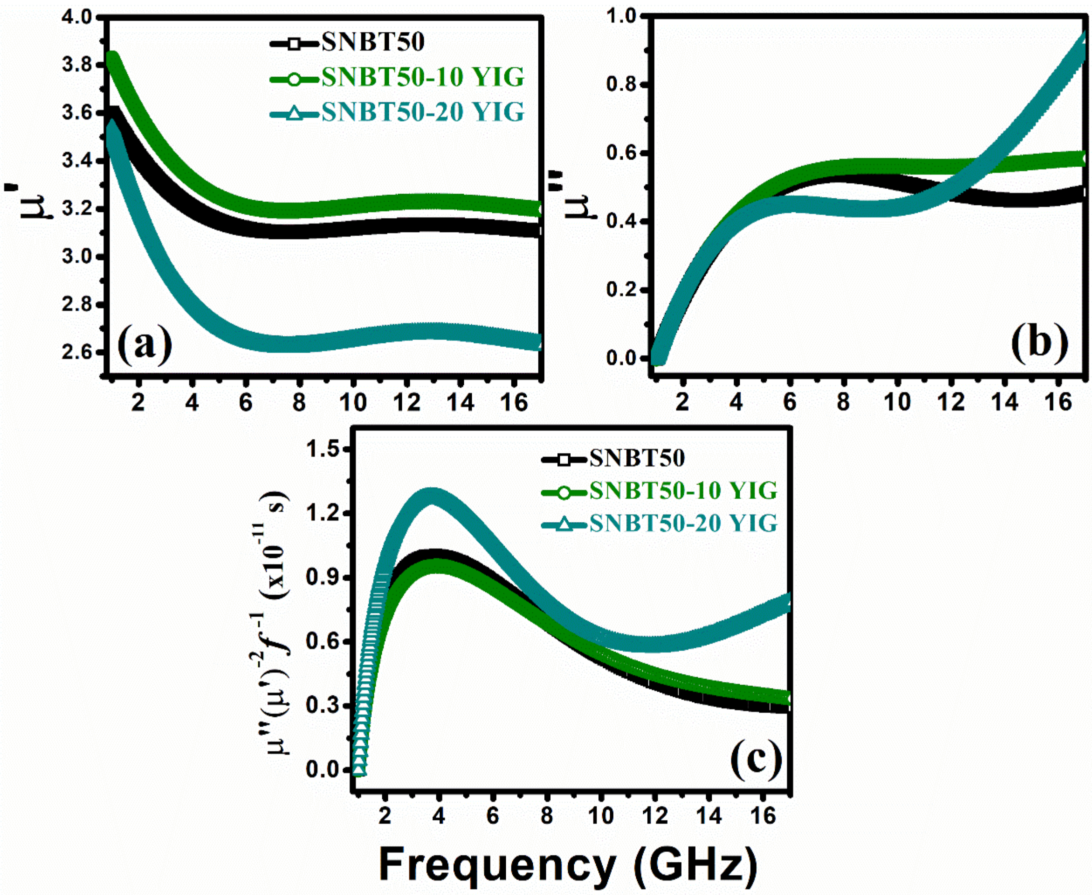

Figure 5.14 Frequency dependence of (a) real and (b) imaginary part of the complex magnetic permeability. (c) shows the variation of $\mu''(\mu')^{-2} f^{-1}$ with changing frequency for all samples.

in the imaginary part of the magnetic permea bility at lower frequency region in any of the samples. However, the large change in the value of μ′′ for SNBT50-20YIG at higher frequency region (>12 GHz) can be explained from the observation of the $\mu'' (\mu')^{-2} f^{-1}$ plot. The almost plateau like region at higher frequency observed for SNBT50 and SNBT50-10YIG explains that the magnetic loss in these samples are mainly governed by eddy current loss. For SNBT50-20YIG, the large variation at higher frequency region implies other than eddy current, it has significant contribution from the resonance as well.

5.3.4 MICROWAVE ABSORPTION

5.3.4.1 $BiFeO_3$ and $Ga_{0.8}Fe_{1.2}O_3$

The magnetic and electric characteristics of a material are closely related to its ability to absorb electromagnetic waves. Among these, reflection loss (RL) enables us to comprehend the effectiveness of reducing the reflected waves, whilst adequate impedance matching is crucial for improved EM wave absorption. Equations 5.3 and 5.4 can be used to express the RL value in terms of electromagnetic parameters for a particular frequency and thickness[13,27]:

$$Z_{in} = Z_0\sqrt{\frac{\mu_r}{\varepsilon_r}}\ tanh\left[j\left(\frac{2\pi tf}{c}\right)\sqrt{\mu_r\varepsilon_r}\right] \tag{5.3}$$

$$RL = 20\ log|(Z_{in} - Z_0)/(Z_{in} + Z_0)| \tag{5.4}$$

where $\mu_r = \mu' - i\mu''$ and $\varepsilon_r = \varepsilon' - i\varepsilon''$ are complex permeability and permittivity of a material, c is the velocity of light, t is the thickness of absorber composite, Z_0 is the complex impedance of free space while Z_{in} is the input impedance of the absorber.

For various composite absorber thicknesses, the frequency dependence of reflection loss is shown in Figure 5.15. At a frequency of 9.89 GHz, a minimum reflection loss of -8.30 dB is discovered for BFO at a thickness of 2 mm. The loss peak shifts from 9.89 GHz to 6.34 GHz as the thickness increases from 2 mm to 3 mm, and the RL rises from -8.30 dB to -10.17 dB. Another loss peak with a loss of -21.31 dB may be seen at 17.68 GHz at a thickness of around 3.01 mm [Figure 5.16(a)]. This peak shifts from 17.68 GHz to 11 GHz when thickness increases from 3 mm to 5 mm, whereas RL declines from -21.31 dB to -17.19 dB. The loss peak comes at 12.28 GHz with a loss of -17.84 dB at a thickness of 4.5 mm. The given literature for BFO agree well to these values of microwave absorption characteristics, such as RL, bandwidth, and frequency regions. An optimal RL of - 67.36 dB at around 6.02

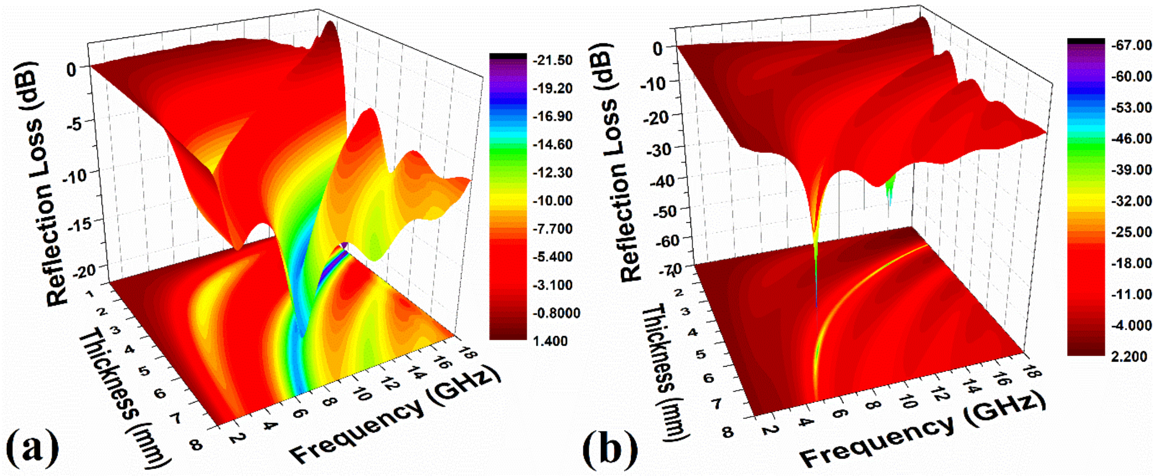

Figure 5.15 3D plots of reflection loss (RL) of (a) BFO, (d) GFO. 4 (b) and (e) depict the plot of reflection loss for different size of the sample in the frequency range from 1-18 GHz. 4 (c) and (f) shows the $|Z_{in}/Z_0|$ ratio vs. frequency showing $|Z_{in}/Z_0|$ ratio is nearest to 1 for GFO sample at thickness 6.2 mm.

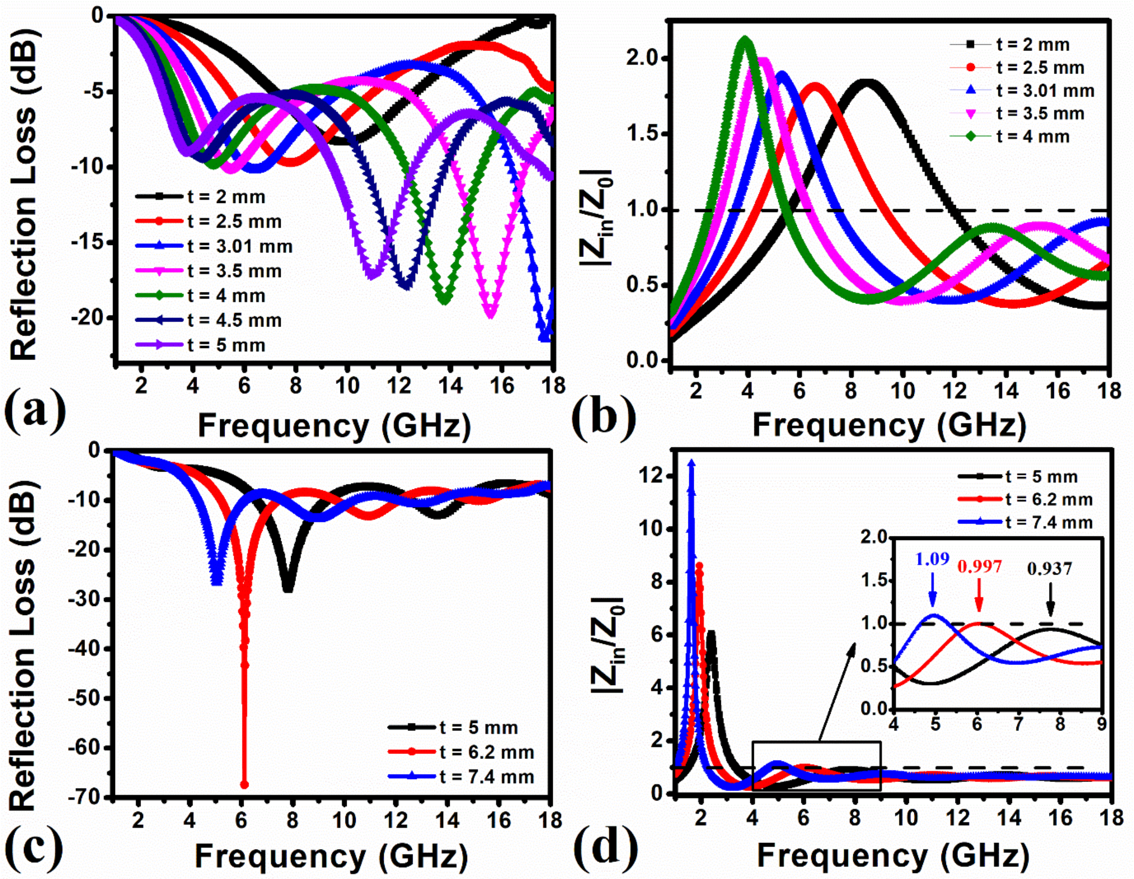

Figure 5.16 3D plots of reflection loss (RL) of (a) BFO, (d) GFO. 4 (b) and (e) depict the plot of reflection loss for different size of the sample in the frequency range from 1-18 GHz. 4 (c) and (f) shows the $|Z_{in}/Z_0|$ ratio vs. frequency showing $|Z_{in}/Z_0|$ ratio is nearest to 1 for GFO sample at thickness 6.2 mm.

GHz is observed for 6.2 mm absorber length of GFO, illustrated in Figure 5.16(c). $|Z_{in}/Z_0|$ versus frequency graphs in Figures 5.16(b) and 5.16(d) for BFO and GFO, respectively, show the best impedance matching is achieved, i.e., $|Z_{in}/Z_0|$ = 0.997, for GFO sample at 6.02 GHz frequency. This value for BFO is, $|Z_{in}/Z_0|$ = 0.915 at frequency of 17.68 GHz. This conclusion, which is supported by the larger attenuation (α) value found for GFO, reveals that GFO's superior EM wave absorption is the result of optimal impedance matching and sufficient dielectric and magnetic losses.

5.3.4.2 Barium and Yttrium Co-doped Bismuth Ferrite Nanoparticles

The 3-D graphs depicting the reflection loss for different thicknesses within the frequency region of 1-17 GHz are plotted in Figure 5.17, calculated using the following equations[13,27]:

$$Z_{in} = Z_0 \sqrt{\frac{\mu_r}{\varepsilon_r}} \tanh\left[j\left(\frac{2\pi t f}{c}\right)\sqrt{\mu_r \varepsilon_r}\right] \tag{5.7}$$

$$RL = 20\, log\left|(Z_{in} - Z_0)/(Z_{in} + Z_0)\right| \tag{5.8}$$

Where $\mu_r = \mu' - i\mu''$ and $\varepsilon_r = \varepsilon' - i\varepsilon''$ are complex permeability and permittivity of a material, c is the velocity of light, t is the thickness of the composite, Z_0 is the complex impedance of free space and Z_{in} is the input complex impedance of the absorber.

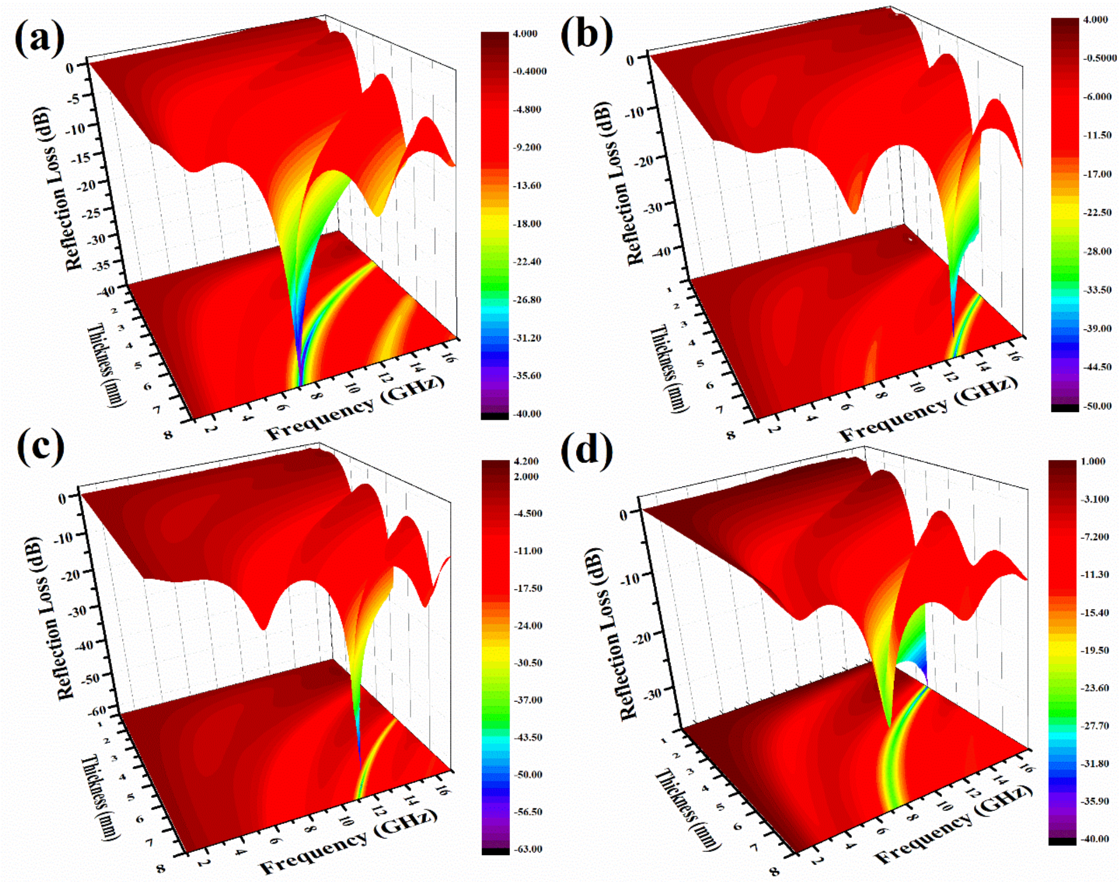

Figure 5.17 3D plots of reflection loss (RL) of (a) BFO, (b) BaBYFO-0, (c) BaBYFO-3, and (d) BaBYFO-5.

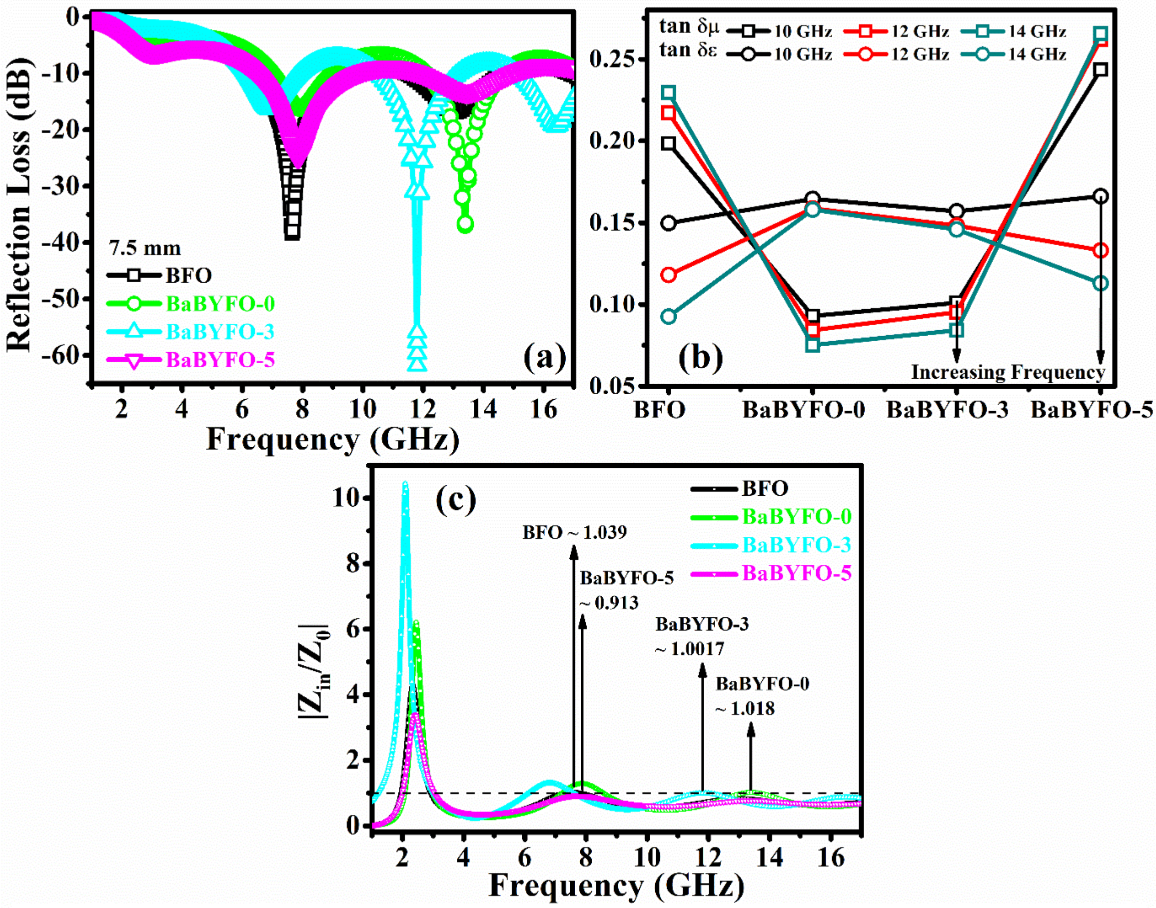

Figure 5.18 (a) depict the plot of reflection loss for 7.5 mm thickness of all samples, (b) shows the dielectric and magnetic loss of all samples for 10 GHz, 12 GHz and 14 GHz frequencies, (c) depicts the frequency variation of $|Z_{in}/Z_0|$ ratio.

The minimum reflection loss is achieved in BaBYFO-3 for a composite length of 7.5 mm [Figure 5.18(a)] shown in Table 5.3. A minimum of -61.7 dB reflection loss is achieved for BaBYFO-3 at a frequency of 11.8 GHz. BFO and BaBYFO-0 are observed to possess a reflection loss of -38.6 dB and -36.6 dB at frequencies 7.63 GHz and 13.38 GHz respectively. BaBYFO-5 possesses the least reflection loss, which is also indicated by its low permittivity and permeability as well. As previously discussed, the Fe-O1-Fe bond angles are observed to decrease with increasing co-doping, but the Fe-O2 becomes largest for BaBYFO-3 sample leading to a reduction in antiferromagnetic superexchange interaction and increment of ferromagnetic interaction. Through the antiferromagnetic superexchange interaction, Fe3+ ions with spin-up electrons possess a magnetic vector opposite to the other. As a result of the energy differential between these two opposed orientations, the spins switch from one state to another, absorbing a substantial amount of electromagnetic energy[6]. Therefore, in addition to eddy current, ferromagnetic resonance explains the magnetic loss and significant absorption reported in BaBYFO-3 at 12 GHz.

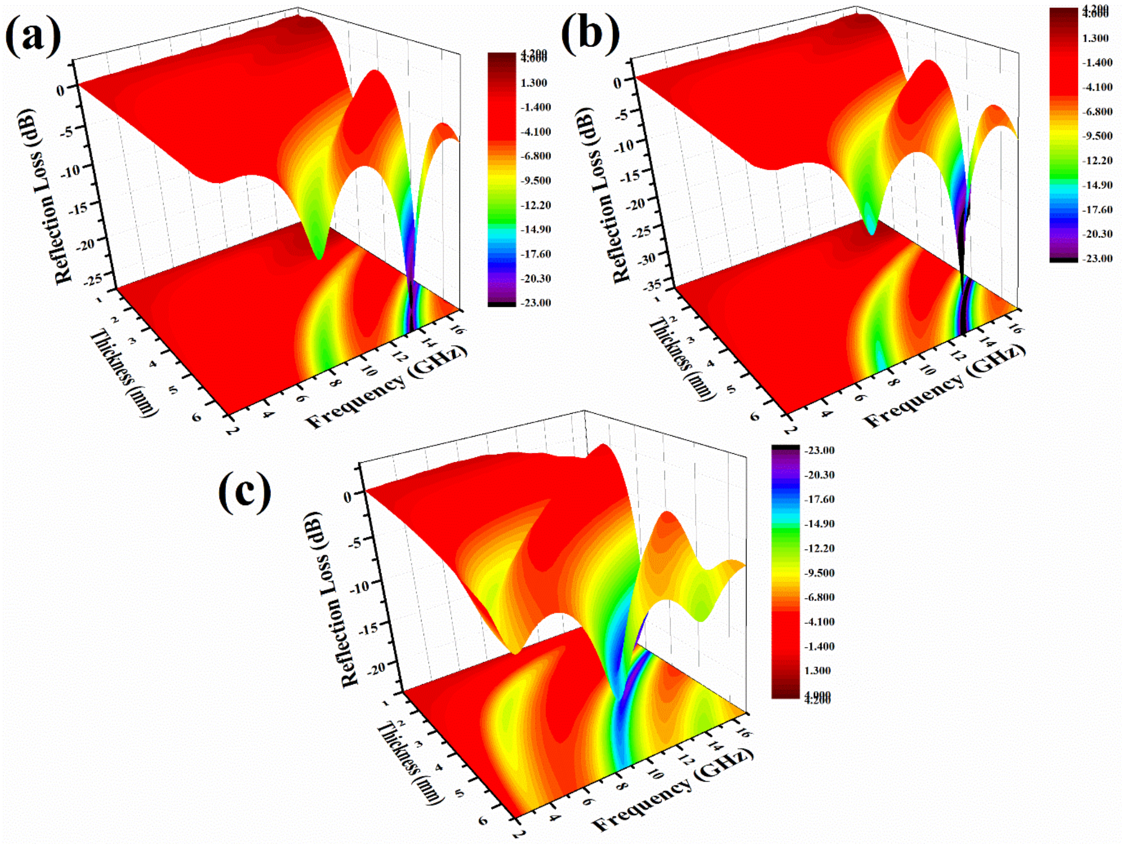

Figure 5.19 The 3D plots of reflection loss with varying frequency and absorber length for (a) SNBT50, (b) SNBT50-10YIG, and (c) SNBT50-20YIG samples.

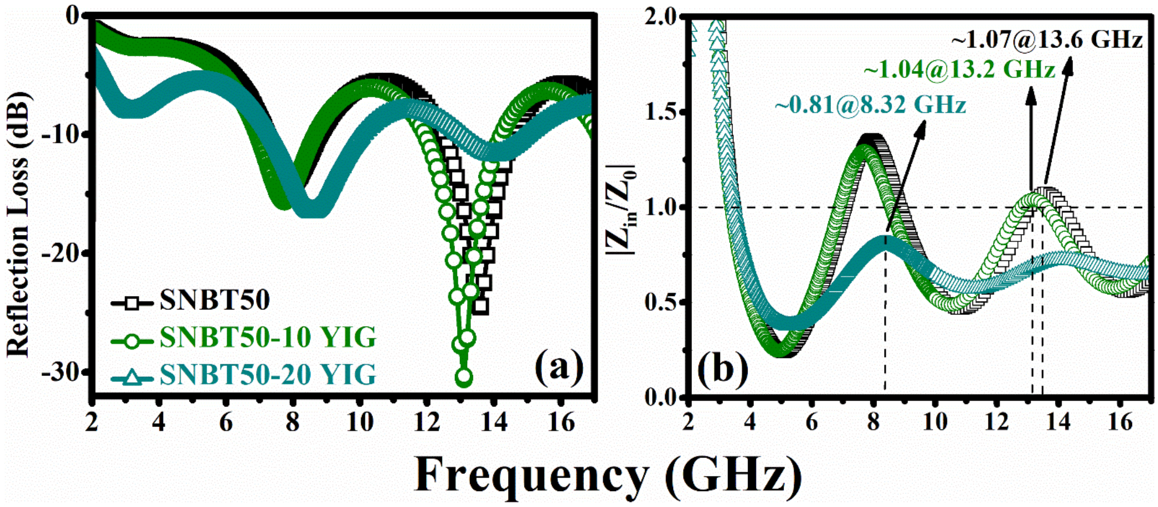

Figure 5.20 (a) The reflection loss versus frequency plot of all samples at fixed absorber length. (b) The variation of |Zin/Z0| with frequency demonstrating the impedance matching of all samples.

With optimized co-doping concentration, as in BaBYFO-3, the values of tanδ_ε and tanδ_μ also come closer to each other, shown in Figure 5.18(b). The capacity of this sample to attenuate such a great quantity of electromagnetic radiation is thus dependent on the matching equation, tanδ_ε = tanδ_μ[28]. With further increase in frequency, the tanδ_ε and tanδ_μ curves for all samples separate away from each other increasing the difference. This supports the fact that the occurrence of the highest reflection loss in BaBYFO-3 absorber of length 7.5 mm is observed around 12 GHz (at 11.8 GHz) where the highest matching is observed. This can be explained as well from the values of $|Z_{in}/Z_0|$ obtained for different samples as shown in Figure 5.18(c) and listed in Table 5.3. The best values of $|Z_{in}/Z_0|$ for the samples are observed to occur at frequencies corresponding to their minimum reflection loss. However, the closest value to 1 is observed for BaBYFO-3 ($|Z_{in}/Z_0|$ ~ 1.0017) explaining the best impedance matching among all the samples.

Table 5.3 - Electromagnetic parameters of all samples depicting the microwave absorption loss

Sample Name (t = 7.5mm)	RL_{min} (dB)	f_{min} (GHz)	BW_{eff} (GHz)	$\|Z_{in}/Z_0\|$
BFO	- 38.13	7.48	5.97	1.039
BaBYFO-0	- 44.49	13.38	4.54	1.018
BaBYFO-3	- 61.67	11.8	7.02	1.0017
BaBYFO-5	- 25.57	7.75	6.4	0.913

5.3.2.3 $Sr_{0.5}(Na_{0.5}Bi_{0.5})_{0.5}TiO_3$ – $Y_3Fe_5O_{12}$ BULK

The 3D plot with frequency along the x-axis, thickness of the absorber along the y-axis, and the reflection loss (RL) along the z-axis are shown in Figure 5.19 for all the samples. It can be observed from Figure 5.20(a) that the sample SNBT50 exhibits minimum reflection loss of -25.12 dB at a frequency of 13.72 GHz for an absorber of length 6mm. For SNBT50-10YIG, the reflection loss is enhanced to a value of -31.89 dB for a shorter absorber length of 5.5mm. For SNBT50-20YIG, however, the reflection loss has significantly deteriorated. These observations can be explained using the impedance matching of the samples shown in Figure 5.20(b). The figure demonstrates that for SNBT50, SNBT50-10YIG, and SNBT50-20YIG, the values of $|Z_{in}/Z_0|$ are ~1.07, 1.04, and 0.81 at a frequency 13.6 GHz, 13.2 GHz, and 8.32 GHz respectively. It is obvious that SNBT50-10YIG has the best impedance matching at 13.2 GHz, where the lowest reflection loss for this sample is found. The increased dielectric permittivity (ε'), magnetic permeability (μ'), and attenuation constant (α) of SNBT50-10YIG relative to its parent sample, SNBT50, explains the substantial reflection loss seen for shorter absorber lengths. For SNBT50-20YIG, the decrease in magnetic permeability affects its overall impedance matching and performance as an excellent microwave absorption material, despite the fact that its dielectric constant and attenuation constant are maximal at higher frequencies.

5.4 CONCLUSIONS

In this chapter, the microwave properties of magnetoelectric gallium ferrite, barium and yttrium co-doped bismuth ferrite nanoparticles and a magnetoelectric composite system of $Sr_{0.5}Bi_{0.25}Na_{0.25}TiO_3$ (SNBT50) – $Y_3Fe_5O_{12}$ (YIG) is studied in detail. Gallium Ferrite ($Ga_{0.8}Fe_{1.2}O_3$) is observed to have a reflection loss of -67.36 dB for an absorber length of 6.2mm attributed to its high dielectric constant and attenuation constant alongside an optimal impedance matching. Elemental substitution of Bismuth with optimised concentration of Barium and Yttrium in Bismuth Ferrite nanoparticles is observed to enhance the reflection loss of Bismuth Ferrite from -38.6 dB to -61.7 dB in a composite of length 7.5mm attributed to enhanced dielectric permittivity, magnetic permeability, and the best balance observed

Table 5.4 - Microwave Absorption observed in GFO compared with some recent advancements

Sl. No.	**Sample Name**	**Peak Positions (GHz)**	**Thickness (mm)**	**RL (dB)**	**Bandwidth (GHz)**
1	$NiFe_2O_4$ nanoparticles[29]	11	2.8	-35	0.4
2	$MnFe_2O_4$@CFO NHS[5]	5.96	4.5	-47	2.2
3	$BiFeO_3$ Nanoparticles[9]	18	5	-18	-
4	$BiFeO_3$ [30]	11.5	3	-40.5	-
5	$Bi_{1-x}Sm_xFeO_3$ nanoparticles[31]	11.7	2	-32.9	2.6
6	$Bi_{1-x}La_xFeO_3$ nanoparticles[12]	11.5	6	-30	-
7	$Bi_{1-x}Nd_xFeO_3$ nanoparticles[13]	8.5	2.3	-42	3
8	$BiCo_xFe_{1-x}O_3$ nanoparticles[32]	4.8	4.5	-39.74	-
9	$NiFe_2O_4$ nanohollowspheres[26]	11.7	2	-59.2	2.82
10	$MnFe_2O_4$ nanohollowspheres with SiO_2 coating[24]	11.7	4.4	-61.02	3.1
11	(1-x) $Sr_{0.5}Bi_{0.25}Na_{0.25}TiO_3$ (SNBT50) – x $Y_3Fe_5O_{12}$ (YIG) composites (This Work)	13.2	5.5	-31.89	3.92
12	$Ga_{0.8}Fe_{1.2}O_3$ (This Work)	6.02	6.2	-67.36	5.23
13	$Ba_{0.1}Bi_{0.87}Y_{0.03}FeO_3$ Nanoparticles (This Work)	11.8	7.5	- 61.67	7.02

between tanδ_ε and tanδ_μ based on the match equation tanδ_ε = tanδ_μ. As can be observed from the literature study in Table 5.4, barium and yttrium co-doping in bismuth ferrite nanoparticles exhibit the highest microwave absorption compared to similar doping at Bi- or Fe- site of bismuth ferrite, to the best of our knowledge. Gallium Ferrite, in comparison, is reported to have the maximum reflection loss of -67.36 dB among all magnetoelectric samples investigated. It also shows very high absorption compared to recently reported studies on ferrites [Table 5.4]. Although several composite structures have been examined and reported [Table 5.4] to increase microwave absorption through improved interfacial polarization, exchange interaction, and impedance matching, comparable investigations for magnetoelectric composites such as SNBT50-YIG are lacking. Not only is formation of multiferroic composites an excellent method to establishing strong coupling, but these forms are also crucial for producing stronger microwave absorption in multiferroic composites and need substantial research. The study on SNBT50-YIG, reported in this thesis, explores the formation of magnetoelectric composites with ferromagnets such as YIG, which is a very suitable material for high frequency applications and ensures enhancement of microwave absorption by tuning their interfacial polarizations and overall magnetism. In conclusion, this thesis reports that magnetoelectric gallium ferrite and single-phase barium and yttrium co-doped bismuth ferrite nanoparticles are viable candidates for use as microwave absorption materials, whereas improvement of microwave properties by formation of SNBT50-YIG composites attracts further research in the field of multiferroic composites as a potential MAM device.

REFERENCES

[1] N. Wu, C. Liu, D. Xu, J. Liu, W. Liu, Q. Shao, Z. Guo, Enhanced Electromagnetic Wave Absorption of Three-Dimensional Porous Fe3O4/C Composite Flowers, ACS Sustain Chem Eng. 6 (2018) 12471–12480. https://doi.org/10.1021/ACSSUSCHEMENG.8B03097/ASSET/IMAGES/ACSSUSCHEMENG.8B03097.SOCIAL.JPEG_V03.

[2] M.S. Cao, W.L. Song, Z.L. Hou, B. Wen, J. Yuan, The effects of temperature and frequency on the dielectric properties, electromagnetic interference shielding and microwave-absorption of short carbon fiber/silica composites, Carbon N Y. 48 (2010) 788–796. https://doi.org/10.1016/J.CARBON.2009.10.028.

[3] G. Sun, B. Dong, M. Cao, B. Wei, C. Hu, Hierarchical dendrite-like magnetic materials of Fe3O 4, γ-Fe2O3, and Fe with high performance of microwave absorption, Chemistry of Materials. 23 (2011) 1587–1593. https://doi.org/10.1021/CM103441U/SUPPL_FILE/CM103441U_SI_001.PDF.

[4] W. Zhu, L. Wang, R. Zhao, J. Ren, G. Lu, Y. Wang, Electromagnetic and microwave-absorbing properties of magnetic nickel ferrite nanocrystals, Nanoscale. 3 (2011) 2862–2864. https://doi.org/10.1039/C1NR10274E.

[5] A. Gorai, D. Mandal, K. Mandal, Multi-layered nano-hollow spheres for efficient electromagnetic wave absorption, Nanotechnology. 32 (2021). https://doi.org/10.1088/1361-6528/ac020e.

[6] M. Zhang, H.J. Yang, Y. Li, W.Q. Cao, X.Y. Fang, J. Yuan, M.S. Cao, Cobalt doping of bismuth ferrite for matched dielectric and magnetic loss, Appl Phys Lett. 115 (2019). https://doi.org/10.1063/1.5134741.

[7] T. Arima, D. Higashiyama, Y. Kaneko, J.P. He, T. Goto, S. Miyasaka, T. Kimura, K. Oikawa, T. Kamiyama, R. Kumai, Y. Tokura, Structural and magnetoelectric properties of Ga2-xFe xO3 single crystals grown by a floating-zone method, Phys Rev B Condens Matter Mater Phys. 70 (2004). https://doi.org/10.1103/PhysRevB.70.064426.

[8] A. Roy, R. Prasad, S. Auluck, A. Garg, Effect of site-disorder on magnetism and magneto-structural coupling in gallium ferrite: A first-principles study, J Appl Phys. 111 (2012). https://doi.org/10.1063/1.3688852.

[9] Y. Hong, J. Li, H. Bai, Z. Song, G. Li, M. Wang, Z. Zhou, Role of finite-size effect in BiFeO3 nanoparticles to enhance ferromagnetism and microwave absorption, Appl Phys Lett. 116 (2020). https://doi.org/10.1063/1.5132780.

[10] Z.J. Li, Z.L. Hou, W.L. Song, X. Da Liu, W.Q. Cao, X.H. Shao, M.S. Cao, Unusual continuous dual absorption peaks in Ca-doped BiFeO3 nanostructures for broadened microwave absorption, Nanoscale. 8 (2016) 10415–10424. https://doi.org/10.1039/c6nr00223d.

[11] Z.L. Hou, H.F. Zhou, L.B. Kong, H.B. Jin, X. Qi, M.S. Cao, Enhanced ferromagnetism and microwave absorption properties of BiFeO3 nanocrystals with Ho substitution, Mater Lett. 84 (2012) 110–113. https://doi.org/10.1016/J.MATLET.2012.06.050.

[12] Y. Li, H.J. Yang, W.G. Yang, Z.L. Hou, J.B. Li, H.B. Jin, J. Yuan, M.S. Cao, Structure, ferromagnetism and microwave absorption properties of la substituted BiFeO3 nanoparticles, Mater Lett. 111 (2013) 130–133. https://doi.org/10.1016/j.matlet.2013.08.061.

[13] Y. Li, W.Q. Cao, J. Yuan, D.W. Wang, M.S. Cao, Nd doping of bismuth ferrite to tune electromagnetic properties and increase microwave absorption by magnetic-dielectric synergy, J Mater Chem C Mater. 3 (2015) 9276–9282. https://doi.org/10.1039/c5tc01684c.

[14] G.M. Shi, D.W. Lu, Y. Zhang, Synthesis and Micro-Wave Absorption Properties of BiFeO3 Coated Fe Nanocapsules, Adv Mat Res. 712–715 (2013) 229–232. https://doi.org/10.4028/WWW.SCIENTIFIC.NET/AMR.712-715.229.

[15] A. Dutta, A. Gorai, D. Mandal, K. Mandal, Dielectric and microwave absorption properties of Na0.5Bi0.5TiO3–SrTiO3 system, Ferroelectrics. 583 (2021) 252–263. https://doi.org/10.1080/00150193.2021.1980324.

[16] K. Fujii, H. Kato, K. Omoto, M. Yashima, J. Chen, X. Xing, This journal is c the Owner Societies, Phys. Chem. Chem. Phys. 15 (2013) 6779. https://doi.org/10.1039/c3cp50236h.

[17] P. Ravindran, V. Ravindran, A. Kjekshus, H. Fjellvåg, O. Eriksson, Theoretical investigation of magnetoelectric behavior in Bi Fe O 3, Physical Review B - PHYS REV B. 74 (2006). https://doi.org/10.1103/PhysRevB.74.224412.

[18] Y. Li, X. Fang, M. Cao, Thermal frequency shift and tunable microwave absorption in BiFeO 3 family, Sci Rep. 6 (2016). https://doi.org/10.1038/srep24837.

[19] V.A. Khomchenko, D.A. Kiselev, M. Kopcewicz, M. Maglione, V. V. Shvartsman, P. Borisov, W. Kleemann, A.M.L. Lopes, Y.G. Pogorelov, J.P. Araujo, R.M. Rubinger, N.A. Sobolev, J.M. Vieira, A.L. Kholkin, Doping strategies for increased performance in BiFeO3, J Magn Magn Mater. 321 (2009) 1692–1698. https://doi.org/10.1016/J.JMMM.2009.02.008.

[20] G.F. Cheng, Y.H. Huang, J.J. Ge, B. Lv, X.S. Wu, Effects of local structural distortion on magnetization in BiFeO3 with Pr, Ba co-doping, J Appl Phys. 111 (2012) 07C707. https://doi.org/10.1063/1.3673821.

[21] X. Zhang, Y. Sui, X. Wang, J. Tang, W. Su, Influence of diamagnetic Pb doping on the crystal structure and multiferroic properties of the BiFeO3 perovskite, J Appl Phys. 105 (2009) 07D918. https://doi.org/10.1063/1.3079770.

[22] D.H. Wang, W.C. Goh, M. Ning, C.K. Ong, Effect of Ba doping on magnetic, ferroelectric, and magnetoelectric properties in mutiferroic BiFeO3 at room temperature, Appl Phys Lett. 88 (2006) 212907. https://doi.org/10.1063/1.2208266.

[23] P. Liu, Y. Huang, J. Yan, Y. Zhao, Magnetic graphene@PANI@porous TiO2 ternary composites for high-performance electromagnetic wave absorption, J Mater Chem C Mater. 4 (2016) 6362–6370. https://doi.org/10.1039/c6tc01718e.

[24] A. Gorai, R. Mandal, D. Mandal, Enhanced Electromagnetic Wave Absorption by Bi-Layered Nano-Hollow Spheres, IEEE Trans Magn. 58 (2022). https://doi.org/10.1109/TMAG.2022.3144601.

[25] Y. Zhang, H. bin Zhang, X. Wu, Z. Deng, E. Zhou, Z.Z. Yu, Nanolayered Cobalt@Carbon Hybrids Derived from Metal-Organic Frameworks for Microwave Absorption, ACS Appl Nano Mater. 2 (2019) 2325–2335. https://doi.org/10.1021/acsanm.9b00226.

[26] D. Mandal, A. Gorai, K. Mandal, Electromagnetic wave trapping in NiFe2O4 nano-hollow spheres: An efficient microwave absorber, J Magn Magn Mater. 485 (2019) 43–48. https://doi.org/10.1016/J.JMMM.2019.04.033.

[27] M. Han, X. Yin, L. Kong, M. Li, W. Duan, L. Zhang, L. Cheng, Graphene-wrapped ZnO hollow spheres with enhanced electromagnetic wave absorption properties, J Mater Chem A Mater. 2 (2014) 16403–16409. https://doi.org/10.1039/c4ta03033h.

[28] M. Cao, R. Qin, C. Qiu, J. Zhu, Matching design and mismatching analysis towards radar absorbing coatings based on conducting plate, Mater Des. 24 (2003) 391–396. https://doi.org/10.1016/S0261-3069(02)00119-X.

[29] M. Mehdipour, H. Shokrollahi, Comparison of microwave absorption properties of SrFe12O 19, SrFe12O19/NiFe2O4, and NiFe2O4 particles, J Appl Phys. 114 (2013). https://doi.org/10.1063/1.4816089.

[30] S.N.A. Rusly, I. Ismail, K.A. Matori, Z. Abbas, A.H. Shaari, I.R. Ibrahim, A study of multiferroic bifeo3/epoxy resin composite as potential coating materials for microwave absorption, in: Solid State Phenomena, Trans Tech Publications Ltd, 2020: pp. 20–25. https://doi.org/10.4028/www.scientific.net/SSP.307.20.

[31] C. Tian, Q. Yao, Z. Tong, H. Zhou, G. Rao, J. Deng, Z. Wang, J. Wang, Effects of Sm-doping on microstructure, magnetic and microwave absorption properties of BiFeO3, Journal of Rare Earths. 39 (2021) 835–843. https://doi.org/10.1016/j.jre.2020.05.003.

[32] M. Zhang, H.J. Yang, Y. Li, W.Q. Cao, X.Y. Fang, J. Yuan, M.S. Cao, Cobalt doping of bismuth ferrite for matched dielectric and magnetic loss, Appl Phys Lett. 115 (2019). https://doi.org/10.1063/1.5134741.

CHAPTER 6

CONCLUSION AND SCOPE FOR FUTURE WORK

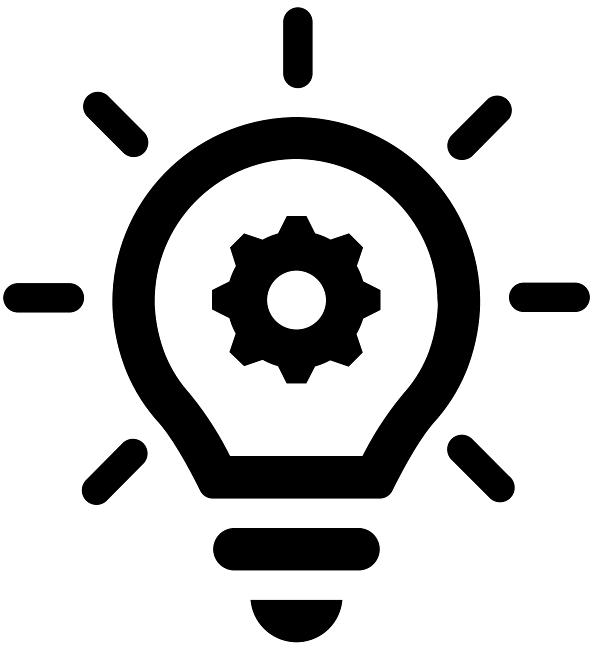

This chapter concludes the outcomes of this thesis and discusses the scopes of future studies.

6.1 EPILOGUE

It is observed that the barium and yttrium co-doping at the bismuth (Bi) site of $BiFeO_3$ (BFO) in the bulk morphology is responsible for a significant improvement in the grain and grain boundary resistances of the materials along with a reduction in conductivity which is very important aspect for the practical application of the materials. Stronger magnetization having a metamagnetic transition along with higher Neel temperature is also achieved by this doping. However, changing the morphology from bulk to nano further improves the magnetic properties of the materials eliminating the metamagnetic transition. Although no sign of ferroelectric domain switching was observed in the bulk form, the nano-structural form having lower yttrium doping concentration reports stronger domain switching. The conduction mechanism of the materials also largely changes from a oxygen vacancy dominated one in the bulk form to an electron dominated one in the nanoparticle form along with a significant enhancement in dielectric and magneto-dielectric properties. Further study of the similar co-doping in the thin film structure also confirms formation of good quality film having larger ferroelectric domains, stronger magnetic properties supported by the observation of larger magnetic domains than the undoped thin film of BFO. Effect of formation of composite with highly resistive (10^{16} Ω.cm) garnet, gadolinium gallium garnet ($Ga_5Gd_3O_{12}$), with another well-known magnetoelectric material with strong magnetoelectric coupling, gallium ferrite ($Ga_{2-x}Fe_xO_3$) is thoroughly investigated at different synthesis conditions. A reduction in leakage by four order of magnitude is achieved in the materials as result of reduction in grain size. Enhanced grain and grain boundary resistances along with significantly reduced conductivity is observed in the synthesized materials due to surrounding of $Ga_{0.8}Fe_{1.2}O_3$ (GFO) grains with highly resistive grains of $Ga_5Gd_3O_{12}$ (GGG). The magnetodielectric study reports enhanced magnetodielectric coupling in the composites along with a significant effect from the modified magnetostriction properties of the materials caused by the grain size reduction. GGG being paramagnetic in room temperature, no effect of the material is observed in the composites, leading us to study the effect of room temperature ferromagnet as well as highly resistive (10^{12} Ω.cm) garnet, Yttrium Iron Garnet ($Y_3Fe_5O_{12}$, YIG) on the formation of composite with GFO. An enhancement in magnetic curie temperature beyond room temperature is achieved through the formation of 0-3 particulate composite between GFO and YIG, along with highly resistive grain and grain boundary resistances. The dielectric properties greatly improved in the composites, while the conductivity significantly reduced. The large enhancement in the magnetodielectric properties of the composites also indicates stronger coupling between the magnetic and electric properties of the formed composites. Although the composites of garnets with gallium ferrite improves the properties from many aspects, GFO only shows ferroelectricity in thin film morphology and piezoelectricity in bulk morphology. This leads us to investigate the effect of formation of composite between YIG and a strong room temperature ferroelectric and diamagnetic material, solid solution of sodium bismuth titanate and strontium titanate ($Sr_{0.5}Na_{0.25}Bi_{0.25}TiO_3$, SNBT50). As expected, the composites exhibit magnetic properties due to the presence of ferromagnetic YIG. Observation of strong domain switching could be observed in the composites which intensified with increasing concentrations of YIG in the composites. The maximum applied electric field could as well be enhanced with increasing concentration of YIG indicating a reduced break down voltage suitable for practical use. Although no average magnetodielectric factor could be observed in the SNBT50 sample, large values of magnetodielectric factor are observed in the composites, increasing with increasing concentration of YIG. This observation proves the implementation of coupling between electric and magnetic properties by formation of ferroelectric SNBT50 and ferromagnetic YIG which intensifies with increasing concentrations of YIG. The microwave application of some of the magnetoelectric materials exhibiting high microwave absorption is also investigated and reported in the thesis in detail. It is observed that although the microwave properties of BFO is thoroughly investigated and reported over the years, another very significant magnetoelectric material, GFO, lacks such study. Therefore, the microwave application of GFO and BFO is studied in detail and the different observation of microwave properties based on the different structural parameters of BFO and GFO is reported. GFO is observed to have a reflection loss of -67.36 dB for an absorber length of 6.2mm attributed to its high dielectric constant and attenuation constant alongside an optimal impedance matching. Elemental substitution of Bismuth with optimised concentration of Barium and Yttrium in Bismuth Ferrite nanoparticles is observed to enhance the reflection loss of Bismuth Ferrite from -38.6 dB to -61.7 dB in a composite of length 7.5mm attributed to enhanced dielectric permittivity, magnetic permeability and the best balance observed between $\tan\delta_\varepsilon$ and $\tan\delta_\mu$ based on the match equation, $\tan\delta_\varepsilon = \tan\delta_\mu$. The SNBT50-YIG magnetoelectric composite exhibits a higher microwave absorption compared to its parent sample, SNBT50, due to its improved dielectric constant, magnetic permeability, and impedance matching. Gallium Ferrite, in comparison, is reported to have the maximum reflection loss of -67.36 dB among all magnetoelectric samples investigated. However, the effective bandwidth (RL > 10 dB) is able to reach higher value (7.02 GHz) compared to that of Gallium Ferrite (5.23 GHz). As a result, it can be stated that magnetoelectric gallium ferrite and single-phase barium and yttrium co-doped bismuth ferrite nanoparticles are viable candidates for use as microwave absorption materials. SNBT50-YIG composites have the potential for further improvement in the reflection loss and effective bandwidth of the material and attracts further research.

6.2 SCOPE FOR FUTURE STUDY

In many ferroelectric materials devoid of centrosymmetry, photovoltaic response (photovoltage and photocurrent) is stable in the polarization direction, i.e., the ferroelectric photovoltaic (FEPV) phenomenon has been observed. FEPV effect differs greatly from normal photovoltaic effect in semiconductor *p-n* junction in that the polarization electric field is the driving factor in FEPV devices to create photocurrent. Typically, the photovoltaic effect in ferroelectrics is caused by spontaneous polarization, and its photocurrent direction may be altered by the orientation of the polarization; this is a characteristic unique to FEPV devices.

As a light-absorbing ferroelectric layer, the photovoltaic effects of ferroelectric oxides such as $BiFeO_3$ (BFO)[1], $BaTiO_3$[2], and $LiNbO_3$[3] have been studied. Due to its low band gap (2.2-2.8 eV), strong ferroelectric polarization value exceeding 100 C/cm2, and one-of-a-kind multiferroic capabilities at ambient temperature, the photovoltaic features of the ferroelectric $BiFeO_3$ family have received considerable interest. It is known that substituting other elements at the A (Bi) and/or B (Fe) sites of $BiFeO_3$ could fine-tune the microstructure structure or electronic band structure of this compound, which has been confirmed as a viable method to increase the photovoltaic output of $BiFeO_3$ photovoltaic devices. In this thesis, we have studied Ba and Y co-doped BFO nanoparticles in its thin film morphology which exhibit good ferroelectric and magnetic characteristics. It will be extremely interesting to study the photovoltaic properties of this material. On the other hand, Gallium Ferrite is a less studied materials in the field of FEPV devices which also has a bandgap of around 2.1 eV[4], which is a very suitable energy band gap for the generation of photocurrent. Therefore, this material should be explored for the application as effective FEPV devices.

Vertically aligned nanocomposite thin films are one very interesting morphology to study exhibiting enhanced magnetoelectric coupling. The composites studied in this thesis can be further studied after fabricating according to this morphological structure.

Excited at high frequency region, ferromagnetic materials display the phenomenon known as ferromagnetic resonance (FMR) [5]. The FMR is connected to the notion that perturbation of the magnetization vectors or magnetic moments / spins will result in a relaxation of the magnetic vector to its new equilibrium position through a precession motion. Ferrite materials exhibit ferromagnetic resonance when the frequency of the precession equals the frequency of the excitation field, which commonly happens at microwave frequencies. Consequently, ferromagnetic resonance devices based on soft ferrite materials are employed in microwave signal processing devices including resonators, band-pass / band-stop filters and phase shifters operating at 1 – 70 GHz. These devices need a *dc* magnetic bias field for operation and frequency adjustment. However, magnetic field tuning has drawbacks such as slow operation, large noise, high power consumption, and limited miniaturization. Radar and communication technologies demand quick and low-power frequency-switching. By substituting the ferrite materials with a multiferroic bi-layer composite, it is able to tune FMR by electric field [6].

On the other hand, microwave phase shifters are crucial equipment for radar applications, telecommunications, and phased array antenna systems. Typical phase shifters often use semiconductors, ferroelectrics and ferrite materials. The functionality of ferrite phase shifters relies on Faraday rotation of electromagnetic radiation in magnetized ferrites, which is problematic since it necessitates application of strong magnetic bias fields. Another operational mechanism of ferrite phase shifters is based on the propagation of spin waves in planar ferrites, which is very desirable owing to its magnetic tunability across a broad frequency range of 1 to 26 GHz. In contrast to magnetic ferrite phase shifters, ferroelectric phase shifters are distinguished by rapid electric tunability, low power consumption, and very high loss at frequencies exceeding 5 GHz. By combining magnetic ferrite materials with ferroelectrics, it is feasible to create a multiferroic composite which functions as a dual phase adjustable microwave device and operates at frequencies far over 5 GHz.

The multiferroic samples studied in this dissertation, namely gallium ferrite $Ga_{0.8}Fe_{1.2}O_3$) and Ba and Y co-doped BFO nanoparticles ($Ba_{0.1}Bi_{0.87}Y_{0.03}FeO_3$) can be further investigated for the formation of multiferroic composites with ferromagnetic materials in two-dimensional thin film structures for the purpose of device applications. (1-x) $Sr_{0.5}Bi_{0.25}Na_{0.25}TiO_3$ (SNBT50) – x $Y_3Fe_5O_{12}$ (YIG) composites should also be researched in bi-layered thin film morphology in order to investigate the propagation of spin wave and their applicability as microwave resonators or phase shifters.

REFERENCES

[1] D.S. Knoche, M. Steimecke, Y. Yun, L. Mühlenbein, A. Bhatnagar, Anomalous circular bulk photovoltaic effect in BiFeO3 thin films with stripe-domain pattern, Nat Commun. 12 (2021). https://doi.org/10.1038/s41467-020-20446-z.

[2] N. Ma, Y. Yang, Boosted photocurrent in ferroelectric BaTiO3 materials via two dimensional planar-structured contact configurations, Nano Energy. 50 (2018) 417–424. https://doi.org/10.1016/j.nanoen.2018.05.069.

[3] S. Shahrokhi, W. Gao, Y. Wang, P.R. Anandan, M.Z. Rahaman, S. Singh, D. Wang, C. Cazorla, G. Yuan, J.M. Liu, T. Wu, Emergence of Ferroelectricity in Halide Perovskites, Small Methods. 4 (2020). https://doi.org/10.1002/smtd.202000149.

[4] S. Mukherjee, M. Mishra, P. Swarnakar, S. Sanwlani, S. Dash, A. Roy, Phase engineered gallium ferrite: a promising narrow bandgap, room-temperature ferroelectric, Mater Adv. 3 (2022) 3980–3988. https://doi.org/10.1039/D2MA00089J.

[5] C. Kittel, On the Theory of Ferromagnetic Resonance Absorption, Physical Review. 73 (1948) 155–161. https://doi.org/10.1103/PhysRev.73.155.

[6] A.A. Semenov, S.F. Karmanenko, V.E. Demidov, B.A. Kalinikos, G. Srinivasan, A.N. Slavin, J. V Mantese, Ferrite-ferroelectric layered structures for electrically and magnetically tunable microwave resonators, Appl Phys Lett. 88 (2006) 033503. https://doi.org/10.1063/1.2166489.